INVESTIGATION OF LOCAL FAILURE MECHANISMS OF INVERTED-T BENT

CAPS AND STRENGTHENING USING CFRP SHEETS

A Dissertation

by

JILONG CUI

Submitted to the Graduate and Professional School of
Texas A&M University
in partial fulfillment of the requirements for the degree of

DOCTOR OF PHILOSOPHY

Chair of Committee,	Stefan Hurlebaus
Co-Chair of Committee,	Anna C. Birely
Committee Members,	John B. Mander
	Jeffrey Falzarano
Head of Department,	Zachary Grasley

December 2021

Major Subject: Civil Engineering

ABSTRACT

Prevalence cracks on in-service inverted-T bent caps were reported over the past decades. These un-desirable cracks formed at the re-entrant corner of inverted-T bent caps are an indication of the local structural deficiencies. To address such a concern, this study presents an experimental and analytical investigation on local failure mechanisms of inverted-T bent caps with emphasis on punching shear, strengthening ledge- and hanger-deficiencies with CFRP, and an analytical study on the impact of various reinforcement layouts on the local behavior of inverted-T bent caps.

Punching shear failure is critical to the ledge of inverted-T bent caps as the ledge is sustaining a concentrated load from the girders with a shallow section. The punching failure mechanisms of the inverted-T bent cap ledges were experimentally investigated with bearing pad size as the primary variable. A nonlinear finite element model was also developed to perform correlative studies between analytical and experimental investigation. The analysis results revealed that enlarging the size of the bearing pad can improve the serviceability and the ultimate punching shear resistance of the inverted-T bent cap ledges. The capacity was also found to be affected by the eccentricity of the bearing pad from the face of the web. The code given estimation on the punching shear capacity was examined by the experimental results and revealed to be conservative. A practical modification to improve the accuracy of capacity estimation was proposed.

Prevalence of cracks in many of in-service inverted-T bent caps was observed and raised a concern to the structural sufficiency of the inverted-T bent caps that were built in

early days. These bent caps may be considered structurally deficient when evaluated using the current design criteria and/or have insufficient strength to accommodate an increase in traffic. To this end, FRP strengthening techniques for in-service inverted-T bent caps with local weakness were developed and experimentally validated. The experimental results showed that the FRP retrofits were able to eliminate the local deficiencies of inverted-T bent caps. The retrofit schemes also benefited the bent caps by improving the serviceability, displacement ductility, and ultimate strength. The design approach of the developed FRP retrofit was provided as a guidance.

Nonlinear finite element model developed for the punching failure mechanism simulation was further calibrated to capture the remaining local failure mechanisms – ledge and hanger failures. A parametric study was carried out to investigate the impact of four different reinforcement layouts on the local behavior of inverted-T bent caps. The variations were given to the configuration of the ledge reinforcement and the spacing of the ledge and hanger reinforcement around the loading region. The analysis results demonstrated that the reinforcement layouts have a slight impact on the strength response of the bent cap while the impact on the crack control of the section was significant. Use of diagonal ledge bar instead of the horizontal ledge bar or combined use of the two layouts around the loading region was recommended by means of crack control.

ACKNOWLEDGEMENTS

responsibility of the authors and do not necessarily represent the official views of the

sponsoring agency.

TABLE OF CONTENTS

LIST OF FIGURES

xi

LIST OF TABLES

1. INTRODUCTION

1.1. Motivation

Inverted-T bent caps are often used to economically satisfy geometric constraints and to provide an aesthetically pleasing appearance. Figure 1-1 shows an overview of inverted-T bent caps that are part of the substructure. Unlike a conventional top-loaded beam, the loads on inverted-T bent caps are introduced into the bottom flange, thereby creating a loading condition not generally encountered in concrete construction. The stem then requires stirrups acting as hangers to transfer the load to the top tension chord. The bottom flanges extend from the web working as a ledge beam to seat the girders, resulting in combined moment and shear at the face of web. The ledges under such complex stress state may encounter some of the localized mechanisms at the regional area around the loading points. Design of inverted-T bent caps should prevent the local failures of the ledge to ensure the bent cap section develop a full strength.
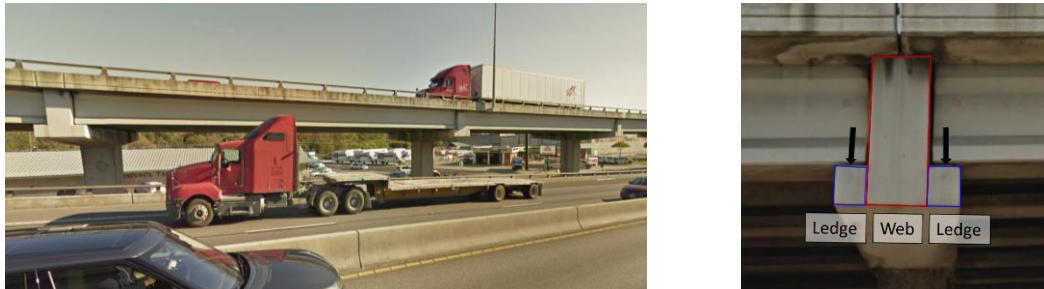
Figure 1-1. In-Service Inverted-T Bent Caps.

The design approach of inverted-T bent caps was changed in the past years with a deeper understanding of the structural behavior. Many of the inverted-T bent caps built in

early days are structurally deficient when evaluated against the current design specifications and/or lack of adequate strength to support planned increases to live load demands. Cracks observed in in-service inverted-T bent caps, as shown in Figure 1-2, describe such a weakness. These cracks typical form at the re-entrant corners at web-ledge interface and their presence is a possible indication of the structural deficiency of the bent caps.

For the design of new structure, the local weakness of inverted-T bent caps should be fully addressed not only in term of ultimate strength but also the service criteria for crack controlling. If the weakness is a part of an existing structure, a retrofit is required as full replacement of the structurally deficient bent caps is not practical.

Figure 1-2. Observed Cracks on In-Service Inverted-T Bent Caps (US 290 in Austin).

The study presented here is a part of a larger study by Hurlebaus et al. (2018a,b,c) to conduct an experimental investigation on the local behavior of inverted-T bent caps and corresponding strengthening techniques. A prototype in-service inverted-T bent cap was evaluated against the current specification and a possible local weakness was identified. Eight half-scale test specimens were then designed based on the prototype bent caps and

altered to highlight the different local failure mechanisms of inverted-T bent caps. Eighteen potential retrofit solutions were designed, rated, and ranked. The top six ranked retrofit solutions were experimentally investigated. Thirty-three individual tests were conducted to investigate the local failure mechanisms and six strengthening solutions. In this dissertation, the following test results are summarized:

- Punching shear strength of inverted-T bent cap ledge,

- CFRP strengthening of inverted-T bent caps with local weakness,

In addition to the analysis of experimental data, this dissertation expands on the study by Hurlebaus et al. (2018a,b,c) to include finite element modeling to capture local failure mechanisms and to investigate alternative designs to improve the service level performance of new designs.

1.2. Objectives and Tasks

The primary objective of this dissertation is to demonstrate the satisfactory performance of retrofit solutions for existing inverted-T bent caps, and to identify design aspects that can improve structural performance. The objectives are achieved through experimental and numerical analysis. The detailed research tasks include:

1) Compile a review on the structural behavior, design approach, and strengthening of inverted-T bent caps.

2) Evaluate in-service inverted-T bent caps against current design specifications incorporate with field inspection to identify any deficiencies that an in-service bent cap may have.

3) Investigate detailed failure mechanisms of test specimens with local weakness through ultimate load testing.

4) Develop nonlinear finite element models to simulate local behavior of inverted-T bent caps and perform analytical investigation on parameters that may impact local failure mechanisms of inverted-T bent caps.

5) Design and validate satisfactory performance of strengthening techniques applicable to existing inverted-T bent caps through experimental testing.

    a. Investigate punching shear performance of inverted-T bent cap ledges with different size bearing pads.

    b. Evaluate effectiveness of CFRP strengthening techniques applied to inverted-T bent caps.

6) Develop design recommendations for inverted-T bent caps with the proposed retrofit solutions.

1.3. Significance

Cracks observed on in-service inverted-T bent caps indicate a possible structural deficiency. The focus of the prior studies on inverted-T bent caps were primarily given to the beam shear behavior while limited research attention was put on the local failure mechanisms. This research is carried out to address the gap by providing valuable information through an experimental and analytical investigation on the local behaviors of inverted-T bent caps and strengthening using CFRP sheets.

The local failure mechanisms of inverted-T bent caps – hanger, ledge, and punching shear – were highlighted in the specimens that identical in dimension but altered in reinforcement and loading distribution. Ultimate testing of these specimens providing both the elastic and post-elastic behaviors including stiffness, deformation and cracking patterns which are essential for understanding the complete structural behavior of the inverted-T bent caps with local weakness at different loading conditions. The distinguished local failures of the specimens provide guidance to identify the failure mechanisms associated with the cracks observed on in-service structures. The recommendations developed for evaluating the capacity of in-service inverted-T bent caps are enabling a more realistic estimation.

The experimental program validates the effectiveness of the retrofit solutions developed to address the local weakness of inverted-T bent caps expands the limited data on strengthening of inverted-T bent caps. The design recommendation developed for the proposed retrofit solution provide guidance for the future implementation. Once implemented, the solutions are expected to provide increased serviceability and capacity to existing structures which enables the structure to accommodate higher traffic demand and have an extended service life.

The nonlinear finite element model (FEM) coupled with the experimental results provides a powerful and cost-effective tool for investigating the structural behavior of inverted-T bent caps. The result of the analytical investigation provides valuable insight to the potential parameters that may impact the performance of inverted-T bent caps.

1.4. Outline of Dissertation

Chapter 2 provides a general review on the structural characteristics of inverted-T bent caps and FRP strengthening on inverted-T and T-shaped beams.

Chapter 3 presents an evaluation of inverted-T bent caps in Austin, Texas. The load carrying capacities of in-service bent caps were evaluated against the current specification.

The remaining chapters, with the exception of the conclusions in Chapter 7, are structured as drafts for manuscript submission to peer-reviewed journals.

Chapter 4 provides an analytical study on the local behavior of inverted-T bent caps. Detailed correlative study between the FEM and experimental results are presented. A parametric study is performed to explore the impact of various reinforcement layouts on the local behavior of inverted-T bent caps.

Chapter 5 presents an experimental investigation of the punching shear mechanisms of inverted-T bent caps with different size of bearing pads. A nonlinear finite element model (FEM) is used to expand the experimental findings to investigate additional parameters not tested in the laboratory.

Chapter 6 presents an experimental investigation of CFRP strengthening of inverted-T bent caps. Two different retrofit schemes are developed and validated by experimental testing. A design approach for the retrofit solution is also provided.

The last chapter, Chapter 7 summarizes the overall research, provides conclusions drawn from the study, and makes recommendations for design and future research.

2. LITERATURE REVIEW

To develop the strengthening methods for the inverted-T bent caps, better understanding of the concept of the inverted-T bent caps is required. In this chapter, previous studies are reviewed to identify relevant technical information on the performance and failure mechanisms of inverted-T bent caps and FRP strengthening of RC structures. The experimental investigation on the structural behavior and strengthening solution of inverted-T bent caps performed by Hurlebaus et al. (2018a,b,c), which formed the base of this study, was also reviewed in detail. More correlated reviews on the previous studies related to the current research are provided in each chapter.

2.1. Structural Behavior of Inverted-T Bent Caps

The first study that provided a comprehensive understanding of the structural behavior of inverted-T bent caps was carried out by Furlong et al. (1971). Twenty-four tests were conducted on six inverted-T bent cap specimens (two full-scale and four one-third scale) to investigate the load carrying mechanisms and reinforcement details of inverted-T bent caps. In addition to testing reinforcement details specified by the Texas Highway Department at the time, the researchers investigated the alternative reinforcement designs shown in Figure 2-1. Based on the test results, the authors noted that (a) loads must be supported by stirrups acting as hangers to transmit vertical forces into the body of the web, (b) flange reinforcement perpendicular to the web is necessary to deliver the flange forces to the hangers, and (c) the application of forces to flanges creates greater torsional forces on the web. The use of diagonal ledge bars was expected to perform behavior than the

horizontal bar, however, was not recommended because of the construction efficiency as the two layouts demonstrated a similar ultimate capacity.
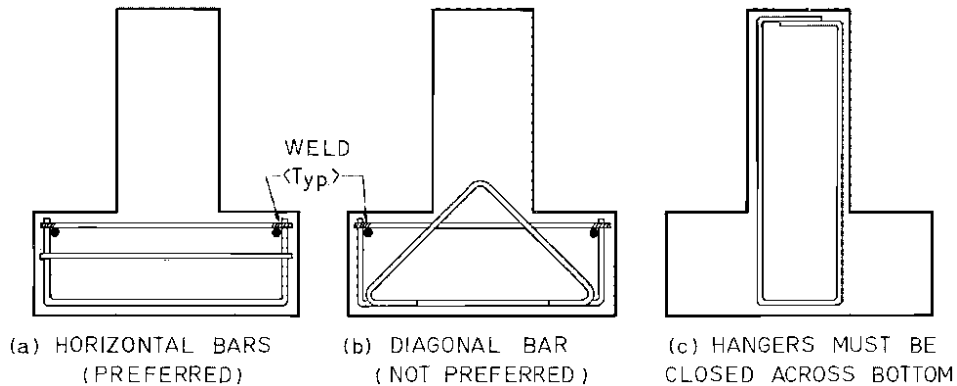
Figure 2-1. Reinforcement Details of Inverted-T Bent Caps (Reprinted from Furlong et al., 1971).

Furlong and Mirza (1974) studied the strength and serviceability of inverted-T bent caps that were subjected to a combination of flexure, shear, and torsional loads. Load tests were conducted on one-third scale prestressed and non-prestressed inverted-T bent specimens. The tests revealed that the prestressed concrete members exhibited fewer cracks under service load and had lower stresses in the transverse reinforcement. Based on the experimental observations, the authors presented an analysis methodology for the reinforcement details and design of inverted-T beams under the consideration of the observed failure mechanisms. The authors categorized the failures of inverted-T beams as: flexure, web-shear, torsion, hanger, ledge and punching failure. The first three failures were the common failure modes encountered in the conventional RC beams whereas the hanger, ledge and punching failure was the localized failures that may take place in the regional area of the ledge around the loading points. Figure 2-2 sketches these local failure

8

mechanisms. Hanger failure is the vertical separation of the bottom flange from the web. The separation begins at the web-ledge interface around the loading point. More hanger cracks (horizontal cracks on the web) will occur as the failure intensified. Excessive vertical deformation will be caused by the failure at the web-ledge interface. Ledge failure is the separation of the bottom flange deform outward and downward from the web due to the combined bending and shear. Punching shear failure is the diagonal tension failure in the concrete underneath the bearing pad due to the excessive concentrated load applied on top of the ledge. The failure is evident from the diagonal cracks emanating from the edges of the bearing pad. As inverted-T bent caps may be susceptible to local failures, the authors recommended that design of the bent cap should provide sufficient web stirrups to act as hangers to transmit loads from the ledge to the web, the transverse reinforcement strength of the ledge must be sufficient to maintain flexural tension and shear friction resistance at the face of web, and the ledge must by sufficiently deep to avoid punching shear failure.

Zhu et al. (2001), Zhu and Hsu (2003), and Zhu et al. (2003), as part of TxDOT Project 0-1854, investigated the causes of diagonal cracking at reentrant corners between the ledges and the webs of an inverted-T bent cap under service load. The authors attributed the cracks to the ultimate strength design methodology that was adopted in the design of inverted-T bents, which did not address cracks at service loads. The study was carried out in three phases. In Phase 1 (Zhu et al., 2001), a two-dimensional (2D) compatibility-aided strut-and-tie model (CASTM) was utilized to predict diagonal crack widths in the interior portion of the inverted-T bent caps. The model was compared to the results from seven experimentally tested 2D specimens that represented the dapped ends

of a bridge girder. In Phase 2 (Zhu and Hsu, 2003), a three-dimensional (3D) CASTM was utilized to predict diagonal crack widths at the end faces of the exterior portion of the inverted-T bent caps. Experimental results from large-scale 3D tests that represented the end portion of an inverted-T bent cap were used to calibrate the 3D CASTM model. In the final phase (Zhu et al., 2003), two full-scale bent cap specimens were tested to investigate impact of hanger spacing and bearing pad size on the service behavior. The following observations were made: (a) the CASTM predictions are well supported by test results; and (b) instead of checking a crack width at service limit state and comparing it to a specified value, the force producing a critical crack width can be calculated and compared to the load designed for service limit state.
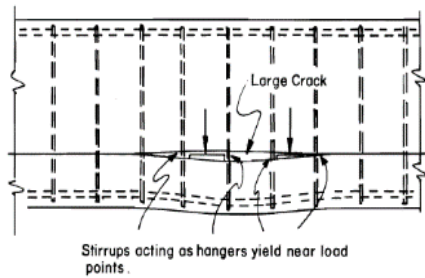
(a) Hanger failure   *(b) Ledge failure*
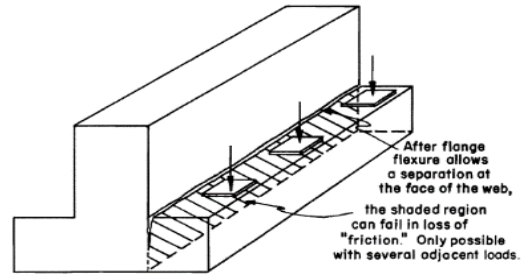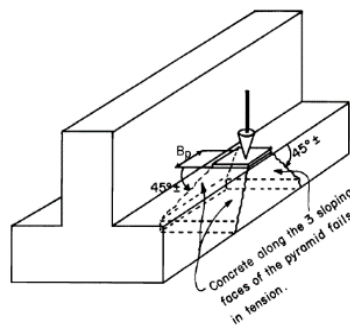
(c) Punching failure

Figure 2-2. Local Failure Mechanisms of Inverted-T Bent Caps (Reprinted from Furlong and Mirza, 1974).

10

Larson et al. (2013) investigated the behavior of reinforced concrete inverted-T straddle bent cap specimens to investigate the causes of diagonal cracking in the ledges. Thirty-three 27 ft 8 in. long specimens were tested to evaluate the impact of ledge depth and length, spacing of web reinforcement, number of point loads, depth of the member, and span and depth ratio. The experimental results showed that increasing the ledge length along the length of the straddle bent increased the shear strength of the inverted-T beams and delayed the appearance of the first diagonal crack, whereas increasing the ledge depth did not have any significant effect on the strength. It was noted that for the diagonal cracking load of inverted-T beams, the primary variables were the shear area and the span-to-depth ratio. For the maximum width of diagonal cracks in inverted-T beams, the primary variable was the quantity of web reinforcement crossing the principal diagonal crack plane. Based on findings from the experimental study, and field inspections of selected field structures, the authors concluded that several existing structures had already been subjected to approximately 70–85 percent of their ultimate capacity. It should be noted that the specimens were designed to emphasize the web-shear failure. During the tests, it was observed that most of the specimens displayed a web shear failure. However, five local failures including two ledge failures and three punching shear failures were also observed.

Garber et al. (2017) summarized these local failures observed during the testing as a subsequent study. A 3-D strut-and-tie (STM) model was proposed to estimate the sectional capacities of inverted-T beam. Based on the analysis, the use of STM yielded a

reasonable prediction on the punching failures but was unable to predict ledge failure modes.

Deifalla and Ghobarah (2014) investigated the behavior of inverted-T reinforced concrete beams under combined shear and torsion loads. Three inverted-T beams were tested under different ratios of applied torque to applied shear. The test setup was designed to fail the specimens in combined shear and torsion. The behavior was affected by the value of the torque-to-shear ratio. Decreasing the applied torque to the applied shear force ratio resulted in the following: (a) a significant reduction in the spacing between diagonal cracks, strut angle of inclination, cracking and ultimate torque, and flange and web stirrup strain; (b) a significant increase in the failure and cracking load, post-cracking torsional rigidity, and cracking and ultimate shear; and (c) a reduction in the efficiency of the stirrup, causing beam failure due to concrete diagonal failure rather than stirrup yield. The authors also developed an analytical model in which the inverted-T beam was divided into several rectangular subdivisions and each subdivision was analyzed independently for combined applied shear and torsion loads. The proposed analytical model showed good agreement with the experimental results for the behavior of flanged beams under combined actions.

Zhou et al. (2020) analytically studied the structural behavior of skewed inverted-T bent caps. A nonlinear finite element model validated using the experimental from Zhu et al. (2003). The impact of shear reinforcement arrangement in the transition region, spacing of shear reinforcement, skew angle of bent cap, and the loading position on the structural behavior of skewed inverted-T bent cap was studied. Based on the analysis, the reinforcement arrangement and spacing was found to have limited effect on the ultimate

load-carrying capacity and ductility of the bent cap while the skew angle significantly affected the structural performance. The loading position, defined as the distance from the center of bearing pad to the free end of the bent cap at the exterior region, was also affected the structural behavior. Increasing the end distance of the bearing pad improved the structural performance of bent cap. The authors noted that the current criteria for the end distance may not be sufficient for skewed bent caps and proposed a practical modification based on the analysis results.

2.2. FRP Retrofit of Reinforced Concrete Structures

ACI 364.2T (ACI Committee 364.2T, 2008) presents methods to increase the shear capacity of existing reinforced concrete structures. Several alternatives are discussed: (a) external reinforcement provided by steel rods, reinforcement bars, post-tensioning, or steel plates; (b) section enlargement using concrete, shotcrete, reinforced concrete, or mortar bonded to the concrete element; (c) internal reinforcement provided by steel or fiber reinforced polymer (FRP) reinforcement installed by drilling holes, and the dowels being effectively grouted; (d) near surface-mounted reinforcement provided by steel or FRP rods into grooves; (e) supplemental members; and (f) externally bonded FRP plates and strips.

Among the various strengthening techniques, the use of externally bonded FRP strips is an attractive strengthening means for inverted-T bent caps which have an irregular sectional shape. The tailorable characteristics of the FRP strips enables flexural ways to strengthen an inverted-T bent cap section. FRP strengthening on the shear capacity of conventional top-loaded reinforced concrete beams has been investigated and validated

by many previous studies. However, the application of FRP strengthening on an inverted-T section is limited in the literature.

Galal and Sekar (2008) carried out an experimental study on CFRP strengthening of inverted-T bent caps. Four one-third scale specimens were designed to highlight different failure modes. Two specimens were designed to emphasize the combined web-shear and hanger weakness while the other two specimens were designed to emphasize the web-shear and punching shear weakness, respectively. The specimen simulated an interior loading region with two girder lines. The specimens were loaded until damage was initiated, then retrofitted with the CFRP sheets and tested to ultimate failure. Figure 2-3 shows the CFRP retrofit schemes used for the specimen with combined web-shear and hanger weakness. An inverted U-wrap was typically used to cover the upper portion of web. Two U-wraps were used in the transverse direction to the cover the bottom flange from each end. Mechanical and FRP anchors were used at mid-height of the web, corner at the web-ledge interface, and mid-width of the ledge to provide anchorage to the CFRP sheets. The anchors at the web-ledge interface were inserted diagonally to avoid de-bonding of CFRP at re-entrant corners. The experimental results demonstrated that the CFRP retrofits were effective in improving the displacement ductility and load-carrying capacity. The CFRP also eliminated the highlighted failure modes of the specimens. The anchored CFRP retrofits demonstrated a better performance compared to the CFRP sheets without anchors.

While the study provided valuable information, the proposed CFRP strengthening schemes may have limited application when considering a practical application to in-

service inverted-T bent caps. CFRP sheets that wrap over the top may not be practical to install if the deck is continuous at bent cap. The diagonal anchor bolts at the web-ledge interface may worsen the inverted-T section as it is the critical region subject to cracking. The cantilever part (exterior) of the bent cap which were having cracking issues were not addressed. Besides the magnitude of strength increase, an application of FRP retrofit on in-service inverted-T bent caps should be designed under the consideration of factors such as in-service conditions, dimensional and clearance constrains, and equipment availability.
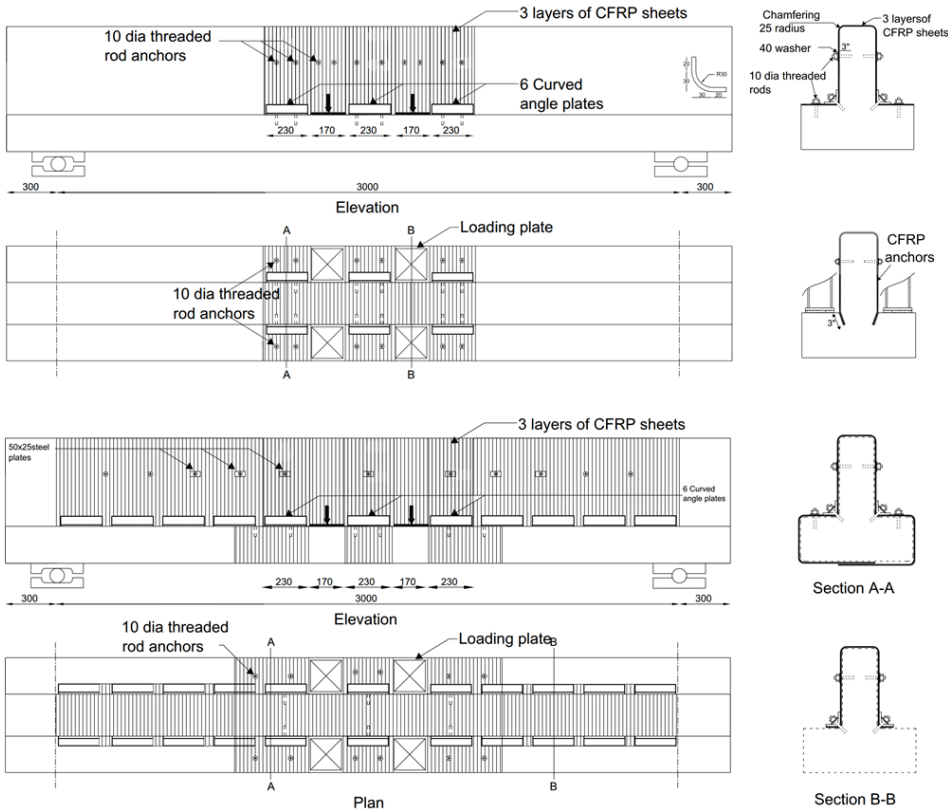
Figure 2-3. CFRP Rehabilitation for Inverted-T Specimen (Reprinted from Galal and Sekar, 2008).

Since the application of FRP retrofit on inverted-T bent caps is scarce, use of FRP retrofits on T-shaped RC beams were also reviewed as a review of the FRP retrofit on the T-beams is expected to provide relevant technical information on the FRP application on RC beams with irregular sectional shapes.

Shahawy and Beitelman (1999) investigated the effectiveness of externally bonded CFRP sheets for flexural strengthening of RC T-beams using experimental tests. The specimens had a flange thickness of 2.32 in., a flange width of 23 in., an overall height of 17.5 in., and a tapered web thickness of 5.91 in. at the flange and 3.58 in. at its bottom. Sixteen specimens, ten with static loading and six with fatigue loading, were tested in this study. The webs were partially or fully wrapped with one, two, three, or four layers of CFRP sheets. Two-point loads were applied at the top of the T-beams. Both the partially and fully wrapped specimens were loaded incrementally to failure for the static test. Fatigue testing was performed using fully wrapped specimens. The fatigue loading was sinusoidal and ranged from 25 percent to 50 percent of the capacity of the control specimen at a frequency of 1 Hz. Based on the experimental results, it was evident that the externally bonded CFRP laminates were effective in improving both static and fatigue performance of RC T-beams. The full wrapping technique was found to be more effective than the partial wrapping technique for increasing capacity. However, the limited number of tests failed to support a definitive conclusion.

Basler et al. (2003) investigated the use of bonded CFRP L-shaped plates as a method of shear strengthening reinforced concrete beams. The L-shaped brackets had a 90-degree bend with an internal radius of 1 in. and were about 0.055 in. thick. For

improved anchorage, the ends of the plate legs to be anchored were coated with a thin layer of adhesive. Advantages of L-shaped CFRP plates include ease of installation, light weight, resistance to corrosion, high strength, predictable mechanical properties, and ability to be produced consistently in a manufacturing unit. Test results indicated that the L-shaped plates were effective in improving the shear capacity of tee beams. In addition, the L-shaped CFRP plates remained undamaged, but local de-bonding was observed on the sides of the beam.

Nanni et al. (2004) experimentally investigated full-scale prestressed concrete bridge girders strengthened with externally bonded precured CFRP laminate. Two damaged prestressed concrete double-T-shaped girders were taken from an overloaded bridge in Kansas and cut longitudinally to provide four single-T specimens. The specimens had a flange thickness of 5 in., a flange width of 36 in., an overall height of 23 in., and a web thickness of 4.5 in. The total length of the specimen was 40 ft. One specimen was not strengthened and tested as the benchmark. Two specimens were strengthened with FRP laminates in flexure, while the remaining specimen was strengthened in flexure with FRP laminates and in shear with near-surface mount (NSM) CFRP rectangular strips, as shown in Figure 2 10 The CFRP strips were installed into 0.25 by 0.75 in. grooves with an incline of 60 degrees. The shear capacity of the specimen increase for shear and flexure strength could not be obtained since the specimen failed due to flexure FRP laminate de-bonding. However, it was observed that this specimen had a substantially larger ultimate capacity than the specimens strengthened only in flexure.

17

Higgins et al. (2009) and Howell (2009) experimentally investigated various shear strengthening techniques on T-shaped RC girders including epoxy injection, external and internal steel stirrups, surface bonded CFRP stirrups, and near surface mounted (NSM) FRP. Fifteen full-scale specimens designed to emphasize shear weakness were tested under four-point bending loads. The T-shaped specimens were placed upside-down and loaded at the top of the web. The strengthening techniques were applied to the specimens after the first cracking. From the experimental results, the strengthening techniques effectively improved the shear capacity of the specimens except the epoxy injection and NSM FRP. The authors noted that reduce the spacing of NSM FRP strips may improve the performance of the retrofit solution. The effect of internal steel stirrups on improving the long-term service life performance of the structure was found to be outstanding among the various retrofits.

Galal and Mofidi (2010) experimentally investigated the use of mechanically anchored un-bonded dry carbon fiber (CF) sheets for the shear strengthening of T-beams. The method essentially eliminated the de-bonding of epoxy bonded CFRP sheets and fully utilized the capacity of dry CF sheets. In this technique, the dry CF sheets were wrapped around and bonded to steel rods, which in turn were anchored to the corners of the web-flange intersection of the T-beam using bolts. The higher tensile strength and modulus of elasticity of dry CF compared to CFRP helped increase the shear strength of the T-beam.

Deifalla and Ghobarah (2010a) experimentally investigated techniques to strengthen T-beams using CFRP. Six T-beam specimens, two control and four strengthened beams, were tested under combined torsion and shear loading. Four different

CFRP configurations – (a) anchored U-wrap, (b) extended U-wrap, (c) full wrapping, and (d) combination of full wrapping and extended U-wrap—were used to strengthen the damaged T-beams. Techniques (a) and (b) were used when the flange was inaccessible, while techniques (c) and (d) were used where there was unrestricted access to the entire beam. From the experimental results, it was noted that the retrofit techniques significantly improved the shear torsion carrying capacities, post-cracking stiffness, and deformability of the retrofitted T-beam compared to the control specimen. Although the full wrapping techniques were the most effective, the implementation of these techniques is rare because of limited access. The U-wrap, which is the most widely used technique that is applicable to various applications, was the least effective solution. However, the extended CFRP U-wrap solution proved to be a viable and effective alternative and considerably improved the ductility when compared to the U-wrap.

Deifalla et al. (2013) investigated the effectiveness of FRP as a method to externally strengthen the flanges of beams subjected to torsion. Unanchored U-wrap strips, anchored U-wrap strips, and extended U-wrap strips were investigated. Various wrapping configurations, like continuous wrapping, vertical strips, and inclined strips were considered. As expected, the anchored solution resulted in greater ultimate strength and ductility compared to the unanchored solutions. The anchored inclined U-wrap strip showed results comparable to the inclined fully wrapped strips. In addition, the extended vertical U-wrap was found to be more effective compared to the vertical U-wrap strip technique.

DeLorenzis and Nanni (2001) investigated shear strengthening of reinforced concrete T-beams by near surface mounted (NSM) CFRP. Eight RC beam specimens with a T-shaped cross-section were tested. Specimens were tested under four-point bending. For the strengthened specimens, vertical or 45-degree grooves were saw-cut on the surface of both web sides over the full depth. Deformed CFRP rods were then embedded in the epoxy-filled grooves. The examined variables included spacing of the rods, strengthening pattern, end anchorage of the rods, and presence of internal steel shear reinforcement. It was found that the NSM CFRP rods were effective in increasing the shear strength capacity of the reinforced concrete T-beams with and without shear reinforcement. The specimen with CFRP rods at 45-degrees exhibited the largest strength increase. One of the failure modes observed in the strengthened specimen was the de-bonding of one or more CFRP rods due to splitting of the epoxy cover. This mechanism could be prevented by increasing the bond length by embedding the bars in the flange or using 45-degree rods at a sufficiently close spacing. Splitting of concrete cover of the longitudinal reinforcement was observed as the controlling factor in beams where de-bonding was prevented.

Dias et al. (2007) carried out an experimental study on low-strength concrete T-beams reinforced in shear with near surface mounted (NSM) CFRP strips. Three control specimens without CFRP reinforcement and 10 NSM shear-strengthened specimens that had different amounts of CFRP strips at 45 degrees, 60 degrees, and 90 degrees were tested. Specimens had internal steel stirrup spacing of 11.81 in. or 7.09 in. CFRP strips applied at 45-degrees and 60-degrees showed better performance than the one at 90-degrees. The authors noted that increasing the amount of internal steel stirrups

20

proportionally reduces the contribution of the CFRP strips and reducing the concrete strength can increase the likeliness of detachment of the cover containing the glued laminates.

Dias and Barros (2008) tested additional T-beams reinforced with near surface mounted (NSM) CFRP to evaluate the influence of the percentage and inclination of the CFRP laminates on the effectiveness of the NSM shear strengthening. The dimensions, CFRP, and groove size of the test specimens were the same as the specimens reported in Dias et al. (2007). Specimens with no internal shear reinforcement and internal steel stirrups spaced at 5.12 in. and 11.81 in. on the center were tested in this study. Inclination angles of 45-degrees, 60-degrees, and 90-degrees were investigated. Three quantities of NSM CFRP were applied to each inclination angle. Specimens were subjected to service loads based on a deflection of L/400 and maximum loads. Based on the test results, it was determined that the CFRP strips with an inclination angle of 60 degrees were the most effective among the adopted shear strengthening arrangements, and the strips at 45-degrees were more effective than those at 90-degrees. Retrofitted specimens, with and without internal steel stirrups spaced at 5.12 in. were able to achieve nearly the same maximum load. The authors also noted that the NSM-CFRP reinforcing contributed significantly to the stiffness of the specimen after the formation of the shear crack. Similar to previous studies by Dias et al. (2007) and Dias and Barros (2008), Dias and Barros (2010) tested T-shaped RC beams reinforced in shear with NSM CFRP. In addition to NSM reinforcing, the tests also included specimens strengthened in shear with an externally bonded reinforcement (EBR) technique. It was found that the NSM

21

strengthening technique more effectively increased the shear capacity of the specimens than did the EBR strengthening technique.

Goebel et al. (2012) experimentally investigate shear strengthening of T-shape girders with near surface mounted (NSM) CFRP. Ten full-sized specimens were tested. Two of them were tested as T-shape and loaded on top of the flange whereas the other eight were inverted and loaded on top of the web. The specimens were tested under four point bending load. Each specimen was designed to have strong and weak side. The strong side of the specimen was over-reinforced while only one-third amount of shear reinforcements were provided to the weak side to force the failure took place at the weak side. The specimens were tested to have first cracking and retrofitted with vertical oriented NSM CFRP at the weak side and tested up to failure. Experimental results demonstrated that NSM CFRP significantly improved the shear capacity of the specimens. The performance of the retrofits barely affected by the fatigue loading and environmental exposure. The authors also noted that ACI 440.2R-08 gives a conservative estimation for the strength of NSM CFRP retrofitted specimens and provided recommendation for modifications.

Chaallal et al. (2011) compared three different FRP retrofit techniques on shear strengthening of RC T-beams. Three types of full-scale specimens were designed to have no transverse reinforcement, 6.9 in. and 10.2 in. spaced transverse reinforcement. The specimens were loaded on top of the flange under three point bending load. The FRP strengthening techniques adopted in the study were: embedded through section (ETS) FRP rod, externally bonded (EB) FRP sheet, and near surface mounted (NSM) FRP rod. The

22

ETS FRP rod method was use of FRP rod embedded in the middle of the cross-section. A vertical hole was drilled through the section at the center. The hole was then filled with epoxy adhesive and FRP rod was installed into the hole. The EB FRP sheet was a conventional method where U-wrap FRP sheet was used to wrap the lower portion of the web. The FRP sheets were applied without any anchorage provided. The NSM FRP rod was use of FRP rod filled into the vertical grooves made on the outside surface of the web. The specimens with EB FRP sheets and NSM FRP rods were subject to de-bonding and concrete cover delamination whereas the ETS FRP rods demonstrated a better performance without such issues. The effectiveness of ETS FRP rods were outstanding when the beam has fewer transverse reinforcements.

Breveglieri et al. (2015) experimentally investigate the embedded through section (ETS) methods with steel and CFRP rods on shear strengthening of RC T-beams. The steel or CFRP rods were embedded into the drilled holes located at the center of the cross-section that was filled with epoxy adhesive. The spacing and inclination of the ETS rods were varied. The retrofit solutions were tested on nineteen specimens with three different web reinforcement ratios (0%, 0.1%, and 0.17%) under three point bending load. Half side of the specimen was over-reinforced to induce the failure occur at the weak side. Based on the experimental results, it was evident that the ETS rods significantly improved the load-carrying capacity of the specimen. The inclined ETS rods (45-degree) demonstrated a superior performance over the vertical (90-degree) oriented rods. The effectiveness of ETS rods were increased as the shear reinforcement ratio of the section

decrease. The CFRP rods were found to be more effective in enhancing the strength of the section while the steel rods may more cost competitive.

2.3. TXDOT 0-6893: Strengthening of Existing Inverted-T Bent Cap

The research in this dissertation was conducted as part of a larger study for Texas Department of Transportation (TXDOT) funded Project 0-6893 (Hurlebaus et al., 2018a,b,c). The objective was to develop designs for effective strengthening techniques for in-service inverted-T bent caps validate using experimental testing, and develop of design standards for the proposed retrofit solutions.

Two in-service inverted-T bent caps built in 1960s were selected as the prototypes and evaluated against the current specification. Figure 2-4 shows the configurations of the prototype bent caps. Though the bent caps were built in early days, the strength of the beam section was found to be sufficient to accommodate the current load demand. However, both bent caps were subject to the local deficiencies on the ledges with an average overstrength factor of 0.82.

To capture the local weakness of the inverted-T bent caps, eighteen potential retrofit solutions were developed to provide enhanced or alternative load paths based on the in-service conditions of the bent caps. The proposed solutions were evaluated using a weighted sum model in terms of six criteria: strength increase, total cost, constructability, clearance constraints, durability, and ease of monitoring. The top six ranked retrofit solutions were tested in the lab on eight half-scale specimens, with tests designed to target

the hanger, ledge, or punching shear capacities. Figure 2-5 presents the schematics of the tested retrofit solutions.

Thirty-three individual tests including six reference tests were conducted to investigate the selected strengthening solutions. The reference tests consist of three different failure mechanisms on exterior and interior loading regions were tested to ultimate failure to provide benchmarks. A successful isolation of the different local failure modes was achieved. The effectiveness of the strengthening solutions was then experimentally validated.

Experimental results were used to develop recommendations to evaluate capacities of in-service inverted-T bent caps. These recommendations include proposed rational modifications for capacity calculations that are less conservative than the current provisions. Design recommendations were provided for the six tested solutions, with fully worked examples provided to guide future implementation (Hurlebaus et al., 2018c).

(a) Double-column bent　　　*(b) Single-column bent*
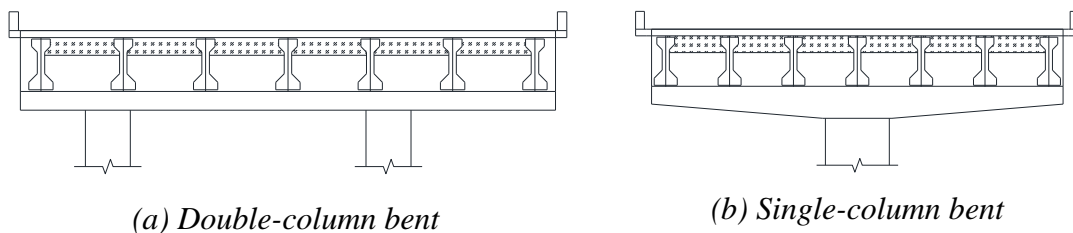
Figure 2-4. Configuration of Prototype In-Service Inverted-T Bent Caps.

(a) Full-depth FRP　　　　　　　　　*(b) Partial-depth FRP*

(c) Large bearing pad　　　　　*(d) Load balancing post-tensioning*

(e) Clamped threadbar　　　　　　*(f) End-region stiffener*
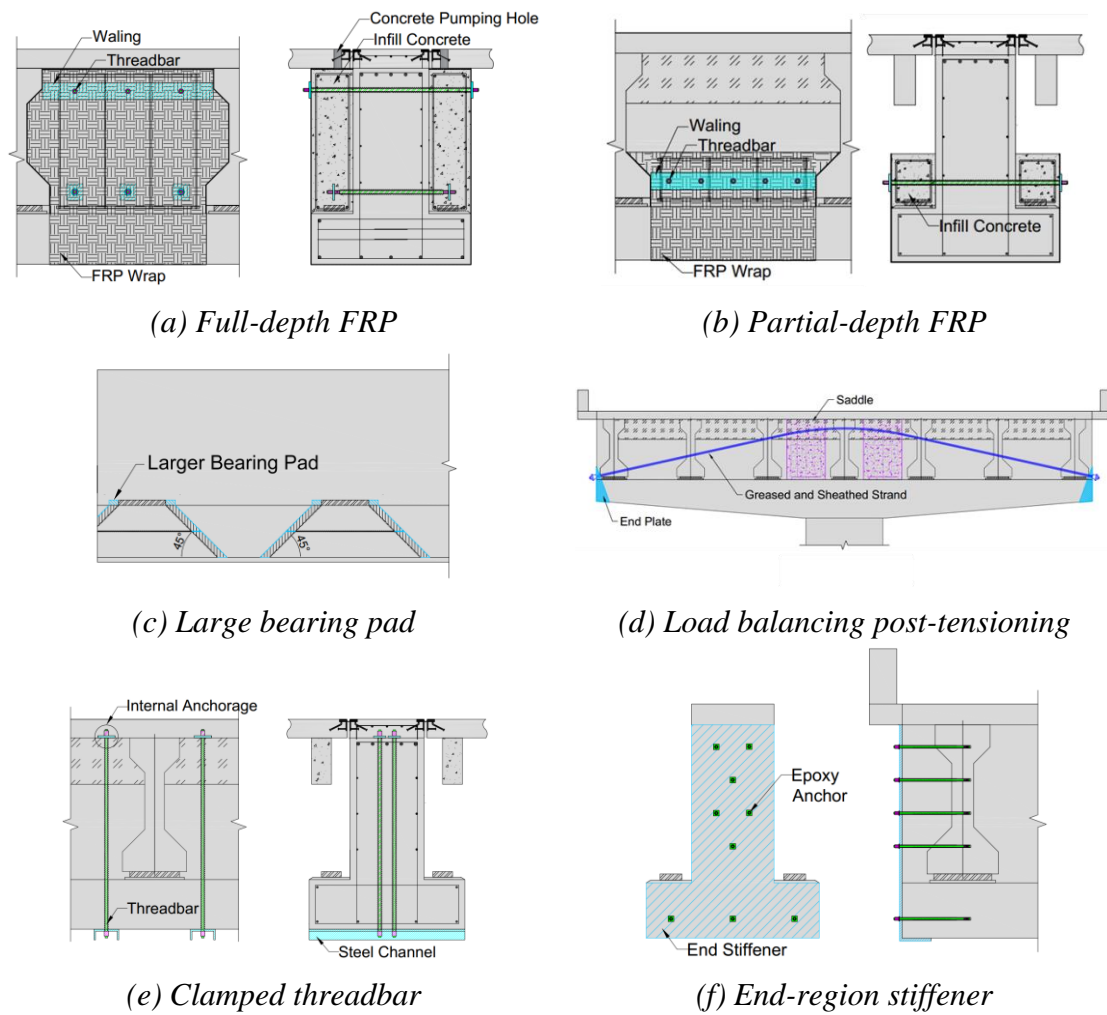
Figure 2-5. Schematic of Six Tested Retrofit Solutions.

2.4. Summary and Research Needs

Many of the existing inverted-T bent caps exhibit undesirable cracks at the web-ledge interface. These bent caps would have been designed during the working stress ear during the 1960s when there was a general lack of understanding on the structural behavior of inverted-T bent caps. Prevalence cracks observed on these bent caps prompted several research on the structural behavior of inverted-T bent caps. While the previous studies

carried out on the design approaches of inverted-T bent caps, the focus was given to the web-shear weakness of inverted-T bent caps. However, the inverted-T bent caps are susceptible to local mechanisms around the loading region. The observed cracks at web-ledge interface on in-service inverted-T bent caps were describing such weaknesses. The local mechanisms once took place will preclude the load distribution around the loading region hence may be critical to an inverted-T section. These mechanisms, either brittle or inducing excessive deformations, are adversely affecting the structural performances. As limited research efforts were paid on the local failure mechanisms of inverted-T bent caps, there is a need on the better understanding of the local behaviors of such bent caps.

Also, the design approach of inverted-T bent caps has changed over the past few decades in response to adoption of LRFD codes and to research prompted by the cracking observed on these structures. Moreover, the load demands under HL-93 have increased specifically if the owner chooses to restripe a bridge for three lanes compared to the two lanes assumed at the time of design. As such, many of early inverted-T bent caps maybe classified as deficient when evaluated against the current design specification and/or lack of adequate strength to support planned increases to live load demand. Replacement of deficient bent caps is not always practical. Therefore, techniques for strengthening these bent caps are needed. To develop a strengthening solution for the existing inverted-T bent caps, the following research questions arose.

- What is the hierarchy of failure mechanism (weakest-to-strongest links in the chain of resistance) for existing inverted-T bent caps?

- Given the relevant demands versus capacities, what mechanisms of a typical inverted-T bent are the most pressing to be addressed by strengthening?

- Given the identified failure hierarchies and critical weakness, what are the most favorable retrofit means and methods?

The strengthening of existing inverted-T bent caps must adequately address the design deficiencies and the observed in service damage. In particular, the retrofit solutions must provide an enhanced or alternative load path and for the case of inverted-T bent caps with existing cracks, the cracks must be restrained. Furthermore, the proposed retrofit solutions need to be able to eliminate the critical failure mechanisms of the inverted-T bent caps.

To validate the proposed retrofit solutions, the test program needs to consider the existing inverted-T bent cap details to realistically mimic the structural characteristics of the in-service structures. The accuracy of capacity estimation procedures given by the current standard (AASHTO LRFD 2020) need to be evaluated first with the specimens reflecting the actual behavior of in-service structures. Any modifications, where appropriate, need to be made to enable a more precise capacity evaluation of in-service inverted-T bent caps. The design approach and recommendation of retrofit solutions need to be developed to enable the implementation of retrofit solutions in the practical fields.

3. EVALUATION OF IN-SERVICE INVERTED-T BENT CAPS

3.1. Summary

To facilitate practical and impactful results in developing strengthening solutions for inverted-T bent caps, in-service bent caps were studied. The specific bent caps selected were part of the elevated lanes of IH 35 in downtown Austin. In addition to allowing for the assessment of structures with older designs, these bent caps were selected to provide an analysis if it was practical to increase the number of lanes on the structure. The capacities of the bent caps were analyzed according to the current design specification using demands based on the provisions at the time of design and the most recent one. Based on the analysis results, the bent caps meet the strength limit demands of the earlier provisions whereas insufficient to meet the service criteria that incorporated into the design provisions after the time of construction. The capacities of the bent caps were insufficient when evaluated against the demands of the current provisions for both service and strength limit with the most critical part being the hanger capacity.

3.2. Bent Characteristics

A field investigation was performed to identify the characteristics of the in-service bent caps. Design drawings were obtained for approximately 24 bents on each of the northbound and southbound elevated lanes of IH35 in Austin, Texas. The structures were built in late 1960s and designed in accordance with the 1965 edition of the AASHO standard specifications and interim revision for design of highway bridges (AASHO, 1965). Design concrete strength was 3.6 ksi and design steel strength was 60 ksi.

3.2.1. **Configuration of Bent Caps**

The evaluated in-service bent caps have two typical configurations: single-column bents and two-column bents. Figure 3-1 shows an overview of the bent caps. Typically, the bent is symmetric about the center of the bent (same overhang length on both ends with same number and location of girders in the overhang region). For some of the double-column bents, the overhangs on the two ends are not identical.

Cross-sectional dimensions are to the same for all double-column bents. The single-column bents have a cross-section at the end similar to the two-column bent caps, but with a ledge that increased gradually until the face of the column. The full height of the inverted-T bent caps is approximately 7 ft, with slight variations due to the slope of the roadway. The minimum ledge depth is 1 ft 8 in. for all bent caps. The full width of the inverted-T bent caps is 5 ft 3 in., and the width of web is 2 ft 6 in.

(a) Single column bent   *(b) Double column bent*
Figure 3-1. Overview of Typical Bent Caps of Elevated Lanes of IH35 in Austin, Texas.

In all bents, the columns are either rectangle or square, and the dimension of the column perpendicular to the cap width is wider than the web. The columns in single-column bents are 6 ft by 4 ft 6 in., providing only 4.5 in. clearance from the edge of the cap on either side (see Figure 3-1(a)). The columns in all two-column bents are square but vary in size. In most instances, two-column bents have either 3 ft 6 in. or 3 ft square columns.

The number of girders supported by the inverted-T bent caps ranges from 6 to 11, depending on the width of the road on the elevated bridge and the length of the span. In most locations, the girders for the forward and reverse spans are aligned. But in some bent caps, the girders are offset from one another on either side of the inverted-T bent caps.

The span length supported by the inverted-T bent caps range from 75 ft to 115 ft. The longest span supported by the single- and double-column bent is 100 ft and 115 ft, respectively. One of each of the single- and double-column bent caps supporting the longest span length was selected as the prototypes and evaluated in the following sections. Figure 3-2 and Figure 3-3 presents the detailed schematics of the prototype bent caps.
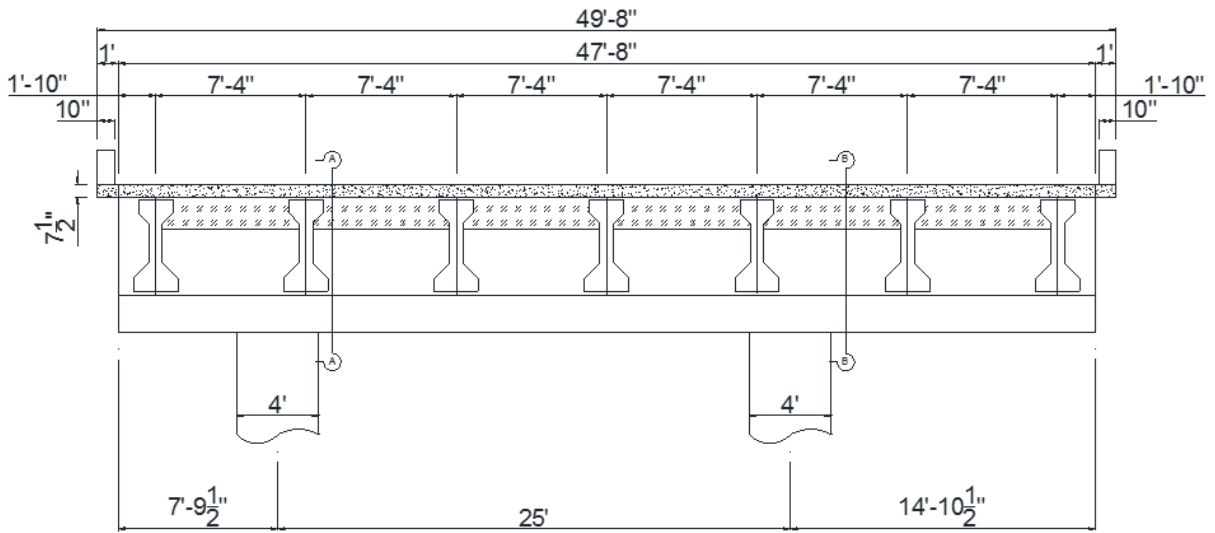
(a) Elevation
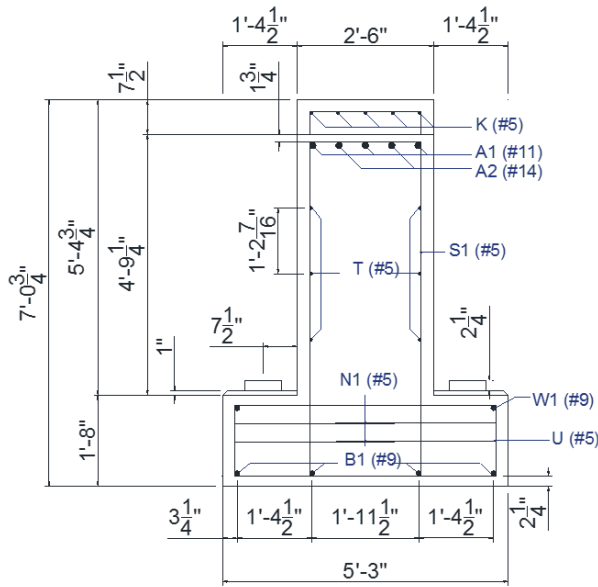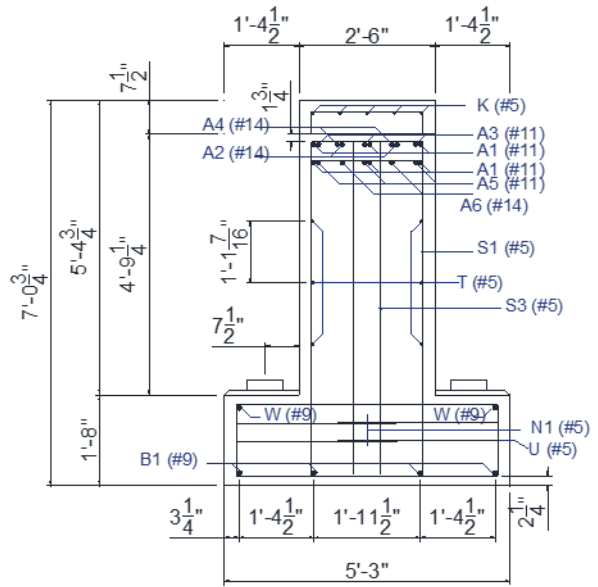
(b) Section A-A   *(c) Section B-B*

Figure 3-2. Schematic of Typical Double-Column Bent Cap.

32
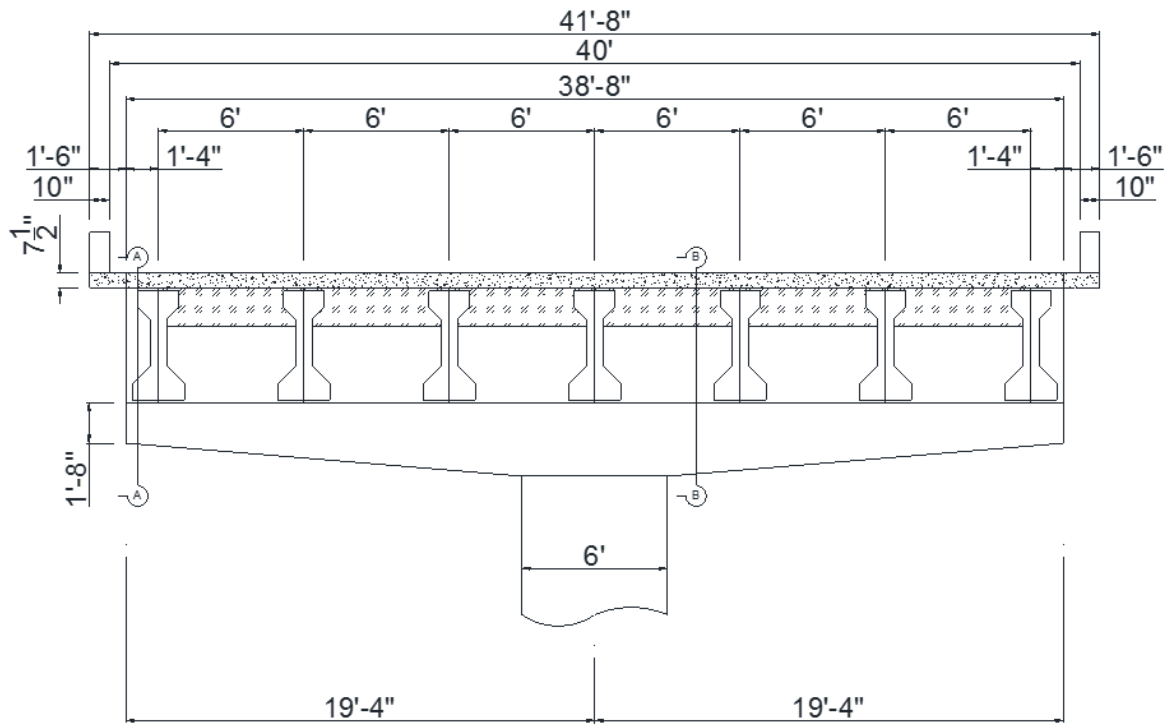
(a) Elevation
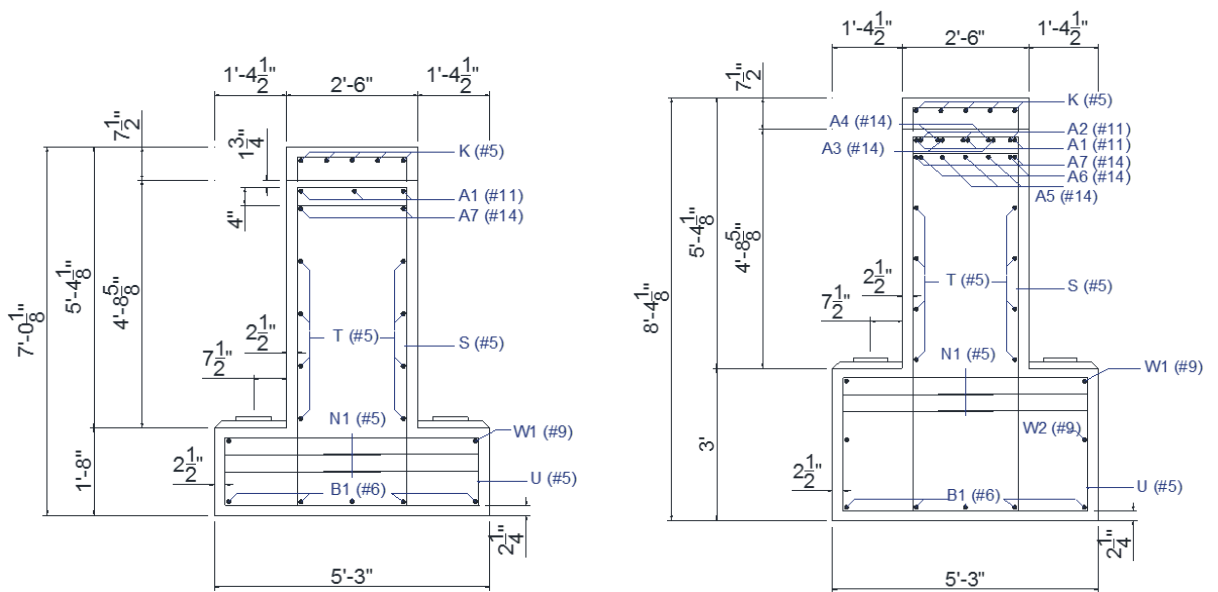
(b) Section A-A
                  (c) Section B-B

Figure 3-3. Schematic of Typical Single-Column Bent Cap.

3.2.2. **Condition of Bent Caps**

Discussions with district engineers indicated the expectation that the number of lanes on the bent caps will be increased from two to three. The damages on the structures that indicating structural deficiencies of the bent caps that would be amplified by increased demands of restriping the bent caps to carry additional lanes were identified during the field visit.

Figure 3-4 presents the observed key damage types on the in-service bent caps. The cracks typically formed at the ledge-web interface. Although the cracks extend slightly downward, it is primary horizontal. The crack extends approximately 1 ft inward toward the centerline of the cap on one of the bent caps (Figure 3-4(a)). On the other two bent caps (Figure 3-4(b) and (c)), cracking and spalling extended along the width of the interface between the web and the ledge was observed.

| *(a)* | *(b)* | *(c)* |
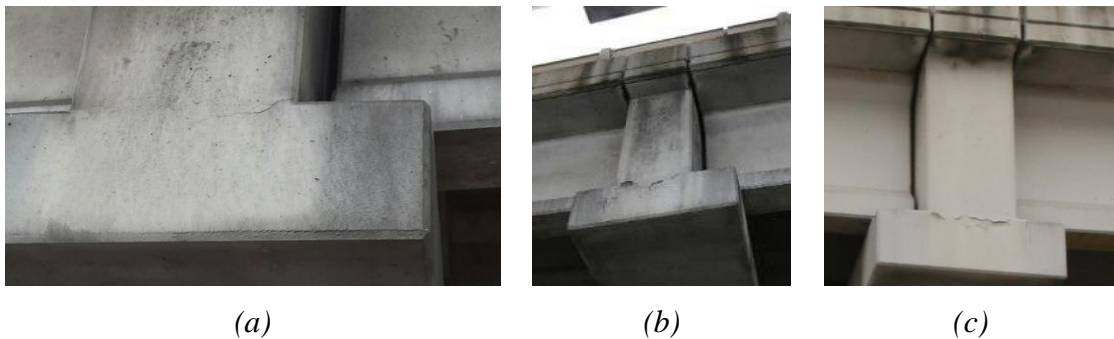
Figure 3-4. Cracking and Spalling Observed at Ends of In-Service Bent Caps.

3.3. Structural Analysis

The IH 35 bent caps considered in this study were designed following the 1965 edition of the AASHO standard specifications and interim revision for design of highway bridges (AASHO, 1965), which is based on the allowable stress design. The design approach has changed over the past few decades as analysis techniques and quality control for materials have improved. A reliability based LRFD was adopted by AASHTO in 1994, and since then these specifications have been updated through nine editions, with the latest edition being published in 2020.

The load carrying capacities of the prototype bent caps were analyzed according to the current specification. The capacities were then evaluated against the demands to evaluate the structural sufficiency.

3.3.1. Demands

Demands of inverted-T bent caps are characterized overall by the internal flexure, shear, and torsion. Demands associated with the local failure mechanisms (e.g. ledge and hanger strengths) are characterized by the girder reactions. The demands for beam behavior were calculated based on the current specification. The demands on the ledges were evaluated based on the earlier (1965 AASHO) and current (2020 AASHTO LRFD) specifications.

3.3.1.1. Beam Demands

The TxDOT bent cap analysis program CAP 18 (Version 6.2.2) was used to determine the beam flexural and shear demands. The program analyzes dead and live loads that conform

to AASHTO LRFD (2020) standard specifications. Both single- and double-column bents were modeled as continuous beams with knife-edge supports. The analysis of the bent caps considered only the Strength 1 limit state specified in article Section 3.4.1.

Dead loads include the self-weight of the girder, deck, and any overlay that may be present. The weight of the rails is distributed evenly among the stringers, up to three stringers per rail. To account for the additional dead load from the haunch of the column to the slab ends, the dead load of the slab is increased by 10 percent (TxDOT, 2015).

Live loads are computed in accordance with Sections 3.6.1.2.2 and 3.6.1.2.4. The vehicular live loading on the roadway consists of the design truck or the design tandem and the design lane load. The maximum live load is governed by the design truck for spans greater than 26 ft. The design truck load was placed in the locations which generates the maximum load effect.
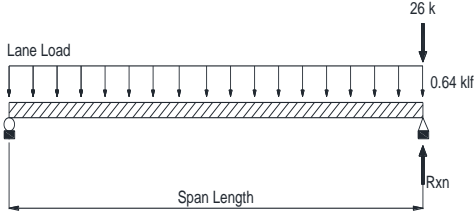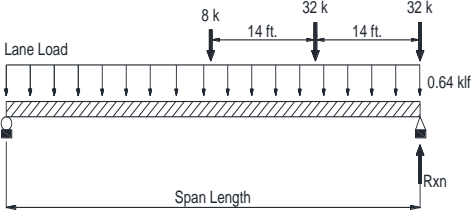
3.3.1.2. Ledge Demands

The ledge demands (girder reactions) were calculated for both 1965 AASHO and 2020 AASHTO LRFD. Table 3-1 compares the major differences in the live load evaluations between the two specifications.

The first major difference is the live load model. 1965 AASHO specifies that the live load be taken as HS 20-44 lane loadings or HS 20-44 truck or tandem loading, which will produce the maximum stresses at the section considered. As shown in Figure 3-5, the HS 20-44 lane load consists of a 0.64 klf uniformly distributed load and a concentrated load with a magnitude of 18 kips for moment and 26 kips for shear traversing the span.

The HS 20-44 truck consists of one front axle weighing 8 kips and two rear axles weighing 32 kips. Tandem loading consists of two 24 kips axles spaced 4 ft apart. While 2020 AASHTO LRFD specifies the live load should be taken as the combinations of 0.64 klf uniformly distributed lane load (HL-93) with the truck or tandem loading whichever produce the maximum stresses at the section considered.

Table 3-1. Comparison of Live Load Evaluations in 1965 AASHO and 2020 AASHTO LRFD.

	1965 AASHO	2014 AASHTO LRFD
Live Load Model	*HS 20-44 Lane Loading*	*HL-93 (combined design truck and lane)*
Impact Factor	$IM = 20.8\%$ for double-column bent $IM = 22.2\%$ for single-column bent	$IM = 33\%$

Live Load Distribution Factor	• Double-column bent (115 ft):
	  - Exterior – 0.63
	  - Interior – 0.67
	• Single-column bent (100 ft):
	  - Exterior – 0.55
	  - Interior – 0.55
		• Double-column bent (115 ft):
		  - Exterior – 0.71
		  - Interior – 0.77
		• Single-column bent (100 ft):
		  - Exterior – 0.60
		  - Interior – 0.67

The second difference between the two specifications is the impact factor. The 1965 AASHO expresses the impact factor as a fraction of live load and a function of span length as:

$$IM = \frac{50}{L + 125} \tag{3-1}$$

where L = span length, ft.

The 2020 AASHTO LRFD gives a constant value for the impact factor depending on the components and limit state under consideration. The impact factor for limit states, other than the fatigue and fracture limit states, turns out to be 0.33. The impact factor for the 1965 AASHO is applicable to truck, lane, and tandem loads; however, the 2020 AASHTO LRFD does not require the lane loading to be increased for dynamic effect.

Another difference between the two standards is the live load distribution factors (DFs). The live load shear forces, including the effects of impact load, are distributed to the individual girders using the live load distribution factors. The 1965 AASHO specifies a simple formula for live load DF for girder bridges in S/D format, where S is the girder spacing in feet and D is 11 (lanes/girder) for a bridge constructed with a concrete deck on prestressed concrete girders carrying two or more lanes of traffic. The effects of various parameters such as skew, continuity, and deck stiffness were ignored in this expression, and it was found to be accurate for a few selected bridge geometries and was inaccurate once the geometry was changed (Hueste et al., 2006). For this reason, changes have occurred in the way live load distribution factors are calculated in the LRFD specifications. The 2020 AASHTO LRFD uses a refined analysis for the live load DF.

More comprehensive formulas are provided that account for the span length, girder location, girder depth, transverse and longitudinal stiffness, skew, limit state, and structural type to yield more accurate DF.

CONCENTRATED LOAD— 18,000 LBS. FOR MOMENT*
26,000 LBS. FOR SHEAR

UNIFORM LOAD 640 LBS. PER LINEAR FOOT OF LOAD LANE

(a) HS 20-44 lane loading

HS20-44	8,000 LBS.	32,000 LBS.*	32,000 LBS.*
HS15-44	6,000 LBS.	24,000 LBS.	24,000 LBS.

0.2W · 14'-0" · 0.8W · V · 0.8W

0.1 W — 0.4 W — 0.4 W

0.1W — 0.4 W — 0.4 W

W = COMBINED WEIGHT ON THE FIRST TWO AXLES WHICH IS THE SAME AS FOR THE CORRESPONDING H TRUCK.
V = VARIABLE SPACING — 14 FEET TO 30 FEET INCLUSIVE SPACING TO BE USED IS THAT WHICH PRODUCES MAXIMUM STRESSES.

CLEARANCE AND LOAD LANE WIDTH
10'-0"

CURB
**

2'-0" · 6'-0" · 2'-0"

(b) HS 20-44 truck configuration

Figure 3-5. Live Load Models (Reprinted from AASHO, 1965).

39

Table 3-2 compares the girder reactions calculated in accordance with the two standards. It is evident from the table that the demands in both service and strength limit for 2020 AASHTO LRFD is greater than the demands based on 1965 AASHO. The average increase for the demands for the service and strength limits are 35 and 45 percent, respectively.

Table 3-2. Girder Reactions for Prototype Bent Caps (kips).

Bent Type	Region	Service Limit State			Strength Limit State		
		1965 Code	2020 Code	Demand Increase	1965 Code	2020 Code	Demand Increase
Double-column	Exterior	135	167	24%	190	247	30%
	Interior	142	191	35%	201	287	43%
Single-column	Exterior	112	140	25%	158	207	31%
	Interior	112	156	39%	158	235	49%

3.3.2. **Bent Cap Capacity Evaluation**

The capacity (*C*) of the prototype bent caps were evaluated based on the sectional method specifies in AASHOT LRFD (2020). The strength of inverted-T bent caps can be divided in two parts: beam and ledge. Flexure, shear, and torsional capacities were considered as the beam strength and compared to the internal demands from the CAP 18 analysis. The ledge capacities of the bent caps were evaluated by comparing the demand (girder reaction) to the capacities of the individual local failure mechanisms that are specified in the code.

The adequacy of each mechanism is evaluated by the ratio of the factored capacity (ϕC) to the demand (D), referred to as the overstrength factor, Ω:

$$\Omega = \phi Capacity(C)/Demand(D) \hspace{4cm} (3\text{-}2)$$

where ϕ = strength reduction factor, 0.9.

Overstrength factors greater than 1.0 are considered to have sufficient capacity to resist demands and are colored green in tables summarizing results. Overstrength factors less than 1.0 are considered to have insufficient capacity and are colored yellow ($0.9 \leqslant \Omega \leqslant 1.0$) or red ($\Omega \leqslant 0.9$) in tables summarizing results. When there is insufficient capacity, the amount of additional strength needed, referred to as the deficiency, is calculated as:

$$Deficiency = Demand(D)/\phi - Capacity(C) \hspace{3cm} (3\text{-}3)$$

3.3.2.1. Beam Sectional Capacities

Flexural capacities of the bent caps are calculated in accordance with Article 5.7.3.2. The negative moment capacity of the bent caps is evaluated at the most critical section on each column (Section A-A and B-B in Figure 3-2 for double-column bent and Section B-B in Figure 3-3[a] for single-column bent). The positive moment capacity for double-column bent is evaluated at the center of the mid-span.

Shear and torsion capacities of the web are calculated following conventional sectional methods in accordance with Article 5.8.3.3 through 5.8.3.6. Note that the maximum torsion and maximum shear is assumed to be concurrent at the critical section near the column surface (Section B-B) for both bent caps in this case. If the maximum

41

shear and maximum torsion do not occur concurrently, then it is necessary to check the location of the maximum torsion with its concurrent shear, and the location of the maximum shear with its concurrent torsion.

Table 3-3 presents analysis results of the beam sectional capacities. The overstrength factors for each mechanism are specified in the last column. It can be seen from the table that the prototype bent caps have sufficient beam sectional capacities to meet the demands.

Table 3-3. Evaluation of Beam Sectional Capacities.

Bent Type	Section	Capacity, ϕC	Demand, D	Overstrength Factor, Ω^*
		Flexural Resistance (kip-ft)		
Double-Column	Section A-A	3448	2988	1.15
	Section B-B	11210	9021	1.24
Single-Column	Section B-B	12324	11850	1.04
		Positive Flexural Resistance (kip-ft)		
Double-Column		1681	2024	1.20
		Shear (kips)		
Double-Column		1342	951	1.41
Single-Column		2554	1678	1.52
		Torsion (kip-ft)		
Double-Column		1329	628	2.12
Single-Column		3096	732	4.23

green – $\Omega > 1$; yellow – $0.9 \leqslant \Omega \leqslant 1.0$; red – $\Omega < 0.9$

3.3.2.2. Inverted-T Local Mechanism Capacities

AASHTO LRFD (2020) specifies two methods that may be uses to evaluate the capacity of inverted-T bent cap ledges: strut-and-tie model (STM) specified in Section 5.8.2, or the sectional stress analysis specified in Section 5.8.4.3. The sectional method is more

effective in distinguishing the different failure modes of the inverted-T bent cap ledges and is considered in this study.

Figure 3-6 depicts the location of potential cracks in inverted-T bent caps. Design of inverted-T bent caps should ensure the section has sufficient strength to resist flexure, shear, and axial forces at the location of Crack 1; tension force in the hanger reinforcement at the location of Crack 2; punching shear points of loading at the location of Crack 3; bearing force at the location of Crack 4. Design requirements for specific components are outlined in Articles 5.8.4.3.2 through 5.8.4.3.6.
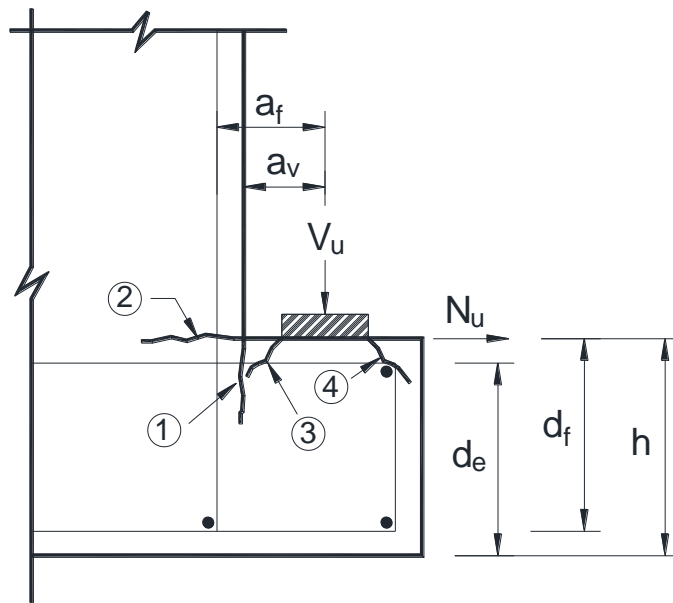
Figure 3-6. Notation and Potential Crack Locations for Ledge Beams (adapted from AASHTO LRFD 2020).

3.3.2.2.1. Ledge Shear Friction and Flexure Capacity

Figure 3-7 presents the internal forces and reinforcement details of the inverted-T bent cap ledges. The top layer of the ledge reinforcement (red) is defined as the primary tension reinforcement, A_s, to sustain concurrent flexural-tension force at the face of the web. The remainder of the ledge reinforcement (blue) is defined as the auxiliary reinforcement, A_h, which were provided to resists shear friction acting normal to the face of the web.

Nominal ledge shear friction (or interface shear) capacity for normal weight concrete is obtained using Equations 5.7.4.3-3, 5.8.4.2.2-1 and 5.8.4.2.2-2 from AASHTO LRFD (2020). The ledge shear friction capacity is the lesser of:

$$V_n = min \begin{cases} 1.4 A_{vf} f_y & \text{(3-4)} \\ 0.2 f_c' b_w d_e & \text{(3-5)} \\ 0.8 b_w d_e & \text{(3-6)} \end{cases}$$

where A_{vf} is the area of shear friction reinforcement within the distribution width as shown in Figure 3-8; f_y is the yield strength of reinforcement; f_c' is the specified concrete strength; b_w is the distribution width for the ledge shear friction; d_e is the effective depth of ledge.

The distribution width, b_w, for shear friction, depicted in Figure 3-8(a), is the lesser of *S* and (*W+4a_v*) for interior girders and *2c* for exterior girders, where *S* is the center-to-center girder spacing; *W* is the width of bearing pad; a_v is the distance from the center of bearing pad to the face of the web; and *c* is the end distance from the center of bearing pad to the free end of bent cap at the exterior region.
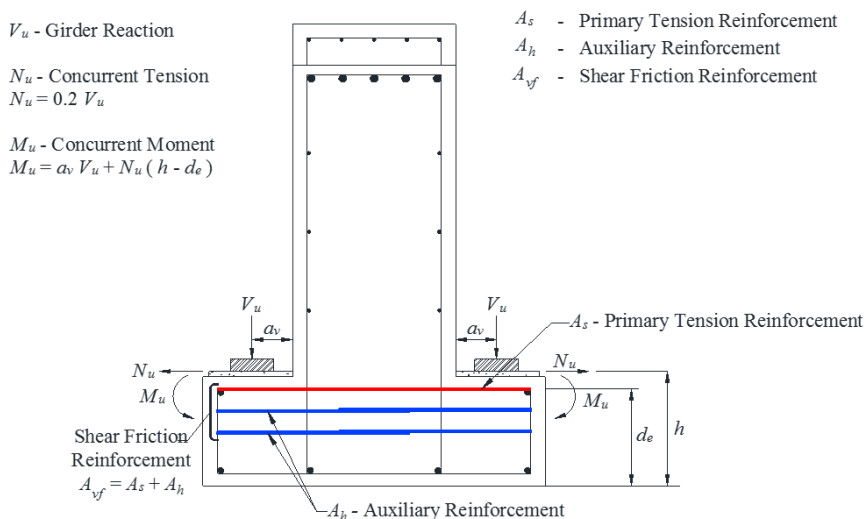
Figure 3-7. Ledge Reinforcement Details and Notations.

The ledge must simultaneously resist a factored girder reaction force, V_u, a factored concurrent horizontal tensile force, N_u, and a factored concurrent moment, M_u. The concurrent horizontal tensile force is regarded as a live load and determined as:

$$N_u = 0.2V_u \tag{3-7}$$

The factored concurrent moment M_u is determined as:

$$M_u = V_u a_v + N_u(h - d_e) \tag{3-8}$$

where h is the depth of ledge.

Based on Article 3.7.3.2, the nominal flexural resistance of the ledge section can be obtained as:

$$M_n = A_s f_y \left(d_e - \frac{a}{2}\right) \tag{3-9}$$

where A_s is the area of ledge primary tension reinforcement; and a is the depth of equivalent stress block.

45

The calculation of a for the ledge should account for the concurrent axial tension force, N_u. The presence of axial force increases the depth of the equivalent stress block hence decreases the ledge flexure capacity. From the equilibrium:

$$\frac{N_u}{\phi} + A_s f_y = 0.85 f_c' a b_m \qquad (3\text{-}10)$$

where ϕ is the load resistance factor; and b_m is the distribution width for ledge flexure, as shown in Figure 3-8(b).

From Equation (3-10), the depth of equivalent stress block can be obtained as:

$$a = \frac{\frac{N_u}{\phi} + A_s f_y}{0.85 f_c' b_m} \qquad (3\text{-}11)$$

At interior girders, the distribution width for ledge flexure is the lesser of S and $(W+5a_f)$, where a_f is the distance from the center of bearing pad to adjacent leg of hanger reinforcement. At exterior girders, the distribution is $2c$.
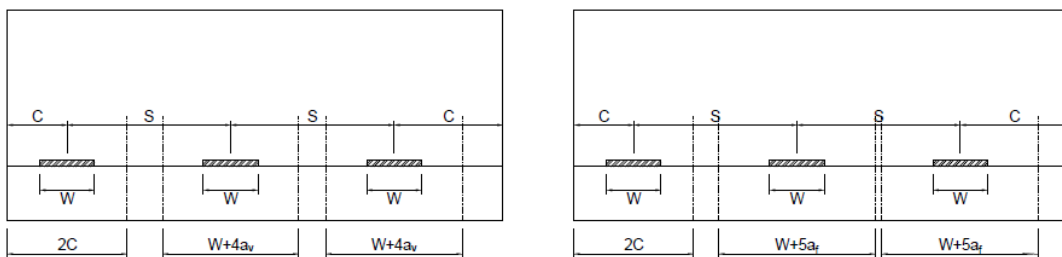
(a) Distribution for ledge shear friction   *(b) Distribution width for ledge flexure*
Figure 3-8. Distribution Width for Ledge Capacity Calculation.

3.3.2.2.2. Hanger Capacity

Hanger capacity must meet both service and strength limit criteria. The service limit for hanger capacity is:

$$V_n = \frac{0.5 A_{hr} f_y}{s}(W + 3a_v) \tag{3-12}$$

where A_{hr} is the area of one leg of hanger reinforcement; s is the spacing of hanger reinforcement. The distribution width ($W+3a_v$) shall not exceed either the girder spacing, S, or the double of end distance, $2c$.

For the strength limit, the hanger capacity is the lesser of:

$$V_n = \frac{A_{hr} f_y}{s} S \tag{3-13}$$

$$V_n = 0.063\sqrt{f_c'}\, b_f d_f + \frac{A_{hr} f_y}{s}(W + 2d_f) \tag{3-14}$$

where b_f is the overall width of the inverted-T ledge.

Equation (3-13) calculates the strength of hanger reinforcement within the longitudinal center-to-center girder spacing, *S,* as shown in Figure 3-9(a). While Equation (3-14) calculates the capacity of the ledge in regional area to distribute the applied girder force to the hanger reinforcements. The latter is limited by the concrete shear capacity combined with the tensile capacity of the hangers within the distribution width of ($W+2d_f$), as shown in Figure 3-9(b). For the exterior girders, the distribution width for both cases are limited by the double of end distance, $2c$.
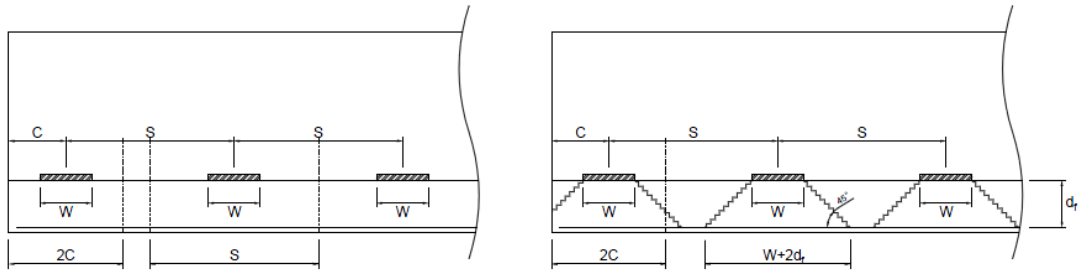
(a) Distribution for hanger reinf.   *(b) Distribution width for combined concrete and hanger reinf.*

Figure 3-9. Distribution Width for Hanger Capacity Calculation.

3.3.2.2.3. Punching Shear and Bearing Capacity

The punching shear capacity of the ledge is determined based on the strength of concrete and the area of the failure plane depicted in Figure 3-10. The area of the truncated pyramid shown in the figure is approximated as the effective depth of the ledge d_f and the perimeter of the failure plane at mid-depth of d_f, assuming 45-degree slopes. The nominal punching shear capacity of ledge is:

$$V_n = 0.125\sqrt{f_c'}\,b_o d_f \tag{3-15}$$

where b_o is the perimeter of the failure plane at mid-depth.

For interior girders,

$$b_o = W + 2L + 2d_f \tag{3-16}$$

where W is the length of bearing pad; and L is the width of bearing pad.

For exterior girders, the failure plane is limited by the end distance as:

$$b_o = 0.5W + L + b_f + c \le W + 2L + 2d_f \tag{3-17}$$

(a) Plan view　　　　*(b) Cross-section*
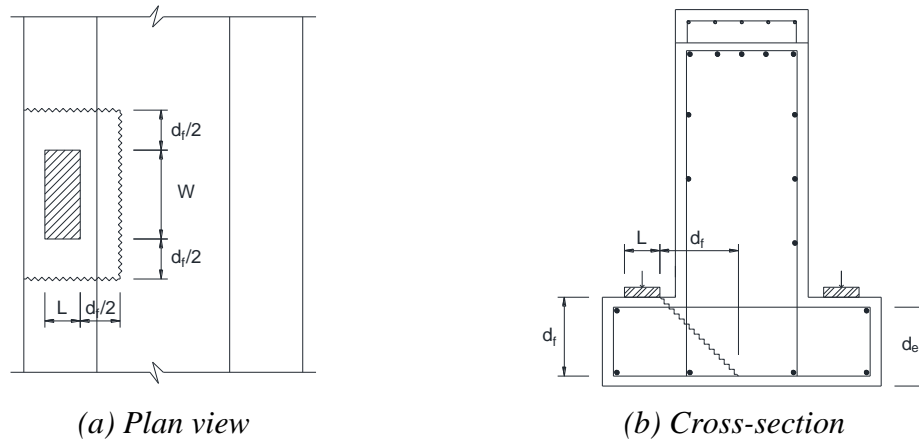
Figure 3-10. Punching Shear Failure Plane.

The bearing strength of the ledge can be obtained by the area of bearing pad and projected area. The nominal bearing strength is given by:

$$V_n = 0.85 f_c' A_1 m \tag{3-18}$$

where A_1 is the area of bearing pad; and m is the confinement modification factor. For a uniformly distributed bearing stresses and the supporting surface is wider than the loaded area on all sides,

$$m = \sqrt{\frac{A_2}{A_1}} \le 2 \tag{3-19}$$

where A_2 is the projected bearing, as shown in Figure 3-11, which can be determined based on the geometry of inverted-T ledges.
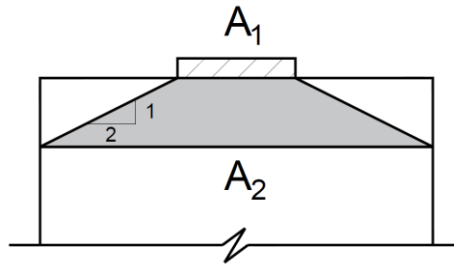
Figure 3-11. Projected Bearing Area.

3.3.2.2.4. Local Mechanism Capacities vs. Demand

Table 3-4 and Table 3-5 compares the ledge capacities to the demands for the double- and single-column bent caps. Although the ledge capacities were evaluated at every girder location, only the controlling values for exterior and interior region are presented. The capacities were evaluated against the demands based on the 1965 AASHO and 2020 AASHTO LRFD. Overstrength factor ($\Omega = \phi C/D$) was used to demonstrate the structural sufficiency of the bent cap local mechanisms. Overstrength factors greater than 1.0 are colored green, in between 0.9 and 1.0 are colored yellow, and smaller than 0.9 are colored red in the tables.

The results of the evaluation using the 1965 AASHO demands are shown in the left portions of the tables. The bent caps are deemed to be structurally adequate with the exception of the exterior hanger capacity of the double-column bent cap, with an overstrength factor of 0.94. The overstrength factor for the interior was 1.03, only slightly larger than the maximum acceptable value of 1.0. The other mechanisms of the double-column bent cap, and all mechanisms of the single-column bent cap satisfied the strength limit.

Table 3-4. Ledge Capacities of Double-Column Bent Caps (kips).

Failure Mode	Region	1965 AASHO			2020 AASHTO LRFD		
		Capacity ϕC	Demand D	Overstrength Factor, Ω	Capacity ϕC	Demand D	Overstrength Factor, Ω
Ledge Shear Friction	Exterior	539	190	2.84	539	247	2.18
	Interior	571	201	2.84	571	287	1.99
Ledge Flexure	Exterior	267	190	1.41	267	247	1.08
	Interior	269	201	1.34	269	287	0.94
Punching Shear	Exterior	209	190	1.10	209	247	0.85
	Interior	257	201	1.28	257	287	0.90
Bearing	Exterior	841	190	4.42	841	247	3.40
	Interior	841	201	4.18	841	287	2.93
Hanger	Exterior	178	190	0.94	178	247	0.72
	Interior	206	201	1.03	206	287	0.72
Hanger (Service)	Exterior	79	135	0.59	79	167	0.47
	Interior	78	142	0.55	78	191	0.41

Table 3-5. Ledge Capacities of Single-Column Bent Caps (kips).

Failure Mode	Region	1965 AASHO			2020 AASHTO LRFD		
		Capacity ϕC	Demand D	Overstrength Factor, Ω	Capacity ϕC	Demand D	Overstrength Factor, Ω
Ledge Shear Friction	Exterior	518	158	3.28	518	207	2.50
	Interior	820	158	5.19	820	235	3.49
Ledge Flexure	Exterior	258	158	1.63	258	207	1.25
	Interior	432	158	2.73	432	235	1.84
Punching Shear	Exterior	213	158	1.35	213	207	1.03
	Interior	445	158	2.81	445	235	1.89
Bearing	Exterior	843	158	5.34	843	207	4.07
	Interior	843	158	5.34	843	235	3.59
Hanger	Exterior	193	158	1.22	193	207	0.93
	Interior	204	158	1.29	204	235	0.87
Hanger (Service)	Exterior	94	112	0.84	94	140	0.67
	Interior	84	112	0.75	84	156	0.54

Service loads were considered only for the hanger capacities. Both double- and single-column bent caps were inadequate to meet the service limit. The overstrength ratio for double- and single-column bent cap was 0.57 and 0.8 on average, respectively. This deficiency is consistent with the damage observed on in-service bent caps (Figure 3-4). The cracks extended horizontally along the web-ledge interface is an indication of the hanger deficiency. One reason for this is the bent caps were constructed in the late 1960s when there was a general lack of understanding of the local mechanisms of inverted-T bent caps. The local behaviors of inverted-T bent caps were first investigated by Mirza and Furlong (1971, 1974). The service criteria for the hanger capacity were incorporated into the design of inverted-T bent caps after the study. Therefore, the bent caps built in early days were subject to serviceability issues.

The results of the evaluation using the current AASHTO LRFD demands are shown in the right portions of the tables. The larger live load demands result in smaller overstrength factors, with many failure mechanisms having factors less than one and thus being classified as structurally deficient.

The double-column bent cap failed to meet the demand for ledge flexure, hanger, and punching shear capacities. The hanger at service limit had the lowest overstrength factors, with factors as low as than 0.41. It was also the lowest mechanism at strength limit with overstrength factors of approximately 0.7. The inverted-T bent caps with hanger deficiencies will have the potential for vertical separation of the ledge from the web. The hanger failure involves the yielding of the web stirrups around the loading region is not a brittle failure. However, the regional area will experience excessive deformations. The

punching shear at the exterior girders also showed an insufficient overstrength factor of 0.85. The punching shear failure involves the diagonal tension failure of the concrete under the girders is brittle in nature, hence should definitely be avoided. The punching shear capacity at interior girders was better than the exterior but also insufficient with an overstrength factor of 0.90. The overstrength factor of ledge flexure at interior (0.94) showed a slightly lower values than 1.0. The ledge shear friction and bearing capacities showed satisfactory capacities in both exterior and interior when compared to the demands.

The single-column bent cap also demonstrated an insufficient hanger capacities at both service and strength limits with the average overstrength factors of 0.6 and 0.9, respectively. The punching shear at exterior girders had an overstrength factor of 1.03 which was close to the limit. The interior punching shear capacities showed a satisfactory overstrength factors. The other local mechanisms of the single-column bent cap demonstrated sufficient overstrength factors. The single-column bent cap had a tapered ledge depth that gradually increases from the end of the bent cap to the face of the support column. Therefore, the capacities of the local mechanism that associate to the ledge depth such as ledge friction, ledge flexure, punching shear and bearing mechanisms were showed a better overstrength factors when compared to the double-column bent cap which has a consistent ledge depth throughout the entire section.

3.4. Closing Remarks

In-service inverted-T bent caps that are part of the IH 35 thruway system located in downtown Austin were evaluated. The bent caps constructed in late 1960s were designed in accordance with the AASHO (1965) specifications. To examine the current structural performance, the bent caps were evaluated against to the AASHTO LRFD (2020) specification. Two typical bents, double- and single-column, that supporting the longest span length were selected as the prototype and evaluated theoretically.

The analysis revealed that the inverted-T bent caps have insufficient hanger, punching shear, and ledge flexure capacities with the hanger being the primary concerns. The structural deficiencies of the hanger mechanism for double-column bent cap were 111 kips and 83 kips in average at service and strength limit, respectively. For the single-column bent cap, it was 65 kips and 25 kips, respectively. Inverted-T bent caps with hanger deficiencies will be subject to excessive deformation at the regional area around the loading point that adversely affecting the structural performance. The hanger mechanism at both service and strength limit needs to be addressed with retrofit solutions. The design aspects that related to the service level performance will also need to be investigated as the deficiencies at service limit was even larger than the strength limit.

The ledge flexure and punching shear was the other mechanisms that had insufficient capacities on double-column bent cap with 20 kips and 37 kips deficiencies, respectively. The single-column bent cap with a tapered ledge depth was free from the ledge deficiencies. The ledge flexure capacity is affected by the depth of the ledge and the ledge transverse reinforcement. While the punching shear capacity is affected by the

54

dimension of the failure plane formed underneath the girders. The depth of the ledge and the dimension of the bearing pad are the factors that affecting the failure plane of the punching shear mechanisms. The deficient capacities of the ledge flexure and punching shear mechanisms can be overcome by varying such design aspects.

4. FINITE ELEMENT INVESTIGATION ON LOCAL FAILURE MECHANISMS OF INVERTED-T BENT CAPS

4.1. Summary

This paper performs a nonlinear finite element analysis to investigate the local failure mechanisms of inverted-T bent caps and the parameters impacting the local behavior. A finite element model was developed to simulate the local failure mechanisms of inverted-T bent caps. Experimental data were used to demonstrate the capability of the finite element model to capture the observed local failure mechanisms. The alternate reinforcement configurations were investigated to explore potential design alternatives. Reinforcement configurations studied include: use of diagonal ledge bars; diagonal ledge bars in addition to horizontal ledge bars; concentration of ledge reinforcement near load points; and concentration of hanger reinforcement near load points. The analysis results reveal that diagonal ledge bars have minimal impact on the strength but significantly reduced the concrete strain at the web-ledge interface and thus may improve serviceability of the bent caps. The combined diagonal and horizontal ledge bars showed better performance than the case with solely use of horizontal ledge bar. Concentrated ledge reinforcement moderately improved the ledge capacity, though the increase was not proportional to the amount of the reinforcement, while the reduction in strain was prominent. Concentrated hanger reinforcement was effective in reducing strain but had minimal effect on the hanger capacity. The interior and exterior loading region demonstrated a similar response while the exterior region found to be less sensitive to the reinforcement variations.

4.2. Introduction

Inverted-T bent caps have been widely used in US to reduce the overall elevation of bridges, to improve the available clearance beneath the beams. Figure 4-1 shows an overview of an inverted-T bent cap system. The bridge girder loads are applied to the ledges at the bottom of the cross-section. This effectively loads the bent cap along its bottom compression with the loads transferred to the upper tension chord via the web, thereby creating a loading condition not generally encountered in conventional RC beams. Mirza and Furlong (1971, 1974) carried out the first study on the structural behavior and the reinforcement details of inverted-T bent caps which formed the basis of the current design standard. The typical failure mechanisms of inverted-T bent caps were categorized and the design procedures were derived from the test data. As noted by Mirza and Furlong, the strength of an inverted-T cross section can be described in terms of flexure, web shear, torsion, ledge, hanger and punching. The flexure, web shear, and the torsion are the common failure mechanisms encountered in top loaded RC beams whereas the ledge, hanger and punching failures are the local failures that can be take place in the regional area of the ledge seating the bridge girders.

Figure 4-2 depicts the local failure mechanisms of inverted-T bent caps. Ledge failure (Figure 4-2(a)) is loss of capacity of the ledge acing as a bracket. Failure can occur as a flexural tension failure of the ledge or as a friction failure at the face of the web, in which the ledge shears off. Hanger failure (Figure 4-2(b)) is defined by a vertical separation of the bottom ledge away from web. This separation is referred to as the primary hanger crack. If sufficient demands are applied, secondary hanger cracks may form higher

in the web. Punching failure (Figure 4-2(c)) occurs when the load applied on top of the ledge exceeds the tensile strength of the concrete along the surface of truncated pyramid. Once these local failures take place, it will preclude the capability of the bent cap to distribute the internal resistance. The strength of an inverted-T bent cap section can only be fully developed if the section has adequate local strengths. As such, two types of transverse reinforcement, shown in Figure 4-3, are used in inverted-T bent cap to aid in transfer of the load. The ledge transverse reinforcement (blue) are the stirrups in the ledge transferring the load from the bearing pad to the web. The web transverse reinforcement, also referred to as hanger reinforcement (red), are the vertical stirrups in the web that transfer the load into the web. The lateral bars parallel to the ledge transverse reinforcement (light blue) and the diagonal bar (green) across the corners of the web-ledge interface are auxiliary ledge reinforcement provided to ensure the ledge has enough resistance to sustain the combined bending moment and the shears along the face of the web. The diagonal bars extending from the lower end of the ledge across the region at web-ledge interface which has complex stress state due to the combined bending and shear is typically not used in modern design but is included in this study as a potential method to reduced service level cracking.
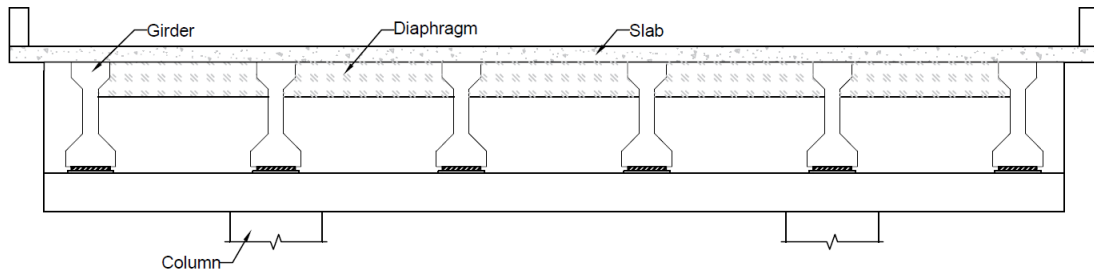
(a) Elevation
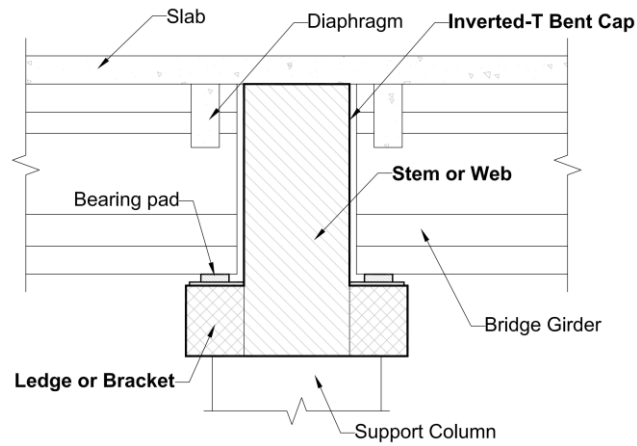
(b) Bent cap components

Figure 4-1. Overview of Inverted-T Bent Cap System.
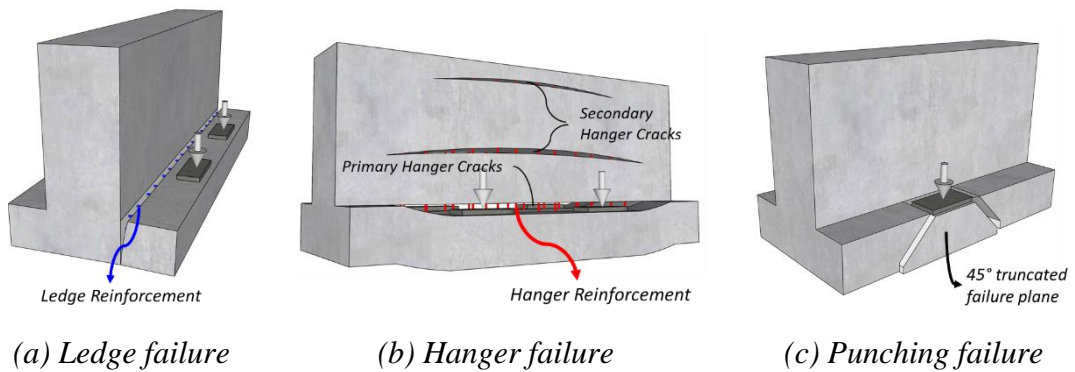
(a) Ledge failure   *(b) Hanger failure*   *(c) Punching failure*

Figure 4-2. Local Failure Mechanisms of Inverted-T Bent Cap.

59
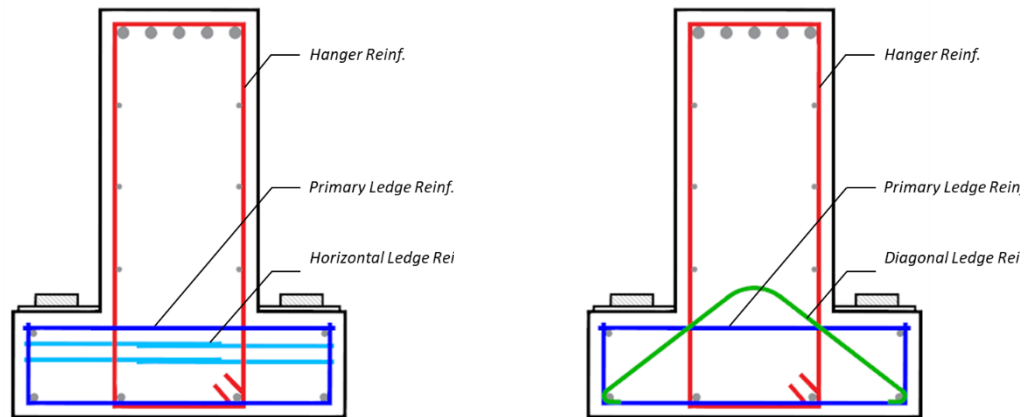
(a) Layout with horizontal ledge bar   *(b) Layout with diagonal ledge bar*

Figure 4-3. Reinforcement Layout of Inverted-T Bent Cap Section.

While design procedures for inverted-T bent cap include the service criteria, a prevalence of cracking at the re-entrant corner of web-ledge interface reported on in-service bent caps prompted several studies on cracking control of inverted-T bent caps. Zhu and Hsu (2003) experimentally investigated the impact of the reinforcement layouts on the crack control of inverted-T sections and proposed a compatibility strut-and-tie model to predict the crack width of the cracks. Seven 2-D specimens that represented an interior slice of an inverted-T bent cap were tested with the variations of the lateral and diagonal ledge reinforcement and the spacing of the transverse reinforcements. The test result demonstrated that the diagonal ledge reinforcement is effective in restraining the crack width of the inverted-T section whereas the lateral ledge reinforcement had minimal effect on the crack width. The effect of reducing hanger reinforcement spacing was found to be moderate in crack control of the inverted-T section. However, the different failure mechanisms of inverted-T bent caps were not captured by the 2-D test specimens that have a limited width (460 mm) with three to six layers of transverse reinforcements. Larson et

60

al. (2013) carried out an experimental study on strength and cracking of straddle inverted-T bent caps and proposed a design recommendation based on strut-and-tie models. A total of 33 specimens were tested to evaluate variables including the dimension of ledge and web, the web reinforcement ratio, the number of point loads, and the shear span-to-depth ratio. From the experimental results it was observed that increasing the ledge length along the length of the straddle bent increased the strength of the inverted-T bent caps, whereas increasing the depth of ledge and web did not have any significant effect on the strength. An increase in the web reinforcement ratio showed an increase in the shear strength of the specimens. The increase of web reinforcement ratio also reduced the diagonal crack widths at a higher level of load. A minimum ratio web reinforcement is recommended to retrain the crack width at service load state. While the study investigated the structural behavior of inverted-T bent caps, the test specimens were designed to emphasize the web shear failures, while local failure mechanisms that may be critical to an inverted-T section were not investigated. It should be noted that five premature failures of the specimens were attributed to punching (three failures), ledge-flexure (one failure), and ledge shear friction (one failure) and are summarized by Garber et al. (2017) who noted that there is a need to further investigate the local failure mechanisms of inverted-T bent caps. Galal and Sekar (2008) studied FRP strengthening on inverted-T bent caps to eliminate local failure mechanisms and to improve strength of the bent cap. The spacing of the ledge and hanger transverse reinforcements were varied to generate the local weakness. However, the specimens emphasized with local failures were either loaded to a moderate level and retrofitted with FRP or retrofitted before the testing. Ultimate testing of the inverted-T

bent cap specimens with local failures were not performed. An ultimate testing would be essential to evaluating the complete response of the local failure mechanisms of inverted-T bent caps as it enables an observation on the post-elastic behavior of stiffness, deformation, and cracking patterns of the bent cap at different loading conditions. Hurlebaus et al. (2018b) performed ultimate testing of inverted-T specimens that were designed to highlight different local failure mechanisms as part of a research effort to develop strengthening techniques of in-service inverted-T bent caps. Different prototype specimens emphasized punching, ledge, and hanger failure. The test results demonstrated a successful isolation of the local failure mechanisms. The load-deflection response, crack patterns and width of the specimens with each of local failure mechanisms were documented. Cracking of the specimens with local weakness at service load state was reported. As the research was aimed to develop strengthening techniques for in-service structures, the potential variables that may affecting the local failure mechanisms of inverted-T section were not explored.

The potentials of varying reinforcement layout to control cracking of inverted-T bent cap section was demonstrated in a previous study (Zhu and Hsu, 2003) on the 2-D sliced specimens. The impacts of the reinforcement layouts on the local behavior of inverted-T bent caps, once proven by a 3-D model with the local mechanisms isolated, will be an effective strategy to control the cracking of inverted-T section. A full-scaled experimental testing would be a desirable way to perform the investigation, however, is limited due to the cost. Therefore, the use of nonlinear finite element analysis correlate with experimental results would be an effective method to investigating the structural

behavior and failure mechanisms of inverted-T bent caps. The capability of finite element model (FEM) to capturing the structural behavior of RC ledge beams subject to complex stress state were proven by several prior studies. Hassan et al. (2007) investigated the effect of the web reinforcement layout on the structural behavior of L-shaped lead beams. The L-shaped ledge beam, with a shallow ledge searing the girder load has a similar structural characteristic to an inverted-T section. A non-linear FEM model was developed and verified the capability to simulate structural behavior of the ledge beams by comparison with the experimental results. Mercan et al. (2010) carried out a FE study on the structural behavior of L-shaped ledge beams. The sensitivity of various parameters including finite element type, material model, loading distribution and boundary conditions were explored. The analysis result showed that the FE models are sensitive to element type and concrete damage model. The mesh configurations have moderate effect, and the varying concrete material models have negligible impact on the load response of the ledge beams. Recently, Zhou et al. (2020) performed a parametric study on the structural behavior and failure mechanisms of skewed inverted-T bent caps by utilizing finite element models. The FE model was calibrated with the experimental results of an inverted-T bent cap specimen that emphasized the web shear failure. The simulation results were correlated well to the experimental observations. The model was able to simulate the structural behavior of the inverted-T sections. The model was used to study the effect of the transverse reinforcement arrangement, spacing, skew angle and the loading positions. The analysis results indicated that the skew angle and load positions have significant effect on the structural behavior of skewed inverted-T bent caps while

63

changing the arrangement of transverse reinforcement had minimal impact and varying the spacing of the transverse reinforcement have a moderate effect on the ultimate capacity and ductility of skewed inverted-T bent caps.

While previous studies have investigated the over structural behavior of inverted-T bent caps, limited efforts were made to investigate each local failure mechanism of inverted-T bent caps as well as the potential parameters that may affecting the local behavior. To this end, this study presents an analytical investigation on the local failure mechanisms of inverted-T bent caps and the impact of changing the reinforcement configuration.

4.3. Finite Element Modeling of Inverted-T Bent Caps

A commercial FE program ABAQUS is used to develop the finite element model and simulate the structural behavior of inverted-T bent caps. The model was built to simulate the inverted-T bent cap specimens that tested by Hurlebaus et al. (2018b). The bent cap specimens were half-scale physical models that designed based on the geometry and reinforcement details of an in-service inverted-T bent cap built in the 1960's. The test results from three groups of ultimate testing that emphasized ledge, hanger, and punching failures were used to validate the FE model. Each group contains ultimate load tests on both the *interior* and *exterior* loading regions. Table 4-1 summarizes the tests considered in this study. Six individual tests were conducted on three different test specimens. The concrete properties of the specimens were also specified in the table. Six FE models were developed to simulate each of these tests.

Table 4-1. Summary of Tests and Compressive Strength of Concrete (MPa).

Specimen	Failure Mode	Test ID	Region	28-day Concrete Strength	Age at Test Day	Test Day Strength
T5	Ledge	T5E1	Exterior	24.4	125	30.7
		T5I1	Interior			
T2	Hanger	T1W1	Exterior	23.4	248	26.9
		T1I1	Interior			
T3	Punching	T3E1	Exterior	24.8	83	26.5
		T3I2	Interior			

*Three 4 in. x 8 in. (100 mm x 200 mm) cylinders were tested per each time to get an average

4.3.1. Specimen and Test Set-up

Two different specimens – *ledge deficient* and *hanger deficient* – were designed to generate the ledge and hanger failures of inverted-T bent cap, respectively. Figure 4-4 presents the reinforcement details of the specimens. The distinct deficiencies were achieved by varying the spacing and size of the ledge and hanger reinforcements, as indicated in blue and red in the figure. The other reinforcements are common to both specimens. The *ledge deficient* specimen was also used to generate the punching failures by varying the loading distribution.

Figure 4-5 presents the test set-up of the specimens. The specimen with a length of 264 in. (6705 mm) was center on two 24 in. (310 mm) square columns spaced 144 in. (3657 mm) on center, providing two exterior and one interior loading regions. A tie-down bar stressed with 75 kips (335 kN) was used to clamp the specimen and the column together onto the strong floor. The interior tests simulated two girder lines spaced at 48 in. (1219 mm), centered on the specimen. While the exterior tests simulated one girder line

centered 12 in. (305 mm) from the edge with an additional loading line was provided over the adjacent column. At each simulated girder line, an actuator was applying loads to a loading frame that transferred load to each ledge. For ledge and hanger tests, the actuator was centered on the loading frame (Figure 4-5(b)) to provide equal loads on each ledge. The interior tests increased the actuator load on the two girder lines equally whereas the exterior tests increased each actuator equally up to dead load, at which point the load over the column was held constant. For punching tests, the actuator was placed 5 5/8 in. (143 mm) off-center (Figure 4-5(c)) to allow for larger loading on one side to generate a punching failure. Both interior and exterior punching tests increased each actuator equally up to dead load. After reaching dead load, only a single actuator was increased up to failure.
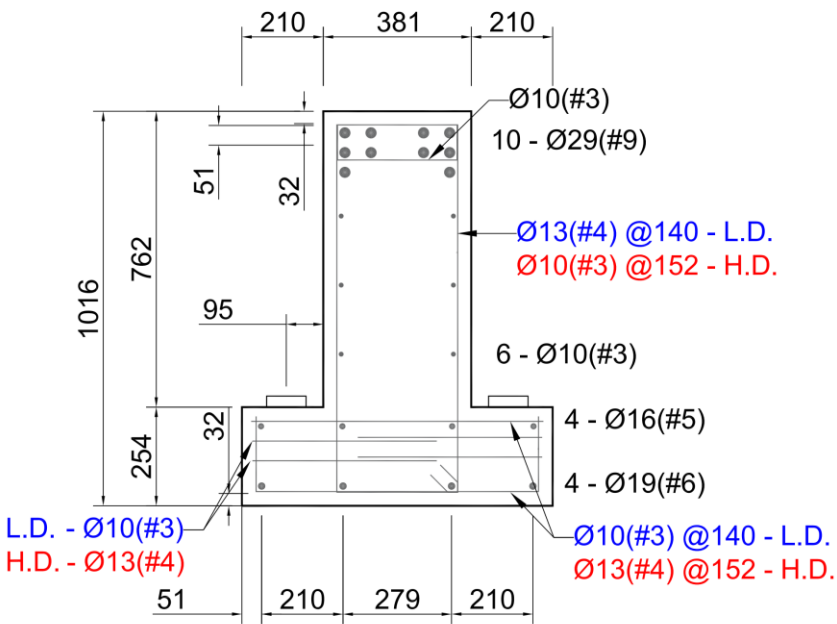
Figure 4-4. Reinforcement Details of Inverted-T Bent Cap Specimens.

The load was locked at critical loading points to check cracks and condition of the specimens which were calculated based on service (SLS) and ultimate (ULS) load demands of the in-service prototype bent cap.
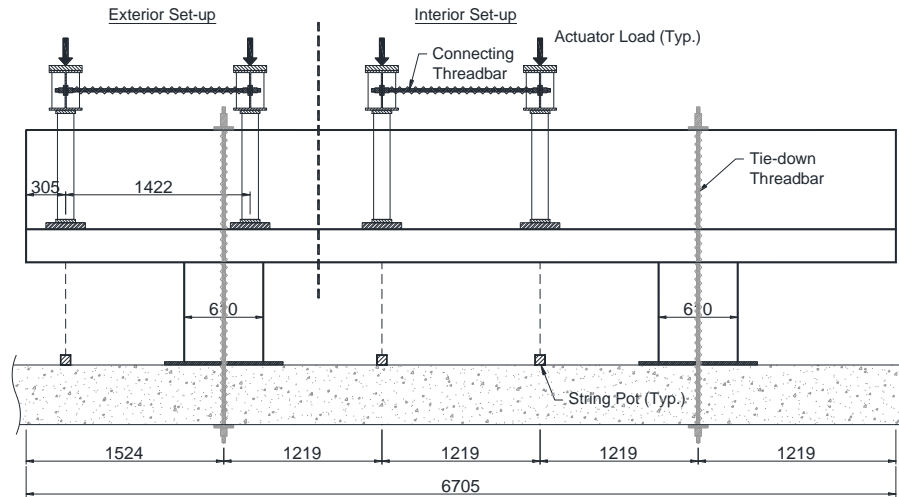
(a) Overview
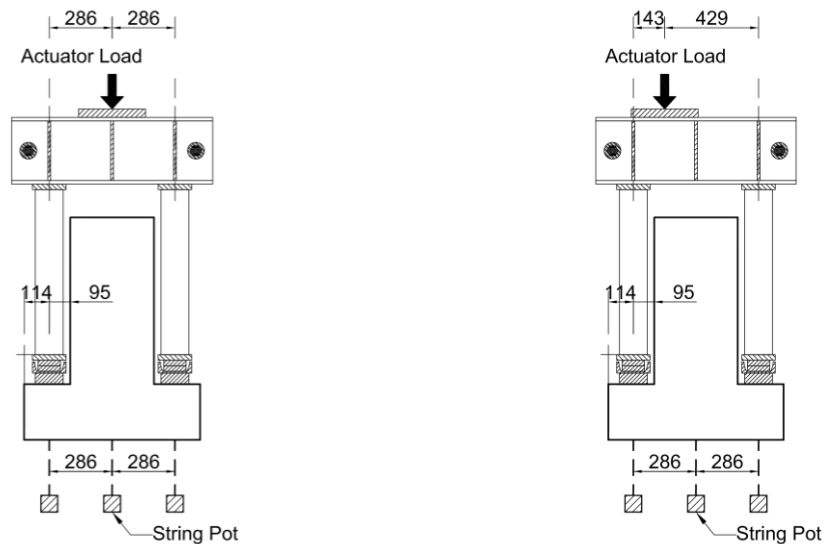
(b) Loading location for ledge and hanger tests

(c) Loading location for punching test

Figure 4-5. Test Set-up (mm).

4.3.2. **Experimental Observations**

Figure 4-6 presents the observed cracks on the test specimens at the measured ultimate load of each test. Cracks formed before SLS were colored purple, between SLS and ULS were colored blue, and after ULS were colored red. The local failure mechanisms, ledge, hanger, and punching shear failures were clearly isolated on each test.

The observed cracks on interior and exterior ledge tests were presented in Figure 4-6(a) and (b), respectively. The initial cracks were formed at the web-ledge interface behind the bearing pad at SLS (48 kips [220 kN]) and before SLS (41 kips [182 kN]) for interior and exterior ledge tests, respectively. The interface cracks propagated along the line of re-entrant corner at both side of the bearing pad, and extended diagonally to the top of ledge as load increased. For the exterior ledge test, the interface crack propagated to the end face, and extended diagonally at the re-entrant corner. More cracks were formed on the ledge around the bearing pad. Shear cracks were also formed on the web. However, the width of the cracks on the web were minimal when compared to the cracks on the ledge. Cracks were more condensed on the ledge rather than the web. The damage condensation on the ledge was clearly shown on the end face (Figure 4-6(b)). The ledge failures were becoming clear as the cracks on the ledge intensified as the load increased whereas the cracks on the web showed no notable differences. The interior ledge test recorded a measured peak strength of 85 kips (378 kN) after ULS (76 kips [340 kN]). While the exterior ledge test reached the peak at 66 kips (293 kN) before ULS (68 kips [300 kN]). The maximum width of the cracks on the ledge and web were 3.5 mm and

0.5 mm respectively for the interior ledge test. For the exterior test, it was 2.5 mm and 0.75 mm, respectively.

(a) T5I1 – ledge interior

(b) T5E1 – ledge exterior

(c) T1I1 – hanger interior

(d) T1W1 – hanger exterior

(e) T3I2 – punching interior

(f) T3E1 – punching exterior
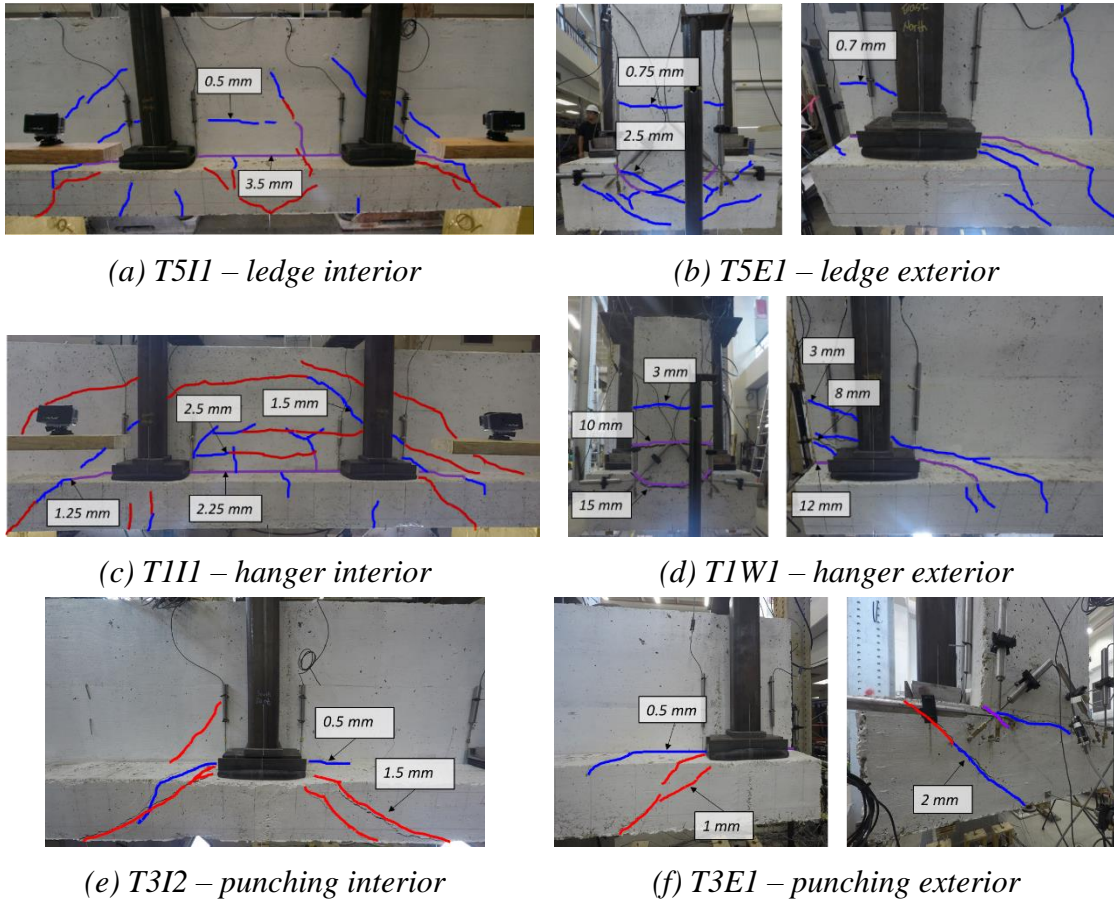
Figure 4-6. Observed Damages on Specimens at Measured Ultimate Load. Cracks formed before SLS in purple, between SLS and ULS in blue, and after ULS in red.

Figure 4-6(c) and (d) is showing the observed cracks on interior and exterior hanger tests, respectively. The initial cracks were formed at the interface and propagated similar to the ledge tests. The first cracks were observed at SLS (48 kips [220 kN]) in interior. For the exterior hanger test, it was observed at 36 kips (158 kN) before SLS (45 kips [200 kN]). The crack formation on the hanger tests were varied from the ledge

tests as the load increased. Cracks were condensed on the web rather than the ledge. The horizontal cracks on the web, hanger cracks were eminent from the hanger tests which were caused by the vertical separation of the ledge from the web. The damages on the end face (Figure 4-6(d)) clearly depicts these hanger cracks. The hanger cracks were extensively widened as the load increased, describing the hanger failure of the specimens. The measured peak strength of the interior hanger test was 90 kips (400 kN) which was higher than ULS (76 kips [340 kN]). The exterior hanger test had a measured peak of 66 kips (294 kN) that was lower than ULS (68 kips [300 kN]). The maximum crack width of the hanger cracks and ledge cracks were 2.5 mm and 1.25 mm for the interior hanger test. While the contrast was dramatic for the exterior hanger test which were 15 mm and 2 mm.

The observed cracks on interior and exterior punching shear tests were shown in Figure 4-6(e) and (f). The cracking of punching shear tests started on the web-ledge interface behind the bearing pads, similar the ledge and hanger tests. The initial crack was observed at 52 kips (231 kN) for the interior punching shear test after SLS (48 kips [220 kN]). While the first crack was observed at SLS (45 kips [200 kN]) for the exterior punching shear test. These cracks were further extended along the interface and propagated diagonally to the top face of the ledge. However, these cracks were not associate to the punching shear failures. The critical damages for punching shear tests were truncated cone cracks formed under the bearing pads. These cone cracks, which were evidence of a punching shear failure, were formed at later stage close to the ultimate strength. The specimen lost load resistance shortly after the formation of the cone cracks,

describing the brittle nature of the punching shear failure. The formation of cone crack was at 88 kips (391 kN) and the measure ultimate strength was 94 kips (418 kN) for the interior punching shear test. For the exterior punching shear test, the formation of cone crack was at 78 kips (347 kN) and the measure ultimate strength was 80 kips (356 kN). Both interior and exterior punching shear tests experienced the failure after ULS. The maximum crack width of the cone cracks and the interface crack at the measured ultimate was 1.5 mm and 0.5 mm for the interior punching shear test, and was 2 mm and 0.5 mm for the exterior punching shear test.

4.3.3. **Description of Finite Element Model**

An overview of the FE model is presented in Figure 4-7. The 3-D components including the bent caps, support columns with base plate, loading frame and the bearing plates were modeled using 8-node solid element (C3D8R) with reduced integration and hourglass control. All components were modeled with as-built dimensions except the upper beam of the loading frame (W-beam) was modeled as a rectangular shape for simplicity. Reinforcing bars were modeled using two-node linear truss element (T3D2) and embedded into the bent cap specimen assuming perfect bond between the rebar and concrete. The model was meshed with a typical element size of 2in. (50 mm).

71
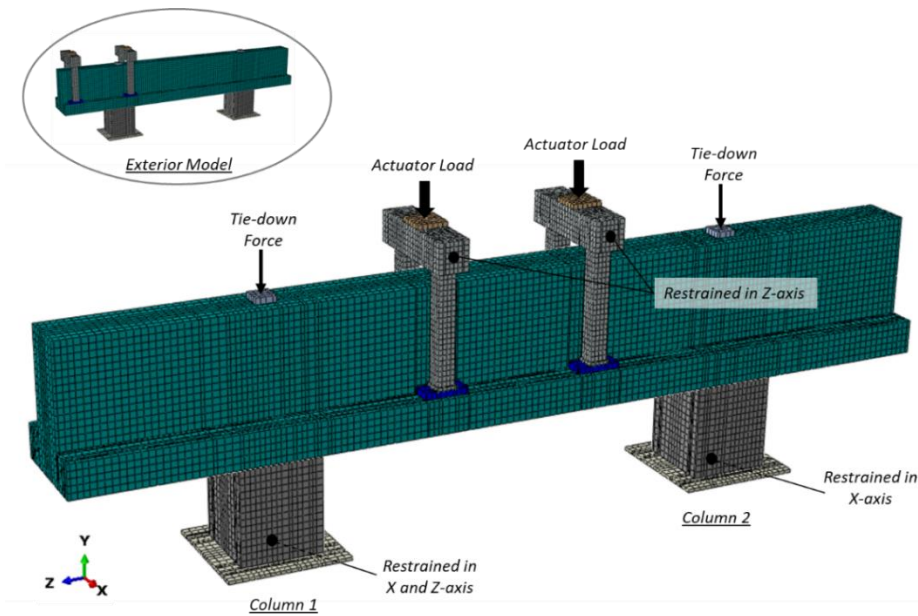
Figure 4-7. Overview of Finite Element Model.

Cracking of the concrete was defined using damage-plasticity model. Table 4-2 lists the values of the critical parameter employed by the model. The stress-strain relationship of concrete under uniaxial compression and the tension stiffening effect of concrete was defined with the cracking stress of concrete set as $6\sqrt{f_c'(psi)}$ $(0.5\sqrt{f_c'(MPa)})$. The strength of the concrete was obtained from the material test. The material model for all steel elements was based on elastic-perfectly plastic behavior. The yield strength of the normal steel member and the reinforcing rebar were defined as 36 ksi (248 MPa) and 62 ksi (427 MPa), respectively. The elastic modulus of steel elements was 29,000 ksi (200 GPa).

Table 4-2. Input Values of Concrete Damaged Plasticity Model.

Dilation Angle	Flow Potential Eccentricity	fb0/fc0	K	Viscosity Parameter
33	0.1	1.16	0.667	0.001

Boundary conditions were given to the bottom-center of the support columns to simulate a simply supported condition. As shown in Figure 4-7, Column 1 was retrained in horizontal (Z-axis) and transverse (X-axis) direction while Column 2 was restrained in transverse direction. Vertical restrains (Y-axis) were given to both columns to simulate the ground support. The loading frames were restrained in longitudinal direction (Z-axis) for stability. Contacts between the different components were described by surface-to-surface interaction. Normal and tangential behaviors between the contacting surfaces were defined to simulate any possible separation and sliding that may occur during the loading.

The general static load procedure was adopted for the analysis. The self-weight of the components was introduced at the first loading step. The prestressing load of the tie-down bar was then applied to the bent cap to simulate the clamping fore. Loads were then applied to the loading frame by displacement control to enable an observation of post-peak behavior of the FE model.

4.4. Validation of FEM with Experimental Results

The analysis results from the FE models are compared to the experimental results to verify the ability describing the structural behavior of inverted-T bent caps. Load-deflection response and crack pattern predicted by the models are primarily compared to the experimental data.

4.4.1. **Concrete Mechanical Properties**

The sensitivity of the FE model response to various concrete mechanical models was firstly evaluated. Figure 4-8 presents the stress-strain relationship for various concrete models considered in this study. The concrete damage-plasticity model (ABAQUS) adopted in this study requires in-elastic concrete properties as the input. Therefore, the post-peak branch of the concrete models are impacting the response of the FE models. Three compression models describing the post-peak falling branch with a linear (Kent and Park, 1971), parabolic (Mander et al., 1988), and bilinear (Karthik and Mander, 2011) shapes were considered. For the tension models, one linear (Bazant and Oh, 1983) and two bilinear (Hillerborg, 1976 / Karthik and Mander, 2011) models were used to describe the post-peak branch. The ledge models which were associated to the concrete failure was selected as the typical case to perform the sensitivity analysis.

Figure 4-9 and Figure 4-10 presents the sensitivity analysis results of the ledge models with the measured concrete cylinder strength ($f'c$) and a reduced concrete strength ($0.85f'c$). The reduced concrete strength, $0.85f'c$, was a conversion of the cylinder strength to the actual strength of the member.

From the analysis, the different concrete models have moderate effect on the response of the FE models. Mostly similar response was observed for all the cases at the initial ascending stage. The response of the FE models diverged when the load close to the peak strength. The post-peak behavior was also affected by the different concrete models. But the variations between the different concrete models were within 10% ranges.

74
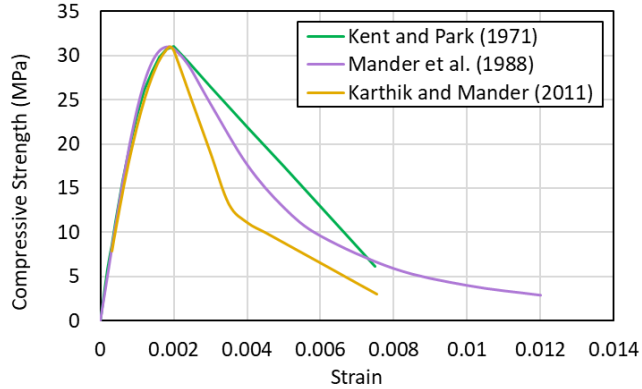
(a) Compression models
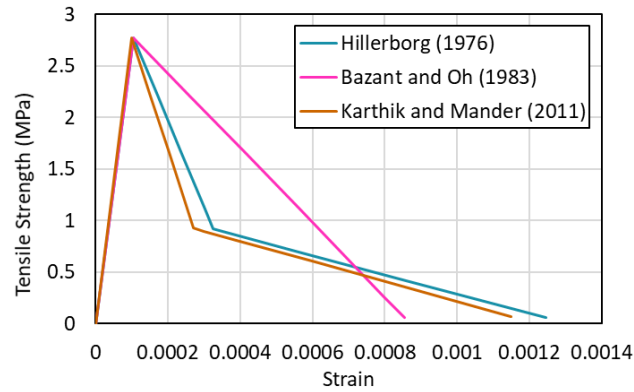
(b) Tension models

Figure 4-8. Stress-Strain Relationship for Various Concrete Models.

For the compression models, the linear post-peak model gives a conservative result than the other two models. The parabolic post-peak model and the bilinear post-peak model gives a slightly reduced response. Overall, the FEM prediction underestimated the peak stage for the interior but overestimated the peak stage for the exterior models. The linear post-peak model match well to the interior while the bilinear post-peak model matches well to the exterior test data.

For the tension models, the linear post-peak model gives a stronger response than the other two bilinear post-peak models, while the response of the two bilinear post-peak

models were similar. The linear post-peak model matches well to the interior while Karthik and Mander's bilinear post-peak model matches well to the exterior test data.

Use of the measured cylinder strength of concrete ($f'c$) slightly overestimated the response of the region from cracking to peak strength. While use of the reduced concrete strength (0.85 $f'c$) gives a more reliable response at the same region. However, it underestimated the peak strength region of the interior cases. For the exterior, the response with reduced concrete strength gives a more correlated result than the cases with the measured cylinder strength.

Overall, a well correlated results were obtained for all the models. For the consistency and simplicity, this study adopted the Kent and Park's compression model and Hillerborg's tension model to generate the analysis results.
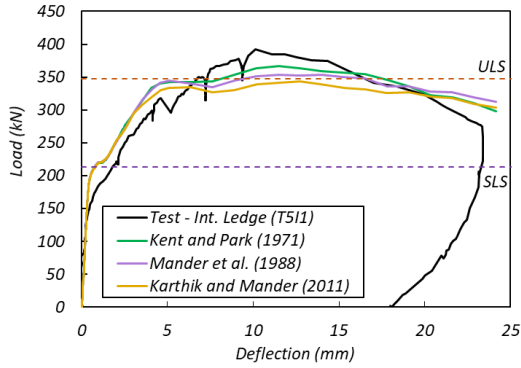
(a) Concrete compression model interior (T5I1)
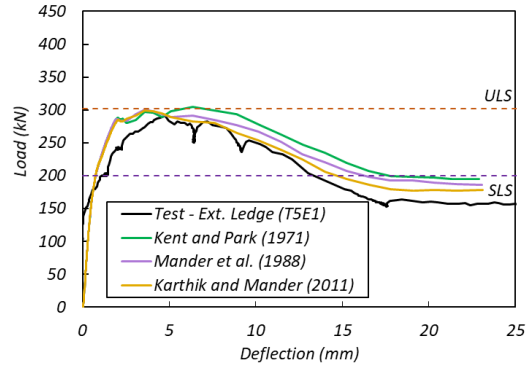
(b) Concrete compression model at exterior (T5E1)
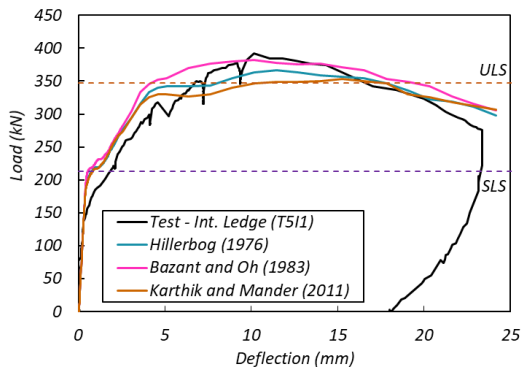
(c) Concrete tension model at interior (T5I1)
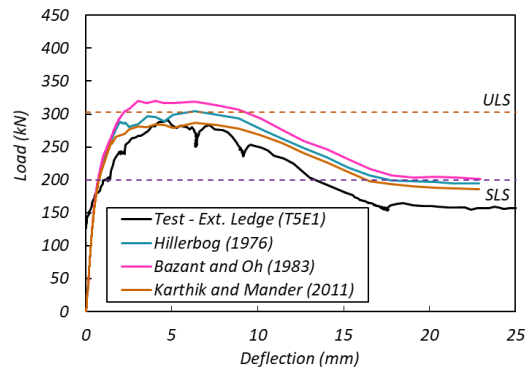
(d) Concrete tension model at exterior (T5E1)

Figure 4-9. Sensitivity Analysis Results for Ledge Models with Various Concrete Models (f'c).
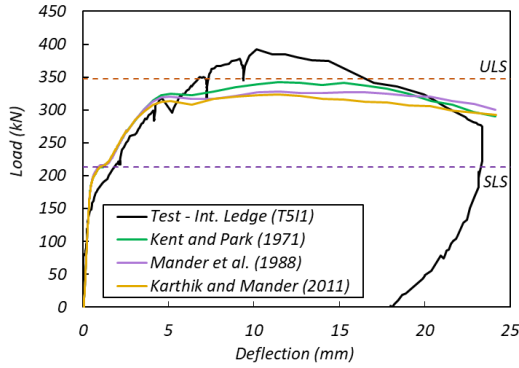
(a) Concrete compression model interior (T5I1)
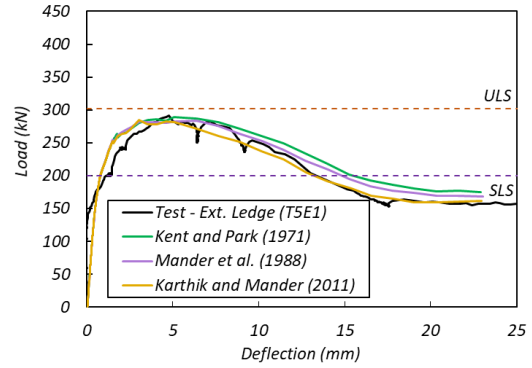
(b) Concrete compression model at exterior (T5E1)
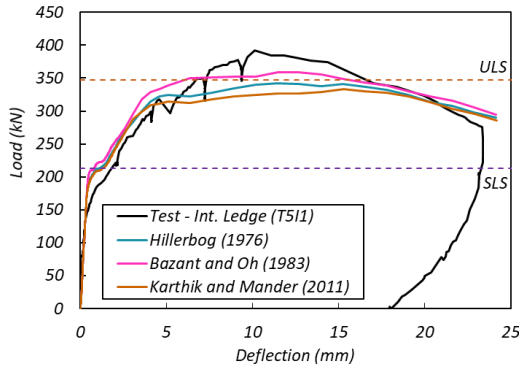
(c) Concrete tension model at interior (T5I1)
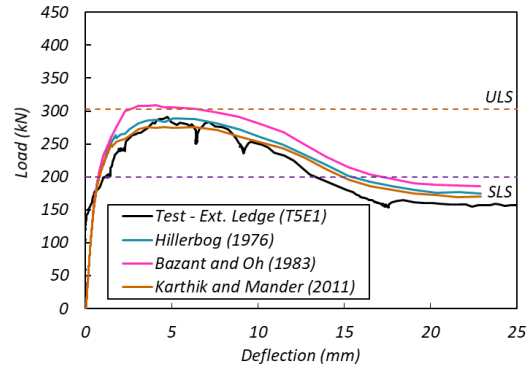
(d) Concrete tension model at exterior (T5E1)

Figure 4-10. Sensitivity Analysis Results for Ledge Models with Various Concrete Models (0.85f'c).

4.4.2. **Load-Deflection Response**

Figure 4-11 presents the load-deflection from the FE modes together with the experimental data. The initial cracking load and ultimate strength are marked on the plots. The cracking load of the FE models are identified as the strength when the maximum tensile stress of concrete element firstly reaches the cracking stress of $6\sqrt{f_c'(psi)}$ $(0.5\sqrt{f_c'(MPa)})$. The first cracking, both from the experimental observation and FEM prediction, occurred at the web-ledge interface behind the loading point for all cases. For hanger and ledge tests, this is the primary location of damage associated with the failure mechanism.

It can be seen from the graphs that the FEM predictions are in good agreement with the experimental data for all cases. Linear behavior before the cracking well predicted by the FEM. Non-linear behavior after cracking up to failure for some cases have divergence though in an acceptable range. Post-peak response of punching and ledge models differ from the experimental data at later stages. The increase of displacement at this stage is primarily due to the increase of crack width. The concrete elements at this stage are subject to a higher principal tensile strain. The strength degradation of concrete axial strength due to principal tensile strain is not described in the concrete damage plasticity model in ABAQUS, which may have caused the higher load response at this post-peak stage.

Table 4-3 compares the predicted cracking load and ultimate strength with the experimental data. The cracking load predicted by the FE models are about 10% lower than the experimental observation. The cracking loads from the testing were recorded at the point where the crack formation is visible during a pause in the testing. Therefore, it

is reasonable that the observed cracking initiated a slightly lower demand than recorded. The ultimate strength of the models correlates well with the experimental results and are within 5% of the measured values.
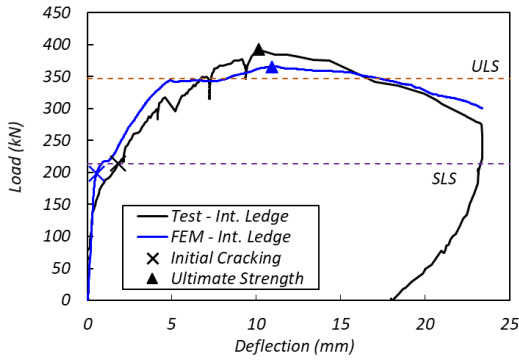
(a) Ledge interior – T5I1
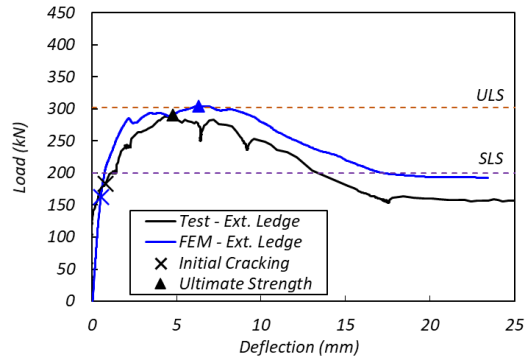
(b) Ledge exterior – T5E1
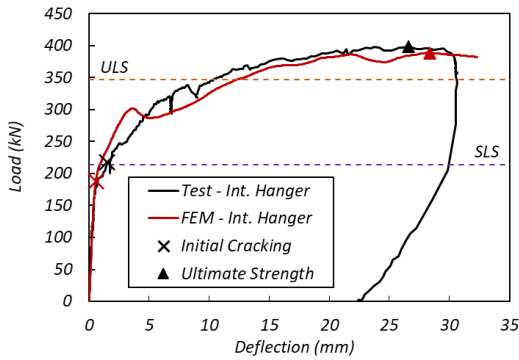
(c) Hanger interior – T1I1
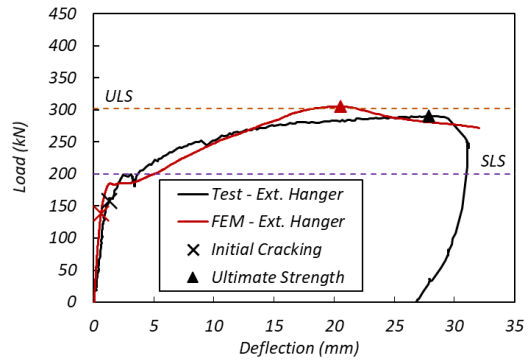
(d) Hanger exterior – T1W1
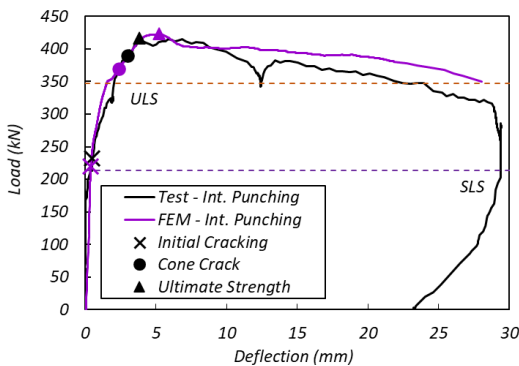
(e) Punching interior – T3I2
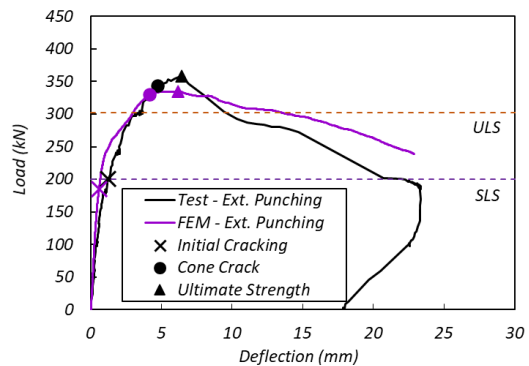
(f) Punching exterior – T3E1

Figure 4-11. Load-Deflection Response from FEM and Test.

Table 4-3. Comparison of Predicted and Observed Strength.

	Interface Cracking (kN)			Ultimate Strength (kN)		
	FEM	**Test**	**FEM/Test**	**FEM**	**Test**	**FEM/Test**
Punching Interior	218	231	*0.94*	423	418	*1.01*
Punching Exterior	184	200	*0.92*	335	356	*0.94*
Ledge Interior	196	214	*0.92*	366	378	*0.97*
Ledge Exterior	161	182	*0.88*	304	294	*1.04*
Hanger Interior	201	214	*0.94*	389	400	*0.97*
Hanger Exterior	140	158	*0.88*	305	294	*1.04*

4.4.3. **Crack Pattern and Failure Mode**

Crack pattern is a key feature to distinguish the different local failure mechanisms of inverted-T bent caps. The crack patterns predicted by the FE models are compared to the experimental observations at critical load states. Stress contours of the concrete element were used to demonstrate the cracking region on the FE models. Cracking potential is defined as the principal tensile stress of a concrete element reaching the cracking stress. Once a crack forms in the model, the normal stress across the crack is reduced, and the stress around the crack is redistributed. The direction of the crack remains fixed after cracking. Therefore, the cracks formed at early stage is not visible at later stage on stress contours. Maximum principal stress is primarily used to depict the cracking area on the FE models. The direction of crack is perpendicular to the direction of the maximum tensile stress. For the punching models, minimum principal stress is also presented to demonstrate the compression struts formed under the bearing pads.

Figure 4-12 presents an overview of the stress contours for all six cases at ultimate strength. The results of ledge and hanger models were presented by maximum principal stress contour while the result of punching model was shown in minimal principal stress contour. Figure 4-13 through Figure 4-15 compares the stress contours of the model in the regional area with the experimental observations at critical load states. The observed damages from testing are presented to provide references. The cracks on the specimens are marked in purple, blue, and red to demonstrate the cracks formed before or at SLS, between SLS and ULS, and after ULS, respectively. The upper limit of the maximum principal stress contour is set as the cracking stress of concrete. That is, red on maximum principal stress contours is indicating the region that potentially have cracked. Any stress exceeds the limit is shown in grey. The stress in concrete element may exceed the cracking stress as the value affected by the adjacent reinforcing steels. The lower limit of the minimum principal stress contour is also set as the (negative) cracking stress. The blue on minimum principal stress contour is indicating the cracking caused by the compression struts. The stress contours and the test photos are also overlayed to verify the predicted damage region.

(a) Ledge interior – T5I1   *(b) Ledge exterior – Max. Principal*

(d) Hanger interior – T1I1   *(e) Hanger exterior – T1W1*

(e) Punching interior – T3I2   *(f) Punching exterior – T3E1*
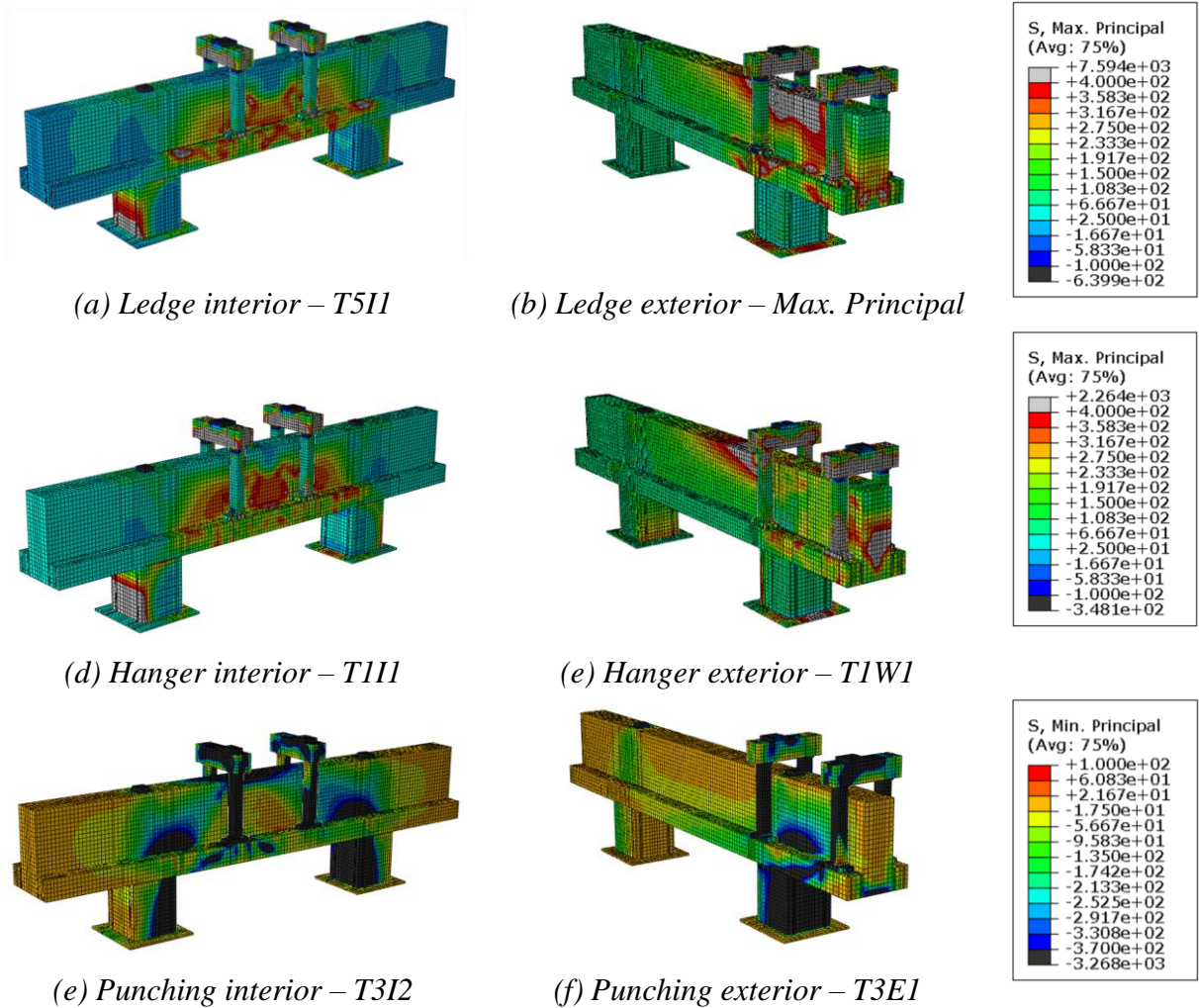
Figure 4-12. Overview of Stress Contour at Ultimate Strength. Ledge and hanger model show the maximum principal stress and punching model show the minimum principal stress.

4.4.3.1. Ledge Failure

Ledge failure (Figure 4-13) is identified as the separation of the ledge outward and away from the web while also deforming downward along the face of the web. The crack pattern predicted by the ledge FE model showed a good agreement with the experimental observation. The interface cracks at SLS were simulated by the FE model. Though the cracking area in stress contour did not propagate along the interface as observed from the

test, a clear tendency of cracking along the interface was captured by the model. The cracks on the ledge were well predicted at ULS whereas the web cracks were not clearly visible on the contours. But the model showed a tendency of the damages propagating toward to the top of the section. The web cracks were captured by the model at later stage. The crack pattern at peak correlate well with the experimental observation. Both ledge and web cracks were predicted with the locations match with the observed cracks. Damages on the ledge were more intensified than the web.

The exterior model also showed a promising result. The cracking area on the stress contour matches with the experimental observations. The damage on the end face at peak was more condensed in a narrower region than the observed damages but formed at the correction regions. The ledge failure was prominent on the exterior simulation. Overall, the ledge FE model was able to simulate the ledge failure mechanism of inverted-T bent cap.
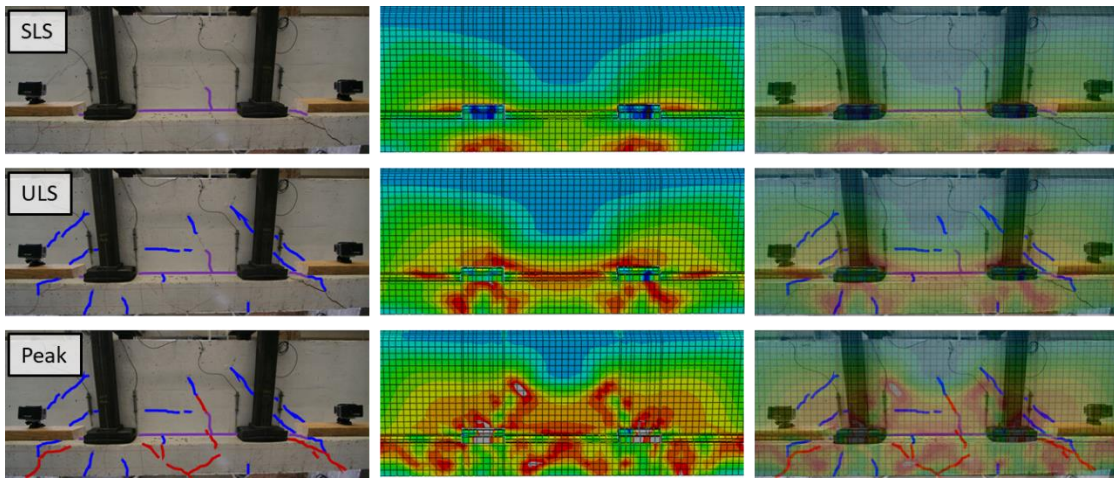
(a) Interior
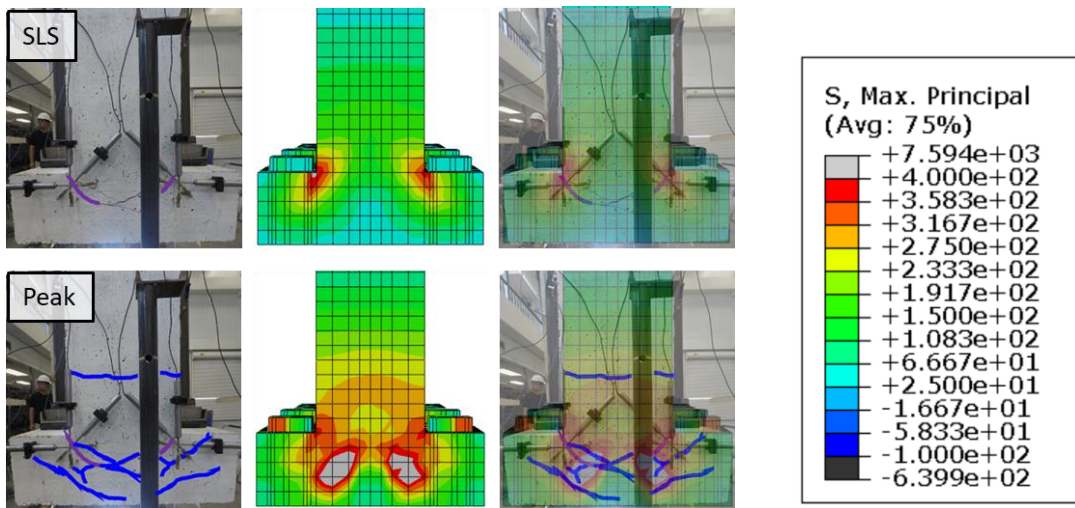
(b) Exterior

Figure 4-13. Comparison of Regional Damage for Ledge Model. FEM results show the maximum principal stress.

4.4.3.2. Hanger Failure

Hanger damage (Figure 4-14) is indicated by the vertical separation of the bottom flange from the web. The separation begins at the web-ledge interface (primary hanger crack), followed by secondary hanger cracks higher up on the web at approximately the neutral axis and near the top of the section as the load increases. The crack pattern shown in the hanger-deficient FE model is well matches with the experimental observation. The model captured the cracks at the web-ledge interface at SLS but in a concentrated region similar to the ledge models. The cracks on the web at ULS and at peak in interior case were well predicted. The location of the cracks matched the experimental observations with cracks primarily located on the web rather than the ledge. The exterior model also showed a reasonable prediction. Interface cracks at SLS was captured. The model at peak showed a large stress concentration area on the end face. The vertical separation of the bottom flange is more significant in exterior case which has limited support. The hanger reinforcement close to the end face subject to a high tensile stress at peak hence affected the adjacent concrete elements on the end face, resulted the grey area on the stress contour at peak where the stresses of the concrete element exceed the cracking stress. The three hanger cracks on the end face as observed from the test is not clearly shown on the stress contour, but the extent of the damaged region falls within that of the experimental observation. The hanger FE model was also able to simulate the hanger failure of inverted-T bent caps.
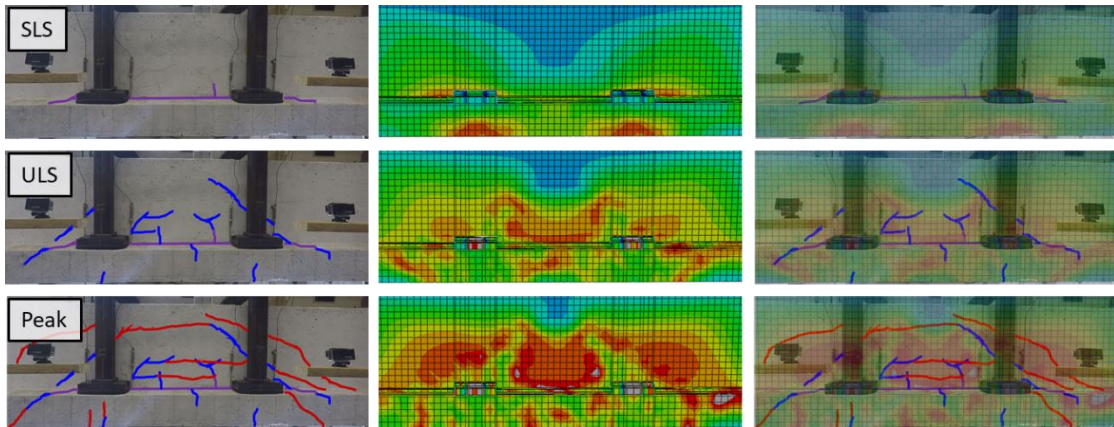
(a) Interior
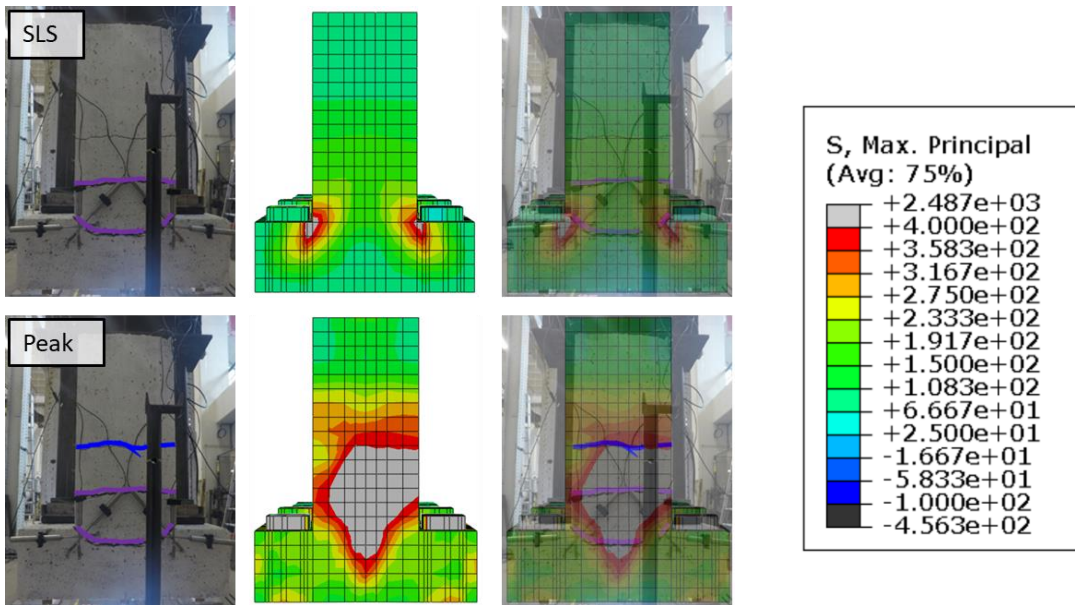
(b) Exterior

Figure 4-14. Comparison of Regional Damage for Hanger Model. FEM results show the maximum principal stress.

4.4.3.3. Punching Failure

Punching failure of inverted-T bent cap is evident by the cone cracks formed under the bearing pad. Figure 4-15 and Figure 4-16 compares the maximum and minimum principial stress contours to the experimental observations, respectively. The cone cracks emanating from the edges of the bearing pad is a form of tension failure of the concrete along the compression strut. The punching FE model for interior load points clearly captured the characteristics of the punching failure. The formation of the interface crack and the propagation was predicted by the model at SLS and ULS states. The cone crack at peak was clearly demonstrated as the stress concentration took place in the direction normal to the cone crack. The cone crack is prominent in the contour of the minimum principal stress. A clear compression strut formed under the bearing pad with the stress exceeds the cracking stress of the concrete. The angle of the cone crack also matched well with the experimental observation. The exterior model also presented a promising prediction. The crack pattern on the side of the bent cap matches well with the experimental observation with the clear cone crack simulated under the bearing pad. The cone crack on the end face was not as clear as the side face, though the propagation of the crack was captured by the model as the stress concentration area emanated at the re-entrant corner moved diagonally toward the bottom of the specimen as the load increased from SLS to the peak. The tendency of the diagonal cracking on the end face was also demonstrated on the minimum principal stress contour. Therefore, the punching FE model was able to capture the punching failure of inverted-T bent caps.

(a) Interior

S, Max. Principal
(Avg: 75%)
+8.091e+02
+3.700e+02
+3.308e+02
+2.917e+02
+2.525e+02
+2.133e+02
+1.742e+02
+1.350e+02
+9.583e+01
+5.667e+01
+1.750e+01
-2.167e+01
-6.083e+01
-1.000e+02
-2.277e+02
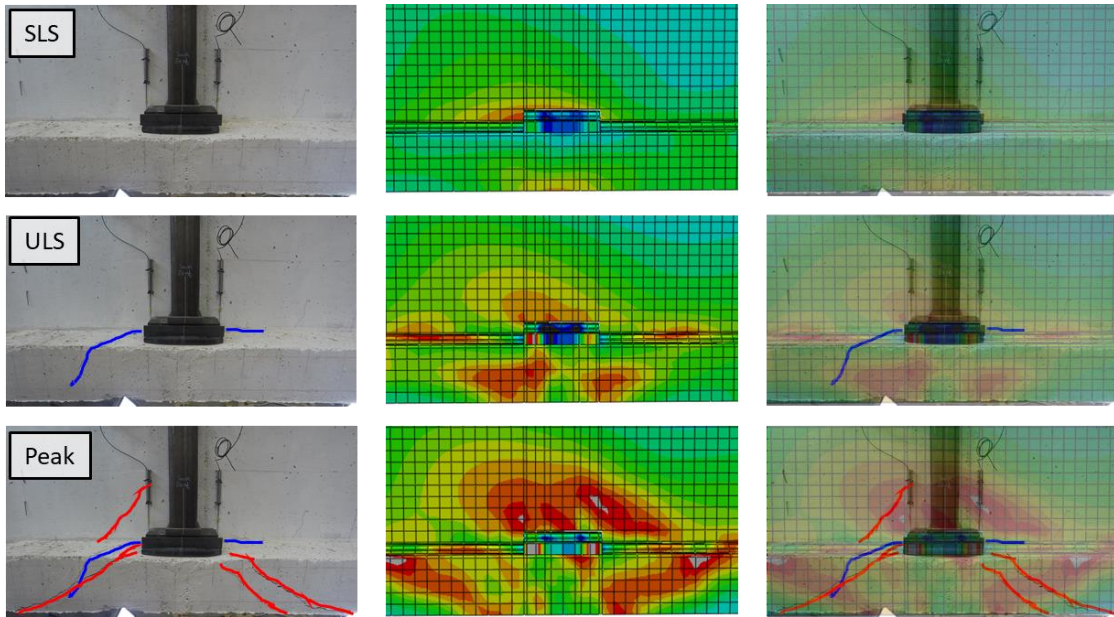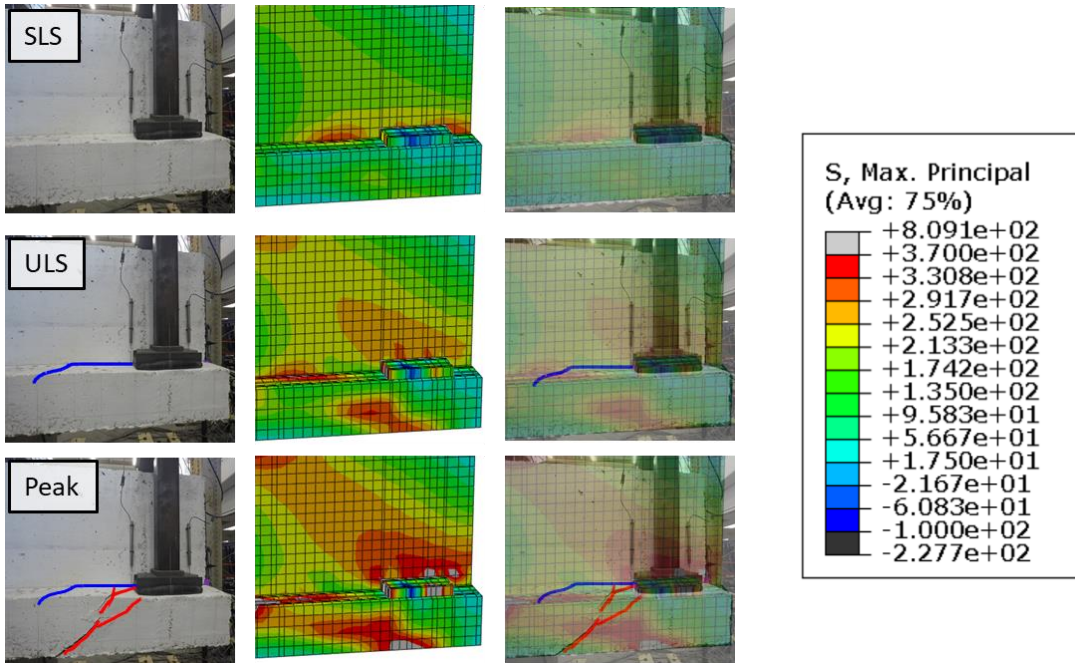
(b) Exterior

Figure 4-15. Comparison of Regional Damage for Punching Model. FEM results show the maximum principal stress.

(a) interior

(b) Exterior
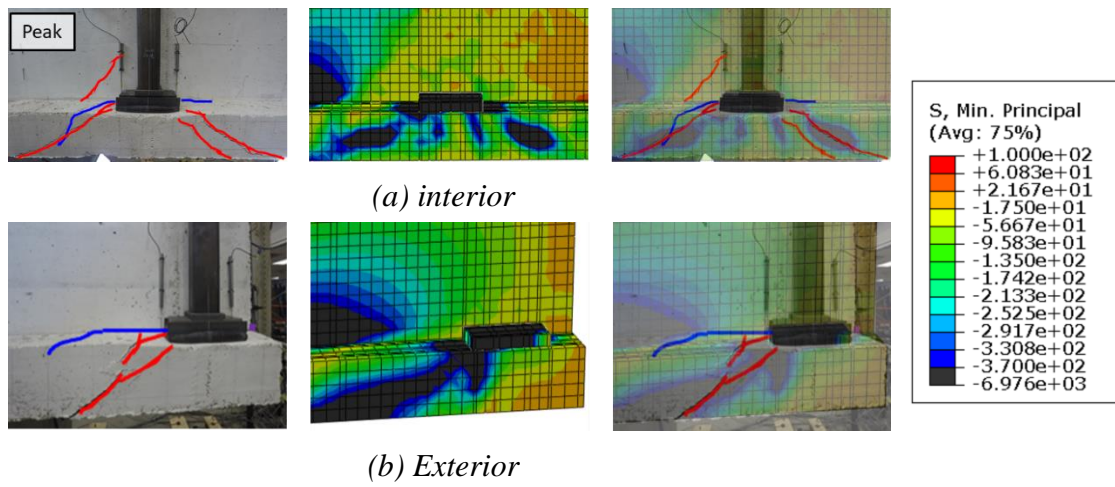
Figure 4-16. Comparison of Regional Damage for Punching Model. FEM results show the minimum principal stress at peak strength.

4.5. Alternative Reinforcement Designs

The FE models validated by the experimental results are utilized to study the impacts of various reinforcement layouts on the local behavior of inverted-T bent caps. Four different reinforcement layouts were considered with the variations given to the ledge bar configuration and the spacing of ledge and hanger reinforcements. Figure 4-17 and Figure 4-18 presents the different reinforcement layout studied on the ledge and hanger deficient specimen, respectively. The variations of the reinforcements are highlighted in the figure.

The first case (C1) is the use of diagonal ledge reinforcement instead of the horizontal ledge reinforcement that being used in the current design standard. The diagonal ledge reinforcement was considered in the study carried out by Mirza and Furlong (1971). It was expected to improve the structural behavior of inverted-T bent caps by placing the reinforcement across the re-entrant corner that subject to complex stress

90

state. The ultimate strength of the specimen was nearly identical to that with the horizontal ledge reinforcement, therefore, was not recommended because of construction efficiency. However, the performance at service state was not investigated. As the cracking at re-entrant corner of inverted-T bent cap at service state becomes an issue, the diagonal ledge reinforcement is studied to investigate the effect on cracking control at service state and any other potential impacts on improving structural performance of inverted-T bent caps.

The other three cases are concentrating ledge or hanger transverse reinforcements within the effective width engaged in local mechanisms. The effective width for local mechanisms were determined based on the Section 5.8.4.3.3 through 5.8.4.3.5 in AASHTO LRFD (2020) with proposed modification on exterior effective widths by Hurlebaus et al. (2018b). Adding more transverse reinforcements can be an effective way to improve the cracking performance and the strength response of inverted-T bent caps. The spacing of the transverse reinforcements at the regional area around the loading points are reduced to half to investigate the impacts of concentrating reinforcements on the local behaviors of inverted-T bent caps. The second case (C2) is providing new layers of the ledge transverse reinforcements with the diagonal ledge bars i.e., it is the combined use of diagonal and horizontal ledge bars around at the loading region. While the third case (C3) is providing more layers of ledge transverse reinforcements but keeping the same reinforcement configuration that has horizontal ledge bars. The last case (C4) is providing more layers of the hanger reinforcement in the regional area.
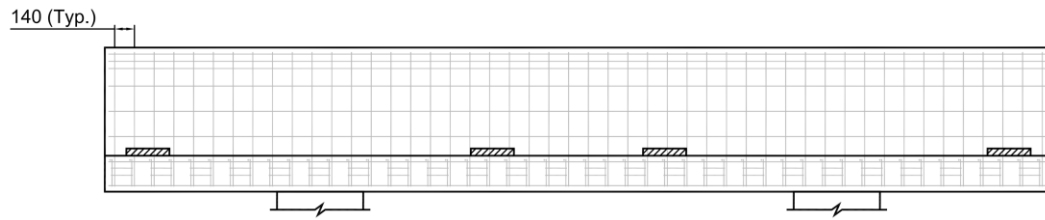
(a) Prototype
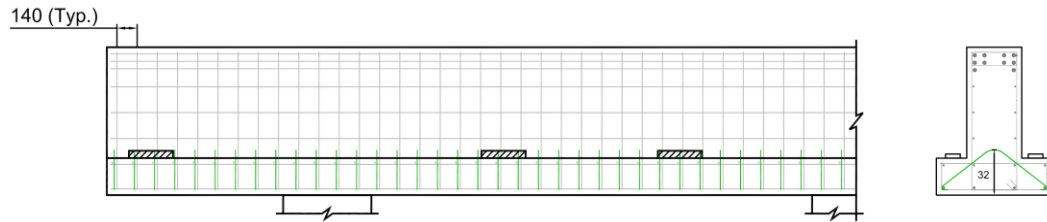
(b) C1: Diagonal ledge reinforcement
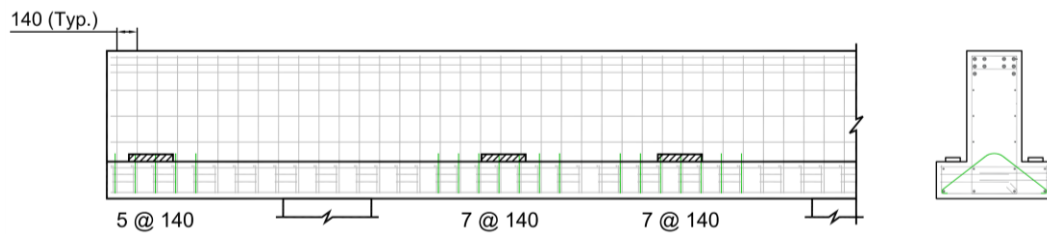
5 @ 140   7 @ 140   7 @ 140

(c) C2: Concentrate ledge reinforcement – combined

9 @ 70   11 @ 70   11 @ 70

(d) C3: Concentrate ledge reinforcement - horizontal

9 @ 70   11 @ 70   11 @ 70
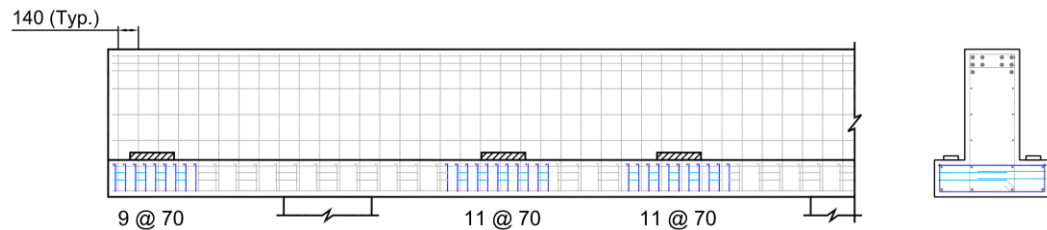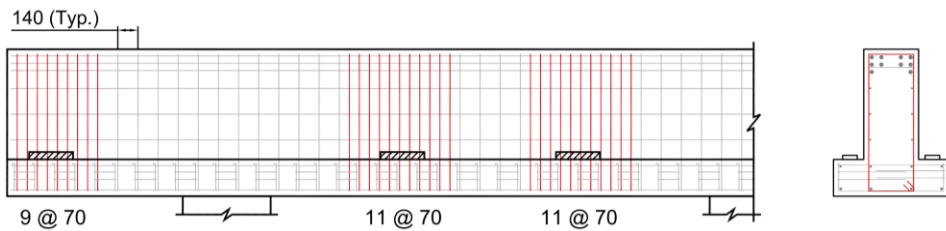
(e) C4: Concentrate hanger reinforcement

Figure 4-17. Reinforcement Layouts for Ledge and Punching Model.
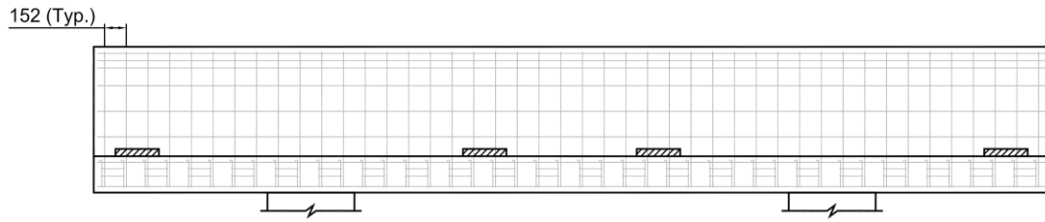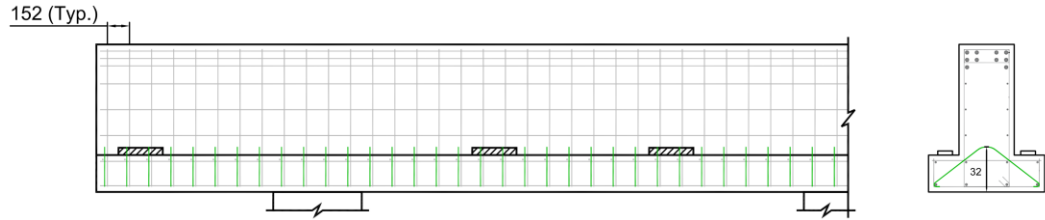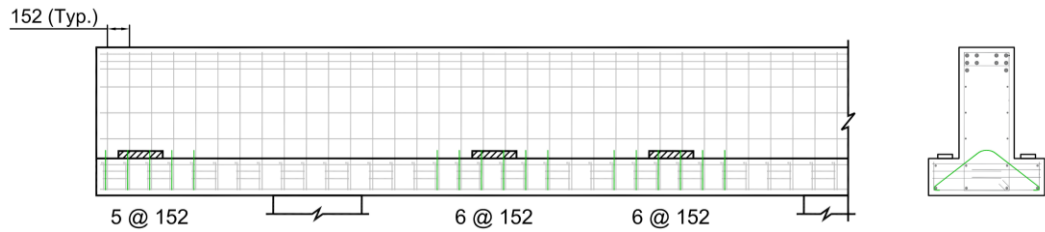
92

(a) Prototype

(b) C1: Diagonal ledge reinforcement

5 @ 152   6 @ 152   6 @ 152

(c) C2: Concentrate ledge reinforcement – combined

9 @ 76   11 @ 76   11 @ 76

(d) C3: Concentrate ledge reinforcement - horizontal

9 @ 76   11 @ 76   11 @ 76
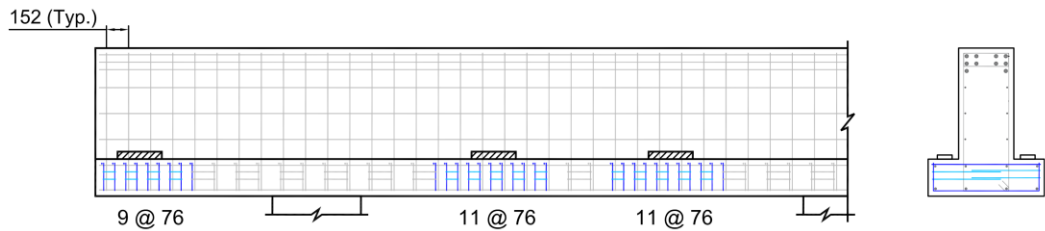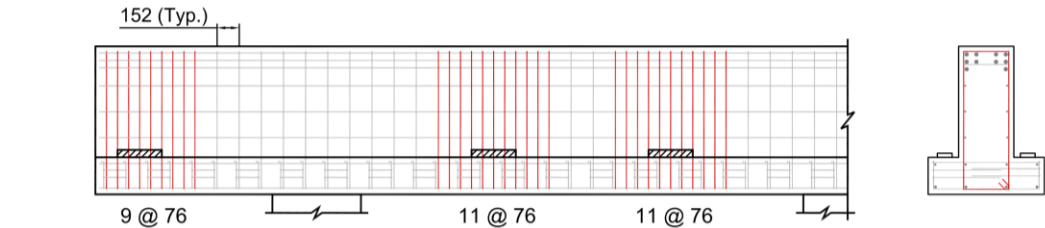
(e) C4: Concentrate hanger reinforcement

Figure 4-18. Reinforcement Layouts for Hanger Model.

93

Total of 30 cases including the prototypes were analyzed. Table 4-4 summarizes the analysis cases with the key outcomes. The model names indicate the type of model (L-, H-, and P- representing the ledge, hanger and punching models, respectively), exterior or interior (E or I, respectively) and the reinforcement modification considered (C1 to C4). The relative ratios of the outcomes of alternative cases to each prototype was presented in the table.

Load-deflection response, cracking and ultimate strength, plastic strain of concrete element at web-ledge interface, and stress distributed on different reinforcement around the loading points are presented to study the impact of the different reinforcement layouts. The cracking strength, as discussed previously, is the strength at the point the stress of concrete element firstly reaches the cracking stress. The plastic strain of concrete element in ABAQUS, calculated as the total strain minus the elastic, is representing the cracking strain of concrete. The concrete elements at the web-ledge interface behind the bearing pads, as indicated in Figure 4-19, are selected to provide the plastic strain data to investigate the cracking control impact of the different reinforcement layouts. Four concrete elements at each loading points are selected, and the average values are presented. Stress distributed on the reinforcement around the loading points, as shown in Figure 4-20(a), are also demonstrated. At each layer, maximum stress on the four different reinforcements as indicated in Figure 4-20(b) are pulled out.

Table 4-4. Summary of Fem Parametric Analysis Results.

Model	#	ID	Description	Strength (kN)				Interface Plastic Strain at SLS (µε)				Interface Plastic Strain at ULS (µε)			
				Crac.	Ratio	Ult.	Ratio	Trans.	Ratio	Vrt.	Ratio	Trans.	Ratio	Vrt.	Ratio
Ledge Interior	1	**L-I-Proto.**	Prototype	196.5	-	365.9	-	1280	-	1233	-	5965	-	3730	-
	2	**L-I-C1**	Diagonal Ledge Reinf.	203.9	*104%*	356.7	*97%*	954	*75%*	930	*75%*	5366	*90%*	3358	*90%*
	3	**L-I-C2**	Conc. Ledge Reinf. - Combined	218.7	*111%*	390.4	*107%*	518	*40%*	466	*38%*	3787	*63%*	2238	*60%*
	4	**L-I-C3**	Conc. Ledge Reinf. - Horizontal	214.4	*109%*	388.3	*106%*	518	*40%*	608	*49%*	3855	*65%*	3189	*85%*
	5	**L-I-C4**	Con. Hanger Reinf.	202.6	*103%*	373.5	*102%*	1092	*85%*	808	*66%*	5287	*89%*	2851	*76%*
Ledge Exterior	6	**L-E-Proto.**	Prototype	161.1	-	304.5	-	1883	-	867	-	4095	-	2523	-
	7	**L-E-C1**	Diagonal Ledge Reinf.	169.0	*105%*	303.0	*99%*	1483	*79%*	678	*78%*	3738	*91%*	2405	*95%*
	8	**L-E-C2**	Conc. Ledge Reinf. - Combined	180.5	*112%*	324.9	*107%*	1097	*58%*	388	*45%*	2783	*68%*	1883	*75%*
	9	**L-E-C3**	Conc. Ledge Reinf. - Horizontal	175.3	*109%*	320.3	*105%*	1118	*59%*	485	*56%*	2859	*70%*	2301	*91%*
	10	**L-E-C4**	Con. Hanger Reinf.	163.5	*102%*	311.4	*102%*	1882	*100%*	510	*59%*	4122	*101%*	1955	*78%*
Hanger Interior	11	**H-I-Proto.**	Prototype	200.6	-	388.6	-	407	-	630	-	4496	-	4726	-
	12	**H-I-C1**	Diagonal Ledge Reinf.	207.8	*104%*	398.5	*103%*	370	*91%*	593	*94%*	3191	*71%*	3452	*73%*
	13	**H-I-C2**	Conc. Ledge Reinf. - Combined	209.9	*105%*	409.6	*105%*	364	*89%*	535	*85%*	2751	*61%*	3381	*72%*
	14	**H-I-C3**	Conc. Ledge Reinf. - Horizontal	209.9	*105%*	390.0	*100%*	367	*90%*	627	*99%*	3007	*67%*	4649	*98%*
	15	**H-I-C4**	Con. Hanger Reinf.	209.8	*105%*	447.7	*115%*	396	*97%*	471	*75%*	4389	*98%*	2568	*54%*
Hanger Exterior	16	**H-E-Proto.**	Prototype	139.7	-	305.2	-	1511	-	1448	-	3435	-	2220	-
	17	**H-E-C1**	Diagonal Ledge Reinf.	146.4	*105%*	310.3	*102%*	1134	*75%*	1124	*78%*	2688	*78%*	1875	*84%*
	18	**H-E-C2**	Conc. Ledge Reinf. - Combined	147.9	*106%*	312.1	*102%*	1019	*67%*	1020	*70%*	2188	*64%*	1820	*82%*
	19	**H-E-C3**	Conc. Ledge Reinf. - Horizontal	148.9	*107%*	307.4	*101%*	1069	*71%*	1373	*95%*	2567	*75%*	2174	*98%*
	20	**H-E-C4**	Con. Hanger Reinf.	149.3	*107%*	322.0	*106%*	1351	*89%*	597	*41%*	3454	*101%*	1386	*62%*
Punching Interior	21	**P-I-Proto.**	Prototype	217.8	-	422.9	-	691	-	375	-	3445	-	2140	-
	22	**P-I-C1**	Diagonal Ledge Reinf.	234.5	*108%*	448.9	*106%*	510	*74%*	216	*57%*	2852	*83%*	1592	*74%*
	23	**P-I-C2**	Conc. Ledge Reinf. - Combined	234.7	*108%*	464.6	*110%*	462	*67%*	196	*52%*	2261	*66%*	1481	*69%*
	24	**P-I-C3**	Conc. Ledge Reinf. - Horizontal	234.7	*108%*	470.9	*111%*	468	*68%*	317	*85%*	2340	*68%*	1923	*90%*
	25	**P-I-C4**	Con. Hanger Reinf.	235.2	*108%*	502.5	*119%*	625	*90%*	171	*46%*	3161	*92%*	1316	*61%*
Punching Exterior	26	**P-E-Proto.**	Prototype	183.9	-	334.5	-	1965	-	1160	-	5410	-	3640	-
	27	**P-E-C1**	Diagonal Ledge Reinf.	188.4	*102%*	347.2	*104%*	1494	*76%*	853	*74%*	4662	*86%*	2852	*78%*
	28	**P-E-C2**	Conc. Ledge Reinf. - Combined	190.6	*104%*	354.0	*106%*	1395	*71%*	834	*72%*	3740	*69%*	2584	*71%*
	29	**P-E-C3**	Conc. Ledge Reinf. - Horizontal	190.1	*103%*	353.4	*106%*	1374	*70%*	1001	*86%*	3835	*71%*	3352	*92%*
	30	**P-E-C4**	Con. Hanger Reinf.	190.7	*104%*	378.2	*113%*	1970	*100%*	735	*63%*	5465	*101%*	2244	*62%*

* Crac. – cracking strength; Ult. – ultimate strength; Trans. – transverse strain; Vrt. – vertical strain; Ratio – relative ratio to prototype
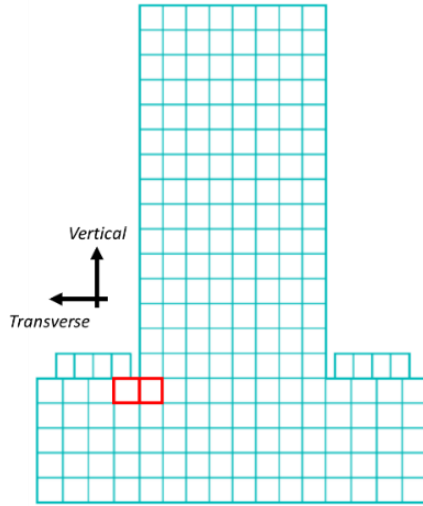
Figure 4-19. Concrete Element to Generate Strain Output.
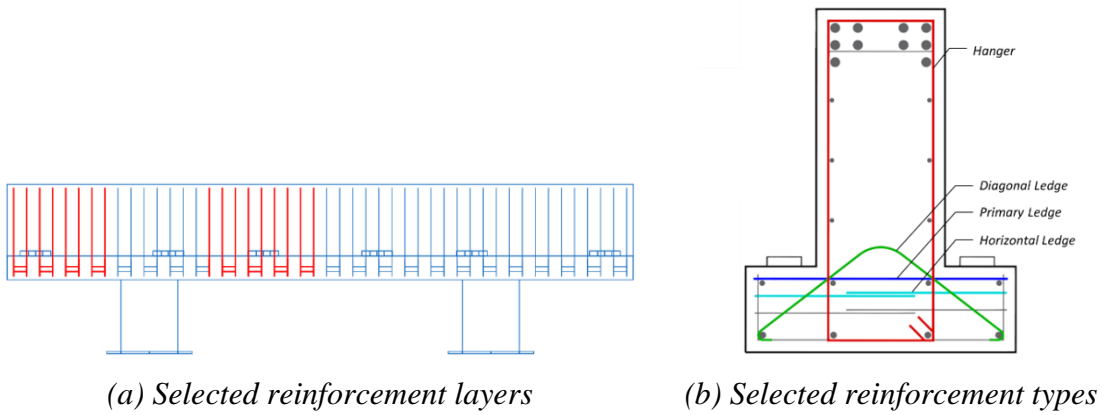
(a) Selected reinforcement layers   *(b) Selected reinforcement types*

Figure 4-20. Reinforcements to Generate Stress Distribution.

4.5.1. **Ledge Model**

The load-deflection response of the ledge models with the different reinforcement layouts are presented in Figure 4-21. The cracking load and ultimate strength are compared in a bar-chart with the relative ratio to the porotype specified. As can be seen from the graph, the models both in interior and exterior showed a similar behavior overall with the changes be the cracking load and the ultimate strength. Identical response was observed at the initial elastic region before cracking. Varying reinforcements, overall, resulted in delayed cracking. Use of the diagonal ledge reinforcement (C1) improved the cracking load by 5%. Concentrating ledge reinforcement at the loading region improved the cracking load about 10% where the impact of the combined case (C2) slightly higher than the horizontal case (C3). Concentrating hanger reinforcement (C4) has minimal effect on the ledge models. Slight increase of the stiffness was observed at the nonlinear region after cracking up to the ultimate except for C1 which shown an almost identical response with the prototype. The increase of the stiffness, though minimal, was observed in C2 and C3. C4 also showed an increase of stiffness but the effect was minimal. Similar post-peak responses were observed for all cases. As presented in Figure 4-21(b), C1 and C4 barely affected the ultimate strength while C2 and C3 improved the strength about 7%. The impact of C2 on the strength is slightly larger than C3.

Figure 4-22 compares the plastic strain of the concrete element at the web-ledge interface at SLS and ULS. Figure 4-23 and Figure 4-24 shows the distribution of stress in the reinforcement around the loading point at interior and exterior, respectively. The FEM analysis result reveals that the impact of the various reinforcements is more pronounced

97

when comparing the strain and stress outcomes. The results for interior and exterior showed a similar tendency with the exterior is less sensitive to the reinforcement variations. Use of diagonal ledge bars (C1) instead of horizontal bars reduced the strain at interface both in transverse and vertical direction by 25% and 10% at SLS and ULS, respectively. Concentrating ledge reinforcements around the loading region showed a more significant improvement. Both C2 and C3 reduced the transverse strain more than 30% at SLS and ULS. The combined use of diagonal and horizontal bar (C2) is a bit better than the case only using horizontal bar (C3). C2 also reduced the vertical strain significantly both at SLS (62%) and ULS (40%). However, C3 showed limited ability to control the vertical strain as it only contains horizontal bars that placed in direction normal to the vertical movement. It reduced the vertical strain by 50% at SLS but the effect was compromised at ULS where the ledge subject to a larger deformation. Concentrating hanger reinforcement (C4) on ledge deficient specimen did not show an outstanding result. It reduced the vertical strain by a certain amount but the effect on the transverse strain was minimal when compared to C2 and C3. For a ledge model, the transverse strain is the primarily component. Considering significant amount of reinforcements were added to C4, it may not be an effective solution to improve the structural performance of ledge model.

The stress distribution over the reinforcements around the loading region supports the above observations. The diagonal bars, shown in green, were taking significant amount of stress as it provided to the ledge. Direct comparison of C1 and prototype reveals that the diagonal bars have advantage over the horizontal bars. It was more activated than the

horizontal bars. The stress on the primary ledge reinforcements were also relieved when the diagonal bars replaced the horizontal bars. C2 and C3, by concentrating ledge reinforcements around the loading region, reduced the overall stresses on the ledge reinforcements. The impact of C2 was slightly better than C3. Whereas C4, with concentrated hanger reinforcements, reduced the stresses on the hanger reinforcements but it barely affected the stresses on the ledge reinforcements.

Overall, use of diagonal ledge reinforcement (C1) benefited the ledge model mainly by reducing the strain at the interface. The strain at SLS was reduced considerably by the diagonal bars. The impact at ULS was not significant though showed an improved performance when compared to the prototype. The strength of the section was not quite affected by the diagonal bars. The cracking strength was improved by a small amount, but the overall load response showed no difference when compared to the prototype. Concentrate ledge reinforcement reduced the interface strains substantially both at SLS and ULS. The combined case (C2) showed a better performance than the horizontal case (C3). C3 with only horizontal bars in the ledge have limited ability to control the vertical strain. The cracking and ultimate strength of the section was improved by C2 and C3, though the increase was not significant. The strength increase was not proportional to the increased quantity of the ledge reinforcements. Concentrating hanger reinforcement (C4) in a ledge model was barely benefited the section, therefore is not recommended.
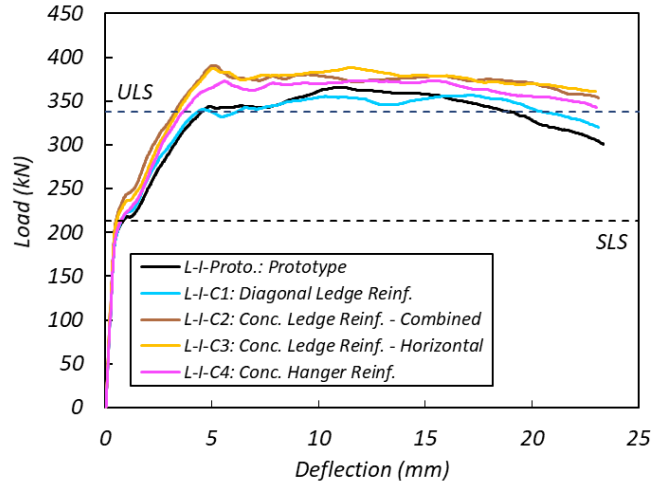
(a) Interior: load-deflection response
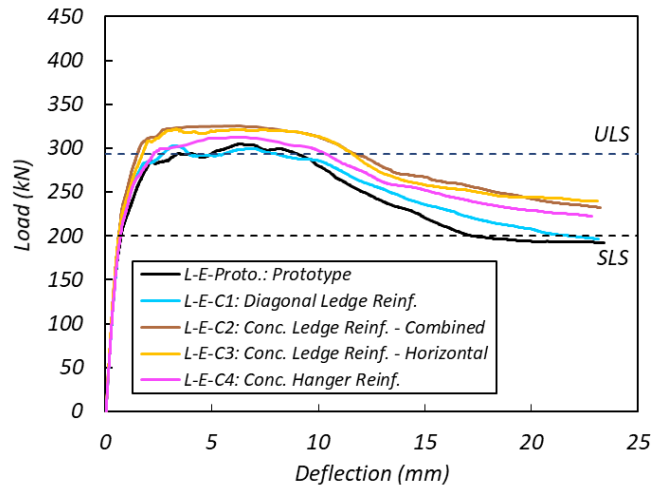
(b) Exterior: load-deflection response
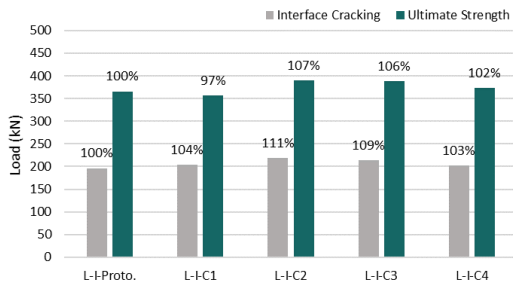
(c) Interior: strength comparison
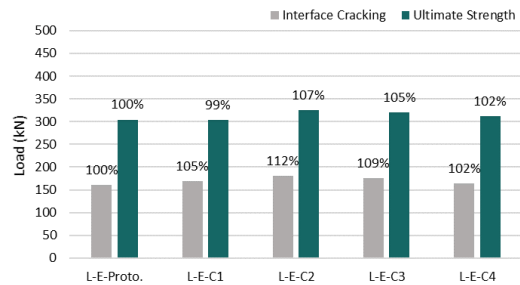
(d) Exterior: strength comparison

Figure 4-21. Load Response of Ledge Model.
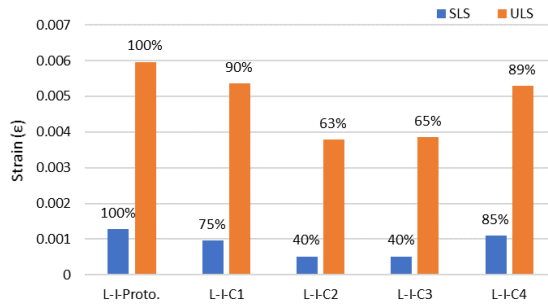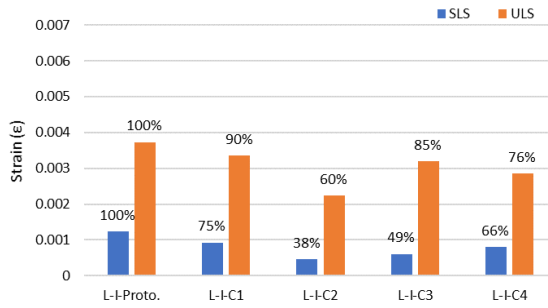
100

(a) Interior: transverse strain at interface

(b) Interior: vertical strain at interface
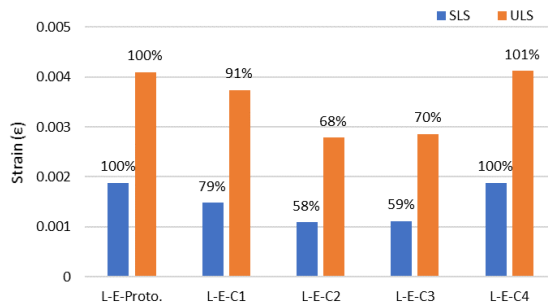
(c) Exterior: transverse strain at interface
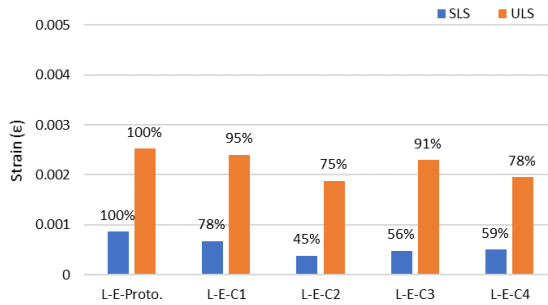
(d) Exterior: vertical strain at interface

Figure 4-22. Strain Data of Ledge Model.
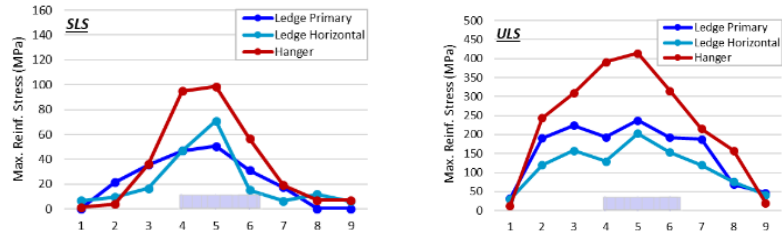
(a) L-I-Proto.: prototype
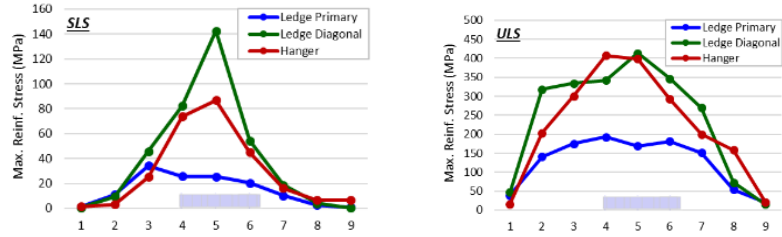
(b) L-I-C1: diagonal ledge reinf.
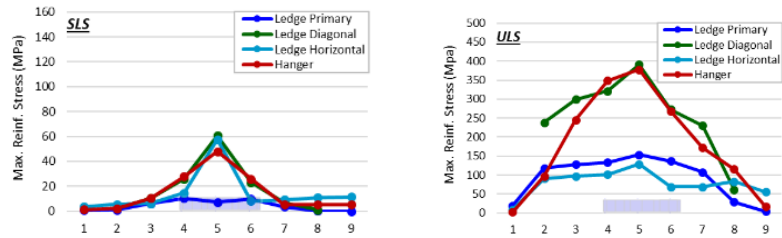
(c) L-I-C2: conc. ledge reinf. - combined

(d) L-I-C3: conc. ledge reinf. - horizontal

(e) L-I-C4: conc. hanger reinf.

Figure 4-23. Reinforcement Stress Distribution of Interior Ledge Model.

102

(a) L-E-Proto.: prototype

(b) L-E-C1: diagonal ledge reinf.

(c) L-E-C2: conc. ledge reinf. - combined

(d) L-E-C3: conc. ledge reinf. - horizontal

(e) L-E-C4: conc. hanger reinf.

Figure 4-24. Reinforcement Stress Distribution of Exterior Ledge Model.

103

4.5.2. **Hanger Model**

Figure 4-25 presents the load-deflection response of the hanger models with various reinforcement layouts. It is evident from the graph that concentrate hanger reinforcement (C4) was the only case that affecting the performance of the hanger model. The impact of the other cases – use of diagonal ledge bar (C1), concentrate ledge reinforcement with combined ledge bar (C2) and only with the horizontal bar (C3) – found to be negligible. Identical response was observed for all cases before the initiation of the plateaus on the load graphs which was triggered by the yielding of hanger reinforcements and the formation of the hanger cracks near the neural axis. The increase of the deflection after this point is primarily due to the increase of the vertical separation of the bottom ledge from the web. C4 with more hanger reinforcements was able to sustain more strength than the other cases. Whereas C1, C2, and C3 with the variations were given to the ledge reinforcements showed no notable changes when compared to the prototype. Similar results were observed at interior and exterior loading points. Reinforcement configurations C1, C2, and C3 did improve the cracking and ultimate strength to some degree but the increase was minimal. The cracking strength was improved about 5% while the increase of the ultimate strength was negligible. C4 increased the cracking strength by 5% and the ultimate strength by 15% in interior. The cracking strength of exterior region improved 7% by C4 however the ultimate strength was less sensitivity to the reinforcement variation compared to the interior. Only 6% increase on the ultimate strength was observed in exterior.

Figure 4-26 presents the interface plastic strain. Figure 4-27 and Figure 4-28 presents the stress distributed on the reinforcements for the interior and exterior hanger models, respectively. The impact of the reinforcement layouts on the interface strain for the hanger models were also notable. It should be noted that, the strain for interior load points at SLS is minimal as it was an early stage right after the cracking loads. The damage at this stage was not significant therefore the strain data for various cases were not quite comparable. The impact of the reinforcement variations become more pronounced at ULS. Use of diagonal ledge reinforcement (C1) reduced both transverse and vertical strain by approximately 28% at ULS. Concentrated ledge reinforcement with combined use of diagonal and horizontal ledge bars (C2) showed a better performance than C1. Concentrated ledge reinforcement (C3) only with horizontal bars was able to reduce the transverse strain but couldn't affect the vertical strain. Concentrated hanger reinforcement (C4) barely affected the transverse strain but the impact on the vertical strain was significant. It reduced the vertical strain by 46% at ULS. As the vertical strain is the main component for the hanger models, C4 was found to be superior to improve the structural behavior of hanger models. The exterior cases demonstrated a similar result as the interior with the strains at SLS also effectively reduced by the various reinforcement layouts. Same tendency was observed for the exterior cases but with a reduced sensitivity.

The effectiveness of the use of diagonal ledge bars and concentrating hanger reinforcement was well described by the stress distribution. C3 with concentrated ledge reinforcement only with horizontal bars barely affected the hanger model when compared to the prototype. The diagonal ledge bars in C1 and C2 actively engaged in the load

resistance. Diagonal ledge bars (C1) showed a better performance in relieving the stress on the hanger reinforcements. Concentrated hanger reinforcement (C4) effectively reduced the overall stress on the hanger reinforcement.

In summary, concentrated hanger reinforcement around the loading region (C4) improved the cracking and ultimate strength, and controlled the interface strain both at SLS and ULS. Diagonal ledge bars (C1 and C2) had minimal impact on the strength, but effectively reduced the interface strain. Both transverse and vertical strain was reduced using diagonal ledge bars. The performance of C2 was slightly better than C1. Whereas C3 with concentrated ledge reinforcements with horizontal bars was able to control the transverse strain but have negligible effect on vertical strain which is the primary component for a model with hanger weakness. The strength of the hanger model was not affected by the C3 reinforcement configuration.
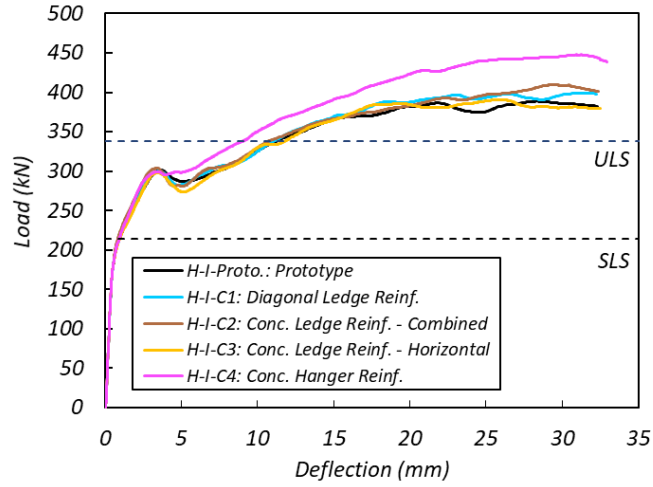
(a) Interior: load-deflection response
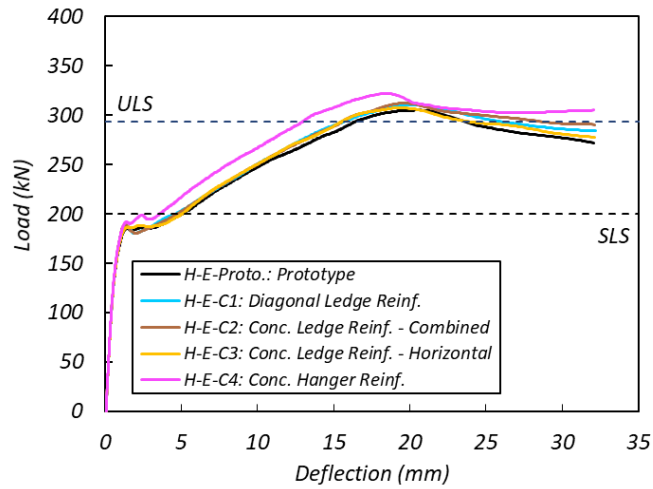
(b) Exterior: load-deflection response
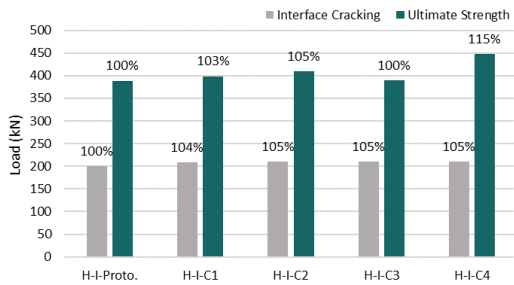
(c) Interior: strength comparison
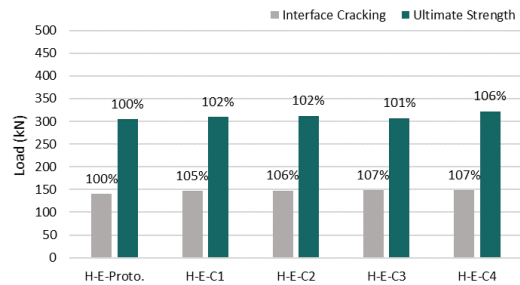

(d) Exterior: strength comparison

**Figure 4-25. Load Response of Hanger Model.**
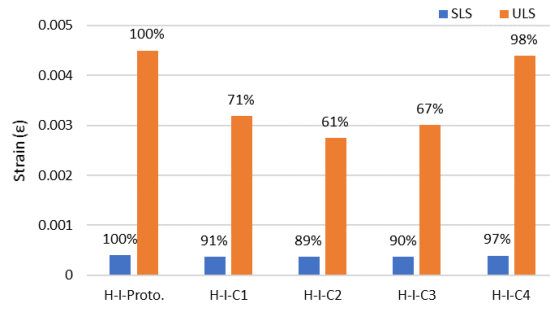
(a) Interior: transverse strain at interface
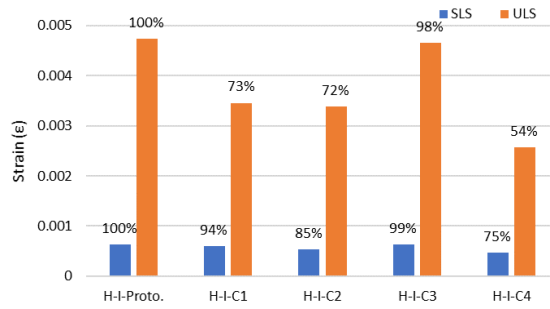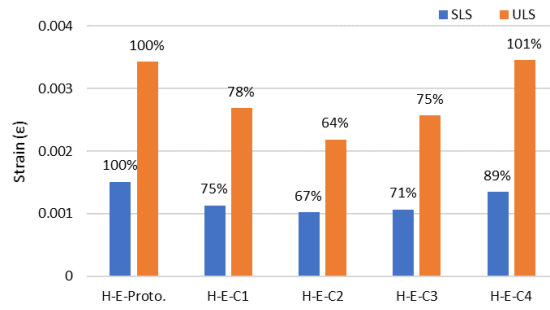


(b) Interior: vertical strain at interface

*(c) Exterior: transverse strain at interface*
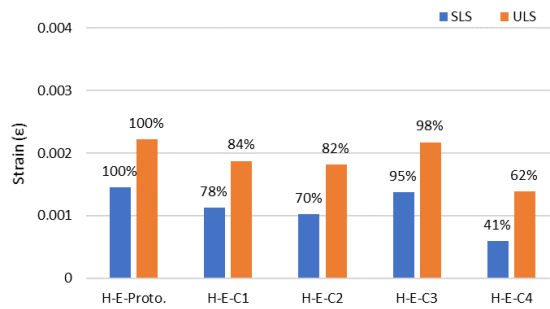

(d) Exterior: vertical strain at interface
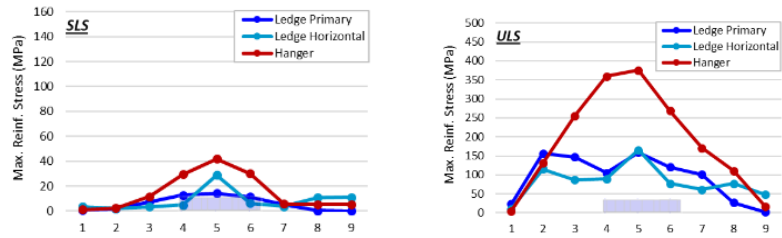
Figure 4-26. Strain Data of Hanger Model.
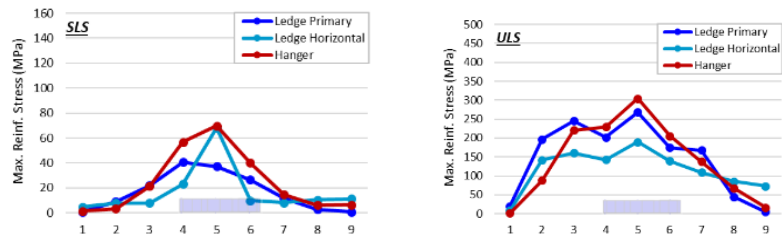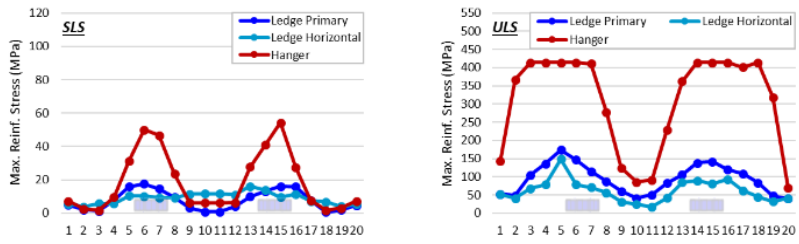
(a) H-I-Proto.: prototype
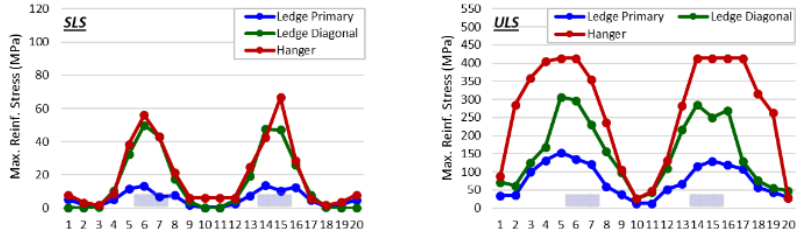
(b) H-I-C1: diagonal ledge reinf.
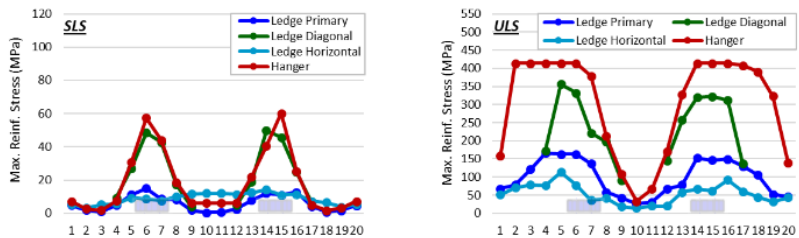
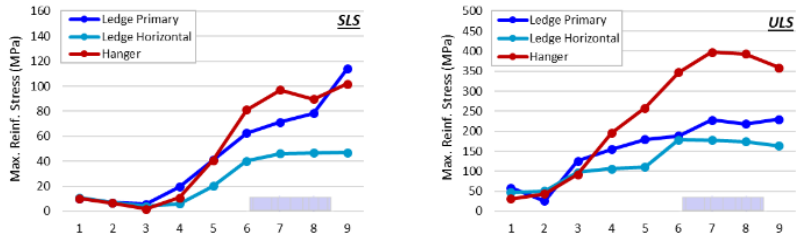*(c) H-I-C2: conc. ledge reinf. - combined*
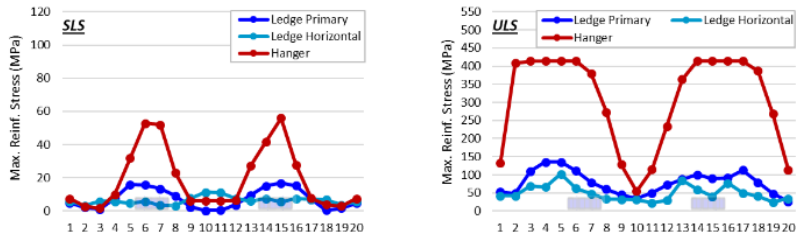
(d) H-I-C3: conc. ledge reinf. - horizontal
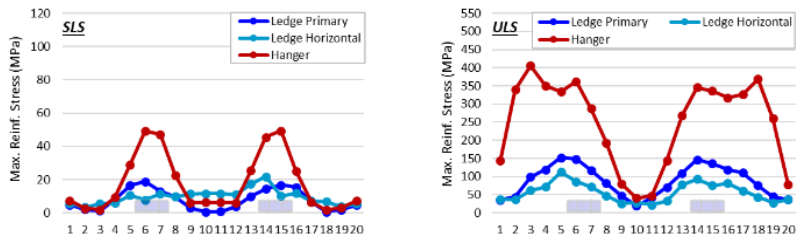
(e) H-I-C4: conc. hanger reinf.

Figure 4-27. Reinforcement Stress Distribution of Interior Hanger Model.

109
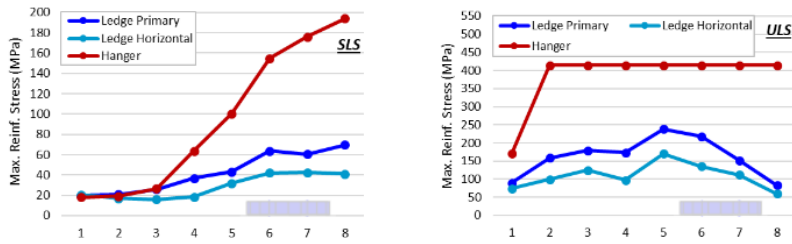
(a) H-E-Proto: prototype
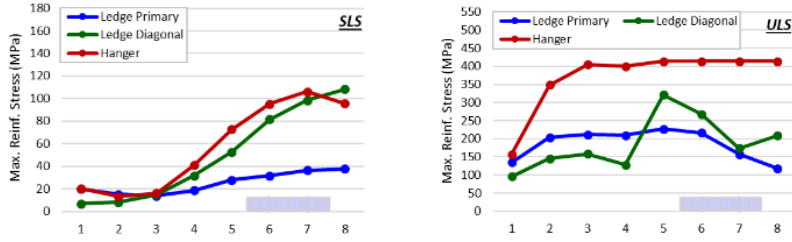
(b) H-E-C1: diagonal ledge reinf.
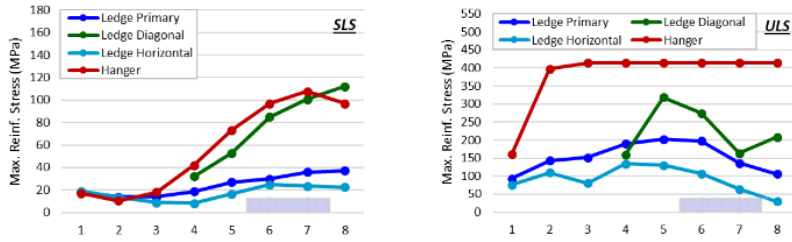
(c) H-E-C2: conc. ledge reinf. - combined
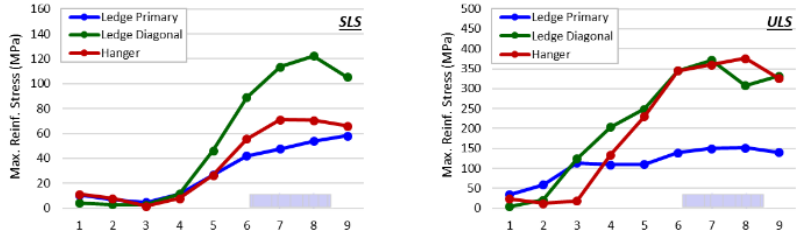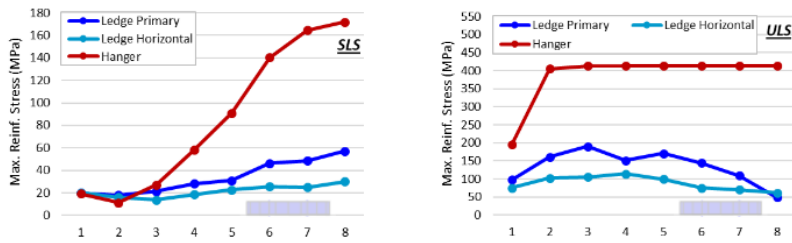

(d) H-E-C3: conc. ledge reinf. - horizontal
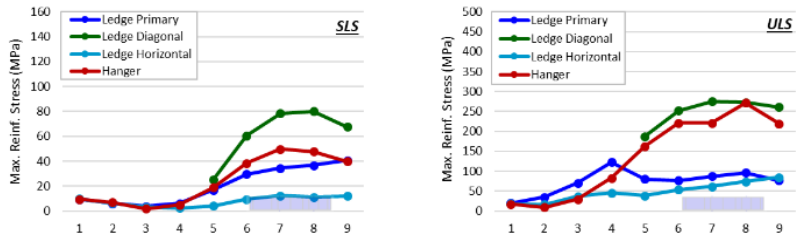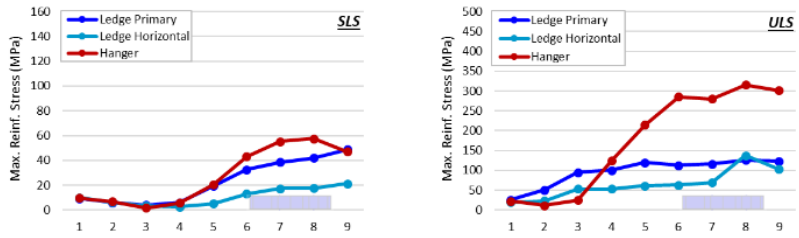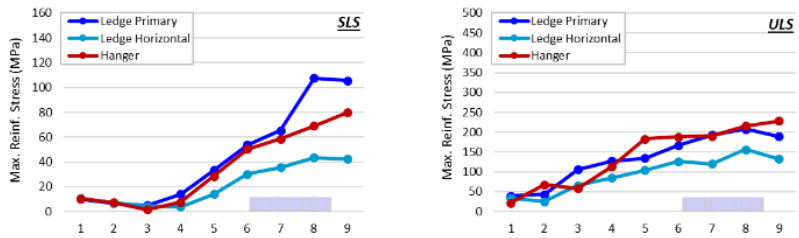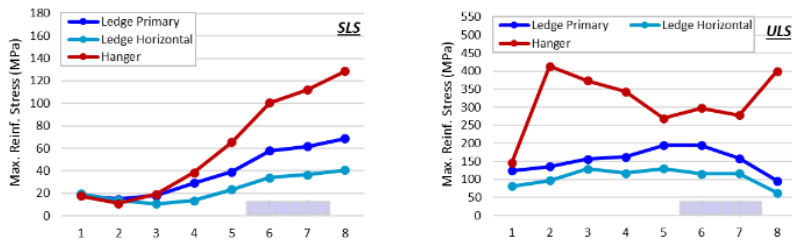

(e) H-E-C4: conc. hanger reinf.

**Figure 4-28. Reinforcement Stress Distribution of Exterior Hanger Model.**

110

4.5.3. **Punching Model**

Figure 4-29 plots the load-deflection response of the punching models with different reinforcement layouts. While the physical details are the same as the ledge deficient models, the loads were applied differently (see Figure 4-5(c)). The graphs for all the models demonstrated a similar behavior with the response of the models with reinforcement variations lifted to a different degree compared to the prototype. The cracking strength of the model increased by an average of 8% with the different reinforcement layouts. Regarding the ultimate strength, diagonal ledge bar (C1) improved the ultimate strength by 6%, concentrated ledge reinforcement with combined (C2) and horizontal bar only (C3) improved the strength about 10%, and concentrated hanger reinforcement (C4) improved the strength by 19%. For exterior load points, the percentage increase less than for the interior load points. The cracking strength of the exterior models with reinforcement variations improved about 3%, and the increase of the ultimate strength for C1, C2, C3 and C4 was 4%, 6%, 6%, and 13%, respectively. However, the increase of the ultimate strength by the various reinforcement layouts may not be meaning for a punching model. The punching failure as revealed from the test was a brittle failure. The failure was evident by the concrete cone formed under the bearing pad. The ultimate strength of the specimen reached shortly after the formation of the cone. The post stage after the formation of the concrete cone was the separation of the concrete chunk from the ledge holding by the reinforcements. The load resistance at this stage was mainly coming from the reinforcements restraining the separation of concrete. The hanger reinforcements with the length fully developed through the height of the web was the most effective

reinforcement contributing the load resistance after the formation of the concrete cone. Therefore, C4 with concentrated hanger reinforcement record a significant ultimate strength. But the ledge after the concrete cone formed subject to a larger deformation thereby may not be usable.

Figure 4-30 presents the interface strain. Figure 4-31 and Figure 4-32 presents the reinforcement stress of the interior and exterior punching models, respectively. Similar tendency was observed as the ledge and hanger models. The different reinforcement layouts effectively reduced the interface strain both at SLS and ULS. Use of diagonal ledge bar instead of horizontal bar (C1) reduced both the transverse and vertical strain. Concentrating ledge reinforcement with combined use of ledge bars (C2) and only with horizontal bar (C3) was pronounce in restrain the transverse strain. C2 with diagonal ledge bars contained was also effectively reduced the vertical strain whereas C3 only with horizontal ledge bars barely affected the vertical strain. Concentrated hanger reinforcement (C4) was only able to control the vertical strain. The exterior cases, again, showed a similar result but was less sensitive to the reinforcement variations compare to the interior.

Diagonal bars once provided to the ledge was also found to be actively engaged in the load resistance mechanisms of the model with punching weakness. Replacing the horizontal ledge bars with the diagonal bars (C1) reduced the stress on the primary ledge bars compared to the prototype. Concentrating ledge reinforcements relieved the overall stresses on the ledge bars hence benefited the performance of punching models. Combined use of the diagonal and horizontal ledge bars (C2) demonstrated a better performance over

the case only using the horizontal ledge bars (C3). Concentrating hanger reinforcement (C4) reduced the stress on the hanger bars but barely affect the stress on the ledge reinforcements. The stress on hanger reinforcements were significant at ULS, demonstrating the significant contribution of the hanger reinforcements at a higher load state.

In sum, the cracking and the ultimate strength of the punching model improved by the varying reinforcement layouts. The increase of the cracking strength was moderate. While the increase of the ultimate strength was notable, it was the reinforcements restraining the concrete separation after the formation of the concrete cone. Therefore, may not be beneficial to the punching performance of the bent cap. Use of diagonal ledge bars (C1) effectively reduced the interface strain. Concentrate ledge reinforcements with combined ledge bars (C2) was the most effective case in controlling the interface strain. C3 with concentrated ledge reinforcements only with horizontal bars was effective in controlling the transvers strain whereas barely affected the vertical strain. On the contrary, concentrating hanger reinforcement (C4) was only effective in controlling the vertical strain while has negligible effect in restraining the transverse strain.
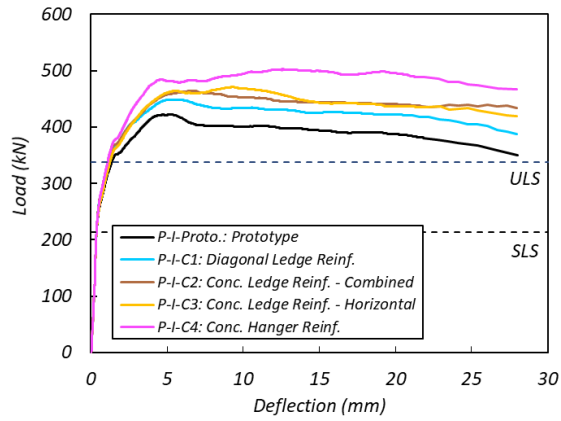
(a) Interior: load-deflection response
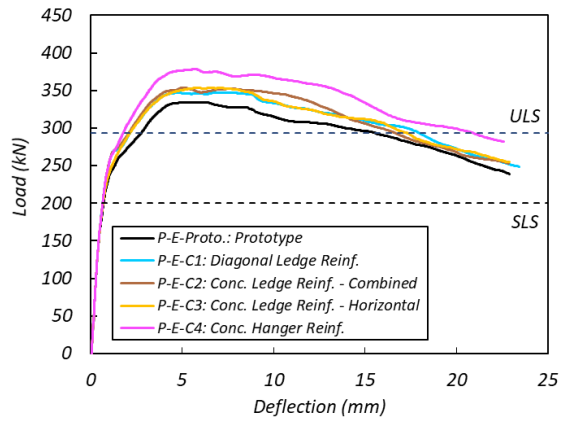
(b) Exterior: load-deflection response
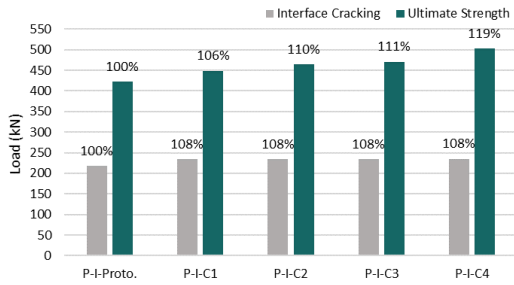
*(c) Interior: strength comparison*
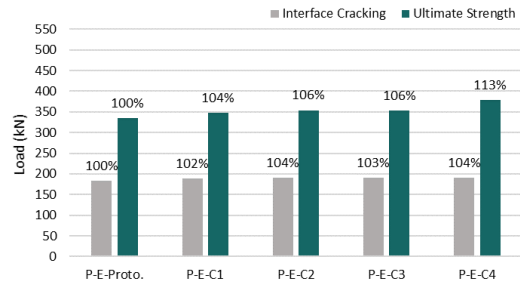
(d) Exterior: strength comparison

Figure 4-29. Load Response of Punching Model.
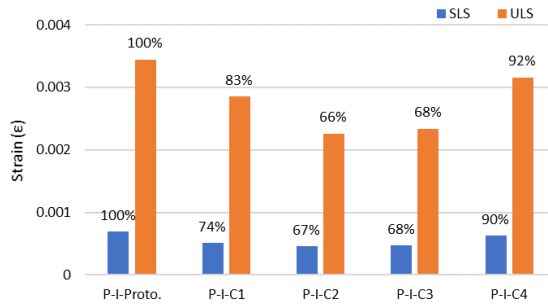
(a) Interior: transverse strain at interface
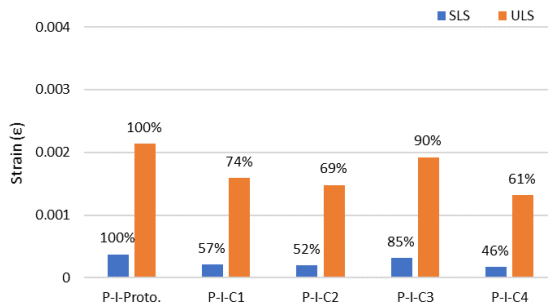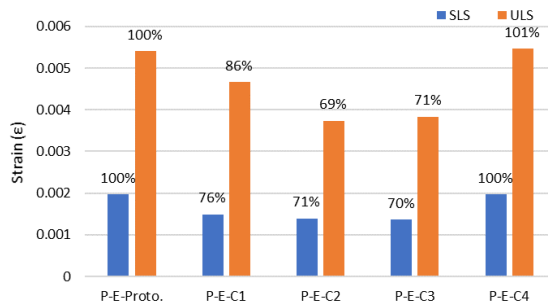
(b) Interior: vertical strain at interface

(c) Exterior: transverse strain at interface
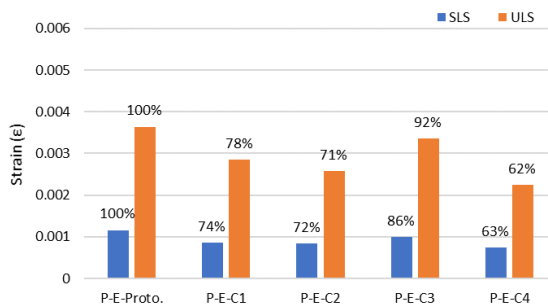
(d) Exterior: vertical strain at interface

Figure 4-30. Strain Data of Punching Model.

115
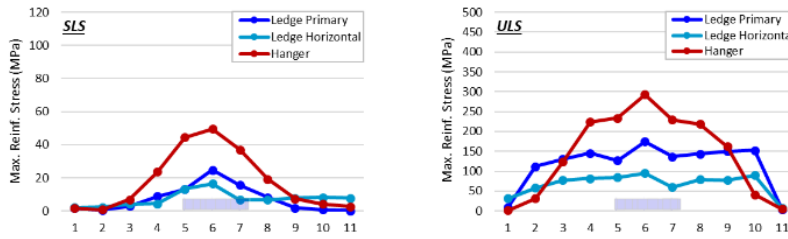
(a) P-I-Proto.: prototype
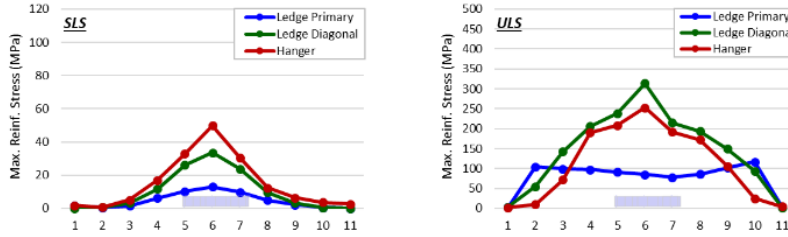
(b) P-I-C1: diagonal ledge reinf.
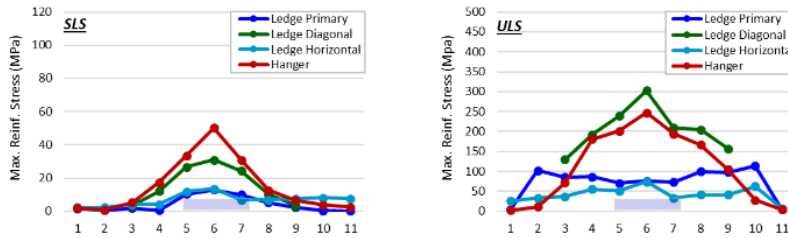
(c) P-I-C2: conc. ledge reinf. - combined
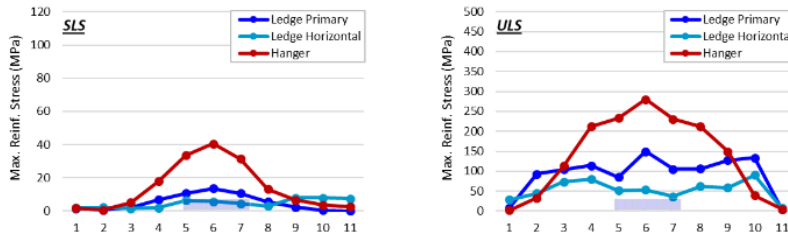
(d) P-I-C3: conc. ledge reinf. - horizontal
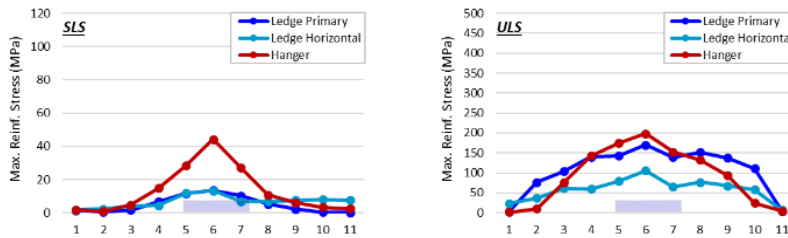
(e) P-I-C4: conc. hanger reinf.

Figure 4-31. Reinforcement Stress Distribution of Interior Punching Model.

116
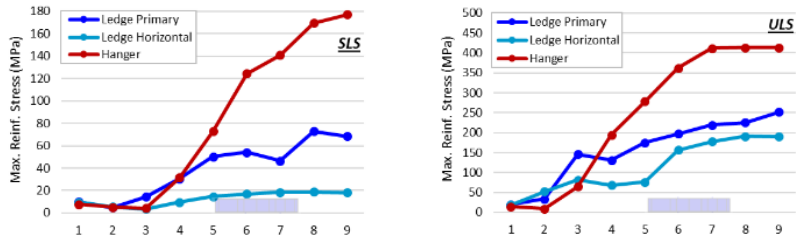
(a) P-E-Proto.: prototype
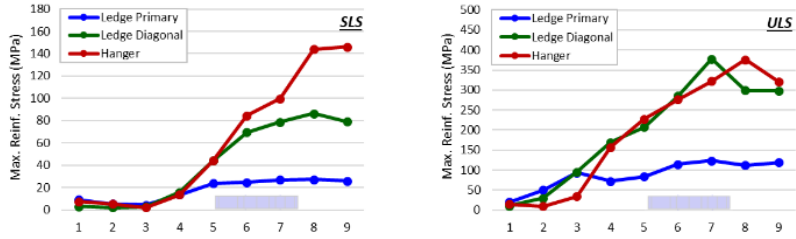
(b) P-E-C1: diagonal ledge reinf.
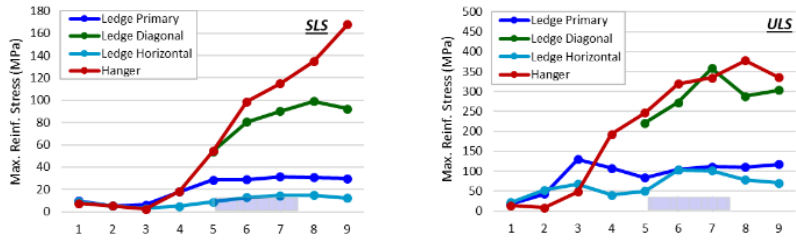
(c) P-E-C2: conc. ledge reinf. - combined
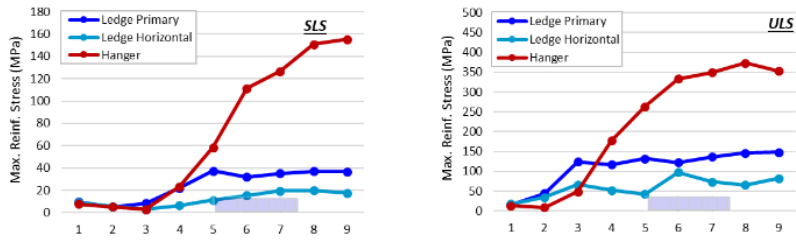
(d) P-E-C3: conc. ledge reinf. - horizontal
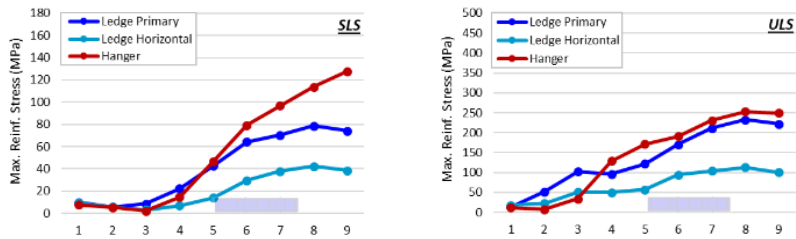
(e) P-E-C4: conc. hanger reinf.

Figure 4-32. Reinforcement Stress Distribution of Exterior Punching Model.

117

4.6. Conclusion

This study investigated the local failure mechanisms of inverted-T bent caps by using a non-linear finite element model. Various reinforcement layouts that affecting the local behaviors were also explored. Three types of FE models were developed to simulate the ledge, hanger, and punching failure of inverted-T bent caps. Each model has interior and exterior loading regions. The FE models were calibrated with the experimental observations. The models then were utilized to perform a parametric analysis. Four different reinforcement layouts – use of diagonal ledge bar instead of horizontal bar; concentrate ledge reinforcement around the loading with combined use of diagonal and horizontal ledge bar; concentrate ledge reinforcement around the loading region only with horizontal ledge bar; concentrate hanger reinforcement around the loading region – were investigate in their effectiveness on the local behavior of inverted-T bent caps. Total of 30 models including the prototypes were studied. Based on the analytical investigation, the following conclusions are drawn:

1. The FE models were able to capture the different local failure mechanisms of inverted-T bent caps. The predicted load-deflection response and the damage patterns were in good agreement with the experimental observation.

2. Use of diagonal ledge bars instead of horizontal ledge bars slightly improved the cracking strength of the models. The ultimate strength of the hanger and punching models were also improved slightly while the strength of the ledge model was barely affected. The overall behavior of the load-deflection response of the models were not changed by the diagonal ledge bars. The impact of the diagonal ledge

bars on controlling interface strain was pronounced. It effectively reduced the interface strain at both service and ultimate load state for all the models. The diagonal ledge bars once provided to the ledge was found to be actively engaging in the load resisting mechanism therefore is beneficial to the inverted-T section.

3. Concentrated ledge reinforcement around the loading region increased both cracking and ultimate strength of the ledge-deficient model and punching shear model. The hanger-deficient model was not affected by the increase of the ledge reinforcements. The strength increase due to the concentrated ledge reinforcement was not significant and was not proportional to the amount of increase in ledge reinforcement. The impact of the concentrated ledge reinforcement on the controlling the interface strain was significant. The strain at the interface was effectively reduced by the concentrated ledge reinforcement. The case with combined use of diagonal and horizontal bar showed an advantage over the case only using horizontal bars. The combined case was effective in reducing both transverse and vertical strain whereas the case with horizontal bars was not able to capture the vertical strains.

4. Concentrated hanger reinforcement around the loading region was the only case that improved the strength of the model with hanger weakness. On the other hand, the other models with ledge and punching weakness was barely affected by the concentrated hanger reinforcement. It was effectively restrained the vertical strain at interface for all the models but could not capture the transvers strain. The transverse strain was the primarily component for the ledge and punching models.

Therefore, concentrating hanger reinforcement was redundant for the ledge and punching models.

5. Use of diagonal ledge bar instead of horizontal ledge bar or combined use of two around the loading region was recommended to improve the serviceability of inverted-T bent caps.

5. PUNCHING SHEAR STRENGTH OF INVERTED-T BENT CAP LEDGES

5.1. Summary

The bottom flanges of inverted-T bent caps that seat girders are vulnerable to punching shear failures. This study experimentally investigated the punching shear mechanism of inverted-T bent cap ledges with bearing pad size as the primary variable. A nonlinear finite element model is also developed to elaborate on the experimental investigation. Based on experimental results and the FEM analysis, use of larger pads can improve the serviceability and the ultimate punching strength of the inverted-T ledges. The load eccentricity is found to be another parameter that affecting the ledge capacity. The code-based capacity estimation is evaluated against the measured strength and appeared to give conservative result. A practical modification is proposed to improve the accuracy of capacity estimation. Based on the analytical comparison, the proposed model improved the accuracy of the capacity estimation by 17%.

5.2. Introduction

Inverted-T bent caps are used to reduce the overall elevation of bridges and to while increasing the available clearance beneath the girders. In inverted-T bent caps, the girders are seated on flanges at the bottom of the cross-section. This effectively loads the cap along its bottom compression chord with the girder loads transferred to the upper tension chord via the stirrups which act as hangers, thereby creating a loading condition not encountered in a conventional bent cap where the girders are seated at the top of the cross-section. The design aspects unique to inverted-T caps, first outlined by Mirza and Furlong

(1983, 1985) include 1) design for this transfer of forces through the stirrups to the top tension chord, 2) design for transfer of the loads from the ledges to the stem, and 3) design of ledges for the loads from individual girders. Design of the ledges at the girders considers bearing and punching shear, with punching shear governing. In a punching failure, a truncated pyramid of concrete beneath a concentrated load is punched from the surrounding concrete. The punching failure is most evident from the appearance of diagonal cracks developed from the edges of the bearing pad.

Punching failure is a shear and diagonal tension separation of the concrete members under a concentrated load. In bridge structures, it is common that maximum loads are applied on the single side of the bent cap instead of both sides as traffic passes across the girder to the other side. The shallow ledges of inverted-T bent caps seating the girder are therefore resisting significant amount of concentrated loads from the bridge girders. Punching failure can take place if the girder load is large enough to punch out the ledge beneath the bearing pad.

The punching failure on ledge beams is also reported in the research on L-shaped beams. The L-shaped beams, with a ledge support thin-stemmed precast concrete members, are widely used in parking garage buildings. Similar to the inverted-T bents, the bottom ledge of the L-shaped beams serves to support the deck members. Klein (1986) reported two unfavorable punching failures observed on the ledges of L-shaped beams. Lucier et al. (2011) documented several unexpected punching failures on the ledges in their study investigating design methodologies for L-shaped beams. Nafadi et al. (2018) experimentally investigated the punching behavior of the L-shaped beam ledges aimed to

develop a design guideline to predict the nominal capacity. Several parameters were investigated that were believed to potentially affect the punching shear capacities of the L-shaped beam ledges. Through the observation, they noted that the concrete strength, load eccentricity, ledge height, and the bearing width are the factors possibly affecting the ledge punching capacities. However, it should be noted that these findings are based on the L-shaped beams which are typically have a smaller dimension than the inverted-T bents. The effectiveness of these research findings on the inverted-T bent cap ledges, which have a much larger dimension, requires verification.

While a few studies have focused on the serviceability and design of inverted-T bent caps, no prior research is available related to the local failure, especially the punching failure mechanisms of the inverted-T ledges. Zhu et al. (2003) investigated the serviceability of inverted T bent caps on a 2-D sliced specimen that represents an interior portion of the inverted T bent caps with a focus on the crack control provision. Based on the experimental results, a compatibility strut-and-tie model was proposed to predict the crack widths. Larson et al. (2013) experimentally investigated the design method for deep inverted-T bent caps. The caps were straddle caps, with ledges for girders running only a portion of the length, with the remaining length having a rectangular cross-section. While the testing of the inverted-T specimens designed to emphasize web-shear failure, the authors observed five localized failures on the ledge including three punching shear failures. Detailed explanation of the punching shear failures, provided by Garber et al. (2017), indicates diagonal cracks were first observed at loads slightly higher than service loads, with progression of the cracking continuing as loads increased. At unidentified

123

loads, the punching shear mechanism became dominate as damage from other mechanisms such as shear stopped progression while the punching cone cracks and associated deformation increased greatly until failure. The punching shear capacities in the tests were found to be on the order of two times the design strength. For the design of new structures, this overstrength is of concern only in the sense that it can lead to overly conservative designs. However, if punching shear capacity is calculated as part of an evaluation of an existing structure, the structure may be deemed deficient and require retrofit when it may not be necessary. Zhou et al. (2020) performed an analytical study to investigate the structural behavior of skewed inverted-T bent caps. A finite element model, verified by an inverted-T bent cap specimen that was designed to emphasize a web-shear failure, was used to conduct a parametric study. The analysis results revealed that the spacing of the shear reinforcement has moderate effect on the ultimate capacity. While the extension length defined as the distance from the center of the bearing pad to the free end of the bent cap at exterior region was found to be a critical parameter that affecting the structural behavior of skewed inverted-T bent caps. A modified requirement to the extension length was proposed to take into account the skew angle of the bent cap.

Hurlebaus et al. (2018a,b) performed experimental research on the local failure mechanisms of inverted-T bent caps. The authors analyzed a prototype bridge, an in-service inverted T bent cap, against current specification and found that the inverted-T bent caps constructed in older days may be vulnerable to the ledge local failures. These local failures – hanger, ledge, and punching – were investigated by the authors on the half-scaled test specimens that were designed to isolate each of the failure modes. As part of

the research, this paper investigating the punching shear mechanisms of the inverted-T bent cap ledges as well as the potential factors that may affect the punching shear capacity. A nonlinear finite element model is also developed in this study to elaborating experimental findings and to provide a closer insight to the punching shear behavior of the inverted-T bent cap ledges.

5.3. Punching Shear Capacity of Inverted-T Bent Caps

The design procedure for the ledge punching of inverted-T bent caps included in AASHTO LRFD Bridge Design Specification (2020) estimates the punching shear strength by the failure plane developing surround the bearing pad. The failure plane, as shown in Figure 5-1, is approximated as the average of the perimeter of the bearing pad and the perimeter at depth, df, assuming 45-degree slopes. If the adjacent failure planes overlap, an investigation of the combined surface areas is necessary. As specified in AASHTO LRFD 5.8.4.3.4, the nominal punching shear resistance of ledge is

$$V_n = 0.125\lambda \sqrt{f_c'} b_o d_f$$

(5-1)

where λ = concrete density modification factor; f_c' = specified concrete strength; b_o = perimeter of critical section for shear enclosing bearing pad; and d_f = effective depth of ledge.

For interior rectangular pads, the perimeter of critical section is,

$$b_o = W + 2L + 2d_f \qquad (5\text{-}2)$$

For exterior rectangular pads, it is

$$b_o = 0.5W + L + d_f + c \leq W + 2L + 2d_f \qquad (5\text{-}3)$$

It can be seen from Equations (5-1)-(5-3) that the nominal punching shear capacity of the ledge is determined based on the perimeter of the assumed failure plane which is a function of ledge depth, end distance, and size of bearing pad. The nature of these parameters enlightened a possible means to enhance the punching shear capacities of inverted-T bent cap ledges. The depth of ledge and end distance is the fixed geometry of the bent cap, whereas the pad size under the bridge girder can be more easily varied. The size effect of the bearing pad on the punching capacity of the ledges has also been shown by Nafadi et al, (2018).

(a) Cross-section   *(b) Elevation*
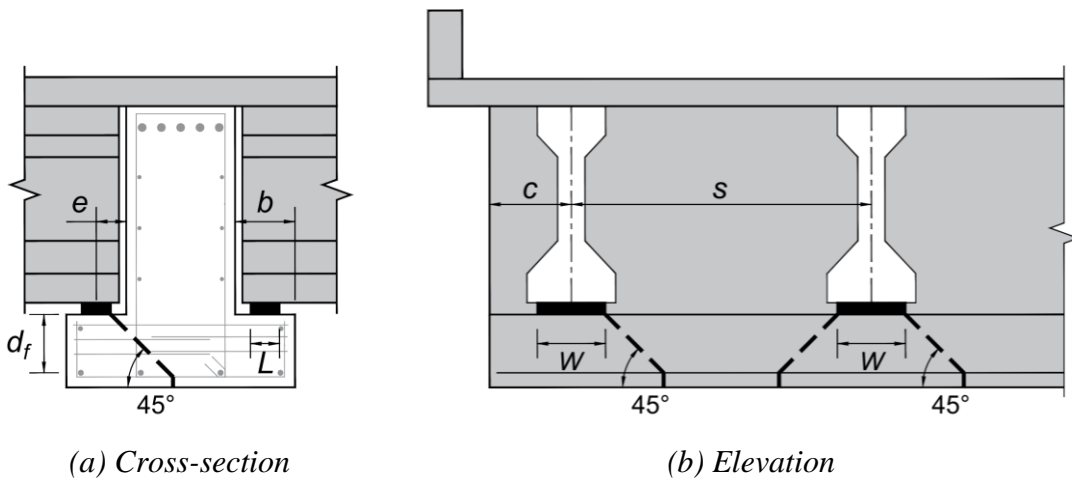
Figure 5-1. Punching Shear Failure Plane Assume by AASHTO LRFD 2020.

5.4. Experimental Investigation

In this paper, results for punching shear tests on one-half scale inverted-T specimens are presented. The punching shear tests were part of a larger test program (Hurlebaus et al., 2018b) to investigate the performance of in-service bent caps and to provide recommendations for retrofits to improve the strength. One method considered for improving the strength is the use of larger bearing pads where punching shear capacity is found to be insufficient. Thus, the primary variable investigated in the presented tests is the size of the bearing pad.

5.4.1. Specimen Description

Figure 5-2 shows the geometry of the test specimens. The bent cap has length of 264 in. (6706 mm), height of 40 in. (1016 mm), and 10 in. (254 mm) deep ledges extending 8.25 in. (210 mm) from the either side of the stem. The width of the web is 15 in. (381 mm). The specimen was supported by two 24 in. (610 mm) square high-strength reinforced columns that are spaced at 144 in. (3657 mm) on center. The two specimens were cast on different date. Ready-mix concrete with design compressive strength of 3.6 ksi (25 MPa) was used for both specimens. The concrete properties of the specimens are listed in Table 5-1. Standard test cylinders, 4 in. x 8 in. (100 mm x 200 mm), were cast, cured, and tested at 28-days and on the day of testing (ASTM C39/C39M test [ASTM 2015]).

The specimen was designed with sufficient hanger capacity to ensure that failure occurred in the ledge. The reinforcement details are provided in Figure 5-2(b). Hanger reinforcement is D13 (#4) and ledge reinforcement is D10 (#3). The hanger and ledge

127

reinforcement were placed with an average spacing of 5.5 in. (140 mm). Grade 60 reinforcement was used. The measured properties of the reinforcing steel are presented in Table 5-2.
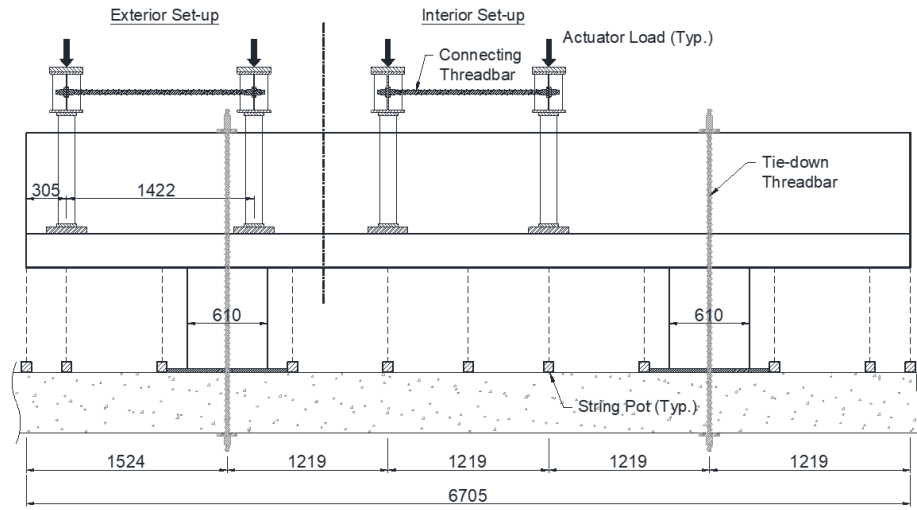
(a) Elevation
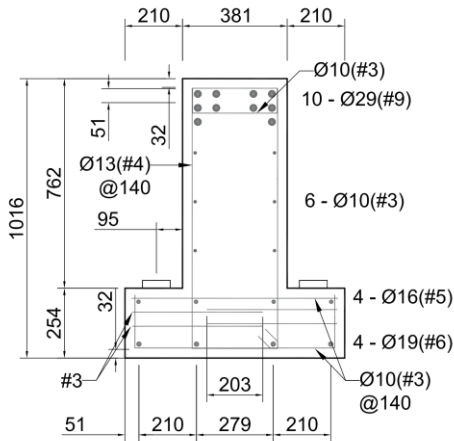
(a) Specimen cross-section

Figure 5-2. Geometry and Reinforcement Details of Test Specimen (mm).

Table 5-1. Compressive Strength of Concrete.

Specimen No.	28-day Strength (Mpa)	Age at Test Day	Test Day Strength (Mpa)
3	25.4	83	26.5
7	24.8	229	35.9

* Three cylinders were tested per each time to get an average

Table 5-2. Reinforcing Rebar Tensile Strength.

Bar No.	Yield Strength (Mpa)	Ultimate Strength (Mpa)
#3 (D10)	441	688
#4 (D13)	467	662
#5 (D16)	441	722
#6 (D19)	425	717
#9 (D29)	479	779

5.4.2. **Test Set-Up**

Figure 5-3 shows the test set-up details. The two-column configuration of the test set-up provided two exterior loading regions representing the overhangs in multi-column and single column bents, and an interior region representing the loading between columns in multi-column bents. Interior tests simulated two girder lines spaced at 48 in. (1219 mm), centered on the specimen. Exterior tests simulated one girder line centered at 12 in. (305 mm) from the edge and an additional girder line was provided over the adjacent column to provide stability to the loading table.

The detail of the loading frame is provided in Figure 5-3(c). At each simulated girder line, a 600 kips (2670 kN) hydraulic jack applied loads to a loading frame consisting of an I beam and hollow structural sections (HSS) that transferred the loads to the ledges

129

on each side. Loading frames were connected by 1 in. (25 mm) diameter threadbars to provide stability during testing. The actuator was placed 5-5/8 in. (143 mm) off center to allow for larger loading on the front side flange (near side). The off-center position was determined as that to provide dead load on the back side flange when the front side load was at Strength-I limit state based on AASHTO LRFD (2020).

Figure 5-3(d) shows the details of the bearing pads. The bearing pads were centered 95 mm from the face of the web. Two different sizes of rubber pads were used to assess the size impact of bearing pad on the ledge punching shear performance. The "regular" pad, 5 in. x 12 in. x 2 in. (127 mm x 305 mm x 50 mm), was adapted from the actual bearing pad size of the in-service prototype bent cap. Use of a larger sized pad is limited due to the space on the ledge. Therefore, a "small" pad, 4 in. x 4 in. x 2 in. (102 mm x 102 mm x 50 mm), was used to investigate the impact of pad size. A commercial grade 50A neoprene rubber was adopted to allow a uniform distribution of the load by self-balancing the contacting surface between the loading plates and the specimen ledge.

String potentiometers (string pots) were placed at 11 longitudinal positions to measure the vertical deflections. At each station, up to three string pots were placed in the transverse direction under the specimen to measure the relative deformation of the ledge.

(a) Exterior test set-up

(b) Interior test set-up
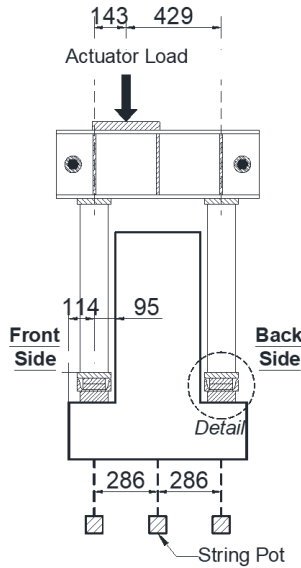
(c) Actuator location
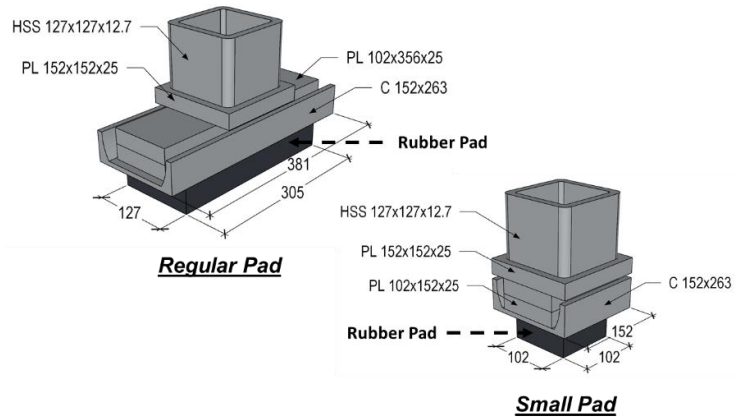
(d) Bearing pad details

Figure 5-3. Overview of Experimental Test Set-up (mm).

5.4.3. **Loading Protocol**

Application of the loads was force-controlled. At key points, the loading was paused to document the condition of the specimen. The key loads, summarized in Table 5-3, are the nominal dead load, the service limit state (SLS), and ultimate limit states (ULS) of the prototype bridge.

131

Each punching test has four loading points: main-front, main-back, sub-front and sub-back as shown in Figure 5-4(a). The main-front loading region is the primary loading region which was loaded to a failure at final state. Consistent bearing pad size was used for the same girder line to minimize the rotation of the frame due to the off centered actuator. A plan view of the loading points is shown in Figure 5-4(b).

The test regions were loaded in two manners. For Case A, an initial load equivalent to the dead load was applied at each girder line. After reaching dead load, the subsidiary jack held constant while the main jack increased. For Case B, both actuators were loaded equally to the ultimate load state. Once the ultimate load was reached, the subsidiary jack was retracted to hold the dead load and the main jack was increased. Both cases were applied to the interior region. Exterior region tests utilized Case A only as the subsidiary jack was located direction over the column. The tests were terminated when the specimen strength dropped about to 80-85% of the measured ultimate load.

Nine punching shear tests, including two exterior and seven interior tests, were conducted on the two test specimens. Table 5-4 summarizes the details of each test. Two of the interior tests (T7I3 and T7I4) were conducted after the other interior punching tests (T7I1 and T7I2) conducted on the opposite side of the specimen. Punching shear tests were not conducted every region on both specimen as some regions were used to investigate other retrofit methods in a larger test program (Hurlebaus et al., 2018b).

Table 5-3. Estimated Limit State Loads.

Limit State	Exterior	Interior
Equivalent dead load	100 kN	120 kN
Service limit state (SLS)	200 kN	220 kN
Ultimate limit state (ULS)	300 kN	340 kN

(a) Overview   *(b) Plan view*
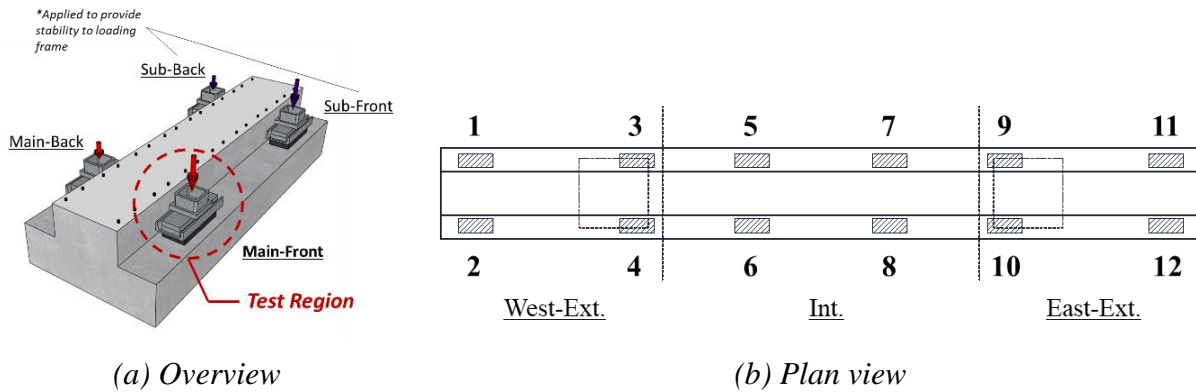
Figure 5-4. Loading Points for Punching Test.

Table 5-4. Test Matrix.

Specimen	Test Region	Test ID	Loading Scheme	Bearing Pad Location / Size			
				Main-Front	Main-Back	Sub-Front	Sub-Back
T3	T3W1	West-Ext.	Case A[1]	1 – S[3]	2 – S	3 – B[4]	4 – B
	T3E1	East-Ext.	Case A	12 – B	11 – B	10 – B	9 – B
	T3I1	Int.	Case A	6 – S	5 – S	8 – B	7 – B
	T3I2	Int.	Case A	7 – B	8 – B	5 – B	6 – B
	T3I3	Int.	Case A	5 – B	6 – B	7 – B	8 – B
T7	T7I1	Int.	Case B[2]	7 – S	8 – S	5 – B	6 – B
	T7I2	Int.	Case A	5 – B	6 – B	7 – S	8 – S
	T7I3	Int.	Case A	8 – S	7 – S	6 – B	5 – B
	T7I4	Int.	Case A	6 – B	5 – B	8 – S	7 – S

Notes: 1 - Sub girder line hold at dead load; 2 - Sub girder line increased simultaneously to ULS than retracted to dead load; 3 - Small sized bearing pad (102 mm x 102 mm); 4 - Big sized bearing pad (127 mm x 305 mm)

5.5. Test Results

All tested locations failed by punching shear at the main-front loading region, evidenced by a truncated pyramid (concrete cone crack) formed under the bearing pad. The test results are summarized in Table 5-5. Crack Initiation load is the load at which the first crack of any type was observed; typically, this was flexure cracks in the ledge or cracks at the web-ledge interface. The Cone Crack Initiation Load is the load at which the diagonal cracks associated with the punching failure mechanism first occurred. Figure 5-5 and Figure 5-6 show the photos of the exterior and interior test regions at final state (post-peak), respectively. The cracks observed before or at SLS are marked in purple, observed between SLS and ULS are marked in blue, observed between ULS and measured ultimate load are marked in red and the cracks observed after measured ultimate load are marked in orange. A black dashed line is used to highlight the main concrete cone crack and the average angel of the cone crack is specified.

Table 5-5. Test Result Summary.

Specimen	Test No.	Test Region	Pad Size	Crack Initiation Load(kN)	Cone Crack Formation Load (kN)	Measured Ultimate Load (kN)	Cone Crack Angle (degree)	Crack Width at Peak (mm)
	T3W1	West-Ext.	Small	178	300	311	32.5	2
	T3E1	East-Ext.	Regular	200	347	356	32.5	2
T3	T3I1	Int.	Small	220	425	463	32.5	1.5
	T3I2	Int.	Regular	231	391	418	35	1.5
	T3I3	Int.	Regular	240	378	418	42	1.5
	T7I1	Int.	Small	220	467	498	32.5	1.5
T7	T7I2	Int.	Regular	236	467	529	34	2
	T7I3	Int.	Small	220	467	498	35	1.5
	T7I4	Int.	Regular	220	445	503	32.5	1.5

5.5.1. Exterior Test with Small Pad

T3W1 was a "small" pad test conducted on exterior region of Specimen T3 at Load Point 1. Figure 5-5(a) shows the observed cracks of T3W1 at the final state. The initiation of the crack was observed at 40 kips (178 kN) before the load reached the SLS (45 kips [200 kN]). It was a diagonal crack formed at the re-entrant corner of the end face. A new crack formed at the web-ledge interface behind the bearing pad at SLS. The cracks grew as the load increased. At ULS (68 kips [300 kN]), the interface crack behind the bearing pad was extended diagonally to the top face of the ledge. The formation of the cone cracks, which is a sign of punch failure, was observed under the bearing pad both on the side of the ledge and the end face at ULS. The specimen reached its measured ultimate load of 70 kips (311 kN) shortly after the formation of the cone cracks. The maximum width of the cone crack was 2 mm at the measured ultimate load and the average angle of the cone cracks was 32.5°.

5.5.2. Exterior Test with Regular Pad

T3E1 was a "regular" pad exterior test conducted on Specimen T3 at Load Point 12. The observed damage at the final state is shown in Figure 5-5(b). The specimen showed no damage before SLS (45 kips [200 kN]). At SLS, a diagonal crack found at the re-entrant corner of the end face. The crack extended toward the web-ledge interface either on the end face and on the ledge behind the bearing pad as the load increased to ULS (68 kips [300 kN]). A new diagonal crack formed on the end face under the bearing pad at ULS. More cracks formed on the top and side of the ledge around the bearing as the load went

beyond ULS. The formation of the main concrete cone on side face of the ledge was observed at the load of 78 kips (347 kN). The measured ultimate load of 80 kips (356 kN) was observed shortly after the main cone crack formed. The maximum width of the cone crack was 2 mm at the measured ultimate load and the average angle of the cone cracks was 32.5°.

(a) T3W1 – Ext. "small"

(b) T3E1 – Ext. "regular"

━━ SLS ━━ ULS ━━ Measured Ultimate ━━ Post-Peak
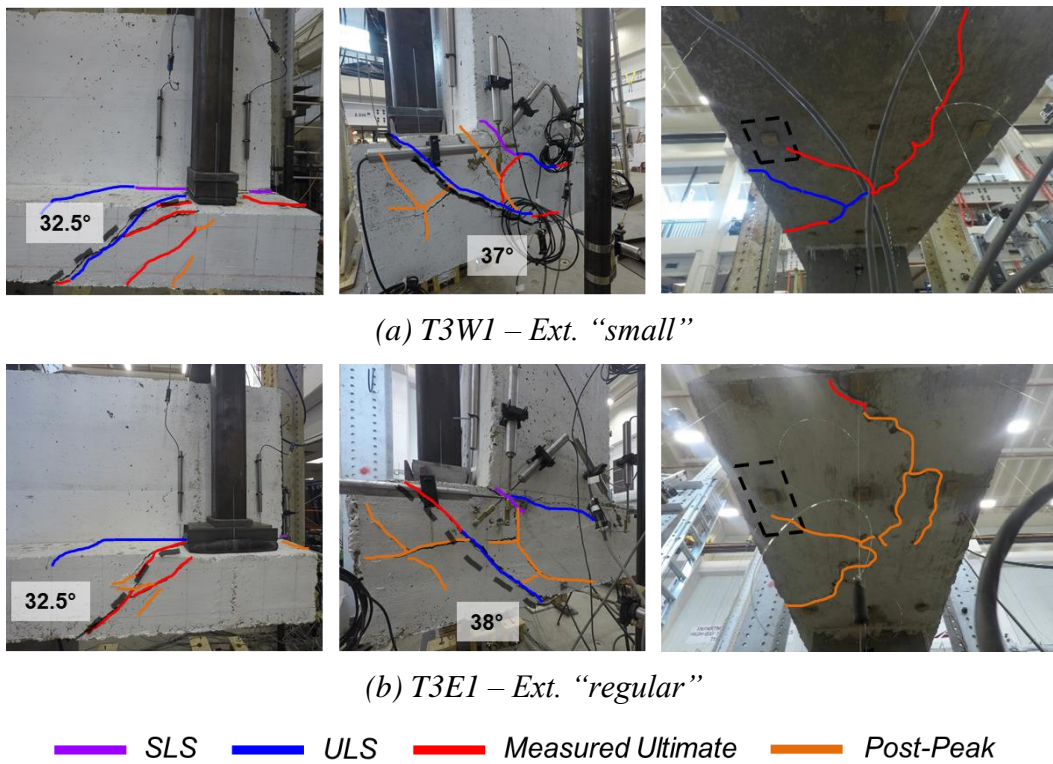
Figure 5-5. Exterior Test Regions at Post-Failure.

5.5.3. **Interior Test with Small Pad**

Three interior punching tests with "small" pad were conducted on two different specimens. Figure 5-6(a) through Figure 5-6(c) shows the observed damages of the interior small pad tests at the final state.

T3I1 was conducted at Load Point 7 on Specimen T3. The first crack was observed at SLS (48 kips [220 kN]). The crack formed along the web-ledge interface behind the bearing pad. It was extended as the load increased to ULS (76 kips [340 kN]) and propagated diagonally to the top face of the ledge. Some flexure cracks found on the side face of the ledge right under bearing pad at ULS. The formation of the main cone crack was observed at 95 kips (425 kN). The specimen then reached its peak strength of 104 kips (463 kN) with a clear cone crack formed under the bearing pad. The maximum width of the cone crack was 1.5 mm at the measured ultimate load and the average angle of the cone cracks was 32.5°.

T7I1 was conducted on Specimen T7 at Load Point 6. The test region was loaded together with "regular" pads at Load Point 8 up to ULS (76 kips [340 kN]). The two regions, on the same side of the bent cap, were loaded simultaneously to allow a comparison between the "small" and "regular" pad until ULS. The first crack was formed at the web ledge interface behind the bearing pad at SLS (48 kips [220 kN]). The interface crack further extended and propagated to the top face of the ledge at ULS (76 kips [340 kN]). Flexure cracks formed under bearing pad about at 85 kips (378 kN). The main cone crack start took place under the bearing pad at 105 kips (467 kN) and the specimen reached its peak strength at 112 kips (498 kN). The maximum width of the cone crack was 1.5 mm at the measured ultimate load and the average angle of the cone cracks was 32.5°.

T7I3 was conducted at Load Point 5. A few flexure and web shear cracks were present in the loading region before the test. The first crack of T7I3 was observed at SLS (48 kips [220 kN]) at the web-ledge interface behind the bearing pad. The crack extended

137

and propagated to the top of ledge at ULS (76 kips [340 kN]). The existing flexure cracks under bearing pad extended at ULS. The main cone start formed at 105 kips (467 kN) and the loading region reached its measured ultimate at 112 kips (498 kN). The maximum width of the cone crack was 1.5 mm at the measured ultimate load and the average angle of the cone cracks was 35°.

5.5.4. Interior Test with Regular Pad

Four interior "regular" pad tests were conducted. T3I2 and T3I3 were conducted on Specimen 3 at Load Points 6 and 8, respectively. The other two, T7I2 and T7I4, was conducted on Specimen 7 at Load Point 8 and 5, respectively. Figure 5-6(d) through Figure 5-6(g) show the observed damages of the interior "regular" pad tests at the final state.

T3I2 had no damage at SLS (48 kips [220 kN]). The first crack was found at 52 kips (231 kN) at the web-ledge interface behind the bearing pad. The interface crack propagated through the top and side face of the ledge at ULS (76 kips [340 kN]). The formation of the cone crack was found at 88 kips (391 kN) under the bearing pad. A diagonal shear crack was also found on the web at this stage. The specimen reached the measured ultimate load of 94 kips (418 kN) after the cone crack formed. The maximum width of the cone crack was 1.5 mm at the measured ultimate load and the average angle of the cone cracks was 35°.

T3I3 was conducted after the completion of T3I2. A similar crack pattern was observed. The test region showed no damage at SLS (48 kips [220 kN]). The first crack

138

formed at the web-ledge interface behind the bearing at 54 kips (240 kN). The crack extended along the interface as the load increased to ULS (76 kips [340 kN]). The main cone crack start formed at 85 kips (378 kN) under the bearing pad. The specimen then reached the peak strength of 94 kips (418 kN) with a clear cone crack. The maximum width of the cone crack was 1.5 mm at the measured ultimate load and the average angle of the cone cracks was 42°.

T7I2 was conducted on Specimen T7 at Load Point 8 and was loaded simultaneously with the adjacent loading area (T7I1 - interior "'small" pad test) up to ULS (76 kips [340 kN]) then retracted to the dead load state while the T7I1 loaded to failure. T7I2 was loaded to failure after the completion of T7I1. No damage was observed until SLS (48 kips [220 kN]). The first crack was observed at 53 kips (236 kN) behind the bearing pad at the web-ledge interface. The cracks extended and propagated to the top of ledge as the load increased to ULS (76 kips [340 kN]). Flexure cracks under the bearing pad and shear crack on the web also observed at ULS. More cracks formed on the top and side of ledge as the load went beyond ULS. The main cone crack start formed at 105 kips (467 kN) and the specimen showed a measured ultimate load of 119 kips (529 kN). The maximum width of the cone crack was 2 mm at the measured ultimate load and the average angle of the cone cracks was 34°.

T7I4 was conducted at Load Point 7 after the completion of T7I2. A few flexure and web shear cracks were present around the loading region from the previous test. The first crack was found at SLS (48 kips [220 kN]) at the web ledge interface behind the bearing pad. At ULS (76 kips [340 kN]), the interface crack extended and propagated to

the top of ledge. A shear crack on the web was also observed. The main cone crack start formed under the bearing pad at 100 kips (445 kN). The test region then reached the measured ultimate load of 113 kips (503 kN). The maximum width of the cone crack was 1.5 mm at the measured ultimate load and the average angle of the cone cracks was 32.5°.

(a) T3I1 – Int. "small" *(b) T3I1 – Int. "small"* *(c) T3I1 – Int. "small"*

(d) T3I2 – Int. "regular" *(e) T3I3 – Int. "regular"*

(f) T7I2 – Int. "regular" *(g) T7I4 – Int. "regular"*

━━━ SLS ━━━ ULS ━━━ Measured Ultimate ━━━ Post-Peak
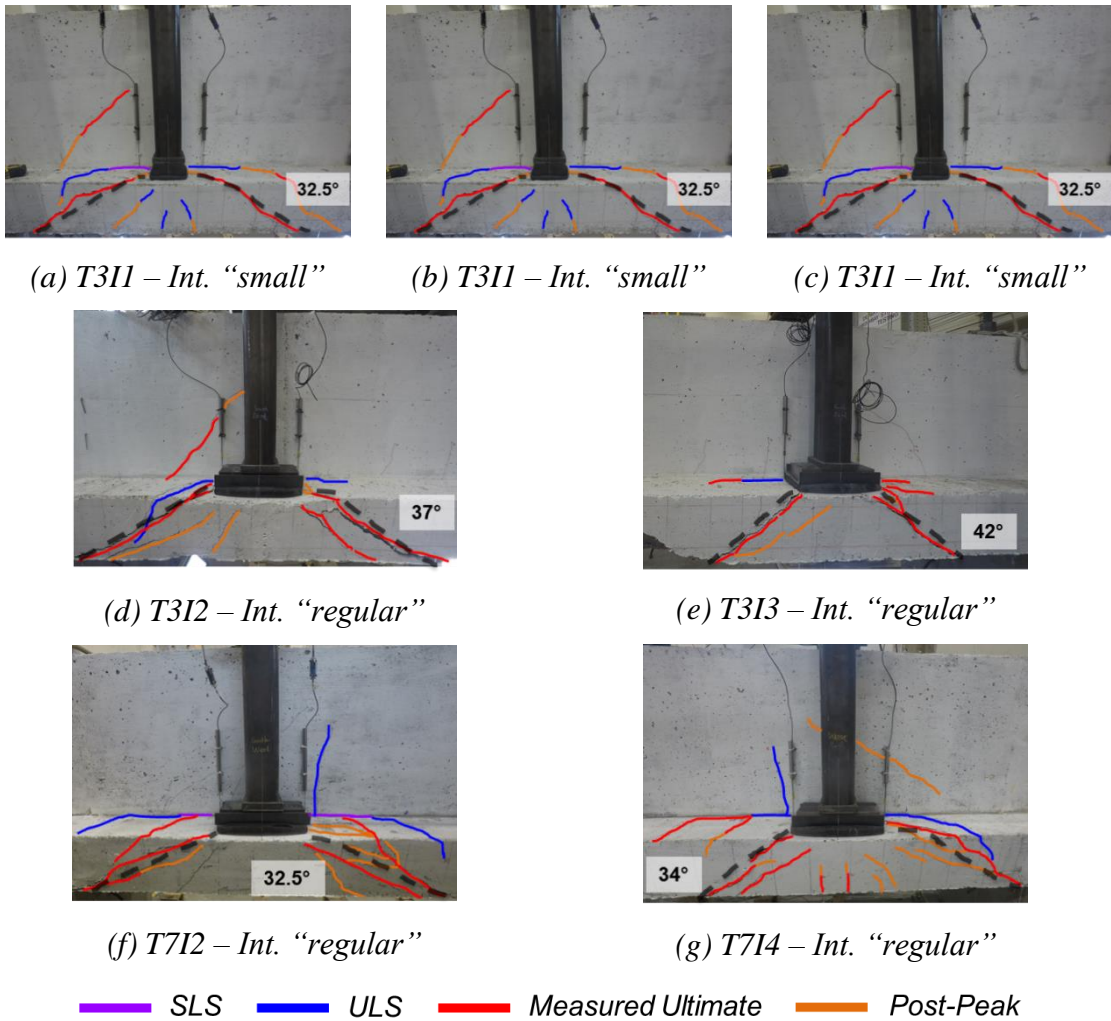
Figure 5-6. Interior Test Regions at Post-Failure.

5.6. Comparative Analysis

The observed performance of the "small" and "regular" pad tests is compared in terms of failure configuration, damage level and nominal capacity. Figure 5-7 shows the measured load deflection response of the punching tests. The deflection was measured at the bottom of the ledge under the center of the bearing pad. The tests conducted on Specimen T3 and Specimen T7 are presented separately since the two have different concrete strengths. Markers indicate initiation of the main cone crack and the measured ultimate loads.

5.6.1. **Failure Configuration**

Overall, a similar damage pattern, as shown in Figure 5-5 and Figure 5-6, was observed for all the tests regardless of the bearing pad size. The typical failure plane was formed initially by cracks developing at the web-ledge interface behind the bearing pad. For the exterior tests, a diagonal crack was also formed at the re-entrant corner on the end face. The interface cracks were diagonally extended on the top face of the ledge as the load increased. However, these cracks are likely ledge shear and flexure cracks, not a part of the punching shear cracks that caused the ledge failure. The main cone cracks which are evidence of punching failure were not visible at early loading stage. The cone cracks were formed shortly before the ultimate strength (triangle mark on Figure 5-7). For the exterior and interior tests, the cone cracks took place when the load increased to 97% and 91% of the measured ultimate load, respectively. The damage on the ledge increased significantly after the measured ultimate load. The cone cracks widened extensively and more cracks formed around the cone cracks.
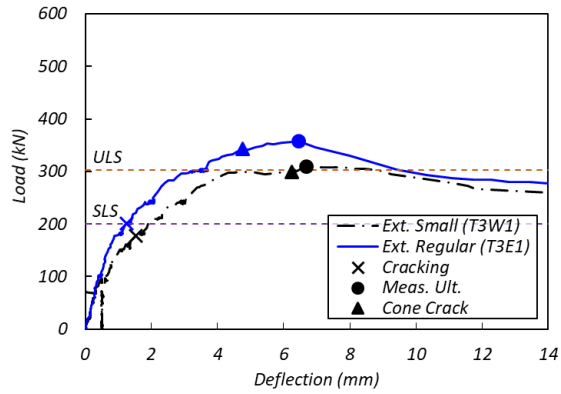
(a) Exterior tests on Specimen T3
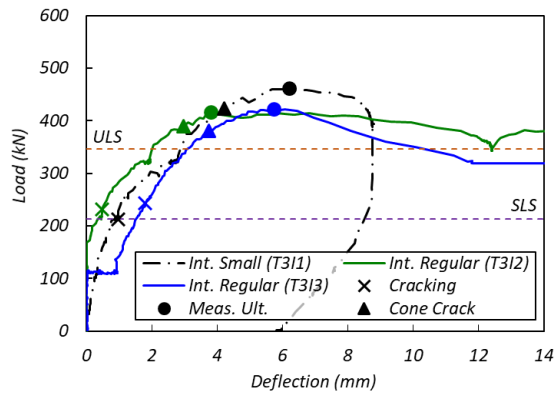
(b) Interior tests on Specimen T3
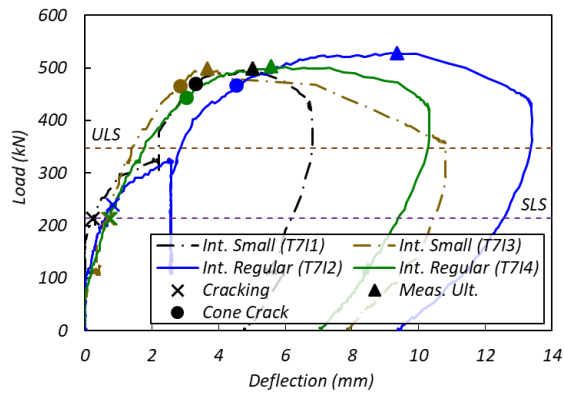
(c) Interior tests on Specimen T7

Figure 5-7. Load-Deflection Curves.

142

It can be seen from the observation that punching shear failure is a brittle and localized failure. The signs of punching failure occur laterally when the ledge capacity reaches its limit and the ledge does not possess much reserve strength once the punching failure initiated. The exterior region (cut-off ledge) showed a more brittle response than the interior region since the end region has limited space to develop a full failure plane to resist applied loading. Also, it should be noted that the observed failure planes generally inclined at a shallower angle while AASHTO LRFD 2020 assumes 45-degree failure planes. The shallower angle provided a larger failure surface at the loading region that resulted a higher ultimate strength. The effect of the failure plane on the capacity of the ledge will be discussed later.

5.6.2. **Damage Level**

At the same loading stages, "regular" pad tests, showed less damages than the "small" pad tests. The crack initiation for the "small" pad tests were observed before or at SLS whereas most of the big pad tests showed no damage at this stage. The crack propagation of the "small" pad tests was also more severe than the "regular" pad tests (purple and blue marks on Figure 5-5 and Figure 5-6). The "small" pad tests showed a distress under the bearing pad at ULS while "regular" pad tests do not. It was clear from the observation of T7I1 and T7I2 which are the "small" and "regular" test, respectively, conducted at an adjacent loading point on the same side of the specimen. The two tests were loaded simultaneously up to ULS, enabled a direct comparison between the "small" and "regular" pad test until ULS. A delayed crack initiation and less cracks were observed on T7I2 ("regular" pad)

when compared to T7I1 ("small" pad). The damage levels after ULS were not quite comparable since each test region has different ultimate strength and thus loaded to different state of loading. From the observation, it was clear that the "regular" pad tests were subject to less damage than the "small" pad tests until ULS.

5.6.3. Nominal Capacity

The load-deflection response plotted in Figure 5-7 compares the response of the tests with "small" and "regular". For the exterior, the "regular" pad test showed a greater stiffness and strength then the small pad test as expected. The measured ultimate load for the exterior "regular" pad test is 14% greater than the "small" pad test. However, for the interior tests, the ultimate strength of "small" pad tests is similar or even higher than the "regular" pad tests. For Specimen 3 interior tests, the "small" pad provided 10% greater capacity than the "regular" pad. For the interior tests conducted on Specimen 7, the "small" pad resulted a 1% and 6% lesser ultimate strength compared to the "regular" pad.

A possible reason for this discrepancy is the rotation of the loading frame due to the off centered actuator position. A 2-inch-thick (50 mm) rubber pad was used in between the bottom of the loading frame and the ledge surface to evenly distribute the applied load. When the load was applied, the rubber pads on two sides were squeezed, but to a different degree. The position of the actuator was designed to provide Strength-I limit state load to the front side when the back-side load was at dead load state. The un-evenly applied load on two sides squeezed the rubber pads to a different degree hence resulted a rotation of the loading frame. Figure 5-8 shows the frame movement at ULS of one of the interior

"small" pad tests (T3I1). As shown in Figure 5-8(a), the un-even load resulted an un-balanced level on two sides of the specimen in vertical direction. The rotation of the frame along with a pressing force also induced a lateral shift of the loading center toward the web (Figure 5-8(b)) at a higher loading state. The frame rotation is significant in the "small" pad tests. The rotation resulted in a reduced load eccentricity for the "small" pad tests which may have affected the ultimate strength of the "small" pad tests. Nafadi et al. (2018) demonstrated that load eccentricity can significantly affect the ledge capacity for ledges in L-shaped beams. Therefore, the observed higher strength of the "small" tests may be due to the reduced load eccentricity that was caused by the frame rotation and the squeezed rubber pad. Whereas for the "regular" pad tests, the frame rotation had a minimal effect since the larger pad had a smaller deformation due to the high stiffness. To clarify the discrepancy, and for a closer investigation of punching behavior of inverted-T beam ledges, a nonlinear finite element model (FEM) was developed.
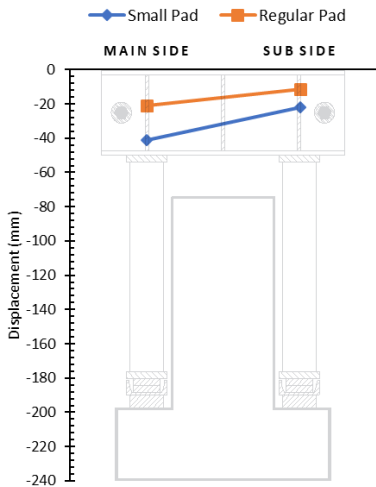
*Specimen shown in reduced scale

(a) Vertical displacement of loading frame   (b) Lateral movement of loading frame

Figure 5-8. Displacement of Load Frames at ULS.

145

5.7. Nonlinear Finite Element Modeling

The commercial FEM program ABAQUS, capable of solving extensive nonlinear problems, was used to model the inverted-T bent cap specimen. Figure 5-9 shows the overview of the FEM model. Specimen T3 was chosen as the prototype to build the FEM model. All four cases, exterior and interior with the small and big pad were modeled and analyzed.
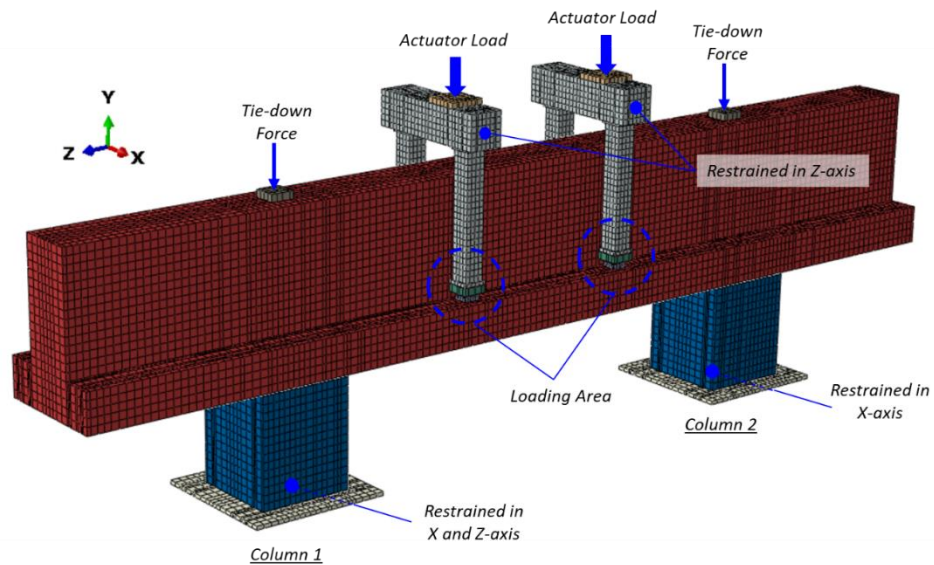
(a) Overview
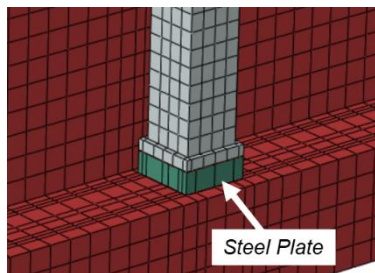
(b) Steel plate model
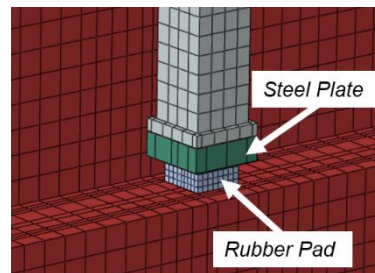
(c) Rubber pad model

Figure 5-9. Overview of FEM Model.

146

The full specimen and test setup was modeled including the support columns, loading frames, the bearing plates and bearing (rubber) pads. The bent cap specimen was placed on the support columns with a hard contact defined between the contacting surface to simulate a possible separation during the loading. The base plate was modeled and tied to the bottom face of the support column. The bottom of the base plate was restrained in the vertical direction (Y-axis) to simulate the ground. The bottom center of Column 1 was restrained in the horizontal (Z-axis) and transverse (X-axis) direction while the base of Column 2 was restrained in the transverse direction to simulate a simply supported condition. A steel plate was modeled on top of the bent cap align with the center of the support column. The tie-down force was applied on top of the steel plate at the first stage of the analysis to simulate the prestressed tie-down bar used to clamp the specimen to the strong floor. The loading frame was modeled based on the as-built dimensions except the upper beam modeled as a rectangular shape for simplicity. The frame was restrained in the longitudinal (Z-axis) direction for stability. The load was applied at the location of the actuators on top of the frame. The steel plates stacked in between the ledge and loading frame were modeled as an integrated plate. Surface-to-surface interaction model was used to define all the contacting surfaces for the steel parts.

Two cases of FEM model were established. One with a rubber pad modeled in between the steel plate and the ledge, the other one that only have steel plate directly placed on the ledge. The model with the rubber pad was developed to simulate the exact conditions of the test. The rubber was modeled to allow a shape deformation to simulate the frame rotation. A friction contact model was used for the contact surface between the

147

rubber pad and the ledge to simulate possible slip during the loading. The model with only the steel plate was built to provide a benchmark.

The concrete was modeled using 8-node solid element with reduced integration and hourglass control. The maximum element size for concrete element is about 2 in. (50 mm). Two node linear 3D truss elements were used to model the reinforcing steel with a typical element size of 50 mm (2 in.). The reinforcing steel was embedded into the concrete solid, assuming perfect bond between the rebar and concrete. The bond-slip interaction between rebar and cracked concrete was indirectly included by defining the tension stiffening effect of concrete. The damage-plasticity model for concrete was used for this study to take into account the behavior of cracked section. The dilation angle was taken as 33°. Default values were used for the rest of the parameters required by ABAQUS/Standard to define the damage-plasticity model. Kent and Park's (1971) model was adopted to define the stress-strain relationship for concrete under uniaxial compression. The tension stiffening effect of concrete was described using Hillerborg's (1976) bi-linear model. The measured concrete compressive strength, 3.8 ksi (26 MPa) of Specimen T3, was used. The yield strengths of normal steel member and reinforcing rebar were taken as 36 ksi (248 MPa) and 62 ksi (427 MPa), respectively. The material model for all steel elements was based on elastic-perfectly plastic behavior. The elastic modulus was assumed to be 29,000 ksi (200 GPa). The general static load procedure was adopted for the analysis. The rubber pad was modeled using hyperelastic material with the strain energy potential coefficients calculated using Mooney-Rivlin model. The temperature dependent parameters for the hyperelastic model, C10, C01, and D1 was taken as 95, 10,

and 0, respectively. The specimen was first analyzed for the self-weight and the initial condition due to the tie-down forces. The actuator load was applied subsequently on the loading frame with a maximum increment of 0.1 kips (0.5 kN).

5.7.1. FEM Result Evaluation

The FEM model is first evaluated by failure mode prediction. Maximum and minimum principal stress is used to present the potential damage areas of the FEM models. Figure 5-10 presents an overview of the minimum principal stress contour at the measured ultimate load. Figure 5-11 and Figure 5-12 compares the maximum and minimum stress contours with the experimental observations, respectively, at the regional areas around the loading points. The predicted contours are overlayed on the test photos at different load states. The upper and lower limit for the maximum and minimum principal stress contours, respectively, was set as the cracking stress of the concrete that assumed to be $6\sqrt{f_c'(psi)}$ $(0.5\sqrt{f_c'(MPa)})$. The red and blue on the maximum and minimum principal stress contour indicates the cracked area, respectively. The direction of the cracks is perpendicular to the stress concentration area on the maximum principal stress contour. While on the minimum principal stress contour, the crack direction is aligned with the stress concentration.

The overview of the minimum principal stress contour at measured ultimate load demonstrates that the FEM was able to simulate a punching shear failure of inverted-T bent cap ledges. The compression struts formed underneath the bearing pads clearly indicate a punching shear failure. A closer comparison at the regional areas indicating that the cracking locations predicted by the FEM were well correlated with the experimental

149

observations. The crack location both at ULS and the measured ultimate load was in good agreement with the experimental results. As revealed in the minimum principal stress contours, the angle of the cone cracks was also well predicted by the FEM. Overall, the FEM effectively captured the punching shear failure mechanism of the inverted-T bent cap specimen.

Figure 5-13 plots the predicted and measured load-deflection response of ledge under bearing pads. The load at initiation of cracking, formation of the cone crack, and the measured ultimate load was marked on the graphs. The cracking load was defined at the point when the tensile stress of the concrete element first reaches the cracking stress of concrete. The formation of the cone crack was identified when the stress at the compression strut under the bearing pad reaches the cracking stress of the concrete. Figure 5-14 compares the critical load values between the FEM and test results.

(a) Exterior regular pad   *(b) Interior regular pad*
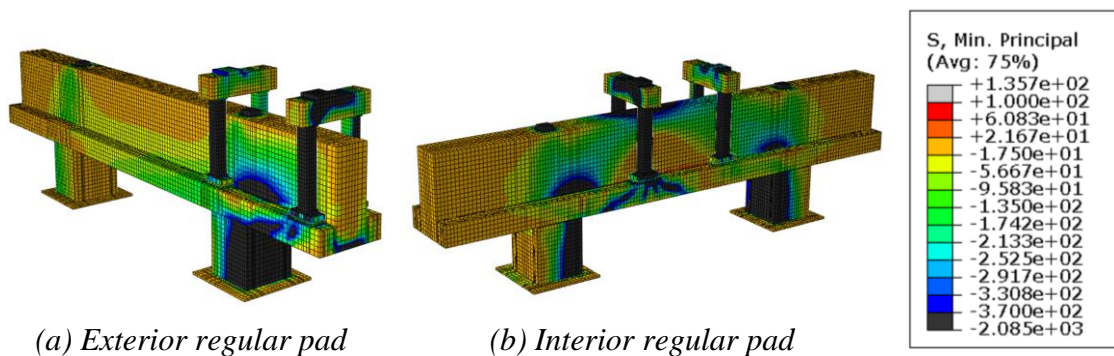
Figure 5-10. Failure Plane at Measured Ultimate Load – FEM vs. Test.
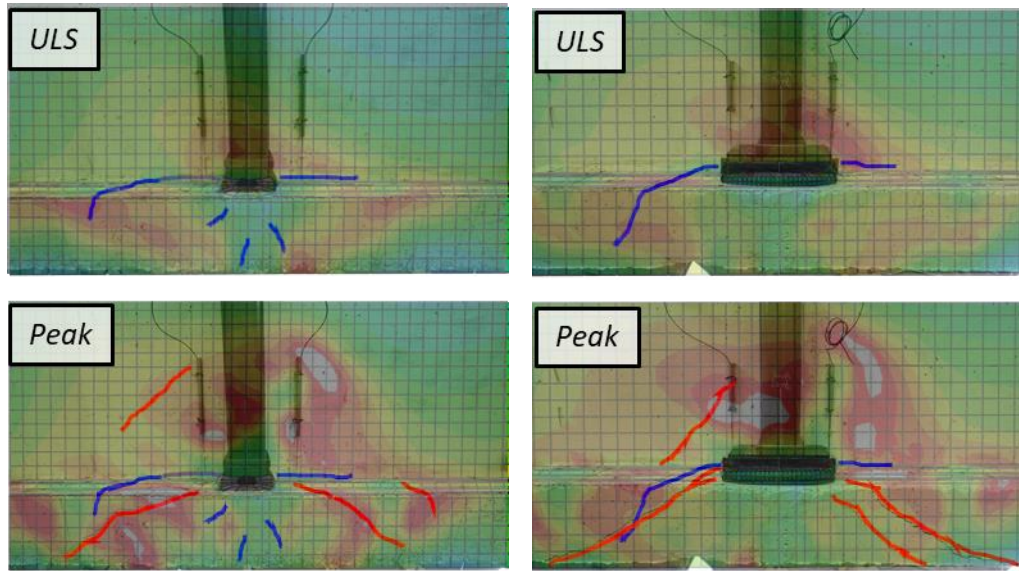
(a) Int. small   *(b) Int. regular*
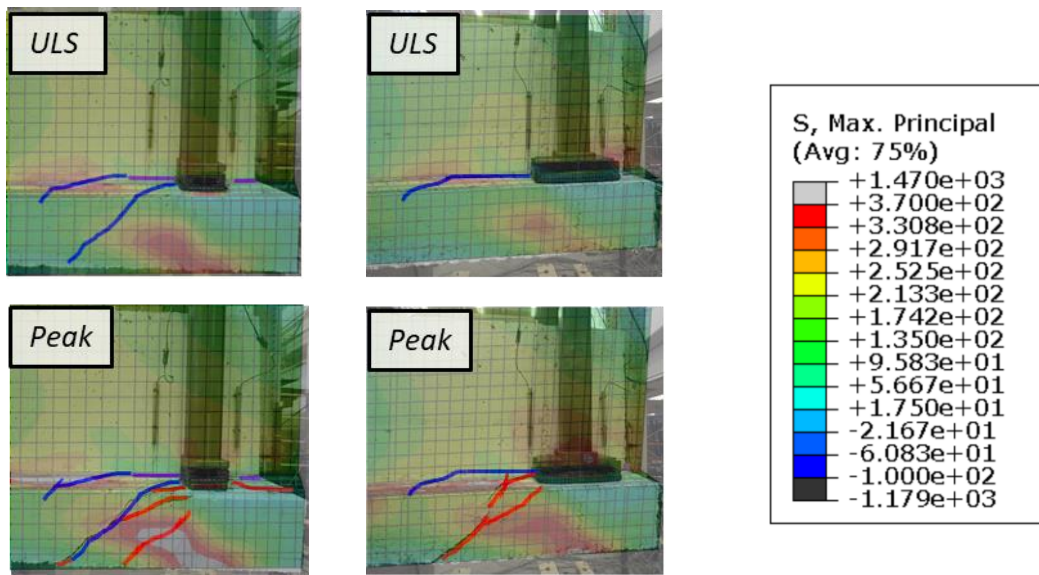
(c) Ext. small   *(d) Ext. regular*

Figure 5-11. Comparison of Failure Plane with Maximum Principal Stress.

<div align="center">

(a) Int. small   *(b) Ext. small*

(c) Int. regular   *(d) Ext. regular*
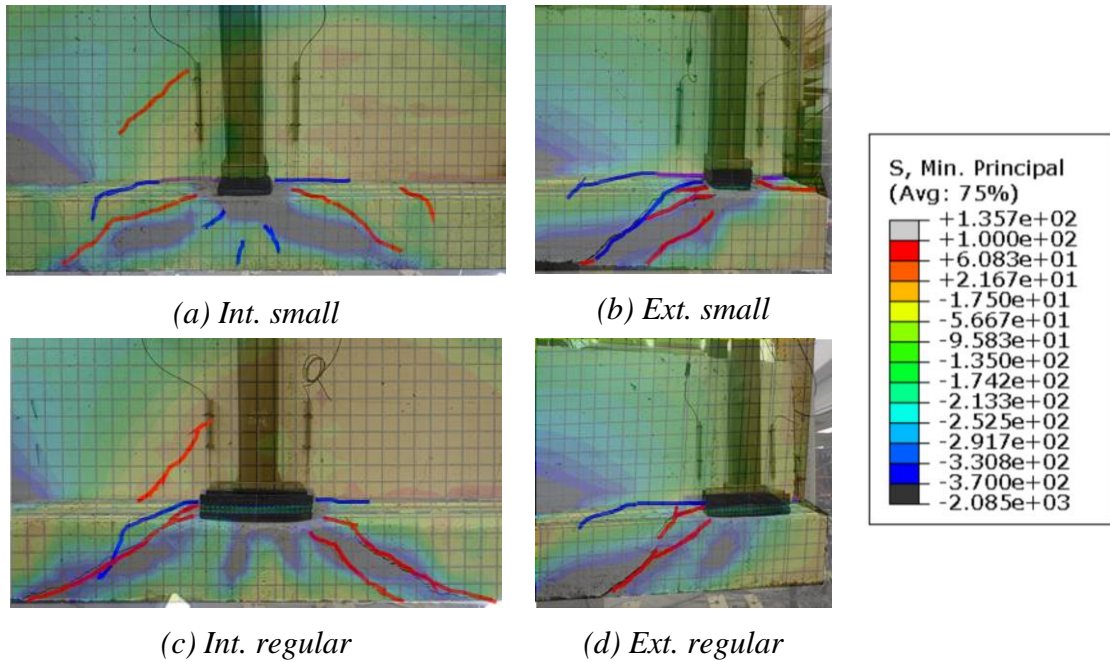
**Figure 5-12. Comparison of Failure Plane at Measure Ultimate Load with
Minimum Principal Stress.**

</div>

The FEM predicted behavior, except the interior "small" pad case, was in good agreement with the measured test data in both terms of stiffness and strength. Linear behavior before the cracking load (around SLS) was well predicted. The cracking load of the FEM was close to the experimental results with the values slightly lower than the measured data. The cracking load from the experiments was recorded when the first cracks became visible. Therefore, it is reasonable that the predicted values were lower than the observed values. The nonlinear behavior followed by the crack initiation up to failure was also well simulated. The steel plate and rubber pad models showed a similar response for both exterior and interior "regular" pad cases. The formation of the cone cracks and the ultimate strength estimated by the FEM was in good agreement with the measured values.

For the exterior "small" pad, the rubber pad model predicted a higher response than the measured test data at the post-peak stage though within an acceptable range.

(a) Exterior small pad

(b) Exterior regular pad

(c) Interior small pad

(d) Interior regular pad
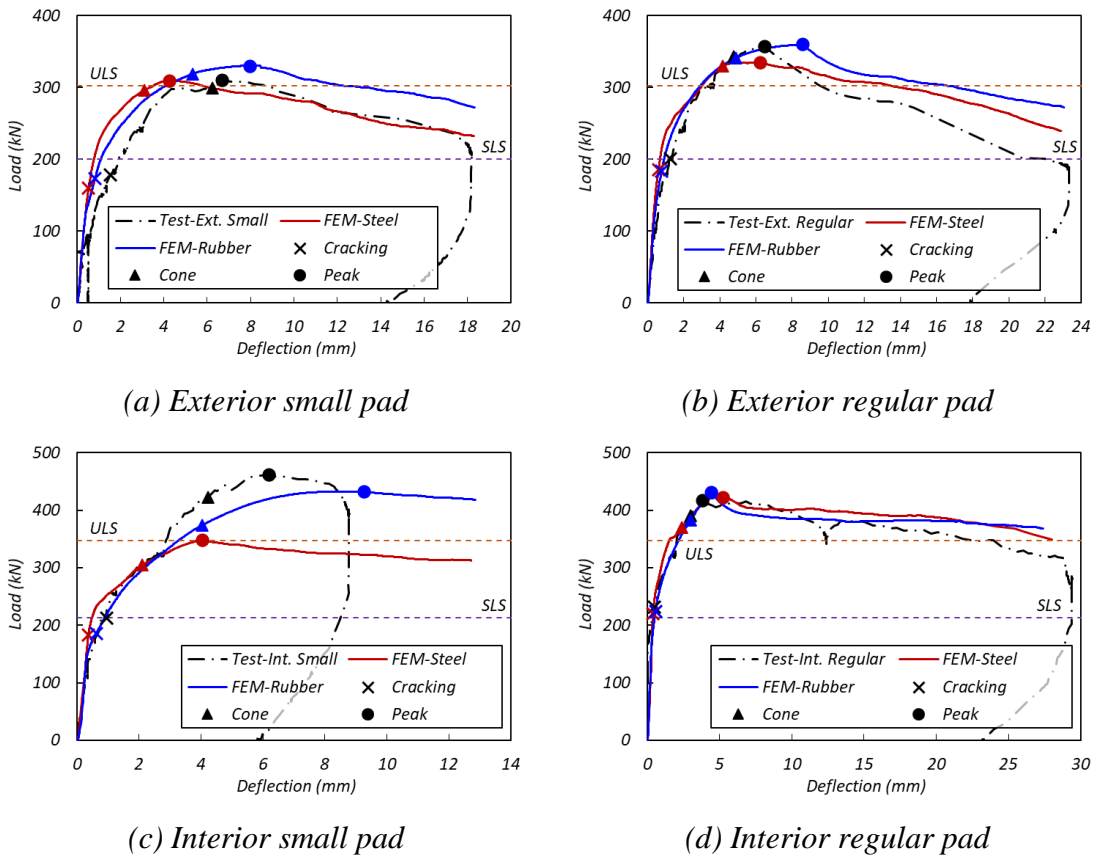
Figure 5-13. Load Deflection Response for Test on Specimen T3 – FEM vs. Test.
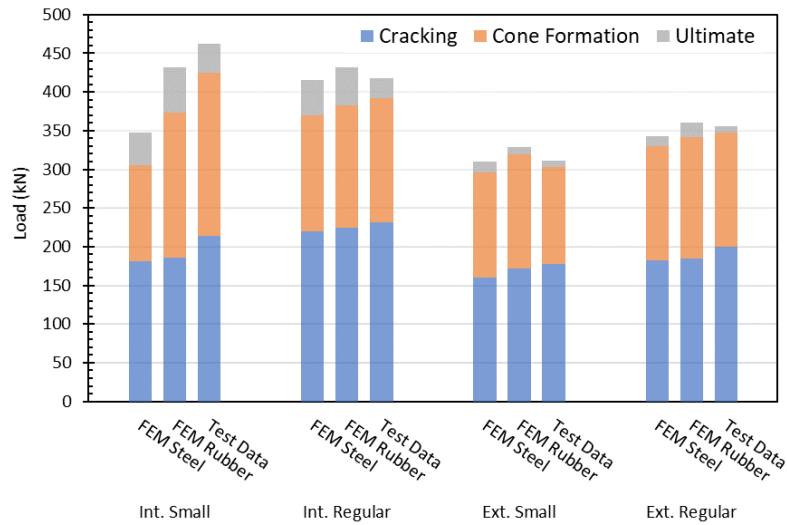
Figure 5-14. Comparison of Key Strength – FEM vs. Test.

Figure 5-15 shows the FEM prediction at the cross-section cut at the tip of the bearing pad at ULS. The experimental observations at ULS were also presented for a comparison. It is evident from the figures that the rubber pads at two sides in the FEM showed an uneven level when the load was applied. The shift of the loading center towards the web was also described. The level of the rubber pad at ULS predicted by the FEM was close to the experimental observations within 9% difference. More sliding of the frame toward the face of the web was occurred in the FEM as the load raised beyond ULS. The rubber pad model, as shown, simulated the squeezing of rubber and the rotation and sliding of loading frame and predicted a stronger strength than the steel plate model as a result.

The load-deflection response of the interior "small" pad test that showed an increase of stiffness from ULS can be explained by such findings from the FEM analysis. As elaborated by the FEM investigation, the stronger response of the interior "small" pad test is caused by the rotation of the frame and the shift of the loading center toward the

154

face of the web due to the un-evenly squeezed rubber pad. The sliding of loading frame towards the web reduced the load eccentricity and resulted more part of the bent cap engaged in the load resistance mechanism around the loading region hence increased the ledge capacity. In addition, the stronger response may also be attributed to the inclined loading frame. As the loading frame rotated, a component of the lateral force is included in the vertical measurement.
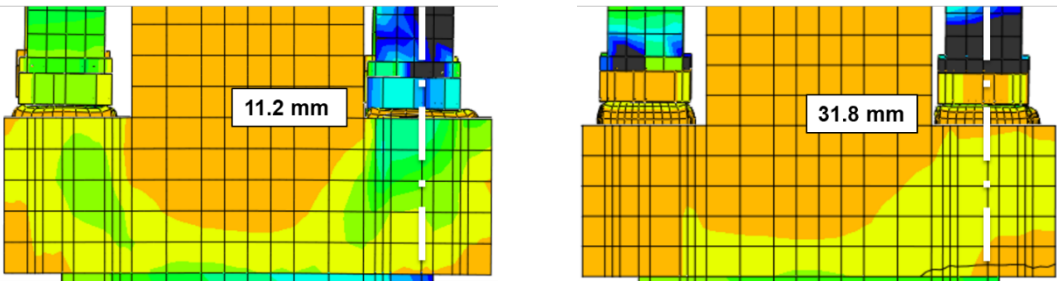
(a) Small – FEM result *(b) Regular – FEM result*
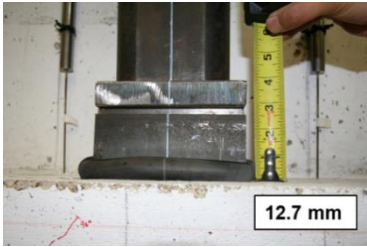
(c) Small – level of rubber pad *(d) Regular – level of rubber pad*
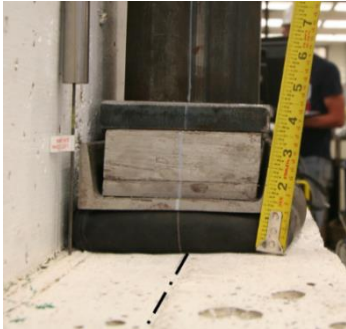
(e) Small – sideview *(f) Regular – sideviw*

Figure 5-15. Squeezed Rubber Pads at ULS.

The exterior "small" pad test was also affected by the deformed rubber pad but less sensitive than the interior region. The rubber pads typically showed an excessive deformation around at 76 kips (340 kN), which is the ULS of interior. Whereas the exterior region, with a limited load resistance due to the cut-off end, experienced a failure at an earlier load stage, therefore less affected by the squeezing of rubber pad. The "regular" pad tests are barely affected as the deformation of the "regular" rubber pad was relatively minimal.

5.7.2. **Parametric Analysis**

Having established the capability of the FEM model to simulate the stiffness, strength, and the punching shear failure mode, the model was utilized to perform a parametric study. The size effect of the bearing pad was further evaluated by the FEM model to elaborate the observed discrepancy and to verify the observed findings. The effect of load eccentricity, defined as the distance from bearing pad to the face of web, was also evaluated as this was considered to be the reason enhanced the interior punching shear capacity.

Figure 5-16 shows an overview of the considered parameters for the FEM parametric study. Four different sized bearing pads (defined as S1 to S4) and two varied load eccentricities (defined as E1 and E2) were analyzed to investigate the impact on the punching shear performance of inverted-T ledges. The steel plate model which gives a reasonable and reliable result was adopted for the parametric study. Fourteen models, including the two prototypes, were analyzed.

Table 5-6 lists the analysis cases with the key results. The key values from the FEM analysis were also compared in Figure 5-17. It is evident from the results that increasing the size of the bearing pad can enhance the ledge punching shear capacity. A gradual increase of strength was observed on both interior and exterior region as the pad size increased from 4 in. x 4 in. (102 mm x 102 mm) to 5 in. x 14 in. (127 mm x 356 mm). All the critical values – cracking load, cone formation as well as the ultimate strength – were enhanced by the increased bearing pad size. The rate of the increase was consistent. The exterior region was found to be less sensitive to the bearing pad size than the interior region. The strength of the interior "small" pad measured from the tests was similar to the "regular" pad tests. Considering the strength of "small" pad tests were enhance by the frame movement, it is clear that the ledges with "regular" pad tests were possessing a higher strength than the "small" pads. Overall, the size of bearing pad, observed from the test and elaborated by the FEM investigation, was found to be effective in enhancing the punching shear capacity of inverted-T ledges.

The load eccentricity, from the FEM investigation, was also have significant effect on the punching shear capacity of the ledges. The analysis results demonstrated that reducing the load eccentricity by 20% resulted 8% and 11% increase of strength in exterior and interior region, respectively. On the contrary, increasing the load eccentricity by 20% resulted 6% and 5% decrease of strength in exterior and interior region, respectively. The impact of the load eccentricity on the punching shear capacity of the ledge was significant than the size of bearing pad.

157
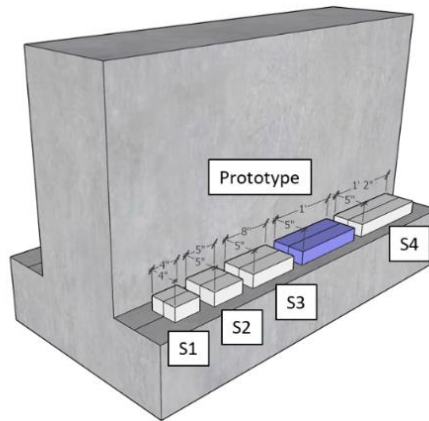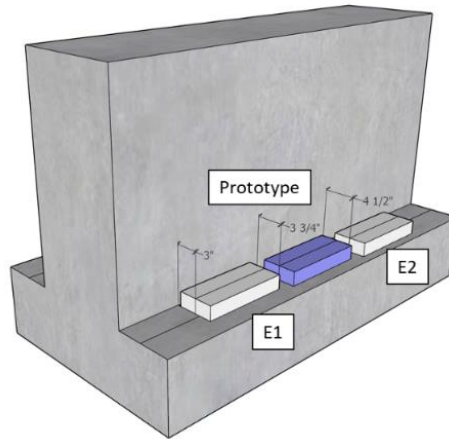
(a) Pad size

(b) Load eccentricity

Figure 5-16. FEM Analysis Parameters.

Table 5-6. FEM Analysis Parameters and Results.

Case ID	Pad Size (mm)	Eccentricity (mm)	Interior (kN)				Exterior (kN)			
			Cracking	Cone Formation	Ultimate Strength	Cone Angle (degree)	Cracking	Cone Formation	Ultimate Strength	Cone Angle (degree)
S1	102x102		182	305	348	32	160	296	310	31
S2	127x127		194	334	364	32	170	305	312	30.5
S3	127x203	95	210	343	390	32	175	314	327	32
S4	127x356		237	376	428	30	185	337	351	30.5
Prototype			220	369	415	32	183	330	343	31
E1	127x305	75	242	400	463	30	191	352	369	30.5
E2		115	209	350	397	32	176	298	320	31

*S – size; E – eccentricity

158
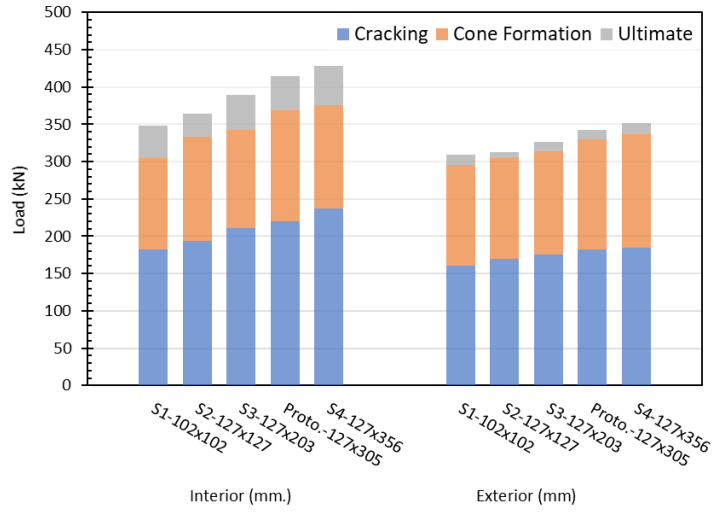
(a) Size of bearing pad
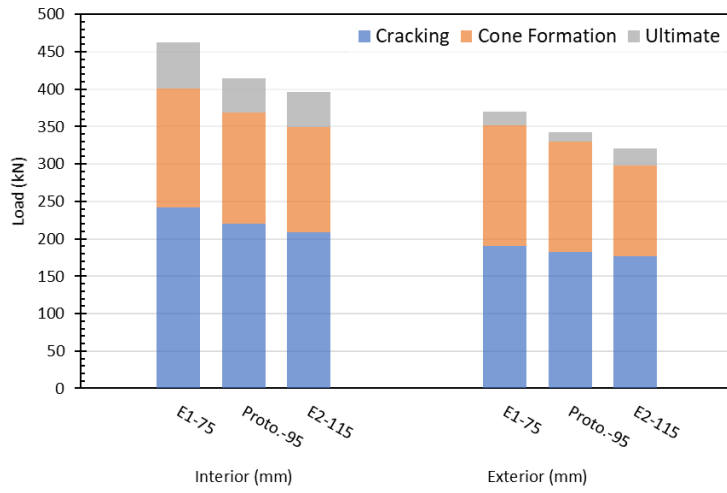
(b) Load eccentricity

Figure 5-17. FEM Parametric Analysis Results.

5.8. Nominal Capacity Evaluation

The nominal punching shear capacity of the ledge estimated based on the current standard (AASHTO LRFD 2020) is compared to the measured values. Table 5-7 lists the estimated capacities and the ratios of estimated capacities to measured values. The estimated capacities utilized the test day material properties, leading to different values for the same pad size and location. It is evident from the relative ratios that the current standard underestimating the punching capacity of inverted T bent cap ledge. For all tests, the observed capacity exceeded the estimated capacity by 47%. Garber et al. (2017) also found the code punching strength equation to be conservative by factor of as large as two 2. One explanation for this is the shallower cone crack angle developed surround the bearing pad. The crack angle discussed here is defined as the inclination of the main cone cracks formed under the bearing pads measured from the longitudinal axis of the bent cap. Figure 5-5 and Figure 5-6 show the observed punching shear damage with the angle of the primary cracks indicated. The main cone cracks had an average angle of 35-degree, shallower than the 45-degree angle assumed in the AASHTO LRFD 2020 procedure. Considering the concrete strength and the area of the failure plane are the two key factors affecting the punching shear strength, the crack angle of main cone takes a significant role on the punching strength of the ledge as it determines the area of the failure plane. Equation (5-1) through (5-3) specified by AASHTO LRFD 2020 to estimate the nominal punching shear capacity can be expressed in a more general form by incorporating the terms of crack angle as follow. The nominal punching shear capacity of ledges is,

$$V_n = 0.125\lambda\sqrt{f_c'}b_o d_f \tag{5-4}$$

For interior rectangular pads,

$$b_o = W + 2L + 2d_f \cot\theta \tag{5-5}$$

where θ = angle of cone crack.

$$b_o = 0.5W + L + d_f \cot\theta + c \le W + 2L + 2d_f \cot\theta \tag{5-6}$$

The angle of main cone crack, θ, is assumed to be 45-degree by the code hence cot θ =1 in the code specified equations. To account for the shallower angle observed in the tests, a crack angle estimation method proposed by Kim and Mander (2000) is adopted. The model was developed to estimate the crack angles forming on concrete beam-column elements based on the continuum truss model. By assuming the external work done on a structural element of unit length due to unit shear force (V_s=1) is identical to the total drift angle, a crack angle θ that minimizing the external work done by the shear and flexure components is achieved. The simplified term of the model was adopted in this study to estimate the crack angle of the ledge. The expression of the crack angle is

$$\theta = \tan^{-1}\left(\frac{\left(\frac{\rho_v}{\rho_t}\right)\left(\frac{A_v}{A_g}\right)}{0.61\Lambda}\right)^{\frac{1}{4}} \tag{5-7}$$

where ρ_v = volumetric ratio of shear reinforcement; ρ_t = volumetric ratio of longitudinal reinforcement; A_v = shear area of concrete section; A_g = gross section area; Λ = fixity parameter taken as 1 for this study.

The model estimates the crack angle based on the ratios of the shear and longitudinal reinforcement in the ledge. The expression can be simplified for the ledge as

$$\theta = \tan^{-1}\left(\frac{A_s l_b}{0.61 A_l s}\right)^{\frac{1}{4}} \tag{5-8}$$

where A_s = area of shear reinforcement in ledge; A_l = area of longitudinal reinforcement area in ledge; l_b = width of ledge; and s = spacing of ledge shear reinforcement.

The formula is validated by evaluating from the tests presented here and other punching shear tests on inverted-T beams (Garber et al., 2017) and L-shaped ledge beams (Nafadi et al., 2018). The validation offset includes 12 inverted-T beam ledge tests and 11 L-shaped beam ledge tests. Table 5-8 summarizes the experimental parameters of these tests. Figure 5-18 compares the calculated crack angles and the measured values documented in literature. The model gives a closer estimation for the inverted-T cases. Some of the L-shaped beam cases show a relatively big variation which may attribute to the reinforcement details of the L-shaped beams. The ledge of the L-shaped beams has C-shaped transverse reinforcement with the opening towards the bottom of the beam while the inverted-T ledges have enclosed rectangular shape transverse reinforcement. A more rigorous analysis would take into account the shear area reduction due to the open shaped transverse reinforcement of the L-shaped beam ledges would give a better estimation. Overall, the crack angle estimation gives a reliable upper limit result that can avoid false positive estimation.

162

Table 5-7. Summary of Comparative Test Results.

Specimen	Test Region	Test ID	Pad Size	Estimated Capacity (kN)	Measured Ultimate Load (kN)	Measured/ Estimated	Modified Estimation (kN)	Measured / Modified Estimation
	West-Ext.	T3W1	Small	227	311	1.37	247	1.26
	East-Ext.	T3E1	Regular	271	356	1.31	289	1.23
T3	Int.	T3I1	Small	245	463	1.89	285	1.63
	Int.	T3I2	Regular	334	418	1.25	374	1.12
	Int.	T3I3	Regular	334	418	1.25	374	1.12
	Int.	T7I1	Small	285	498	1.75	331	1.50
T7	Int.	T7I2	Regular	387	529	1.37	431	1.23
	Int.	T7I3	Small	285	498	1.75	331	1.50
	Int.	T7I4	Regular	387	503	1.30	431	1.16

Table 5-8. Experimental Parameters for Ledges Reported by Previous Researchers.

Structural Type	Test ID	Ledge Width (in.)	Longitudinal Bar	Transverse Bar	Transverse Bar Spacing	Observed Crack Angle (degree)	Estimated Crack Angle (degree)
Inverted-T Ledge (This paper)	T3W1	210	D16 & D19	D10	140	32.4	37.8
	T3E1	210	D16 & D19	D10	140	32.6	37.8
	T3I1	210	D16 & D19	D10	140	32.7	37.8
	T3I2	210	D16 & D19	D10	140	37	37.8
	T3I3	210	D16 & D19	D10	140	42	37.8
	T7I1	210	D16 & D19	D10	140	32.3	37.8
	T7I2	210	D16 & D19	D10	140	34	37.8
	T7I3	210	D16 & D19	D10	140	35	37.8
	T7I4	210	D16 & D19	D10	140	32.5	37.8
Inverted-T Ledge (Garber et al. 2017)	SS1-75-1.85-06	267	3 D29 & 2 D36	D19	89	37	37.6
	SS1-75-2.50-06	267	3 D29 & 2 D36	D19	76	39	38.7
	SS1-75-2.50-03	267	3 D29 & 2 D36	D19	44.5	41	42.5
L-shape Ledge (Nafadi et al. 2018)	RS3-M	203	2 D13	D10	127	34	42.7
	RS3-E1	203	2 D13	D10	127	34	42.7
	RS5-D-M	203	2 D16	D10	127	32	39.6
	RS5-M	203	2 D16	D10	127	39	39.6
	RS1-D-M	203	2 D13	D10	152	34	41.4
	RS4-M	203	2 D16	D10	203	45	40.5
	EX-RS4-M	203	2 D13	D10	76	45	45.0
	RS1-D-E2	203	2 D13	D10	152	32	41.4
	RS1-E1	203	2 D13	D10	152	34	41.4
	RS1-E2	203	2 D13	D10	152	39	41.4
	RS2-E2	203	2 D13	D10	178	35	40.3

Note: D10 - #3 bar; D13 - #4 bar; D16 - #5 bar; D29 - #9; D36 - #11; and D19 - #6 bar

The estimated crack angles are incorporated into the capacity estimation and compared to the code-based estimations as well as the measured values. The last two columns of Table 5-7 lists the estimation given by the proposed model as well as the ratio to the measured strength. The comparison is also visualized in Figure 5-19 by a bar chart. It is evident from the comparison that the proposed model gives a more practical estimation with an improved the accuracy of 16%. The remaining gap between the estimated and measured values may because of the transverse reinforcement of the ledge. By sorely take into account the concrete strength, the capacity estimation neglects the contribution of the transverse reinforcement. It is believed that the transverse reinforcements are contributing strength to the punching capacity of the ledges. Nafadi et al. (2018) demonstrated that concentrating transverse around the loading area can effectively enhances the punching shear capacity of the L-shaped beam ledges. An estimation reflects the reinforcement contribution may give a more accurate result. However, considering the brittle nature of the punching shear failure, the reinforcement contribution can be reserved as spare strength to avoid a sudden failure of the ledges. Additionally, a special consideration should give to the load eccentricity which is excluded from the code-based capacity estimation. It is factor that found to be affecting the ledge punching capacity. The interior region is more susceptible by this factor than the exterior.
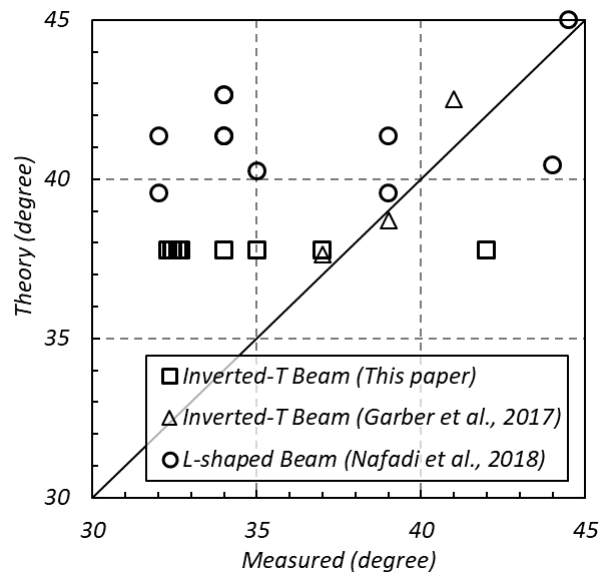
Figure 5-18. Crack Angle Comparison between Theory and Experiments.
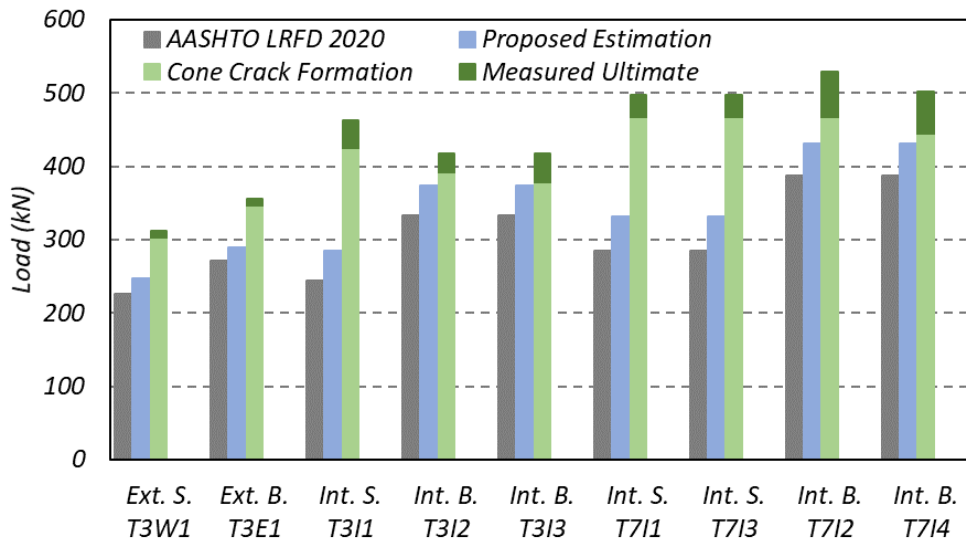
Figure 5-19. Comparison of Estimated and Measured Punching Shear Capacity.

5.9. Conclusion

The punching shear failure on the ledges of inverted-T bent caps are experimentally investigated on the half-scaled test specimens. Nine tests – two exterior and seven interior – were conducted on two specimens that are designed to emphasize the ledge punching failure. Two bearing pad sizes were considered. A nonlinear finite element model is developed to elaborate the experimental findings and to analytically investigate the structural behavior of inverted-T ledge. Based on the experimental investigation and analysis herein, the following conclusions are drawn:

1. The tests are successful in isolating the punching failure of the inverted-T ledge evidenced by the clear truncated concrete cone developed under the bearing pad. The brittle nature of the punching failure is proved by the test on the ledges of inverted-T bents. The signs of punching failure generally initiate at a later stage when the ledge closely reached the strength limit. A rapidly developed failure is followed by the initiation of the main cone crack. The observed crack angle of the main cone crack generally inclined shallower than the code assumed 45-degree, resulted a larger failure plane developed under the bearing pad.

2. The developed FEM model successfully simulated the structural performance of the inverted-T bent cap ledges. The prediction of the FEM model matches well with the measured values either in terms of stiffness or the strength. It is also effectively captured the punching failure of the inverted-T ledges.

3. The use of the large pad presented a better serviceability than the small pad. The large pad showed a delayed crack initiation relative to the small pad, and was

subjected to less damage at same limit state. The large pad, as demonstrated by the experimental results, is able to enhance the ultimate punching shear capacity of the exterior region. While for the interior, the small pad showed a similar ultimate strength to that of the large pad due to the experimental setting. By elaboration with FEM analysis, and combine with the findings from the experiment, it is also concluded that the use of a larger pad can enhance the ultimate punching capacity of the interior region.

4. The load eccentricity, defined by the distance from the center of bearing pad to the web, is found to be a factor affecting the ledge punching capacity. The analysis result demonstrate that interior region is more susceptible to the load eccentricity than the exterior region.

5. The code-based estimation of punching shear capacity found to be over conservative. A modification is proposed for a practical capacity estimation. The proposed model by incorporating the effect of crack angle is proved to be effectively increased the estimation accuracy tough still in conservative side.

6. The modification is recommended for the evaluation of existing structures where the structure may be deemed deficient based on the code-based estimation when it may not be the case. For the design of new structure, the code-based estimation is recommended to ensure reserve strengths.

6. STRENGTHENING IN-SERVICE INVERTED-T BENT CAP LEDGE AND HANGER CAPACITIES USING FIBER REINFORCED POLYMER (FRP) FABRIC

6.1. Summary

Plans to increase traffic and observed cracks at web-ledge interfaces in many in-service bent caps led to the need to design and evaluate strengthening solutions for inverted-T bent caps. The objective of this study is to experimentally investigate the application of FRP strengthening technique on inverted T bent caps. FRP retrofit schemes are developed based on the geometry of in-service bent caps to address the ledge and hanger weakness which are the local mechanisms encountered in inverted T sections. The experimental results demonstrated that prototype specimens were able to capture the local failure mechanisms. The FRP retrofit schemes effectively improved the serviceability, displacement ductility and the ultimate load carrying capacities. The estimated strength of the FRP retrofitted system in accordance with the specification are compared to the experimental results and determined to be reasonable.

6.2. Introduction

Inverted-T bent caps supporting the bridge girders with a cantilever ledge is sometimes used for bridge piers to satisfy geometric constrains and to provide an aesthetically pleasing appearance. Such bent caps are typically under complex states of stress along most of their spans due to disturbed stress regions are induced by changes in the cross-section. Many early inverted-T bent caps built to historic specifications are found to be deficient when evaluated against the current design approach and/or lack adequate

strength to support planned increases to live load demands. Undesirable diagonal cracks at the reentrant corners between the cantilever ledges and the web in older, existing inverted-T bent caps have been reported over the past decades, as shown in Figure 6-1. Zhu et al. (2001) and Zhu and Hsu (2003) studied the cause of these diagonal cracks. They attributed the cracking to the design methodology of inverted-T bent cap that did not address cracking at service loads and proposed a crack control design provision. Larson et al. (2013) investigated the cause of diagonal cracking in the ledges of inverted-T bent caps. Various variables such as the ledge depth and length, web reinforcement quality, number of point loads, depth of the member, and the span to depth were evaluated. Based on the findings, they reported that several existing structures had already been subjected to about 70-80% of their ultimate capacity. A design recommendation of future inverted-T bent caps was also proposed. While these studies focused on the design methodology of inverted-T bent caps, minimal research attention is available on the retrofit of inverted T's that are somewhat old or show signs of distress.

Replacement of deficient bent caps is not always practical due to cost, interruption to traffic, and the acceptable condition of other parts of the structure. Therefore, proven techniques for strengthening these bent caps are needed to enhance the longevity as well as to provide sufficient capacity for increased traffic load demands in the future. To meet such a need, Hurlebaus et al. (2018a,b) designed and evaluated eighteen potential strengthening solution for in-service inverted-T bent caps including fiber reinforced polymer (FRP) solutions, mechanical solutions, and external post-tensioning solutions.

The most effective and viable six solutions were selected to experimentally evaluated. As part of the research, this study focuses on FRP strengthening of inverted-T bent caps.

Externally bonded FRP reinforcement is an attractive rehabilitation technique due to its tailorable performance characteristics, ease of application, high strength-to-weight ratio, and non-corrosive characteristics. The effectiveness of FRP composite sheets on the shear strengthening of conventional top-loaded reinforced concrete (RC) rectangular or T-beams are proven by many previous researchers. However, inverted-T bent caps possess different structural behavior when compared to the common top-loaded T-sections. Figure 6-2 shows the components of the inverted-T bent caps and the load path represented by a strut-and-tie (SAT) model. The loads from the girders are introduced near the bottom rather than the top of the cross-section and therefore require stirrups acting as hangers to transmit the applied loads back up into the web. The bottom flange, with reinforcement transverse to web, must have sufficient capacity to be able to transmit the applied loads to the web. Such a structural feature leads inverted-T bent caps subject to the localized failures, as classified by Mirza and Furlong (1983, 1985) – hanger, ledge and punching failures. Figure 6-3 sketches these local failures. Hanger failure is defined by vertical separation at the web-ledge interface resulting in yielding of the hanger reinforcement. Ledge failure is loss of capacity of the ledge acting as a bracket. Failure can occur as a flexural failure of the ledge or as friction failure at the face of the web, in which the ledge shears off. Punching failure occurs when the applied load exceeds the tensile strength of the concrete along the surface of a truncated pyramid under.
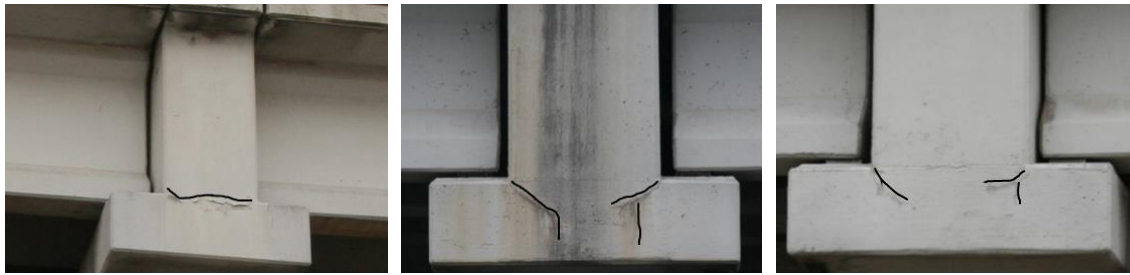
(a)   *(b)*   *(c)*

Figure 6-1. Observed Cracks on In-Service Inverted-T Bent Caps.
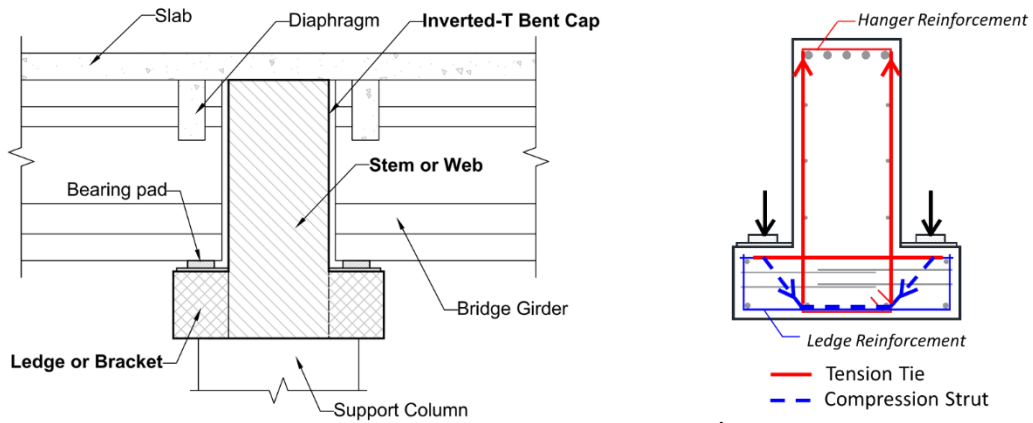
(a) Components of inverted-T bent cap   *(b) Load path by strut-and-tie model*

Figure 6-2. Inverted-T Bent Cap System.
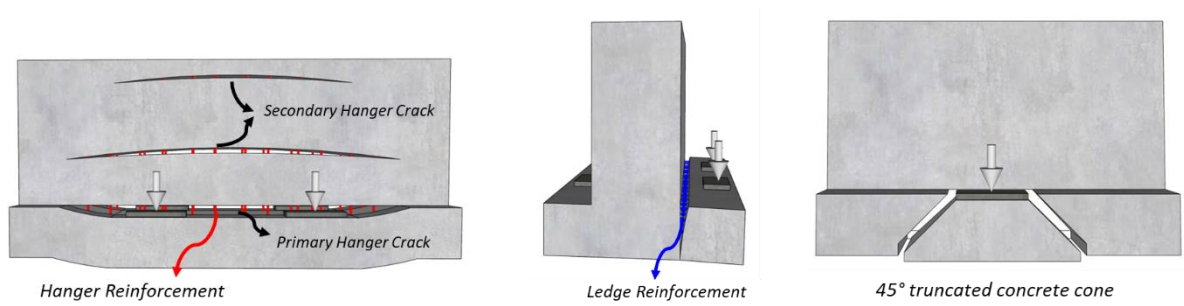
(a) Hanger failure   *(b) Ledge failure*   *(c) Punching failure*

Figure 6-3. Local Failure Modes of Inverted-T Bent Caps.

171

The strength of the entire cross section of the inverted-T beams can be reached only if there exist adequate local strength to support the concentrated forces applied on the bottom flange. Locally, the ledge must have enough strength to avoid punching shear weakness, the ledge reinforcement must be strong enough to maintain flexural tension and shear friction resistance at the face of the web, and hanger reinforcement must be sufficient to transmit flange force into the web (Mirza and Furlong, 1983). Hurlebaus et al. (2018a) reported that some existing inverted-T bent caps may be susceptible to these local failures. The prevalence of cracking at the re-entrant corners observed on the in-service inverted-T bent caps also suggest such a vulnerability. Therefore, the application of FRP composite system on the inverted-T bent caps should effectively capture these local failures.

While many prior studies have been conducted to investigate the shear strengthening of FRP on rectangular or T-beams, very limited data is available on the FRP strengthening of inverted T beams despite the popularity of such a system. Galal and Sekar (2008) experimentally investigated the effectiveness of using anchored FRP sheets to eliminate the brittle failure mechanism and to improve strength of the inverted-T bent caps. The FRP composites were designed to address the web-shear, hanger and punching failure. The FRP wraps mostly composed of U-wrap or inverted U-wrap covers the bottom flange or the web of the inverted-T specimens. An extended U-wrap, extend the end of U-wrap to cover top face of the flange, was also considered. Mechanical anchor and embedded FRP fan anchors were used to provide anchorage to the FRP composites. Diagonal anchorages were used at the web-ledge interface to prevent peeling-off of the FRP wrap at the intersection or to provide an end-anchorage for some cases. Based on the

172

experimental results it was evident that the anchored FRP sheets were effective in improving the displacement ductility, and the load carrying capacity of the inverted-T bent caps. Though the study presented a successful use of FRP composite for strengthening the inverted-T bent caps, there are still some aspects need to be better understood. An inverted U-wrap scheme was used to cover the web from the top. However, the top of the web is normally connected to the bridge deck for in-service inverted-T bent caps, therefore, it may not be practical for implementation. Diagonal anchorages were used at the web-ledge interface to provide end anchorage to the inverted U-wrap covers the web or a fixture to FRP wraps that covers pass around the web-ledge interface. Whereas the web-ledge interface of the inverted-T beam is generally vulnerable for cracking. Use of anchorage at the web-ledge interface should be avoid which may weaken an inverted-T beam. As revealed by the study, the configuration of the FRP wrap for the inverted-T beam can be a challenge due to the geometry where the flange is located at the bottom of the section with a load acting on top of the cantilever wings. The effect of end anchorage, to prevent debonding of the FRP, is demonstrated to be another significant factor affecting the performance of the FRP retrofitted system. The retrofit solution with sufficient anchorages showed better performance when compared to not using enough anchors.

The configuration and the end-anchorage for the FRP composite was also reported as a significant factor affecting the overall performance of FRP retrofitted system on the other prior studies of FRP shear strengthening of RC T-sections. Deifalla and Ghobarah (2010) experimentally investigated shear strengthening of T-beams using CFRP composite sheets with various configurations. They noted that wrapping the entire section

173

with CFRP was the most effective solution though the implementation is rare because of limited access. The U-wraps, cover the bottom web of the T-beam, which are the most widely used technique was found to be least effective. A modified U-wraps, extend the tip of U-wraps to bottom of the flange, was proved to be a viable and effective alternative. Chaallal et al. (2011) note that the FRP strengthening methods for shear strengthening of a RC beam may have high potential for debonding as the FRP sheet debonding and separation of side concrete were observed in the externally bonded FRP retrofits. They noted that there is high uncertainty in the FRP-to-concrete bond and therefore the FRP composite system requires a proper surface preparation in advance. Deifalla et al. (2013) compared the performance of un-anchored and anchored FRP U-wrap retrofit system on the shear strengthening of T-beams and demonstrated that the anchored solutions resulted in greater ultimate strength and ductility when compared to the unanchored solutions. Galal and Mofidi (2010) experimentally investigated the use of mechanically anchored unbonded dry carbon fiber (CF) sheets for the shear strengthening of RC T-beams. The CF sheets were wrapped around and bonded to steel rods, which in turn were anchored to the corners of the web-flange intersection of the T-beam using bolts. The system sorely relies on the end anchorage demonstrated an increase on the shear strength of the T-beam.

6.3. Design Concept

As revealed herein, the design of the FRP retrofit solution should consider the wrapping scheme and the use of end-anchorage to achieve a fully-developed FRP contribution. These factors may particularly be essential for the inverted-T bent caps which have a non-

174

rectangular cross-section. Surrounding the inverted-T section would require the FRP composite to wrap around multiple corners, including the intersection of the web and the ledge where debonding or fracture of the FRP may become a concern. A strategy that can eliminate the application of FRP at these re-entrant corners would be required. Additionally, the FRP application on the cantilever region (cut-off end) of inverted-T bent cap, which was not considered in previous studies, should also be investigated.

Under the consideration of such factors, two retrofit schemes were developed for strengthening in-service inverted T bent caps: full- depth FRP and partial-depth FRP. The proposed retrofit solutions address the deficiencies of in-service bent caps by providing alternative load paths from the point of the girder load to the stem. Figure 6-4 presents the conceptual diagrams of the FRP retrofit solutions with load paths represented by strut-and-tie (SAT) model. The SAT model, with compression strut and tension tie, provides insight to the force distribution in the bent cap section. The load paths of the original inverted-T section are depicted in black and the supplemental load paths provided by the FRP retrofit is depicted in blue and red representing compression strut and tension tie, respectively.

Figure 6-4(a) shows the full-depth FRP solution which is designed to augment hanger, ledge, and punching deficiencies. Infill concrete is cast on top of the ledge to transform the inverted-T cross-section to a rectangular cross-section. The U-wrap FRP sheet is used to wrap the transformed section externally. Through threadbars are used at the top, working to provide a clamping force to a steel waling to anchor the FRP using compressive forces instead of traditional anchors. The FRP sheet provides a supplemental

175

load path that collects load in the ledges and transfers it to stem. With a height fully developed to the top of the section, the FRP sheet is able to supplement the hanger reinforcement. The transformation of the cross-section to a rectangle essentially minimizes the bends in the FRP sheet to reduce the potential for FRP de-bonding, also ensure the transition of the load along the FRP sheet.

Figure 6-4(b) shows the partial-depth FRP solution which is designed for bent caps where the full stem is not accessible, as may be the case where diaphragms are used at the ends of girders. The partial depth is able to enhance the ledge and punching deficiencies, but not the hanger capacity. Infill concrete is used to transforming the inverted-T section similar to the full-depth solution, but with a shallower height due to the limited accessibility. The transformed section is wrapped with a U-shaped FRP sheet and anchored at the top by steel walings. The solution with a partial-depth FRP sheet is able to transfer the load from the ledge to the web and thus can improve the ledge and punching shear capacity. However, the FRP cannot supplement the hanger capacity since it does not extend the full-depth of the stem.

Figure 6-4(c) shows the FRP retrofit solution for the exterior region. Either the full- or partial-depth solution can be used at the inner side of the girder based on the deficiencies. At the end face, the FRP is provided by multiple sheets to cover the web and bottom flange on the end face. Additional FRP strips can also be applied to wrap along the inverted-T section at the outside of the girder. Infill concrete with U-shaped FRP sheets at the inner side of the girder provides supplemental load paths for part of the girder load. At the end face, the FRP strip covers the web is working as an external hanger to transfer

176

the girder load to the top tension chord. The FRP strip covers the flange on the end face, and wraps around the inverted-T section at the outside of the girder is provided as a subsidiary part to catches the load passing through the ledge.
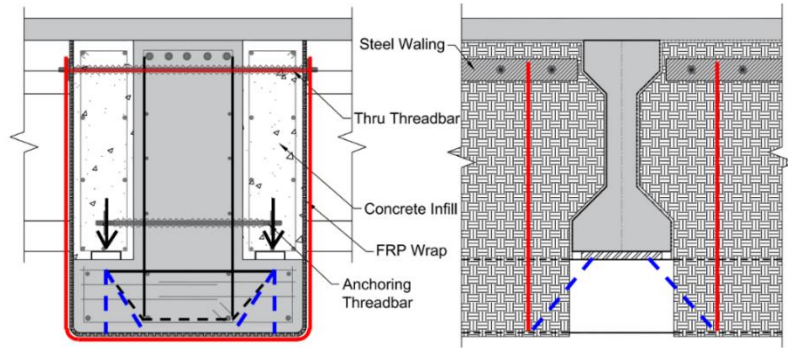
(a) Full-depth solution
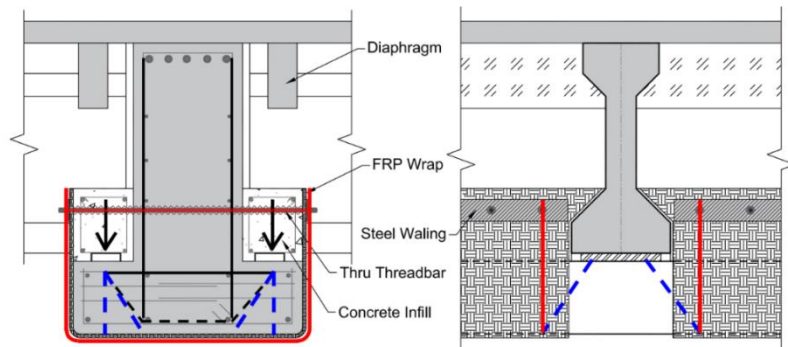
(b) Partial-depth solution
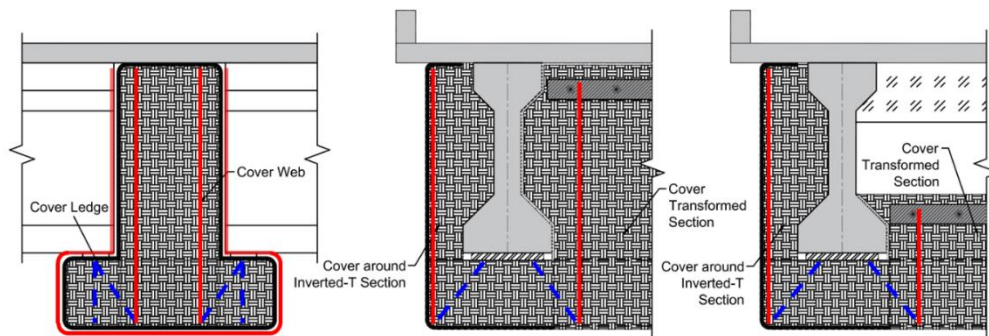
(c) Retrofit scheme for exterior region (cut-off end)

Note: load path of retrofit system demonstrated using SAT model: black - indicating load path of original strcuture; blue and red - indicating alternative load path provided by retrofit solution.

Figure 6-4. FRP Retrofit Solutions for Inverted-T Bent Caps.

6.4. Experimental Investigation

The FRP retrofit solutions were tested on one-half scaled test specimens that were designed for strain and stress similitude to represent the characteristics of a prototype in-service bent cap. Nine individual tests – four control tests and five retrofit tests – were conducted on four test specimens. Each test was designated based on the specimen number, tested region and the test order. Table 6-1 summarizes the tests conducted on each specimen. The tests presented in this paper were part of a larger experimental program (Hurlebaus et al., 2018b) to develop retrofit solutions for in-service inverted-T bent caps.

6.4.1. Specimen Description

Figure 6-5 presents the details of test specimens and test set-up. All test specimens have the same geometry and configuration. The bent cap is 264 in. (6706 mm) long and is supported by two 24 in. (610 mm) square reinforced columns spaced at 144 in. (3657 mm) on center to provide two *exterior* (cantilever overhang) and one *interior* (seated between support) loading regions. The support columns with a 1.5 in. (38 mm) diameter steel pipe in the center were seated on a 1 in. (25 mm) thick steel base plate. A tie-down threadbar was used to clamp the test specimen to the strong floor through the support columns. The overall height of the bent cap is 40 in. (1016 mm) with 10 in. (264 mm) deep ledges that extend 8.25 in. (210 mm) from either face of the stem.

Table 6-1. Test Matrix.

Specimen[1]	Test ID[2]	Retrofit Solution	Purpose of Retrofit[3]	Scheme
T1 (H.D.)	T1W1	None	Hanger Reference	
	T1I1	None	Hanger Reference	
T2 (H.D.)	T2W2	Full-Depth	H, L, P	
	T2I2	Full-Depth[a]	H, L, P	
T5 (L.D.)	T5E1	None	Ledge Reference	
	T5I1	None	Ledge Reference	
T6 (L.D.)	T6W1	Partial-Depth	L, P	
	T6I1	Partial-Depth	L, P	
	T6E1	Full-Depth[b]	H, L, P	

1. H.D. = hanger-deficient and L.D. = ledge-deficient
2. T # = specimen number, W,E,I # = test location indicating west and east exterior, and interior with loading number at the loading point
3. H = hanger, L = ledge, and P = punching shear

179

Two reinforcement configurations were used to emphasize ledge and hanger deficiencies. Figure 6-5(b) shows the reinforcement details of the test specimens. The *ledge-deficient (L.D.)* specimen, with D10 (#3) ledge reinforcement and D13 (#4) hanger reinforcement spaced 5.5 in. (140 mm), on average, was designed to isolate the ledge failure mechanisms. The *hanger-deficient (H.D.)* specimen was designed to isolate the hanger failure mechanisms with D13 (#4) ledge reinforcement and D10 (#3) hanger reinforcement spaced 6 in. (152 mm), on average.

Two ledge-deficient and two hanger-deficient specimens are presented herein. Specimen T1 and T2 were the *hanger-deficient* specimens cast on the same day. Specimen T5 and T6 were the *ledge-deficient* specimens that cast together on different date. Table 6-2 lists the measured properties of the concrete. For the bent caps, a 3.6 ksi (25 MPa) 28-day strength concrete with 3/8 in. (9.5 mm) aggregate was specified. Standard 4 in. x 8 in. (100 mm x 200 mm) test cylinders were made per each concrete pour and tested to establish 7, 14, 28, and test day compressive strengths. Grade 60 reinforcement was used with the measured yield and ultimate strength given in Table 6-3.
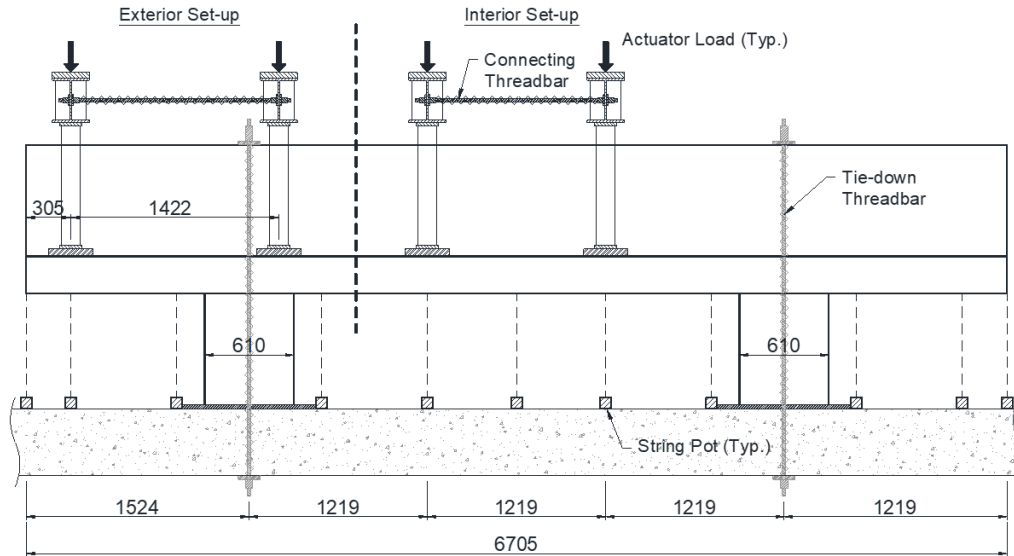
(a) Schematic of test set-up
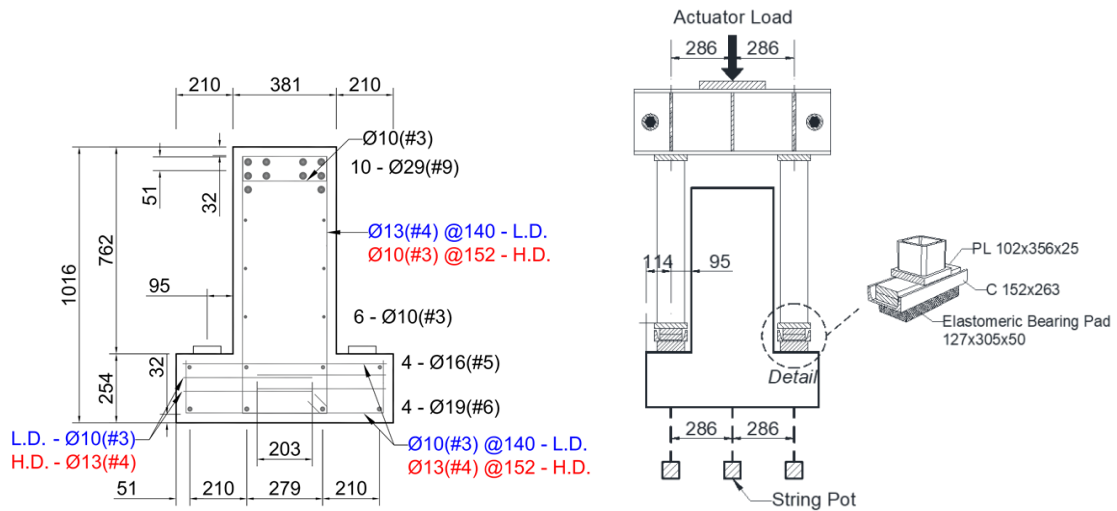
(b) Reinforcement details   *(b) Loading frame and bearing pads*

Figure 6-5. Experimental Test Set-up (mm).

181

Table 6-2. Mechanical Properties of Concrete.

Specimen Type	Specimen No.	Slump (mm)	7-day Strength (MPa)	14-day Strength (MPa)	28-day Strength (MPa)	Age at Test Day	Test Day Strength (MPa)
Hanger-deficient	1	140	15.4	18.3	23.4	175	30.0
	2					248	26.9
Ledge-deficient	5	140	17.3	20.3	24.4	125	30.7
	6					183	27.9

Table 6-3. Tensile Strength of Reinforcing Rebar.

Bar No.	Yield Strength (MPa)	Ultimate Strength (MPa)
#3 (D10)	441	688
#4 (D13)	467	662
#5 (D16)	441	722
#6 (D19)	425	717
#9 (D29)	479	779

6.4.2. **Description of Retrofit Solutions**

The retrofit solutions were adapted from the solutions designed for the in-service prototype bent caps, with appropriate adaptations made for the half-scale tests and laboratory constraints. Figure 6-6 and Figure 6-7 presents the details of the full- and partial-depth FRP solution adapted for the test specimens.
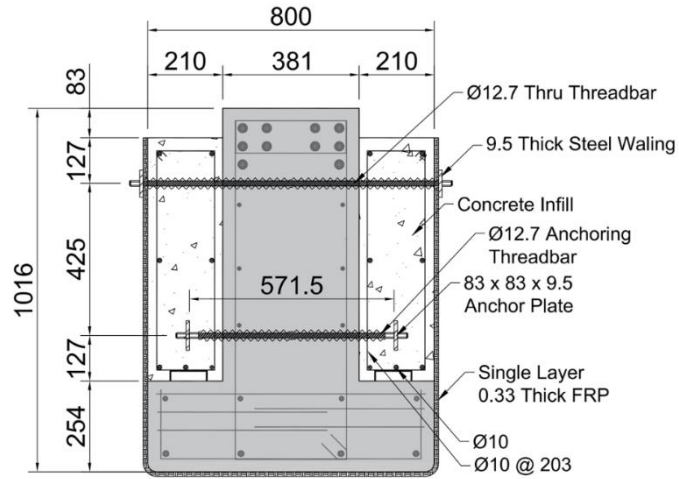
(a) Full-depth FRP solution
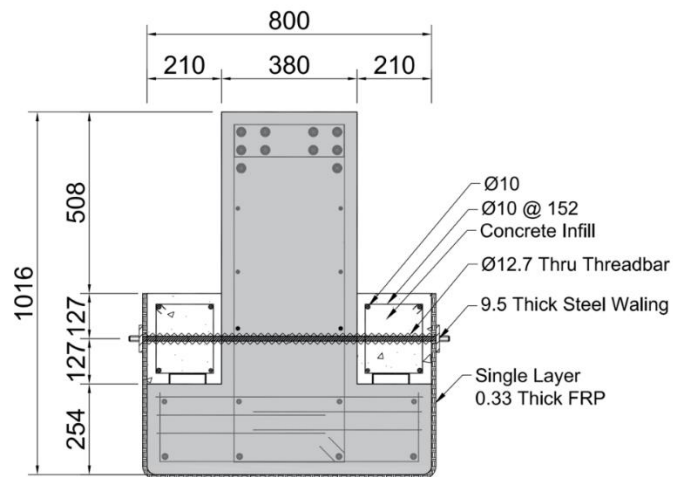
(b) Partial-depth FRP solution

Figure 6-6. Cross-Section Details of FRP Retrofit Solutions Adopted for Test.
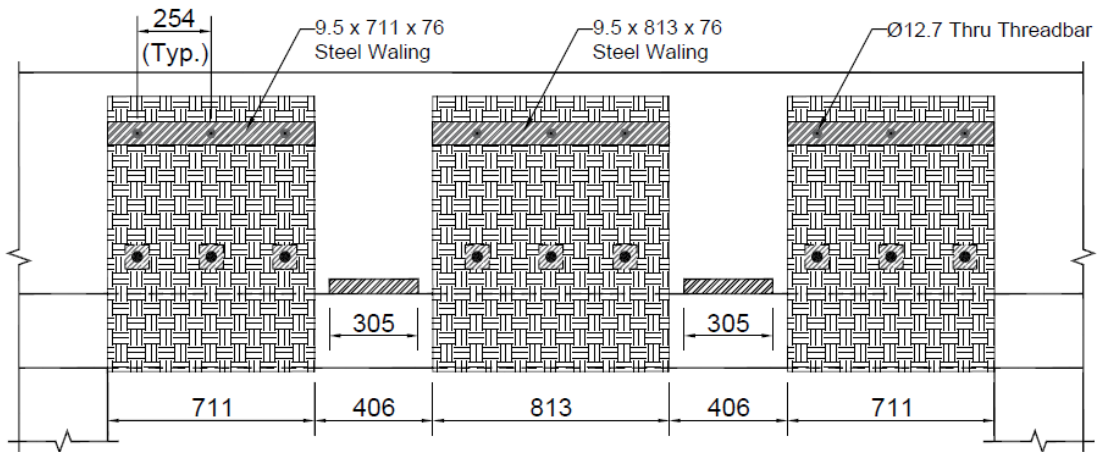
(a) Interior full-depth – T2I2
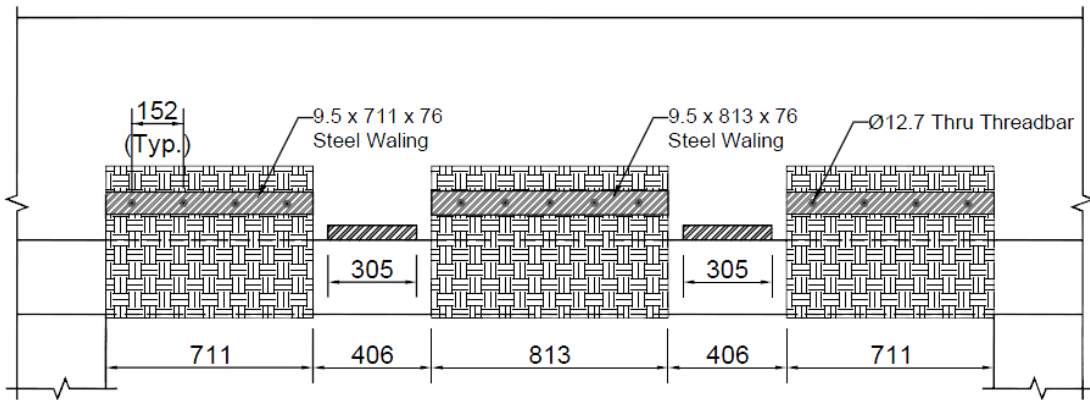
(b) Interior partial-depth – T6I1
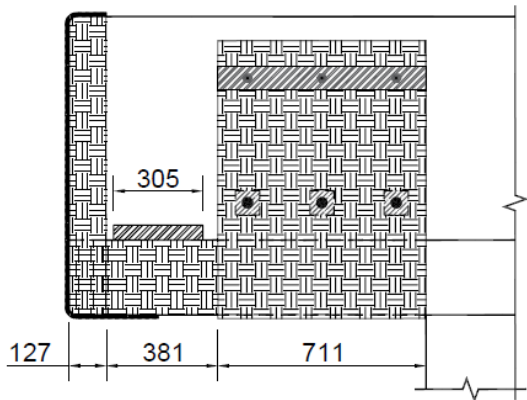
(c) Exterior full-depth – T2W2
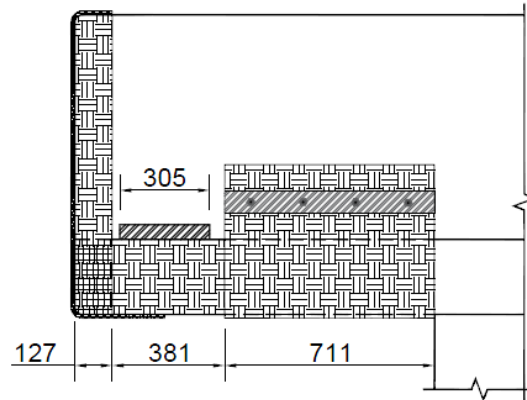
(d) Exterior partial-depth – T6W1

Figure 6-7. Elevation of FRP Retrofit Solutions Adopted for Test.

184

For interior regions, concrete infills were cast between the loading area and the support columns to transform the inverted-T cross-section to a rectangular cross-section. FRP sheets were used to wrap the transformed section. The steel walings were used to provide end-anchorage to the FRP sheets. For the full-depth solution, anchoring threadbars were used at the lower portion of the section to connect the concrete infill to the specimen.

For exterior regions, concrete infills were cast on the column side of the loading area similar to the interior application, while different wrapping schemes were adopted at the end region. Figure 6-8(a) illustrates the exterior FRP application for partial-depth solution. Part 1 is a U-shaped FRP sheet attached to the transformed section at the column side of the loading area. Part 2 is a 127 mm wide FRP strip applied around the inverted-T section at the end of the specimen, with a splice of 381 mm at the top of the web. Part 3 and 4 are U-shaped FRP sheets applied on the end face of the specimen. Part 3 is a vertical strip applied to cover the web. It has a 127 mm extension at the top and a 254 mm extension at the bottom. Part 4 is a strip applied in transverse direction to cover the bottom flange of the specimen. Part 4 extends 457 mm along the sides of the ledge, providing no overlap with Part 1. The wrapping scheme for the full-depth exterior solution is similar to the partial-depth solution with the difference being the length of Part 4 and the use of bandage strip. A longer development length is used for Part 4 of the full-depth exterior solution. An additional 203 mm wide bandage strip passes below the ledge to provide end-anchorage for the bottom of Part 3 by overlapping the tip of Part 3 by 102 mm. For full-depth exterior solution[a], shown in Figure 6-8(b), the bandage strip terminates at the top edge of the ledge, is providing a *moderate end anchorage*. For full-depth exterior

185

solution[b], shown in Figure 6-8(c), the bandage strip extends to the center of the bearing pad on top of the ledge, is providing a *strong end anchorage*. For all the exterior applications, the FRP strips were applied following the part number and the bandage strips were applied at the last.

Figure 6-9 shows the photos of FRP retrofit installed on the specimen. The infill concretes were constructed using the same concrete as the test specimen. Minimum reinforcements were provided for the infill concrete block. The threadbars (1/2 in. [12.7 mm] diameter) were placed in position before casting the infill concrete. The pre-surface treatments for the FRP sheets were performed three days after the infill concrete was cast. The bottom corners of the specimen were rounded with a minimum curvature of 1.5 in. (38 mm) to prevent sharp-corner-induced premature failure of the FRP sheets. Any coatings, laitance, and all miscellaneous surface contaminates were removed. The surface then smoothed with 80 grit sandpaper to meet the surface profile recommendation given by the manufacture. Debris was removed with a vacuum and pressurized air.

MasterBrace unidirectional carbon fiber composite system – MasterBrace FIB 600/50 CFS – was used for the FRP solutions. Table 6-4 lists the properties of the composite system provided by the supplier. The FRP sheets were delivered in 35 in. (890 mm) rolls with two-component epoxy resin that were mixed and applied to the fabrics to form the composite system. The surface was pre-treated using epoxy primer and paste following the guidelines provided by the supplier. The epoxy resin was applied to the concrete face to a wet film thickness of 0.46 mm to 0.56 mm and the FRP sheets were

attached subsequently. The second layer of epoxy encapsulation resin was then applied

over the fabric to a wet film thickness of 0.46 mm to 0.56 mm. The steel waling plates

were installed on the specimen after the FRP application. The epoxy encapsulation resin

was applied to the surface of the steel waling plate prior to the installation. The steel waling

plates were positioned and tightened to avoid damaging the fabric but to ensure uniform

contact was achieved. Tests were conducted a minimum of 14 days after concrete

placement and 24 hours after FRP installation.

| (a) Partial-depth | (b) Full-depth [a] | (c) Full-depth [b] |
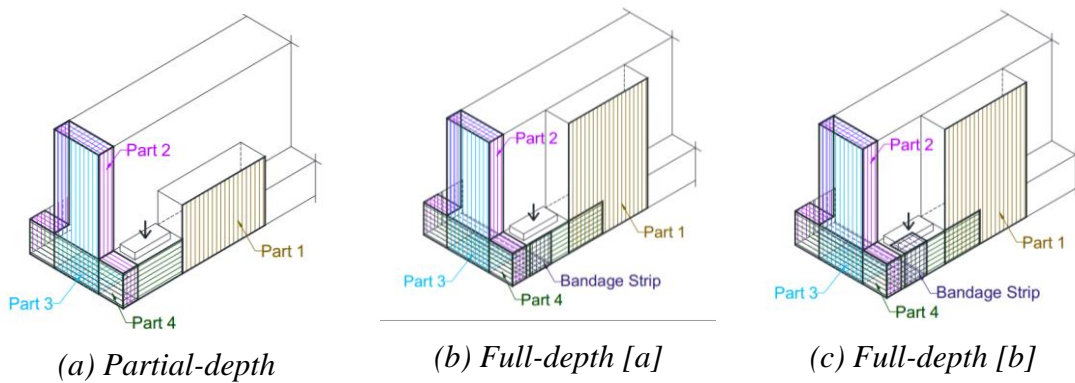
Figure 6-8. FRP Retrofit Scheme for Cut-off Region.

| (a) Interior | (b) Exterior |
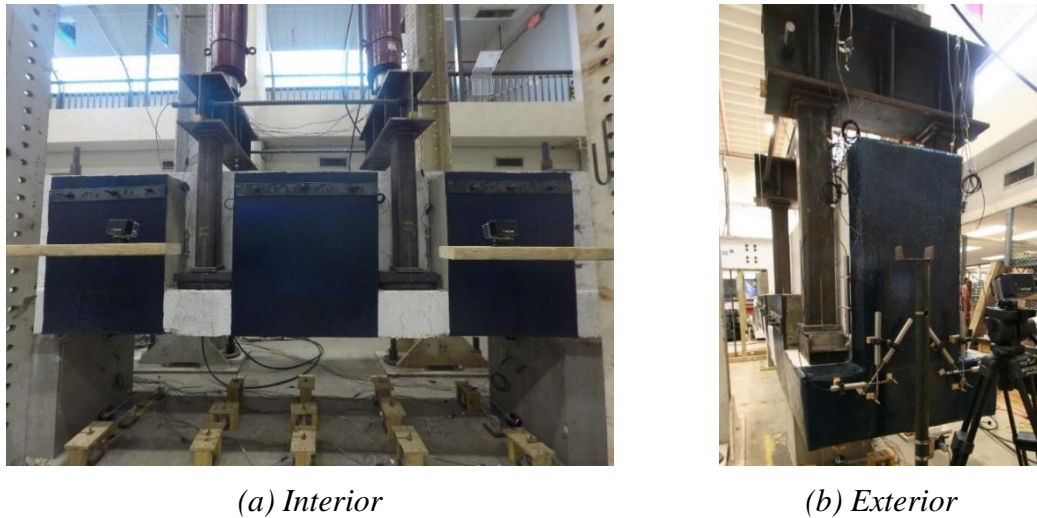
Figure 6-9. Test Specimen with FRP Retrofit Solutions.

**Table 6-4. Mechanical Properties of Fiber Reinforced Polymer
(BASF MasterBrace FIB 600/50 CFS).**

Dry Fiber Properties	
Nominal thickness	0.33 mm
Tensile strength	4950 MPa
Composite Laminate Properties (ASTM D-3039)	
Ultimate tensile strength (primary direction)	3800 MPa
Tensile modulus	227 GPa
Ultimate rupture strain	1.67%

6.4.3. **Test Set-up**

The schematic of the experimental test set-up with the instrument plan is shown in Figure 6-5(a). Exterior tests simulated one girder line by centering a loading frame 305 mm from the end of the specimen. An additional loading frame was placed over the adjacent column and connected using threadbar to provide stability. Interior tests simulated two girder lines by placing two loading frames spaced at 48 in. (1219 mm) and centered on the specimen. The two loading frames were connected by threadbars to ensure stability. Figure 6-5(c) shows the configuration of the loading frame. A 600 kips (2670 kN) hydraulic jack was used at each simulated girder line to apply loads to the loading frame that consist of an I-beam and hollow structural sections (HSS). The hydraulic jack was positioned at the center of the loading frame to equally transfer the load to either side of the ledge. The detail of bearing plates used in between the ledge and the bottom of the loading frame is also shown in Figure 6-5(c). Two layers of 2 in. (25 mm) thick steel plates piled up on C152 x 263 channel were placed upon a 2 in. (50 mm) thick rubber pad to enable a uniform distribution of the load. String potentiometers (string pots) were placed under the specimen to measure the vertical

displacement at eleven locations along the length of the bent cap. At each longitudinal location, three string pots were installed in transverse direction to measure the relative deflection of the ledges and stem.

The test specimens were loaded up to failure, with pauses at critical loading points to document cracks and condition of the specimen. The critical loading points were calculated based on nominal dead load, service limit state (SLS), and ultimate limit state (ULS) of the prototype in-service bent cap. For interior tests, the critical loading rates were, 26 kips (120 kN), 48 kips (220 kN), and 76 kips (340 kN). For exterior tests, it was 24 kips (100 kN), 45 kips (200 kN), and 68 kips (300 kN). The two hydraulic jacks for interior tests were increased equally until the failure of the specimen. Exterior tests increased each jack equally up to dead load, at which point the load over the column was held constant while the main jack increased up to failure.

6.5. Test Results

Figure 6-10 through Figure 6-13 present the photos of test regions with the documented damages at various load states. The damage formed before or at SLS marked in purple, in between SLS and ULS or at ULS marked in blue, and the damage formed after ULS are marked in red. The critical crack width at the corresponding load states is also specified. It should be noted that, the FRP strips concealed some part of the specimen may interfered the observation of the cracks. However, the critical regions – web-ledge interface and the web around the bearing pad – that having first cracking and most severe damages at the final state was clearly visible during the test hence enabled the damage observation.

Figure 6-14 summarizes typical damages on the FRP strips. The load-deflection response of the tests conducted on hanger-deficient and ledge-deficient specimens are plotted in Figure 6-15 and Figure 6-16, respectively. The deflection is measured at the bottom of the ledge at the center of the loading points. Maximum response among the loading points is plotted.

6.5.1. Experimental Results for Hanger-Deficient Specimen

Two hanger-deficient specimens were used to conduct the control and retrofit tests. Specimen T1 is the control specimen that performed the reference interior and exterior tests. Specimen T2 is used to conduct one interior and one exterior retrofit test with the full-depth FRP solution.

6.5.1.1. Interior Region Damage and Failure Mode

T1I1 is the interior reference test for hanger-deficient specimens. Cracks are shown in Figure 6-10(a), with cracks formed before SLS colored purple, between SLS and ULS colored blue, and after ULS colored red. The first cracking was observed at the web-ledge interface at SLS (48 kips [220 kN]). The cracks formed along the interface between the bearing pads, and diagonally propagated to the top of the ledge at the column side of the bearing pads (Crack 1). A nearly vertical crack extends from the interface was found on the web in between the bearing pads (Crack 2). It propagated toward the top of the bent cap as the load increased. Flexural cracks were found at 56 kips (249 kN) on the bottom and front face of the ledge under the bearing pads (Crack 3). Web shear cracks started

forming at 65 kips (289 kN) around the bearing pads and extended as the load increased (Crack 4). At ULS (76 kips [340 kN]), more cracks were observed on the web. These cracks, tending horizontally, were located around the neutral axis of the bent cap (Crack 5). It is a sign of the vertical separation of the lower part of the bent cap that believed to associate with the hanger failure mechanism. These horizontal web cracks are referred to as hanger cracks. The hanger cracks extended and widened significantly compared to the cracks on other part as the load went above ULS. The interface cracks further extended to the front face of the ledge (Crack 6). The web shear cracks turned horizontally and extended toward the center of the bent cap (Crack 7). More diagonal cracks formed on the web in between the bearing pad and column (Crack 8). Theses cracks were also turned horizontally as it propagated toward the center of the bent cap. At the measured ultimate load of 90 kips (400 kN), the web shear cracks connected horizontally formed another hanger crack close to the top of the bent cap (Crack 7). An additional diagonal crack, extends from the tip of the bearing pad at the column side, was found on the front face of the ledge (Crack 9). Most of the damages were condensed on the web. The hanger crack (Crack 5) with a maximum width of 2.5 mm, was the widest crack at the measured peak. The width of the diagonal shear crack behind the bearing pad (Crack 4) was 1.5 mm. The *hanger failure* was evident by the significant width increase of the hanger cracks as the specimen loaded further after the peak.

T2I2 is an interior repair test with the full-depth FRP solution. The observed cracks were shown in Figure 6-10(b) and (c) The test region was damaged to service level before the FRP installation to simulate the condition of the in-service bent caps. New crack

formation was not observed at SLS (48 kips [220 kN]) on retrofitted specimen. First cracking was observed at 74 kips (329 kN) at the web-ledge interface behind the bearing pads (Crack 1). At ULS (76 kips [340 kN]), additional interface cracks were found between the ledge and concrete block (Crack 2). Flexural cracks were observed on the bottom and front face of the ledge (Crack 3). Diagonal cracks start formed on the web at 85 kips (378 kN) around the bearing pads (Crack 4). Figure 6-10(b) shows the damage on the retrofitted specimen at the peak strength of the reference test (90 kips [400 kN]). Moderate damages were observed. The widest crack at this stage was the web shear crack around the bearing pad with a width of 0.5 mm. More cracks were found on the web (Crack 5). The web cracks showed a tendency to turn horizontally as the load increased. Separation of the FRP was first observed at 107 kips (476 kN) at the top corner of the concrete block at the bearing pad side. The separation started at the top corner and propagated vertically along the edge of the concrete block as the load increased, and was accompanied by vertical cracking on the FRP strips (Crack 6) approximately 65 mm from the edge of the concrete block at the bearing pad side. The specimen reached the first peak of 110 kips (489 kN) at which point the hanger cracks, horizontal web crack, formed on the web above the concrete blocks around at the center of the specimen. These hanger cracks are not shown on the photos because of the camera angle. The measured strength dropped to 105 kips (467 kN) after the formation of the hanger cracks. The strength of the specimen picked up again after the first peak and increased gradually. The cracks on the web widened significantly during this period. The specimen reached the second peak i.e. the measured ultimate load at 111 kips (494 kN) and failed in *flexure* as the concrete

crushing occurred on top of the web around the center of the specimen. The web shear

crack (Crack 4) was the widest crack at this stage with a width of 3.5 mm.
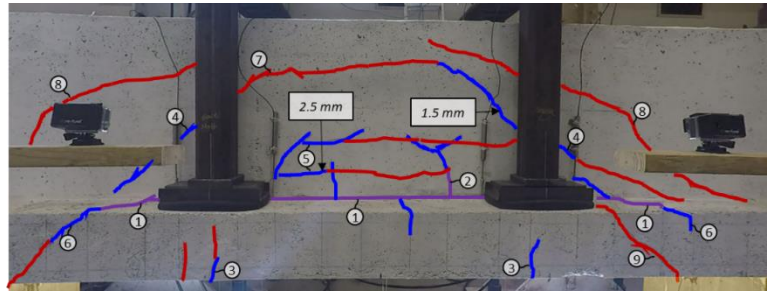
(a) T1I1 – interior hanger reference at measured peak 400 kN
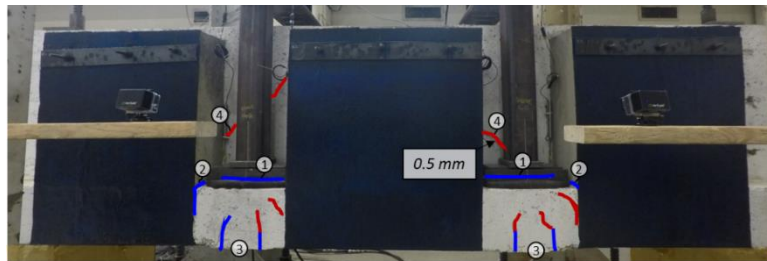
(b) T2I2 at measured peak of reference test 400 kN
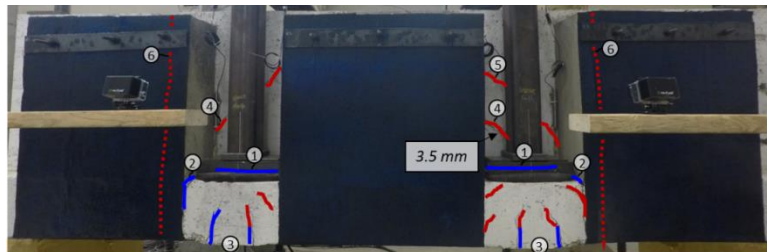
(c) T2I2 at measured peak 494 kN

Figure 6-10. Interior Tests on Hanger-Deficient Specimen.

6.5.1.2. Exterior Region Damage and Failure Mode

T1W1 is the exterior reference test for hanger-deficient specimens. The observed cracks

were shown in Figure 6-11(a). Crack initiation was observed at 36 kips (158 kN) before

SLS (45 kips [200 kN]) at the web-ledge interface behind the bearing pad (Crack 1). The

interface crack propagated to the end face and formed a nearly horizontal crack through the web around at the web-ledge interface (Crack 2). It is a sign of vertical separation of the bottom ledge from the web of the bent cap that associated to hanger failure mechanism. Similar to the horizontal web cracks in the interior tests, these cracks are named hanger crack. At SLS, the interface crack behind the bearing pad extended toward the column side a bit longer than the width of the bearing pad. The crack then turned diagonally to the top of the ledge and propagated to the free edge (Crack 3). It was further extended to the front face of the ledge as the load increased. An additional hanger crack was observed on the web at SLS (Crack 4). The second hanger crack was located near the neutral axis of the bent cap on the end face. It was extended diagonally along the side face of the web toward the column side as the load increased (Crack 5). At 57 kips (253 kN), third hanger crack formed on the end face above the second hanger crack (Crack 6). The third hanger crack extended along the side face of the web and propagated diagonally all the way to the ledge (Crack 7). The specimen reached a peak at 66 kips (294 kN) before ULS (68 kips [300 kN]). The *hanger failure* was evident by the extensively developed hanger cracks on the end face. The width of the first, second, and third hanger cracks on the end face were 15 mm, 10 mm, and 3 mm at the measured ultimate load, respectively. The width of the extensions of these cracks on the web were 12 mm, 8 mm, and 3 mm, respectively.

**T2W2** is an exterior repair test with the full-depth FRP solution. The observed cracks were shown in Figure 6-11(b) and (c). The end wrapping scheme for T2W2 is presented in Figure 6-8(c). The test region was loaded to service level before the FRP installation to simulate the condition of the in-service structure. New crack formation was

not observed at SLS (45 kips [200 kN]). The first crack, Crack 1, was a diagonal crack formed on the web at 248 kN (58 kips). The crack was formed around the neutral axis of the bent cap close to the end face. It is likely an extension of the hanger crack on the end face which is not visible due to the FRP strips. This crack was the only visible damage at the peak strength of the reference test (66 kips [294 kN]). The width of the crack at this stage was 0.5 mm. At ULS (68 kips [300 kN]), interface cracks were observed on the ledge (Crack 2). Additional diagonal crack was found on the web close to the end face (Crack 3). The crack, formed above Crack 1, is likely an extension of another hanger crack on the end face. Horizontal cracks on the flange FRP, Crack 4, on the end face start appear at 349 kN (78 kips). At the measured ultimate load of 92 kips (409 kN), the edge of the bandage strip that covers the bottom of Part 3 strip showed a de-bonding (Figure 6-14(b)). The de-bonding of FRP resulted a slight drop of measured strength. A separation of the FRP strip approximately 55 mm from the edge was also observed at the top corner of the concrete block at the bearing pad side, induced a vertical cracking on the FRP strip (Crack 5). The separation propagated downward a bit along the edge of the concrete block but maintained above the steel wailing at the measured peak. Additional vertical cracking was observed on the lower part of the FRP on the concrete block (Crack 6). The specimen sustained a steady load resistance of 90 kips (400 kN) after the measured peak load. The measured strength dropped to 80 kips (356 kN) as the de-bonding of the bottom tip of Part 3 intensified. Delamination of the FRP on the concrete block was also observed (Figure 6-14(e)). The load resistance stabled again after the drop. The FRP delamination on the concrete block worsened significantly during this stage. The specimen lost load

resistance at the final state as the *FRP delamination and rupture* took place on the concrete block. Nearly half width of the FRP strips on the concrete block experienced delamination and rupture at the final state.
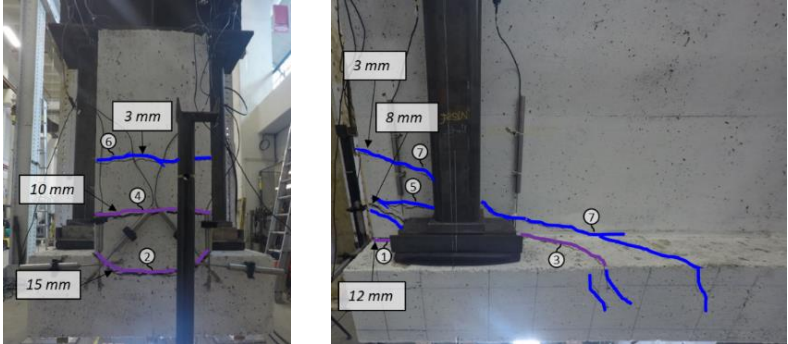
(a) T1W1 – exterior hanger reference at measured peak 294 kN
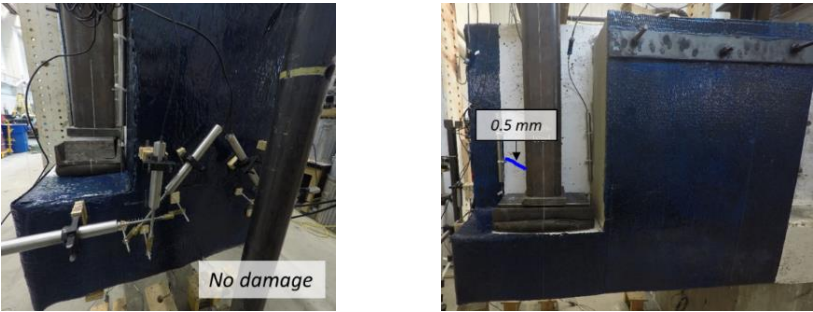
(b) T2W2 at measured peak of reference test 294 kN
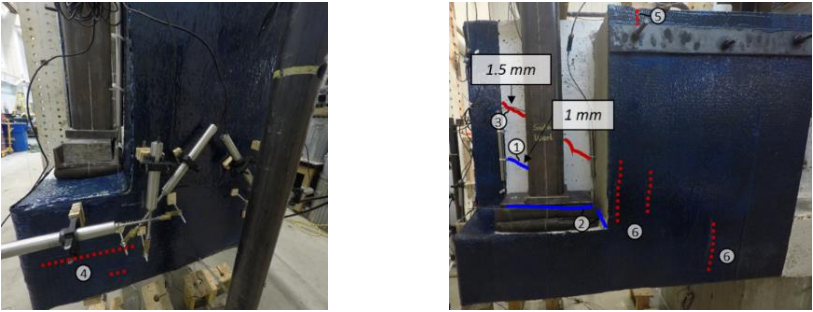
(c) T2W2 at measured peak 409 kN

Figure 6-11. Exterior Tests on Hanger-Deficient Specimen.

6.5.2. **Experimental Results for Ledge-Deficient Specimen**

Two ledge-deficient specimens, Specimen T5 and T6, were used to conduct the control and retrofit tests. Specimen T5 was the control specimen to provide benchmark comparison. Two reference tests were conducted on the interior and the exterior region of Specimen T5. Specimen T6 was used to perform the retrofit tests. One interior and two exterior retrofit tests were conducted on Specimen T6.

### 6.5.2.1. Interior Region Damage and Failure Mode

T5I1 is the interior reference test for the ledge-deficient specimens. The observed cracks were shown in Figure 6-12(a). The initial crack was observed at SLS (48 kips [220 kN]) at the web-ledge interface behind the bearing pads (Crack 1). It propagated to the top of the ledge as the load increased (Crack 2). A nearly vertical shear crack was found on the web in between the bearing pads (Crack 3). The crack extended vertically toward the top of the bent cap as the load increased. At ULS (76 kips [340 kN]), the interface cracks were further propagated to the front face of the ledge (Crack 4). Diagonal shear cracks formed on the web between the bearing pads and the support columns (Crack 5). A horizontal crack (hanger crack) formed on the web approximately at the neutral axis of the bent cap between the two bearing pads (Crack 6). Flexural cracks were found on the bottom and front of the ledge under the bearing pads (Crack 7). More diagonal cracks formed on the front face of the ledge near the bearing pads as the load increased (Crack 8). The specimen reached the measured peak at 85 kips (378 kN). The interface crack (Crack 1) was appearing to be the widest crack at the measured ultimate load with a width of 3.5 mm.

The width of the hanger crack (Crack 6) was 0.4 mm. The specimen was further loaded after the peak and the *ledge failure* becomes clear as the damages on the ledge intensified.

T6I1 is the interior retrofit test with partial-depth FRP solution designed to address the ledge and punching deficiencies. The observed cracks were shown in Figure 6-12(b) and (c). The first cracks were found at SLS (48 kips [220 kN]) at the web-ledge interface behind the bearing pads (Crack 1). Diagonal shear cracks formed on the web (Crack 2) as the load close to the ULS (76 kips [340 kN]). At ULS, flexural cracks were found on the bottom and front face of the ledge under the bearing pads (Crack 3). A diagonal crack was observed on the web above the concrete block (Crack 4). More cracks formed on the front face of the ledge under the bearing pads as the load increased (Crack 5). A nearly horizontal crack, Crack 6, was observed on the web at 81 kips (360 kN). It is a hanger crack formed above the concrete block. The crack turned vertically and propagated toward the top of the bent cap as the load increased. Only moderate cracking was observed at the measured peak load of the control specimen (85 kips [378 kN]). The width of the hanger crack (Crack 6) was 0.5 mm at this stage. End separation of the FRP sheets were first observed approximately 40 mm from the edge on the concrete blocks at 87 kips (390 kN). The separations typically started at the top corner of the concrete blocks at the bearing pad side. The separations then propagated vertically along the edges as the load increased, induced vertical cracking on the FRP strips (Crack 7). The separations only occurred at the regions near the edges of the concrete block at the bearing pad side. At 90 kips (400 kN), nearly horizontal cracks start formed on the web close to the top of the bent cap (Crack 8). These are another hanger cracks. The width of the hanger cracks widened

significantly then the other cracks as the load increased. The capacity after the formation of the hanger cracks reached a peak at 103 kips (458 kN). The hanger crack close to the top (Crack 8) was the widest crack at the measured peak with a width of 3.5 mm. Another hanger crack near the top of the concrete block (Crack 6) was 1.25 mm. The specimen maintained a steady load resistance after the peak and experienced a *hanger failure* ultimately as the width of the hanger cracks increased to more than 6 mm.

(a) T5I1 – interior ledge reference at measured peak 378 kN
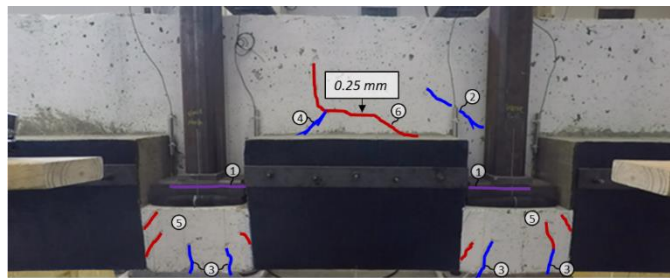
(b) T6I1 at measured peak of reference test 378 kN
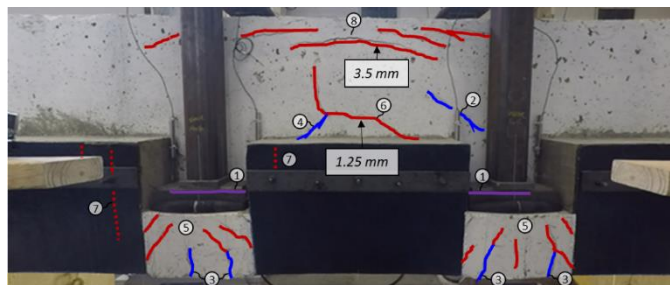
(c) T6I1 at measured peak 458 kN

Figure 6-12. Interior Tests on Ledge-Deficient Specimen.

6.5.2.2. Interior Region Damage and Failure Mode

T5E1 is the exterior reference test for ledge-deficient specimens. The observed cracks were shown in Figure 6-13(a). The first crack initiation was found at the web-ledge interface behind bearing pad (Crack 1) 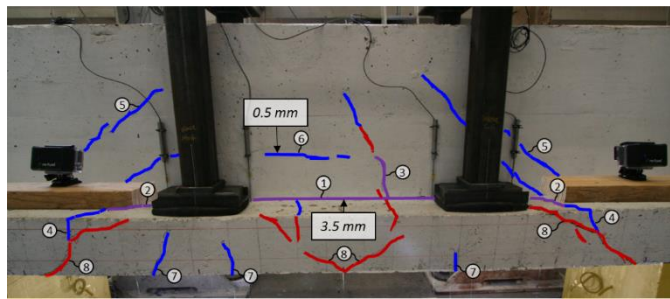at 41 kips (182 kN), before SLS (45 kips [200 kN]). The crack propagated to the end face at SLS, and extended diagonally at the re-entrant corner on the end face (Crack 2). It was also propagated to the column side (Crack 3). After extended to a distance a bit longer than the bearing pads, the cracks were turned diagonally to the top of the ledge and extended to the free edge as the load increased. At the end face, the diagonal cracks at the re-entrant corner further extended with a shallower angle. The cracks at the two sides of the bent cap connected horizontally at 54 kips (240 kN) formed an inverted parabola shape (Crack 4). More cracks formed on the lower ledge at the end face as the load increased (Crack 5). At the column side of the bearing pads, the interface cracks further extended to the side face of the ledge (Crack 6). More diagonal cracks formed on the front face of the ledge under the bearing pads (Crack 7). Shear cracks were also observed on the web (Crack 8). A hanger crack, horizontal crack through the web on the end face (Crack 9), formed on the end face near the neutral axis at 60 kips (270 kN). The hanger crack also extended to the side face of the web, and propagated diagonally to the ledge (Crack 10). The specimen reached the measure ultimate load at 66 kips (293 kN) before ULS (68 kips [300 kN]). Cracks around the bearing pads on the ledge were appeared to be sever than the other parts. The cracks around the interface (Crack 2), with a maximum width of 2.5 mm, were the widest crack at the measured ultimate load. The width of the hanger crack on the end face (Crack 9) was 0.75 mm, and

the width of the extension of this crack on the web (Crack 10) was 0.7 mm. The specimen showed a clear loss of load resistance after the measured ultimate load. The damages on the ledge around the bearing pads were mainly intensified after the peak while the hanger crack showed no notable difference. A *ledge failure* was observed at the final state.

T6W1 is an exterior retrofit test with the partial-depth FRP solution. The observed cracks were shown in Figure 6-13(b) and (c). The FRP wrapping scheme for the tested region is presented in Figure 6-8(a). No damage was found before ULS (68 kips [300 kN]). The measured peak strength of the reference test was 66 kips (293 kN). At ULS, interface cracks were observed on the ledge (Crack 1). End separation of FRP was also occurred approximately 30 mm from the edge at the top corner of the concrete block at the bearing pad side. The separation propagated vertically along the edge as the load increased, resulted a vertical cracking on the FRP strip (Crack 2). Web shear cracks, Crack 3, were observed at 90 kips (400 kN) above the concrete block. At 95 kips (425 kN), cracks formed on the web around the neutral axis of the bent cap close to the end face (Crack 4). These cracks, tending to spread horizontally, are likely the extension of the hanger cracks on the end face which are not visible due to the FRP cover. More cracks formed on the web near the end face (Crack 5). Flexural cracks were also found at the top of the specimen at the column side (Crack 6). The specimen reached the measured ultimate load of 102 kips (454 kN) as a de-bonding of FRP occurred at the bottom tip of the Part 3 strip that vertically covers the web on the end face (Figure 6-14(b)). The de-bonding resulted a sharp drop of the measured capacity to 90 kips (400 kN). The crack on the web (Crack 4) with 1 mm width was the widest crack at this stage. The specimen maintained a

steady resistance after the de-bonding. The width of the FRP end separation along the edge of the concrete block was 32 mm. The ledge deformed excessively after the measured peak. The specimen showed a clear loss of capacity as a concrete cover delamination occurred on the ledge under the bearing pad as shown in Figure 6-14(c). The specimen experienced a *ledge failure* at the final state.

T6E1 is an exterior retrofit test with the full-depth FRP solution. The observed cracks were shown in Figure 6-13(d) and (e). It was the last test conducted on Specimen T6 after the two ultimate testing - T6W1 and T6I1. The structural performance of the specimen may have been affected by the two previous ultimate testing. A different FRP wrapping scheme was adopted for T6E1 as shown in Figure 6-8(b). An extended Part 3 and a bandage strip was used at the end region. No damage was visible before ULS (68 kips [300 kN]). At ULS, interface cracks formed on the ledge (Crack 1). Web shear cracks were also observed on the web (Crack 2). A crack on the web around the neutral axis of the bent cap was observed at 88 kips (391 kN) near the end face of the specimen (Crack 3). It was likely an extension of the hanger crack formed on the end face. End separation of the FRP strip was observed at the top corner of the concrete block at the bearing pad side, induced a vertical crack on the FRP strip (Crack 4). The separation, with a width of 60 mm, propagated vertically as the load increased while did not go further below to the steel waling. Additional crack on the web close to the top of the bent cap, Crack 5, was observed at 108 kips (480 kN). It was likely an extension of another hanger crack on the end face. The capacity steady increased to the measured ultimate strength of 120 kips (534 kN). Horizontal cracks on the FRP were observed on the lower ledge at the

end face (Crack 6). The crack on the web (Crack 3) with a width of 1.25 mm was the widest crack at the measured peak. The load response maintained a short plateau after the peak and showed a sharp drop as the shear compression induced *delamination and rupture of the FRP* sheets took place around the edge of the concrete block (Figure 6-14(d)). Nearly one-third width of the FRP strips on the concrete block delaminated at the final state. The bottom tip of Part 3 strip showed no signs of de-boding till the final state.
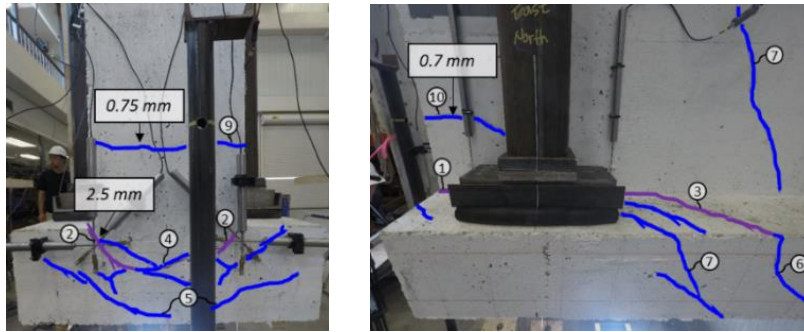
(a) T5E1 – exterior ledge reference at measured peak 293 kN

(b) T6W1 at measured peak of reference test 293 kN
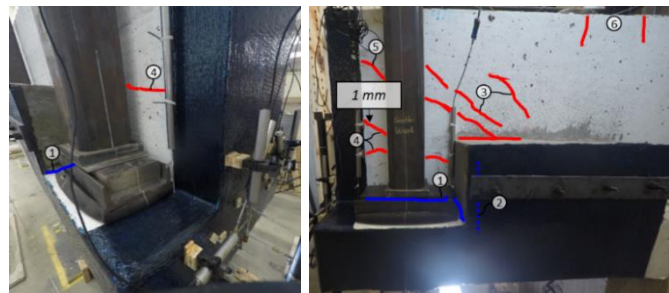
(c) T6W1 at measured peak 454 kN

(d) T6E1 at measured peak of reference test 293 kN
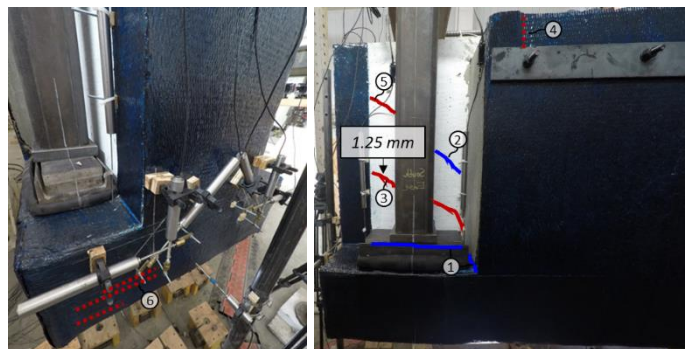
(e) T6E1 at measured peak 534 kN

Figure 6-13. Exterior Tests on Ledge-Deficient Specimen.
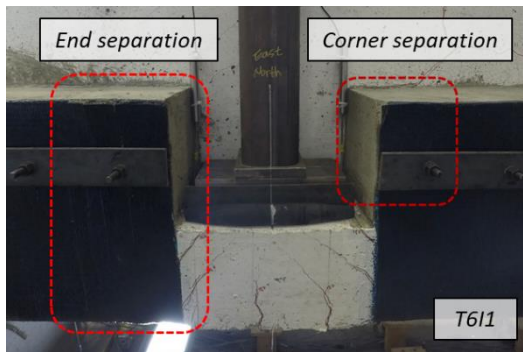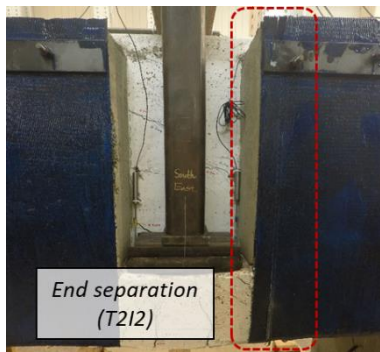
(a) Separation of FRP on concrete block for interior tests
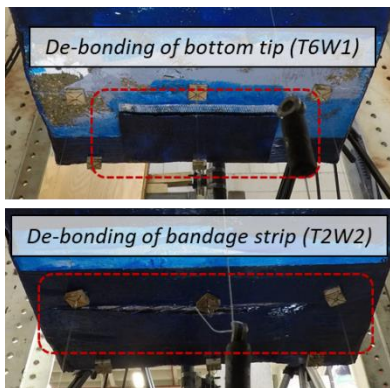
(b) De-bonding of FRP at bottom tip

(c) Concrete cover delamination
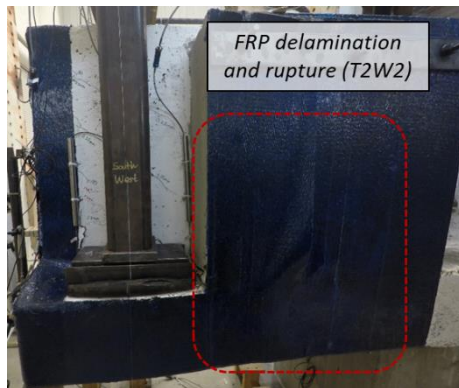
(d) FRP failure on exterior H.D. specimen
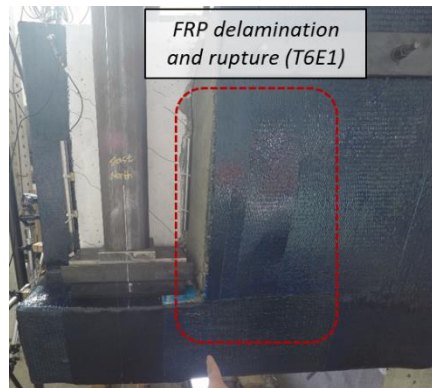
(e) FRP failure on exterior L.D. specimen

Figure 6-14. Typical Behavior of FRP Sheets.
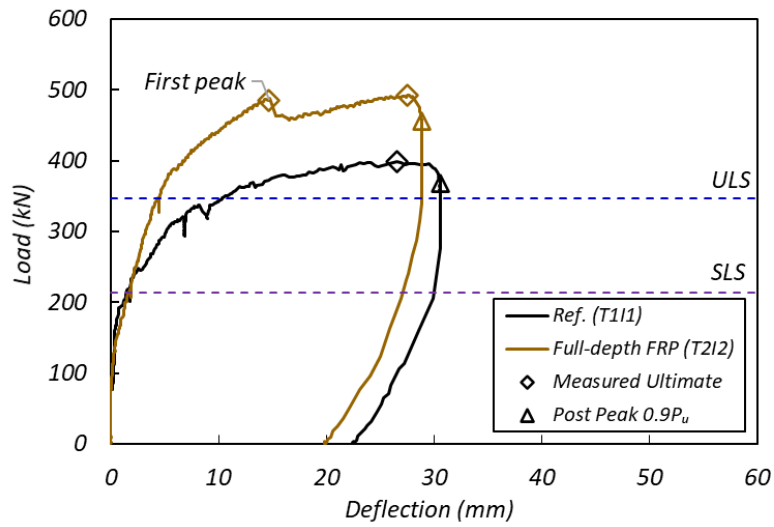
(a) Interior tests
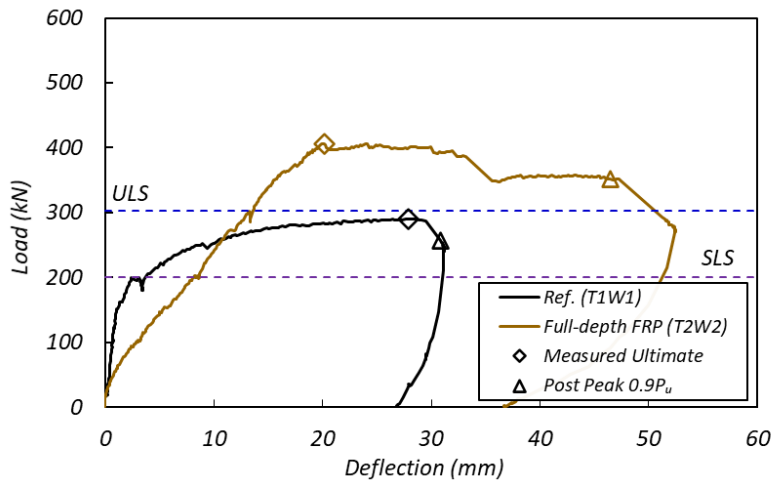
(b) Exterior tests

Figure 6-15. Load vs. Deflection Response of Tests on Hanger-Deficient Specimen.

206
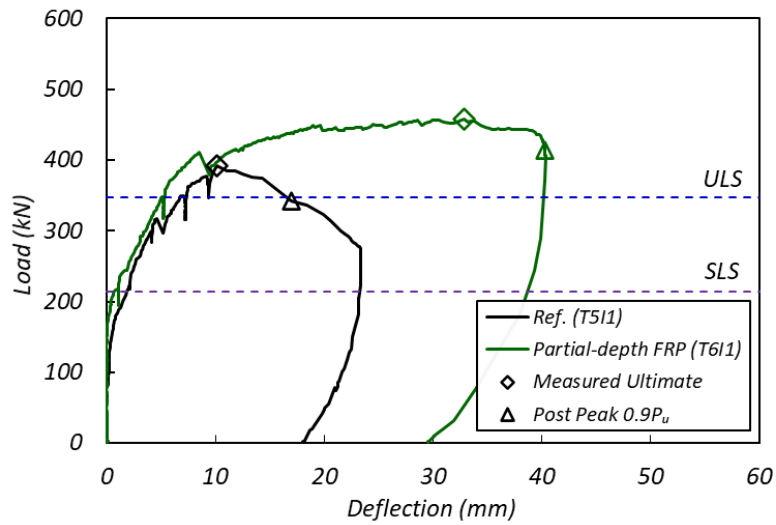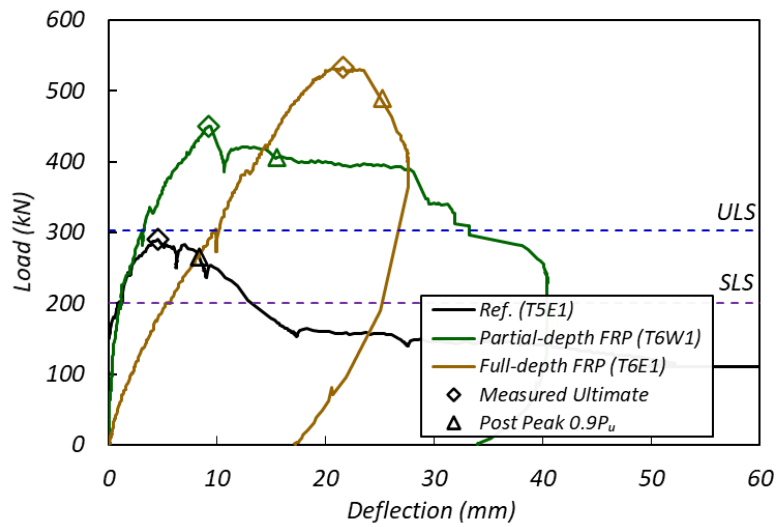
(a) Interior tests

(b) Exterior tests

Figure 6-16. Load vs. Deflection Response of Tests on Ledge-Deficient Specimen.

6.6. Behavior of FRP Retrofitted Specimen

The experimental results obtained from the tests are summarized in Table 6-5. The measured ultimate load attained from the tests and the relative strength of the retrofit tests compared to the reference tests are listed. The width of the cracks on the web observed from the reference and retrofit tests are compared. The crack on the web around at the neutral axis of the bent cap behind the bearing pad is chosen to be compared. It is the common the location where the reference and retrofit tests having cracks. The width of the crack in the table for the retrofit tests are measured at the peak strength of the corresponding reference tests. The deflection of the ledge at $0.9P_u$ after the peak as well as the observed failure modes of each test are also presented.

As listed in Table 6-5, the retrofit solutions improved the ultimate strength of the interior and exterior region of the specimen by 23% and 59% on average. Both interior and exterior region attained significant strength from the FRP retrofit. The exterior region, which has a lower strength due to the cut-off end, benefited more from the retrofit than did the interior region. While the retrofit solutions demonstrated the ability to increase the ultimate capacity, the gain of capacity alone may not be sufficient to assess the impact of the FRP retrofit solution. The performance of the FRP retrofit solutions are further evaluated in terms of serviceability, load-deflection response, and failure mode in the subsequent sections.

Table 6-5. Summary of Test Results.

Specimen ID[1]	Test ID	Retrofit Solution	Meas. Ult.[2] (kN)	Relative Strength[3]	Web Crack Width[4] (mm)	Ledge Deflection[5] (mm)	Failure Mode
H.D. Int.	T1I1	*Reference*	400	-	1.5	30.6	Hanger
	T2I2	Full-depth	498	1.24	0.5	28.8	Flexure
H.D. Ext.	T1W1	*Reference*	294	-	3	30.8	Hanger
	T2W2	Full-depth[a]	409	1.39	0.5	46.5	FRP[6]
L.D. Int.	T5I1	*Reference*	378	-	0.5	17.0	Ledge
	T6I1	Partial-depth	458	1.21	0.25	40.2	Hanger
L.D. Ext.	T5E1	*Reference*	293	-	0.7	8.3	Ledge
	T6W1	Partial-depth	454	1.55	No crack	15.5	Ledge
	T6E1	Full-depth[b]	534	1.82	No crack	25.2	FRP

1. L.D. = ledge-deficient and H.D. = hanger-deficient
2. Meas. Ult. = measured ultimate load
3. Relative Strength = measured ultimate load of retrofitted / reference
4. Cracks at same location on reference and retrofit test. Cracks on retrofit test measured at peak strength of corresponding reference test
5. Deflection at post peak 0.9 P_u
6. FRP delamination and rupture

6.6.1. Serviceability

The damage condition of the reference tests at the measured ultimate load are compared to the retrofit tests at the corresponding load state in Figure 6-10 through Figure 6-13. The width of cracks at the comparable locations are indicated. As can be seen from the figures, the retrofit solutions significantly alleviated the damage on the specimen when compared to the reference tests. The reference tests experienced cracking before or at SLS and subject to intensive damages at ULS. The exterior reference tests, for both ledge- and hanger-deficient specimens, experienced a failure before ULS. Whereas most of the retrofit tests showed a delayed crack initiation at or close to ULS and maintained an ascending load resistance at the measured ultimate load of the reference tests with only moderate- or un-damaged conditions. The crack width observed on the retrofit test was considerably lower than the cracks on the reference test at the same load state. Overall,

the FRP retrofit solutions demonstrated a solid ability for improving the serviceability of the bent cap specimen.

6.6.2. **Load-Deflection Response**

The load-deflection response of the tests on hanger- and ledge-deficient specimen is plotted in Figure 6-15 and Figure 6-16, respectively. The measured peak and the post peak at $0.9P_u$ is specified on the graphs.

The stiffness of the specimen, overall, is not affected by the FRP retrofits. The reference and retrofit tests showed a similar stiffness on the load-deflection response. The two retrofit tests conducted on the hanger-deficient specimen were a repair test. The specimen was loaded to the SLS before the supplication of the FRP retrofit to simulate the condition of in-service bent caps. The damaged specimen resulted a lower stiffness on the exterior retrofit test (T2W2) whereas the response of interior retrofit test (T2I2) was barely affected. The retrofit test on the exterior of the ledge-deficient specimen, T6E1, was the final test conducted on the specimen and was done after ultimate test on the interior and the other exterior end. The two ultimate testing conducted before T6E1 induced damage to the test specimen, resulting in the lower stiffness response of T6E1.

The use of the FRP retrofit on the interior region of the hanger-deficient specimen did not induce much change to the deflection response. The reference (T1I1) and retrofit test (T2I2) showed a similar deflection at the final (post peak of $0.9P_u$), whereas the retrofit test on the exterior of the hanger-deficient specimen (T2W2) experienced a higher

deflection then the reference test at the final. The deflection ratio between the retrofit and reference test is 1.5.

The ledge failure of the inverted-T involves failure by concrete sliding or separating from the web and is more a brittle than a hanger failure. The use of FRP retrofit on the ledge-deficient specimen led a notable change to the deflection response. The retrofit on the interior of the ledge-deficient specimen (T6I1) showed a significant increase of the deflection at the final with a deflection ratio of 2.4 compared to the reference test. The exterior with the FRP retrofit was also showed a substantially greater deflection compared to the reference test. The deflection ratio between the reference and the retrofitted specimen is 1.9 and 3.0 for the partial-depth (T6W1) and full-depth (T6E1) solution, respectively. The full-depth solution (T6E1), with a longer development length for the FRP strips, showed a higher deflection response compared to the partial-depth solution.

6.6.3. Failure Mode

The isolation of the local failure modes was successfully achieved on both hanger- and ledge-deficient specimens. The hanger and ledge failure on the corresponding specimens were clearly observed on both interior and exterior regions. These local failure modes of the specimens are expected to be captured by the applied retrofit solutions. A well-functioning retrofit solution should be able to eliminate the local failure modes of the inverted-T specimens to ensure the load capacity is not limited in one or more of those local failure mechanisms.

6.6.3.1. Hanger-Deficient Specimen

The use of *interior full-depth* solution on the hanger-deficient specimen (T2I2) to enhance the weak hanger mechanism showed a desirable result. The specimen experienced a drop of capacity after the first peak (Figure 6-15(a)) as a hanger crack formed on the web above the concrete blocks. The capacity then increased again and reached the measured ultimate strength after maintained a plateau. The retrofitted specimen failed due to a concrete crushing at the top-center of the specimen with a similar deflection, but a higher ultimate strength compares to the reference test. The FRP sheets at the final state, as shown in Figure 6-14(a), maintained a good shape only with moderate damages along the side edge of the concrete block. The specimen could not fully utilize the FRP retrofit. A specimen with a stronger beam capacity would gain more strength from the FRP retrofit system.

The *exterior full-depth solution* tested on the hanger-deficient specimen (T2W2) was also captured the hanger deficiency of the specimen. T2W2 experienced a FRP debonding at the bottom part of the specimen (Figure 6-14(b)). The initiation of de-bonding at the bottom tip of the web cover FRP strip (Part 3 in Figure 6-8) triggered a plateau on the load response after a slight drop in capacity. The load response had a sharp drop as the de-bonding intensified but still sustained a load resistance. Only the bottom part of Part 3 strip de-bonded during the test. It was not propagated to the web. The main reason caused the failure of the specimen was the FRP strips on the concrete block (Part 1 in Figure 6-8). The damage on the Part 1 strip intensified at the later stage and the FRP strip failed due to shear-compression at the final state. Half the width of the Part 1 strip delaminated and ruptured as shown in Figure 6-14(d).

6.6.3.2. Ledge-Deficient Specimen

The *interior partial-depth* solution applied on the ledge-deficient specimen (T6I1) effectively captured the ledge deficiencies. The specimen failed in hanger rather than the ledge. Figure 6-14(a) shows the condition of the FRP strips at the final state. The FRP strips close to the loading area experienced an end-separation along the edge of the concrete block. The separation only occurred in the narrow region close to the loading area. The rest of the FRP strips maintained a good shape. The specimen had a hanger failure before the FRP contribution was fully attained.

The *exterior partial-depth* solution applied on the ledge-deficient specimen (T6W1) failed in the ledge at the final state similar to the reference specimen. The partial-depth solution with a limited height of the concrete block is proposed to enhance the ledge and punching failure of the inverted-T bent cap. However, the exterior application of the partial-depth solution contains a FRP strip that covers the full height of the web on the end face (Part 3 Figure 6-8). This web covering FRP strip, acting as external hanger reinforcement, is able to transfer the flange load to the top tension chord. Therefore, the hanger capacity of the exterior region of the ledge-deficient specimen was also augmented by part of the exterior partial-depth solution. The conservatively designed hanger capacity adds up the partial contribution of the retrofit system resulted the hanger capacity of the retrofitted system stronger than the ledge capacity. Therefore, the ledge failure remained as the critical failure mode on the retrofitted specimen. Additionally, the FRP retrofit on the specimen was not able to develop a full strength due to the de-bonding and concrete

213

cover delamination (Figure 6-14(b) and (c)) caused by the limited end anchorage and development length. The anchoring effect on the FRP system will be discussed in the later section. The exterior partial-depth solution on the ledge-deficient specimen, though enhance the ultimate strength of the specimen by 55%, was not effectively eliminate the ledge failure mechanism of the specimen.

The *exterior full-depth* solution tested on the ledge-deficient specimen (T6E1) demonstrated a solid ability addressing the local mechanisms of the inverted-T bent cap. The test region attained maximum contribution from the FRP retrofit solution among all tests. The local failures were not observed during the test. The specimen failed due to the FRP delamination and rupture on the concrete block as shown in Figure 6-14(e). One-third width of the FRP strips on the concrete block delaminated and ruptured due to the shear compression force at the loading region.

6.6.3.3. Anchored FRP Sheets

The FRP sheets cover the infill concrete were anchored at the termination region by the steel walings. From the observation, the steel waling provides an effective anchorage to the FRP sheets as there is no pre-mature FRP debonding occurred on the concrete block during the tests. Figure 6-14(a) shows the condition of the FRP sheets applied on the concrete block at the final state. The FRP sheets close to the edge of the concrete block experienced end separations which were induced because of the pull-down tension force from the bottom flange. However, these separations occurred after the strength of the FRP sheets fully developed. The separation did not result in a drop in the capacity to the

214

specimen. The width of the end separation at the measured peak strength of the tests ranged from 30 mm to 70 mm. The width of the end separation of FRP sheets on the partial-depth solutions, with a shorter FRP development length, were typically wider than the FRP sheets on the full-depth solutions.

For the cut-off end region where a concrete infill could not be constructed due to the limited space, the FRP strips were applied on the specimen in several parts. The end wrapping schemes of the FRP strips adopted for the tests are shown in Figure 6-8. The difference is primarily in the use of the bandage strip to anchor the web FRP (Part 3) and the development length of the flange FRP (Part 4). The anchorage and development length of the FRP on the exterior region is essential where the bottom end of the specimen, as shown in Figure 6-17, is the critical region that subjects to excessive compressive load. Three different applications were used at the end region with no anchorage, moderate anchorage, and a strong anchorage provided to the FRP strips.

Require strong anchorage
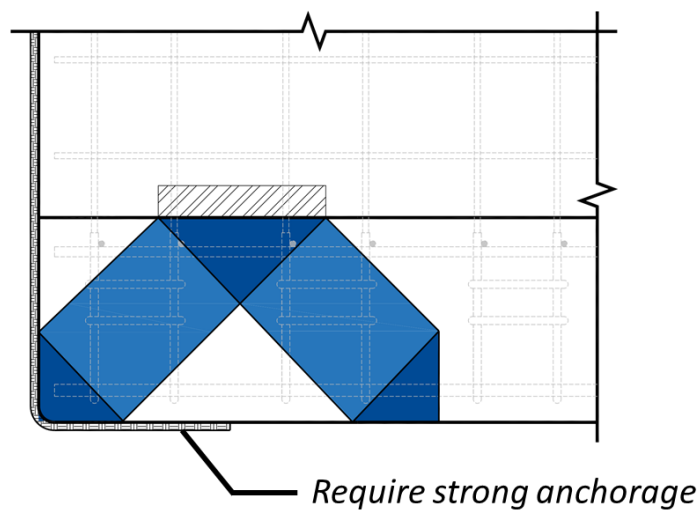
Figure 6-17. Compression-Strut at Free End.

215

The first case, shown in Figure 6-8(a), is providing the web FRP without an end-anchorage. The flange FRP for the first case also has limited development length. It was applied to one of the exterior regions on ledge-deficient specimen (T6W1). The web FRP without anchorage experienced pre-mature debonding during the test as shown in Figure 6-14(b). The debonding resulted in a sudden drop on the capacity of the specimen. The flange FRP with limited development length also caused a concrete cover delamination on the front face of the ledge at the later stage of the testing as shown in Figure 6-14(c). The first case, overall, with lack of end-anchorage and limited development length, was failed to fully utilize the strength of the FRP retrofit system.

The second case, shown in Figure 6-8(b), is utilizing a bandage strip to provide an end-anchorage to the bottom tip of the web FRP. The bandage strip, with the tip cut at the top edge of the ledge, is providing a moderate level anchorage. The flange FRP is also have an extended development length. The tip of the FRP strip is extended to half-width of the concrete block. The second case was used for the exterior region of the hanger-deficient specimen (T2W2). The solution with a moderate anchorage was also experienced a de-bonding of the web FRP at the bottom tip. However, the de-bonding of the web FRP for the second case had a lower impact on the capacity of the specimen. The specimen maintained a steady load resistance after a slight drop in the capacity as the de-bonding occurred. It was capable to gain sufficient strength from the FRP retrofit after the de-bonding. The specimen failed due to the FRP delamination and rupture on the side of the concrete block. It is a failure on FRP due to the shear compression mechanism on the beam instead of a pre-mature de-bonding. Figure 6-18 illustrates the load path of the exterior

216

region using a SAT model. The failure of the FRP took place approximately at the mid-width of the concrete block, which is the center of the compression strut. The FRP delaminated and ruptured because of the increased volume of the concrete in the direction of the compression strut and because of the sliding along the line of the shear crack.

The last case, shown in Figure 6-8(c), is providing a strong anchorage by extending the tip of the bandage strip to the top of the ledge and placing beneath the bearing pad. The flange FRP for the last case is also have an extended development length. It was tested on the exterior region of the ledge-deficient specimen (T6E1). The last case with a strong anchorage provided, was free to pre-mature de-bonding of the FRP until the final state. The specimen failed due to the FRP delamination and rupture similar to the second case after achieving sufficient strength from the FRP retrofit system.

FRP delamination
and rupture
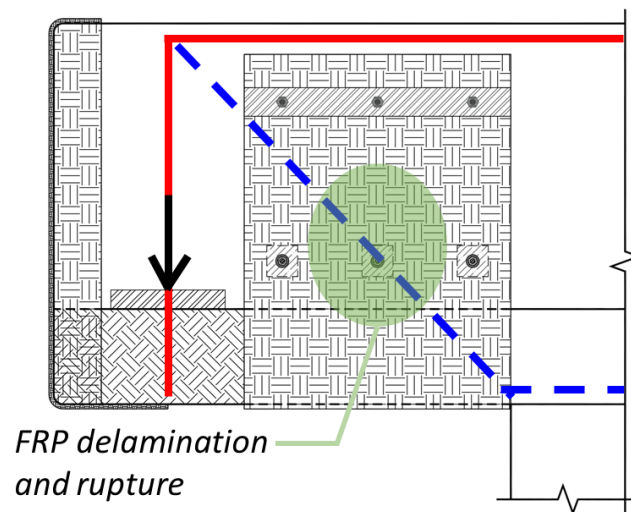
Figure 6-18. Load Path on Exterior Region.

6.7. Design Approach

For a bent cap with a capacity (C) requires a retrofit, the strength deficiency that need to be addressed by the retrofit can be identified based on the demand (D) as,

$$Deficiency = D/\phi - C \qquad (6\text{-}1)$$

where ϕ = strength reduction factor.

In other words, to retrofit the bent cap using FRP composites, the strength gain from the FRP should be higher than the deficiency. In general, the nominal strength of a reinforced concrete beam strengthened with FRP composites is given by,

$$V_n = V_c + V_s + V_f \qquad (6\text{-}2)$$

in which V_c = the contribution of the concrete; V_s = the contribution of the transverse steel; and V_f = the contribution of the FRP. The contribution of the concrete and the transverse steel, $V_c + V_s$, in this case is the sectional capacities of inverted-T bent cap. The contribution of the FRP, V_f, should be designed to fulfil the required deficiency.

6.7.1. Capacity of Inverted-T Bent Cap

To calculate the sectional capacities of the inverted-T bent caps, this study adopted the design methods specified in AASHTO LRFD 2020 with a rational modification proposed by Hurlebaus et al. (2018b). As specified in AASHTO LRFD 2020, the ledge of inverted-T bent cap requires a special consideration in addition to the beam shear and flexure strength that common to the conventional RC beams. The ledge of inverted-T bent cap, based on the code, must possess enough strength to resist (a) flexure, shear, and horizontal forces

(ledge); (b) punching shear at points of loading; (c) tension force in the supporting element (hanger); and (d) bearing force.

Table 6-6 lists the estimated capacities of the hanger- and ledge-deficient reference specimen, according to the code. The capacities are evaluated by five critical failure modes including beam shear and flexure. The bearing capacity of the inverted-T ledge is generally sufficient to resist applied load, therefore, is not accounted as a critical failure mode in this study. The test day material strengths are used for the calculation. The strength of the inverted-T bent cap governed by the failure mode that has the minimum strength. The estimated capacities based on the code are compared to the measured strength obtained from the tests. As can be seen from the relative ratio presented in the last column, the code estimations are giving conservative results compared to the measured strength. The code estimations for the interior and exterior hanger capacities are 61% and 57% higher than the measured strength. The exterior ledge capacity also has a conservative estimation with a ratio of 38%. For a more practical estimation, a rational modification recommended by Hurlebaus et al. (2018b) is adopted. The authors recommended a modified tributary width for the exterior ledge capacity estimation to account for all reinforcement involves in the failure mechanism. For the hanger capacity estimation, use of higher stress instead of the yield stress for the hanger reinforcement was recommended to account for the significant strain hardening occur in the hanger reinforcement during a hanger failure. The capacities calculated based on the adopted practical modification is given in Table 6-6. The adopted practical modification improves the accuracy of the capacity estimate by 28%, on average.

Table 6-6. Capacity Analysis for Reference Specimen.

Test ID	Method	Failure Mode (kN)					Control Mode	Est. Capacity (kN)	Meas. Ult. (kN)	Meas. / Est.
		L	P	H	BS	F				
H.D. Int. - T1I1	Code	627	369	249	365	440	H	249	400	1.61
	Modified	-	-	311	-	-		311		1.28
H.D. Ext. - T1W1	Code	405	298	187	347	1090	H	187	294	1.57
	Modified	516	-	236	-	-		236		1.25
L.D. Int. - T5I1	Code	329	374	391	587	445	L	329	378	1.15
	Modified	-	-	431	-	-		329		1.15
L.D. Ext.-T5E1	Code	214	302	365	560	1090	L	214	294	1.38
	Modified	271	-	405	-	-		271		1.08

Note: L= ledge, P=punching, H=hanger, BS=beam shear, and F=flexure

6.7.2. **Strength of FRP Composites**

The strength of the FRP composite, according to ACI 440.2R (ACI Committee 440), is given by,

$$V_f = \frac{A_{fv}f_{fe}(\sin\alpha + \cos\alpha)d_{fv}}{s_f} \tag{6-3}$$

where, f_{fe} = effective tensile stress of FRP strip; d_{fv} = effective depth of FRP strip; α = inclination angle of FRP strip; s_f = spacing of FRP strip; and A_{fv} = area of FRP shear reinforcement within the spacing s_f. The area of FRP shear reinforcement A_{fv} is given by:

$$A_{fv} = 2nt_f w_f \tag{6-4}$$

where n = number of FRP layers per strip; t_f = thickness of FRP layer; and w_f = width of FRP strip. By substituting Equation (6-4) into (6-3), the expression of V_f will have the term w_f/s_f which represents the ratio of the width of FRP strip to its spacing. For a case

220

of continuous strip, the ratio has a value of 1. The tensile stress f_{fe} of the FRP composites at nominal strength is obtained by multiplying the elastic modulus of the FRP by the effective strain as follows:

$$f_{fe} = \varepsilon_{fe} E_f \qquad (6\text{-}5)$$

where E_f = elastic modulus of FRP; and ε_{fe} = effective strain of FRP. The effective strain ε_{fe}, defined as the maximum strain that can be achieved in the FRP system at nominal strength, is the essential parameter to determine the strength contribution of the FRP composites. ACI 440.2R recommends an upper limit value of 0.004 for FRP effective strain for fully wrapped sections or properly anchored FRP strips. Otherwise a bond-reduction coefficient should be considered as follow:

$$\varepsilon_{fe} = k_v \varepsilon_{fu} \leq 0.004 \qquad (6\text{-}6)$$

where ε_{fu} = ultimate strain of FRP strip and k_v = bond-reduction coefficient. The bond-reduction coefficient k_v is a function of concrete strength, FRP stiffness, and FRP wrapping scheme.

The FRP strips used in this study were anchored at the termination region by the steel walings which demonstrated a solid ability to anchoring the FRP composites. Thereby, the effective strain of the U-wrap FRP composite is taken as 0.004 to estimate the strength contribution. For the case of FRP composite on exterior region with no anchorage and moderate anchorage, a reduced effective strain as described in the ACI 440.2R is used.

6.7.3. **Infill Concrete and Steel Waling**

Infill concrete is cast on the ledge to transform the cross-section from inverted-T to rectangular shape. Concrete with same properties as the bent cap is used. As the infill concrete is not loaded with significant force, minimum reinforcement based on ACI 318-14 is provided. The reinforcements are arranged to avoid the steel wailings. High-strength threadbars (Grad B7) are used as the waiilngs. Threadbars are provided to resist required shear demand. The design shear strength of the threadbars is taken as 60% of the tensile strength. Steel plates positioned by the threadbars are attached at the surface of FRP composites. The size of the steel plate is determined to ensure sufficient bond strength can be developed in between the waling and FRP composites. The thickness of the steel plate, t, is designed based on the bearing strength at the holes as specified in AISC specification,

$$t \geq \frac{V_u}{\phi 1.5 L_c F_u} \tag{6-7}$$

where V_u = shear demand, ϕ = load resistance factor (0.75), L_c = clear distance in direction of force between edge of hole and edge of steel plate and F_u = tensile strength of steel plate.

6.7.4. **Comparison of Predicted Strength with Test Results**

The predicted strength of the retrofitted specimen is compared to the measured strength obtained from the tests in Table 6-7. The estimated failure mode is also verified by the observation from the test. The capacities of the bent cap for each failure modes are

specified. The strength contribution from the FRP is added to corresponding failure modes to get the controlling capacities of the retrofitted specimen.

Table 6-7. Capacity Analysis for Retrofitted Specimen.

Test ID	Retrofit Solution	Strength	Failure Mode (kN)					Control Mode	Est. Capacity (kN)	Observed Failure	Meas. Ult. Load (kN)	Est./Meas.
			L	P	H	BS	F					
H.D. Int. - T2I2	Full-Depth	Bent Cap	623	347	311	356	440	Flexure	440	Flexure	498	1.13
		FRP	227	227	227	454	-					
		Total	850	574	538	810	*440*					
H.D. Ext. - T2W2	Full-Depth [a]	Bent Cap	512	285	236	338	1081	Hanger	383	FRP	409	1.07
		FRP	147	147	147	431	-					
		Total	658	431	*383*	770	1081					
L.D. Int. - T6I1	Partial-Depth	Bent Cap	325	356	427	578	436	Hanger	427	Hanger	458	1.07
		FRP	227	227	-	-	-					
		Total	552	583	*427*	578	436					
L.D. Ext. - T6W1	Partial-Depth	Bent Cap	271	289	400	552	1081	Ledge	418	Ledge	454	1.09
		FRP	147	147	40	-	-					
		Total	*418*	436	440	552	1081					
L.D. Ext. - T6E1	Full-Depth [b]	Bent Cap	271	289	400	552	1081	Ledge	436	FRP	534	1.22
		FRP	165	165	165	431	-					
		Total	*436*	454	565	983	1081					

Note: L= ledge, P=punching, H=hanger, BS=beam shear, and F=flexure

It is evident from the table that the predicted strength and failure mode correlate well with the experimental results. The estimated strengths correlate well with the experimental results with an average of 11.6% conservativeness. The predicted failure modes for the interior retrofit tests are exactly match with the experimental observation. Use of the FRP retrofit switched the failure modes of the specimen though the specimen failed in other part of the beam mechanism before attaining full strength form the FRP retrofit. The exterior retrofits with anchorage (T6E1 and T2W2) are fully utilized by the specimen as the FRP failure observed at the final state. For the exterior retrofit with no

anchorage (T6W1), the FRP on the specimen experienced a pre-mature de-bonding hence failed to eliminate the local failure mechanism of the bent cap. The predicted failure mode though is matches with the test observation.

6.8. Conclusion

FRP retrofit schemes developed to enhance the local failure mechanisms of inverted-T bent caps were experimentally investigated. Two cases of FRP retrofit solutions were developed to enhance corresponding local weakness based on the geometry of the in-service bent caps. The FRP solutions were tested on four half-scaled test specimens designed to emphasize different local failure mechanisms. The test results demonstrated that the developed FRP retrofit schemes effectively captured the local failure mechanisms and enhanced the capacity of inverted-T bent cap ledges. Based on the experimental investigation, the following conclusions are drawn:

1. The ledge and hanger local failure mechanisms were clearly isolated on the test specimens. The ledge failure appears to be brittle whereas the hanger failure exhibited a ductile mechanism. The capacities of the reference specimens estimated based on AASHTO LRFD 2020 are found to be conservative, especially for the hanger which was underestimated by over 50%.

2. The use of FRP retrofit solutions significantly improved the serviceability of the specimen by significantly delaying the crack initiation and alleviating the damage level at same load rate when compared to the reference specimen.

3. The partial-depth FRP solution developed to enhance the ledge and punching weakness effectively eliminated the local failure mechanisms and increased the load carrying capacity. The retrofit solution also remarkably increased the displacement ductility of the specimen with ledge deficiencies.

4. The full-depth FRP solution developed to enhance the hanger, ledge and punching capacities demonstrated solid ability to eliminate the local failure mechanisms and enhance the load carrying capacity for both ledge- and hanger-deficient specimens. The strength gain from the full-depth solution is higher than the partial-depth solution.

5. The performance of FPR retrofit scheme on the exterior region (cut-off end) greatly impacted by the provided anchorage and the development length of FRP strip. The exterior FRP scheme with end-anchorage and longer development length eliminated the local failure mechanism of the specimen while the case without anchorage subject to pre-mature de-bonding and failed to capture the local weakness. The strength gain from the exterior FRP retrofit scheme was proportional to the provided anchorage and the development length.

6. Design recommendations for the FRP retrofits were provided. The strength of FRP retrofit was recommended to estimate based on the ACI 440.2R procedure which shows a good agreement with the test results.

7. SUMMARY AND CONCLUSIONS

Inverted-T bent caps are widely used to overcome geometric constraints beneath the bridges. Traffic volume increases and design provisions have changed over the decades, and many in-service inverted-T bent caps are deficient for future needs. This study carried out an experimental and numerical investigation to develop strengthening solutions for existing inverted-T bent caps and to identify design aspects to improve structural performance.

Two in-service inverted-T bent caps in downtown Austin (IH 35) that were constructed in the late 1960s were evaluated under the current specification to identify critical weaknesses. An experimental investigation was carried out on half-scale inverted-T bent cap specimens that were designed to simulate the structural characteristics of in-service bent caps. The distinguished local behaviors of inverted-T bent caps were emphasized on the test specimens. Ultimate testing of these specimens was conducted to provide insight into the different local failure mechanisms of inverted-T bent caps at various load states. A nonlinear finite element model (FEM) was also developed to simulate the local behaviors of inverted-T bent caps. Correlative studies between the analytical analysis and the experimental observation were presented. Punching shear mechanisms of the inverted-T ledges were experimentally investigated with bearing pad size as the primary variable. CFRP strengthening techniques for the inverted-T bent caps with local weakness were developed and experimentally validated.

226

7.1. Conclusions

Two typical shaped in-service bent caps, double- and single-column bent caps were evaluated against the current design specification. The bent caps were part of the elevated highways of IH 35 in downtown Austin. The structures were constructed in late 1960s and designed in accordance with the 1965 AASHO standard specifications. To identify the current structural sufficiency, the capacities of the bent caps were analyzed based on the current standard specifications, 2020 AASHTO LRFD. The estimated capacities were compared to the demands of the 1964 AASHO and 2020 AASHTO LRFD. Based on the analysis results:

1. The in-service inverted-T bent caps have sufficient capacities to meet the strength limit demands of 1965 AASHO. However, it was inadequate to meet the service criteria that incorporated into the design provisions after the time of construction.

2. The bent caps were structurally deficient when evaluated against the demands of 2020 AASHTO LRFD in both service and strength limit. The analysis revealed that the bent caps have inadequate hanger, punching shear, and ledge flexure capacities with the most critical part being the hanger capacity.

A nonlinear finite element model (FEM) was developed to simulate the distinguished failure mechanisms of inverted-T bent caps. The test results from three groups of ultimate testing carried out by Hurlebaus et al. (2018b) were used to validate the FE models. Each group, with interior and exterior loading regions, was tested to isolate different local behaviors of inverted-T bent caps: ledge, hanger, and punching shear failure. Six reference

FE models were developed to simulate each of these tests. A numerical investigation was carried out using the FE models on four different alternative reinforcement designs. The design alternatives considered in the study were: use of diagonal ledge bar instead of horizontal ledge bar; concentrate ledge reinforcement around the loading region with combined used of diagonal and horizontal ledge bar and solely use of horizontal ledge bar and concentrate hanger reinforcement around the loading region. Total of 30 cases, including the reference models, were analyzed. Based on the analysis:

1. The models validated by the experimental results were able to capture the ledge, hanger, and punching shear failure mechanisms of inverted-T bent caps. The load response and the failure mode predicted by the models correlated well with the experimental observations.

2. Varying reinforcement layouts have a slight impact on the load response of inverted-T bent caps. The cracking and ultimate strength of the models were improved by the reinforcement variations but with limited impacts. The increase of the strength for the concentrated reinforcement cases was not proportional to the increased amount of the reinforcements.

3. The various reinforcement layouts demonstrated a significant impact on cracking control of the inverted-T bent cap sections. The concrete strain of the inverted-T bent cap at the web-ledge interface was substantially reduced by the different reinforcement layouts. The diagonal ledge bars were actively engaged in the load resistance mechanisms once provided to the section, thereby reducing the cracking strain of the section at both service and ultimate load state. Concentrating ledge or

228

hanger reinforcement around the loading region was found to be beneficial to the bent caps with ledge and hanger deficiencies, respectively. The combined use of diagonal and horizontal ledge bar demonstrated a better performance than the case solely using horizontal ledge bar. The diagonal bar with the legs across the corner at the web-ledge of the section was able to restrain both transverse and vertical strain. Whereas the horizontal ledge bar has limited ability affecting the vertical strain.

4. The use of a diagonal ledge bar was recommended as a design alternative to improve the serviceability of inverted-T bent caps.

The punching shear failure of the inverted-T bent ledge was experimentally investigated on two different test specimens. Two exterior and seven interior tests were conducted with different sizes of bearing pads. A nonlinear finite element model (FEM) was utilized to elaborate the experimental findings, and to numerically investigate the parameters that can affect punching shear performance.

1. The punching shear failure was evident from the truncated concrete cone formed underneath the bearing pads. The pattern of the failure plane was not affected by the size of the bearing pads. The signs of punching failures were generally notable at a later stage when the applied load is near the ultimate strength. The distress of the ledge comes shortly after the initiation of the concrete cone, describing the brittle nature of the punching shear failure.

2. The failure plane of the punching shear failure appeared to be larger than the code estimation. The concrete cones radiate from the tip of the bearing pads with an angle shallower than the code assumed 45-degree. The capacity based on the code equations is thereby conservative compared to the experimental results. A rational modification was proposed by incorporating the estimated crack angle of the concrete cones. The proposed modification improved the accuracy of the capacity estimation by 17%.

3. Experimental results combined with the FEM analysis demonstrated that use of a larger bearing pad could improve the serviceability and the ultimate punching shear capacity of the ledge. The eccentricity of the bearing pad, defined as the distance from the bearing pad to the face of the web, was found to be another factor impacting the punching shear capacity of the ledges. The capacity improved by reducing the eccentricity of the bearing pad.

FRP strengthening solutions for inverted-T bent caps were developed and experimentally validated on the tests specimens designed to have ledge and hanger local weakness. Two different FRP retrofit solutions were developed based on the geometry and purpose of strengthening. A full-depth FRP solution was developed to enhance the hanger, ledge, and punching shear capacity for the bent caps that have full accessibility under the decks. For the bent caps that have limited accessibility, a partial-depth FRP solution can be used. The partial-depth solution was aimed to enhance the ledge and punching capacity of the bent

caps. Nine individual tests consisted of four reference tests and five retrofit tests were conducted on four different test specimens. Based on the experimental results:

1. Ledge and hanger failure mechanisms were clearly isolated on the distinguished tests specimens. The ledge failure (separation of the ledge from the face of the web) was found to be brittle as it involves concrete failures. The hanger failure was found to be more ductile than the other local failures however was subject to excessive deformations at a lower load state. The code estimated ledge and hanger capacities were conservative compared to the experimental results. A rational modification proposed by Hurlebaus et al. (2018b) was recommended for more realistic capacity estimation.

2. The partial-depth solution was able to enhance the ledge and punching capacity of the bent caps while the full-depth solution was effectively captured all of the local failure mechanisms of inverted-T bent cap.

3. Use of FRP solutions significantly improved the serviceability of the specimens. The crack initiation was delayed by the FRP, and the damage was less severe than the damage in the reference specimen. The ultimate load-carrying was also substantially increased by the FRP retrofit. The FRP retrofits improved the deflection response of the ledge-deficient specimens while the hanger-deficient specimens were barely affected.

4. The performance of the FRP retrofits was significantly affected by the anchorage and the development length of the FRP sheets. The exterior region was more susceptible than the interior. The walings provided at the top of the FRP sheets to

provide end-anchorages demonstrated superior performance. The FRP sheets with walings were able to develop the full strength without pre-mature failures due to the de-bonding. Three different levels of anchorage were tested at the exterior region, demonstrating that the performance of the FRP sheets was proportional to the provided anchorage levels.

5. Design recommendations were provided for the developed FRP retrofit solutions. It was recommended to estimate the inverted-T bent cap capacities in accordance with AASHTO LRFD 2020 with the modified distribution proposed by Hurlebaus et al. (2018b). The estimated failure mode and ultimate strength of the specimens with FRP retrofits, calculated using ACI 440.2R recommendations, correlated well with the experimental observations.

7.2. Recommendations

The following recommendations were drawn from the study to extend the results of this research.

1. The current provision gives a very conservative estimation on the punching shear capacity of inverted-T bent cap ledges when compared to the experimental results. A rational modification was proposed to take into account the crack angle of the failure plane. Although the proposed modification improved the accuracy of the capacity estimation by 17%, the estimated values still have 30% conservativeness. This difference comes from the contribution of the reinforcements. The capacity estimation only considers the strength of concrete. The reinforcements, proven by

the FEM analysis, are impacting the punching shear capacity of the ledges. The accuracy of the capacity estimation would be improved more by taking into account the strength contribution from the reinforcements.

2. This study proposed a rational modification for the punching shear capacity estimation by including an estimated crack angle to the code provided equations. The estimation of the crack angle was adopted a model proposed by Kim and Mander (2000). The model was developed based on the conventional concrete beam-column element that supported at the end of the span. The ledge of inverted-T bent cap, however, is a longitudinal cantilever shelf continuously supported by the web in the manner of a fixed edge, hence having a distinctive characteristic. A modification to the crack angle estimation model to take into account the boundary conditions of inverted-T bent ledges is recommended for a more reasonable estimation.

3. The CFRP strengthening from the experimental results demonstrated a solid capability in improving the structural performance of inverted-T bent caps in various aspects. The performance of the CFRP retrofits was significantly affected by the provided anchorages. The walings used for the CFRP sheets on the transformed section showed superior performance in anchoring the CFRP sheets. The exterior retrofits were tested under limited anchorage because of the limited space at the end region. As a result, the exterior retrofits were subject to loss of resistance due to the de-bonding of CFRP sheets. Although the CFRP bandages that were used to provide anchorage to the exterior retrofit stabled the performance

of CFRP retrofits, it was also experienced a loss of resistance before the CFRP sheets developed their full strength. Therefore, further investigations on the CFRP retrofits for the exterior region with more effective anchorages are recommended. Use of mechanical and/or FRP anchors, extended development length of CFRP sheets etc. would improve the performance of exterior CFRP retrofits.

4. The nonlinear finite element model (FEM) developed in this study effectively captured the different local failure mechanisms of inverted-T bent caps. The model was calibrated by the prototype specimens that emphasized the different local failures and utilized to investigate the impact of reinforcement layouts on the structural performance of inverted-T bent caps. As an extension, the FEM can be further developed to simulate the bent cap specimens with retrofit solutions. The experimental program in this study provides valuable data for the inverted-T bent cap specimens retrofitted with various strengthening techniques including mechanical supplemental, CFRP composites, and external post-tensioning solutions. The retrofit solutions tested under the experimental program can be included in the FEM and calibrated by the experimental results. The FEM with retrofit solutions, once proven by the experimental results, will be an effective and powerful tool to provide insights to the specimens with various strengthening techniques. The FEM can also be re-generated to simulate other potential retrofit solutions to provide promising predictions on the structural performance of such systems without experimental testing.

REFERENCES

AASHO. (1965). "Standard Specifications for Highway Bridges," Ninth edition, American Association of State Highway Officials, Washington DC.

AASHTO. (2020). "LRFD Bridge Design Specifications," Seventh edition, American Association of State Highway and Transportation Officials, Washington DC.

ABAQUS. (2010). "ABAQUS Theory Manual," Providence, RI: ABAQUS.

ACI Committee 318. (2014). "Building Code Requirements for Structural Concrete and Commentary," American Concrete Institute, Farmington Hills, MI.

ACI Committee 364.2T. (2008). "Increasing Shear Capacity within Existing Reinforced Concrete Structures," American Concrete Institute, Farmington Hills, MI.

ACI Committee 440. (2008). "Guide for the Design and Construction of Externally Bonded FRP Systems for Strengthening Concrete Structures," American Concrete Institute, Farmington Hills, MI.

AISC (2010). "Steel Construction Manual," American Institute of Steel Construction, Chicago, IL.

ASTM. (2015). "ASTM C39/C39M, Standard Test Method for Compressive Strength of Cylindrical Concrete Specimens," West Conshohocken, PA: ASTM.

Basler, M., White, D., and Desroches, M. (2003) "Shear Strengthening with Bonded CFRP L shaped Plates," ACI International SP-215-23, pp. 373–384.

Breveglieri, M., Aprile, A., and Barros, J.A.O. (2015) "Embedded Through-Section Shear Strengthening Technique using Steel and CFRP Bars in RC Beams of Different Percentage of Existing Stirrups," Composite Structure, Vo. 126, pp. 101-113.

Bazant, Z.P., and Oh, B.H. (1983) "Crack Band Theory for Fracture of Concrete," Materials and Structures Vo. 16, pp. 155–177.

Chaallal, O., Mofidi, A., Benmokrane, B., and Neale, K. (2011). "Embedded Through-Section FRP Rod Method for Shear Strengthening of RC Beams: Performance and Comparison with Existing Techniques," Journal of Composites for Construction, Vo. 15, Issue 3, pp. 374–383.

Deifalla, A., and Ghobarah, A. (2010). "Strengthening RC T-beams Subjected to Combined Torsion and Shear Using FRP Fabrics: Experimental Study," Journal of Composite Construction, Vol. 14, Issue 3, pp. 301–311.

235

Deifalla, A., Awad, A., and Elgarhy, M. (2013). "Effectiveness of Externally Bonded CFRP Strips for Strengthening Flanged Beams Under Torsion: An Experimental Study," Engineering Structures, Vol. 56, pp. 2065-2075.

Deifalla, A., and Ghobarah, A. (2014). "Behavior and Analysis of Inverted T-shaped RC Beams under Shear and Torsion," Engineering Structures, Vol. 68, pp. 57-70.

De Lorenzis, L., and Nanni, A. (2001) "Shear Strength of Reinforced Concrete Beams with Near-Surface Mounted Fiber-Reinforced Polymer Rods," ACI Structural Journal, Vol. 98, No. 1, pp. 60-68.

Dias, S.J.E., V. Baincco, J.O.A., and Barros, G. Monti. (2007) "Low strength T-cross section RC beams shear-strengthened by NSM technique," FAELLA, C. [et al.], ed. – Materiali ed approcci innovativi per il progetto in zona sismica e la mitigazione della vulnerabilità delle strutture : atti del Workshop, Fisciano, Itália. [S.l.]: Polimetrica, ISBN 978-88-7699-065-6.

Dias, S.J.E., and J.O.A. Barros. (2008) "Shear Strengthening of T Cross Section Reinforced Concrete Beams by Near-Surface Mounted Technique," Journal of Composites for Construction, Vol. 12, Issue 3, pp. 300-311.

Dias, S.J.E., and J.O.A. Barros. (2010) "Performance of reinforced concrete T beams strengthened in shear with NSM CFRP laminates," Engineering Structures, Vol. 32, Issue 2, pp. 373-384.

Furlong, R.W., Ferguson, P.M., and Ma, J.S. (1971). "Shear and Anchorage Study of Reinforcement in Inverted T-beam Bent-Cap Girders," TxDOT Report#113-4, Center for Highway Research, The University of Texas at Austin, Austin, TX.

Furlong, R.W., and Mirza, S.A. (1974). "Strength and Serviceability of Inverted T-beam Bent-Caps Subject to Combined Flexure, Shear, and Torsion," TxDOT Report#153-1F, Center for Highway Research, University of Texas at Austin, Austin, TX.

Galal, K., and Sekar, M. (2008). "Rehabilitation of RC Inverted T Girders using Anchored CFRP Sheets," Composites: Part B, Vol. 39, Issue 4, pp. 604–617.

Galal, K., and Mofidi, A. (2010). "Shear Strengthening of RC T-beams Using Mechanically Anchored Unbonded Dry Carbon Fiber Sheets," Journal of Performance and Constructed Facilities, Vol. 24, Issue 1, pp. 31–39.

Garber, D.B., Varney, N.L, Gomez, E.F., and Bayrak, O. (2017). "Performance of Ledges in Inveretd-T Beams," ACI Structural Journal. 114(2), pp. 487-498.

Goebel, J.H., Johnson, B.A., and Higgins, C. (2012) "Strength and Durability of Nea-Surface Mounted CFRP Bars for Shear Strengthening Reinforced Concrete Bridge

Girders," SPR 712, Oregon Department of Transportation & FHWA, Oregon State University.

Hassan, T., Lucier, G., Rizkalla, S., Zia, P., and Klein, G. (2007). "Modeling of L-shaped, precast, prestressed concrete spandrels," PCI Journal. 52(2), pp. 62-76.

Higgins, C., Howell, D.A., Smith, M.T., and Senturk A.E. (2009) "Shear Repair Methods for Conventionally Reinforced Concrete Girders and Bent Caps," SPR 636, Oregon Department of Transportation & FHWA, Oregon State University.

Hillerborg, A., Modeer, M., and Petersson P-E. (1976). "Analysis of Crack Formation and Crack Growth in Concrete by Means of Fracture Mechanics and Finite Elements," Cement and Concrete Research. 6(6), pp. 773-782.

Howell, D.A., (2009) "Shear Repair Methods for Conventionally Reinforced Concrete Girders and Deep Beams," Doctor's Thesis, Oregon State University.

Hueste, M.B.D., Adil, M.S.U., Adman, M., and Keating, P.B. (2006). "Impact of LRFD Specifications on Design of Texas Bridges Volume 1: Parametric Study," Rep. No. FHWA/TX-07/0-4751-1 Vol. 1, Texas A&M Transportation Institute, The Texas A&M University System.

Hurlebaus, S., Mander, J.B, Birely, A.C., Terzioglu, T., Cui, J., and Park, Sh.H. (2018 a). "Strengthening of Existing Inverted-T Bent Caps – Volume 1: Preliminary Design," Rep. No. FHWA/TX-18/0-6893-R1-Vol1, Texas A&M Transportation Institute, The Texas A&M University System.

Hurlebaus, S., Mander, J.B., Birely, A.C., Terzioglu, T., Cui, J., and Park, S.H. (2018 b). "Strengthening of Existing Inverted-T Bent Caps—Volume 2: Experimental Test Program," Rep. No. FHWA/TX-18/0-6893-R1-Vol2, Texas A&M Transportation Institute, The Texas A&M University System.

Hurlebaus, S., Mander, J.B., Birely, A.C., Terzioglu, T., Cui, J., and Park, S.H. (2018 c). "Strengthening of Existing Inverted-T Bent Caps: Design Recommendations and Examples," Rep. No. FHWA/TX-18/0-6893-P1, Texas A&M Transportation Institute, The Texas A&M University System.

Karthik, M.M., and Mander, J.B. (2011). "Stress-Block Parameters for Unconfined and Confined Concrete Based on Unified Stress-Strain Model," Journal of Structural Engineering. 137(2), pp. 270-273.

Kent, D.C., and Park, R. (1971). "Flexural Members with Confined Concrete," Journal of the Structural Division. 97(ST7), pp. 1969-1990.

Kim, J.H. and Mander, J.B. (2007). "Influence of Transverse Reinforcement on Elastic Shear Stiffness of Cracked Concrete Elements," Engineering Structures. 29, pp. 1798-1807.

Klein, G.J. (1986). "Design of Spandrel Beams," PCI Journal. 31(5), pp. 76-124.

Larson, N., Gómez, E.F., Garber, D., Bayrak, O., and Ghannoum, W., (2013). "Strength and Serviceability Design of Reinforced Concrete Inverted T beams," TxDOT Report#0-6416-1, Center for Highway Research, University of Texas at Austin, Austin, TX.

Lucier, G., Walter, C., Rizkalla, S., Zia, P. and Klein, G., (2011). "Development of a Rational Design Methodology for Precast Concrete Slender Spandrel Beams: Part 1, Experimental Results," PCI Journal, Vol. 56, Issue 2, pp. 88-112.

Mander, J.B., Priestley, M.J.N., and Park, R. (1988). "Theoretical Stress-Strain Model for Confined Concrete," J. Struct. Eng. 114(8), pp. 1804-1826.

Mercan, B., Schultz, A. E., and Stolarski, H. K. (2010). "Finite Element Modeling of Prestressed Concrete Spandrel Beams," Engineering Structures. 32(9), pp. 2804-2813.

Mirza, S.A. and Furlong R.W. (1983a). "Serviceability Behavior and Failure Mechanisms of Concrete Inverted T-Beam Bridge Bent Caps," ACI Journal, 8(4), pp. 294-304.

Mirza, S.A. and Furlong R.W. (1983b). "Strength Criteria for Concrete Inverted T-Girders," J. Struct. Eng., 109(8), pp. 1836-1853.

Mirza, S.A. and Furlong R.W. (1985). "Design of Reinforced and Prestressed Concrete Inverted T Beams for Bridge Structures," PCI Journal, 30(4), pp. 112-136.

Nafadi, M.K., Khalafalls, O.M., Lucier, G.W., Rizkalla, S., Zia, P., and Klein, G.J. (2018) "Ledge Behavior and Strength of Short-Span L-Shaped Beams," PCI Journal, March-April pp. 67-86.

Nanni, A., Di Ludovico, M., and Parretti, R. (2004) "Shear Strengthening of a PC Bridge Girder with NSM CFRP Rectangular Bars," Advances in Structural engineering Vol. 7, No. 4, pp. 97-109.

Shahawy, M., and Beitelman, T.E., (1999) "Static and Fatigue Performance of RC Beams Strengthened with CFRP Laminates," Journal of Structural Engineering, Vol. 125, Issue 6, pp. 613-621.

Zhou, T., Roy, S. S., Wang, J., Nie, X., Chen, H., and Mo, Y. L. (2020). "Parametric Study on th Structural Behavior and Failure Mechanism of Skewed Inverted-T Bent Caps," Journal of Bridge Engineering. 25(11).

Zhu, R.H., Wanichakorn, W., and Hsu, T.T.C. (2001). "Crack Width Prediction for Interior Portion of Inverted T Bent-Caps," TxDOT Report#0-1854-3, Department of Civil and Environmental Engineering, University of Houston, Houston, TX.

Zhu, R.H., and Hsu, T.T.C. (2003). "Crack Width Prediction for Exterior Portion of Inverted T Bent-Caps," TxDOT Report#0-1854-4, Department of Civil and Environmental Engineering, University of Houston, Houston, TX.

Zhu, R.H., Dhonde, H., and Hsu, T.T.C. (2003). "Crack Control of Ledges in Inverted T Bent-Caps," TxDOT Report#0-1854-5, Department of Civil and Environmental Engineering, University of Houston, Houston, TX.